Electronic delocalisation in linear and cyclic porphyrin oligomers

Martin D. Peeks

Exeter College

University of Oxford

A thesis submitted for the degree of

Doctor of Philosophy

Michaelmas 2016

Nothing in life is to be feared, it is only to be understood. Now is the time to understand more, so that we may fear less.

— Marie Skłodowska Curie, as quoted in Our Precarious Habitat (1973) by Melvin A. Benarde, p. v

Acknowledgements

A supervisor can make or break a DPhil. I have been extremely fortunate to have Prof. Harry L. Anderson as a supervisor. His support, gentle encouragement and motivation have been essential. I am particularly grateful to have had the opportunity to freely explore so many different projects from a variety of directions.

The results from several excellent collaborators in Oxford are included in this thesis: Dr Claudia Tait (EPR) and her supervisor (Prof. Christiane Timmel), and Ms. Juliane Gong (photophysics) and her supervisor (Prof. Laura M. Herz). Thanks go to Prof. Tim Claridge, Dr Barbara Odell, Prof. Tony Parker (Central Laser Facility, CLF, Harwell), and Prof. John McGrady for helpful discussions. Several projects are not included in this thesis, but those involved (in the Anderson, Timmel, Herz and Baldwin groups at Oxford, the team at the CLF, and Heisler and Meech at UEA) are warmly acknowledged. Thanks also to Dr Arjen Cnossen, Ms. Renee Haver, Mr Takayuki Kobatake, and Dr Patrik Neuhaus for providing gifts of molecules.

Most of the work in this thesis was funded by the European Research Council (ERC, grant 320969). Additional funding came from Exeter College and the Department of Chemistry (Oxford) and computational time was generously provided by the Oxford Advanced Research Computing Facility.

Special thanks go to Prof. Harry L. Anderson, Ms. Isabell Grübner, and Ms. Kirstie McLoughlin for proofreading parts of this thesis, often with very short notice and/or during their holidays. Thank you for your patience, tenacity, and helpful comments.

Without the technical support at Oxford Chemistry, this work would not have been possible. Thanks to Ms. Terri Adams (glassblowing), Prof. Tim Claridge, Dr Barbara Odell, Ms. Tina Jackson and Ms. Maria Marshall (NMR), Prof. James McCullagh and Mr Colin Sparrow (mass spec.), Dr Robert Jacobs (SAF), and the workshop and facilities teams in the CRL, ICL and PTCL for all their help and commitment.

Around the time of ICPP in 2014, the HLA group (informally) upgraded itself to *The Amazing Andersons*. The name is no exaggeration. The group is friendly and supportive, and diverse enough that everyone can find their niche. First thanks go to Dr Patrik Neuhaus, who proved an excellent mentor and introduced me to porphyrin chemistry and DFT. Dr Arjen Cnossen, Dr Christiane Knappke and Dr Sophie Rousseaux kept the G1 ship afloat in my first year or two. They ran an excellent lab and were fantastic fonts of knowledge. Thanks are owed to everyone in G1 and G2, past and present, for maintaining such a supportive and fun environment in the lab. Particular thanks to (in [very] roughly chronological order): Patrik, Christiane, Arjen, Julien, Dima, Sophie, Rene, Cécile, Wilf, Levon, Nun, Renee, Jonathan,

Dan, Yaoyao, Isa, Sabine, Ibo and James (variously for their enthusiasm, helpful discussions, commitment to the coffee/tea break schedule, pub, and steak night).

My final and most profound thanks go to my family and to Kirstie, for their unquestioning and seemingly infinite support and patience. Thank you.

Abstract

This thesis presents a combined experimental and computational evaluation of the physical-organic properties of butadiyne-linked porphyrin oligomers. The principal result from the thesis is the synthesis and characterisation of the largest aromatic and antiaromatic systems to date, in the form of an oxidised [6]-porphyrin nanoring, with diameter 2.4 nm. This large electronically coherent system provides insight into the connection between aromatic ring currents and persistent currents in metal and semiconductor mesoscopic rings.

Chapter 1 briefly reviews the concepts used in the remainder of the thesis, with a particular focus on aromaticity.

In Chapter 2, the barrier to inter-porphyrin torsional rotation in a butadiyne-linked porphyrin dimer is determined computationally and experimentally to be 3 kJ mol^{-1}. The barrier height is closely related to the resonance delocalisation energy between the porphyrin subunits.

In Chapter 3 we show that by oxidising a butadiyne-linked [6]-porphyrin nanoring to its 4+ and 6+ oxidation states, the nanoring becomes antiaromatic and aromatic respectively. In contrast, the neutral oxidation state exhibits only local aromaticity for the six porphyrin units. The 12+ cation can also be generated, and exhibits local antiaromaticity for each porphyrin unit. The characterisation of (anti)aromaticity employs NMR and computational techniques.

In Chapter 4, the properties of cation radicals of linear and cyclic porphyrin oligomers are explored. Cations generated by spectroelectrochemistry are measured by optical spectroscopies, and chemically generated radical monocations are examined by cw/pulsed EPR spectroscopies. EPR and optical spectroscopies agree that the dimer monocation radical is fully delocalised, in Robin-Day Class III, whereas the monocations of longer oligomers are localised over 2–3 porphyrin units (Class II).

In Chapter 5, photophysical and computational investigations into excited state aromaticity in porphyrin nanorings are presented. The computational results suggest the presence of aromaticity in the triplet excited states, but experiment fails to convincingly demonstrate the effect.

Computational results in Chapter 6 show that a butadiyne linked [6]-porphyrin nanoring in which one butadiyne (C≡C−C≡C) is truncated to an alkyne (C≡C) exhibits a reversal of aromaticity and antiaromaticity in its oxidised states, compared to the all-butadiyne linked nanoring, consistent with Hückel's law.

Supplement to Statement of Authorship

In Chapter 4, EPR results for c.w. and ENDOR measurements of porphyrin radical cations are summarised. These results were obtained and processed by Dr Claudia E. Tait (under the supervision of Prof. C. R. Timmel and with the collaboration of Dr J. Harmer).

In Chapter 5, some photophysical results are presented. The radiative rates of differently sized porphyrin nanorings were measured by Ms. Juliane Q. Gong (under the supervision of Prof L. M. Herz).

Contents

List of Publications

1. S. Richert, J. Cremers, I. Kuprov, M. D. Peeks, H. L. Anderson and C. R. Timmel, 'Constructive quantum interference in a bis-copper six-porphyrin nanoring', *Nat. Commun.*, 2017, **8**, 14842

2. M. D. Peeks, T. D. W. Claridge and H. L. Anderson, 'Aromatic and antiaromatic ring currents in a molecular nanoring', *Nature*, 2017, **541**, 200–203

3. S. Richert, M. D. Peeks, C. E. Tait, H. L. Anderson and C. R. Timmel, 'Photogenerated triplet states in supramolecular porphyrin ladder assemblies: An EPR study', *Phys. Chem. Chem. Phys.*, 2016, **18**, 24171–24175

4. G. Karunanithy, A. Cnossen, H. Müller, M. D. Peeks, N. H. Rees, T. D. W. Claridge, H. L. Anderson and A. J. Baldwin, 'Harnessing NMR relaxation interference effects to characterise supramolecular assemblies', *Chem. Comm.*, 2016, **52**, 7450–7453

5. P. Liu, Y. Hisamune, M. D. Peeks, B. Odell, J. Q. Gong, L. M. Herz and H. L. Anderson, 'Synthesis of Five-Porphyrin Nanorings by Using Ferrocene and Corannulene Templates', *Angew. Chem. Int. Ed.*, 2016, **55**, 8358–8362

6. C. E. Tait, P. Neuhaus, M. D. Peeks, H. L. Anderson and C. R. Timmel, 'Excitation wavelength-dependent EPR study on the influence of the conformation of multiporphyrin arrays on triplet state delocalization', *Phys. Chem. Chem. Phys.*, 2016, **18**, 5275–5280

7. M. D. Peeks, P. Neuhaus and H. L. Anderson, 'Experimental and Computational Evaluation of the Barrier to Torsional Rotation in a Butadiyne-Linked Porphyrin Dimer', *Phys. Chem. Chem. Phys.*, 2016, **18**, 5264–5274

8. C. E. Tait, P. Neuhaus, M. D. Peeks, H. L. Anderson and C. R. Timmel, 'Transient EPR Reveals Triplet State Delocalization in a Series of Cyclic and Linear π-Conjugated Porphyrin Oligomers', *J. Am. Chem. Soc.*, 2015, **137**, 8284–8293

9. L. D. Movsisyan, M. D. Peeks, G. M. Greetham, M. Towrie, A. L. Thompson, A. W. Parker and H. L. Anderson, 'Photophysics of Threaded sp-Carbon Chains: The Polyyne is a Sink for Singlet and Triplet Excitation', *J. Am. Chem. Soc.*, 2014, **136**, 17996–18008

List of Numbered Structures

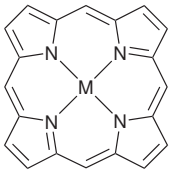 **1**	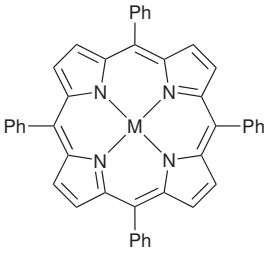 **2**
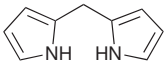 **3**	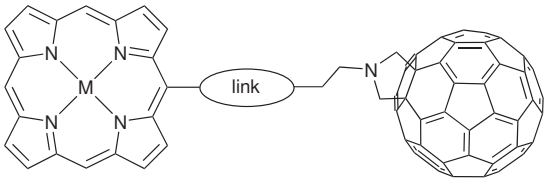 **4**
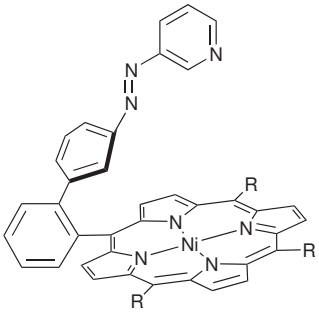 **5**	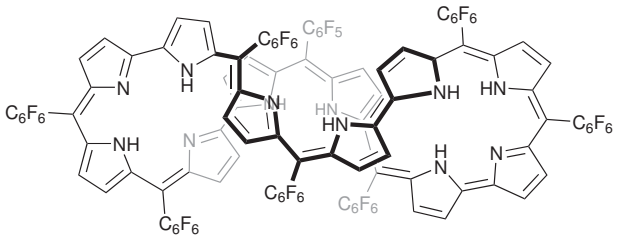 **6**
 **7**	 **8**
 **9**	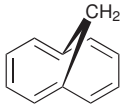 **10**
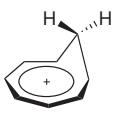 **11**	 **12**

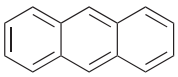

13

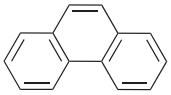

14

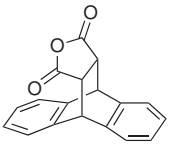

15

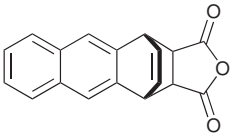

16

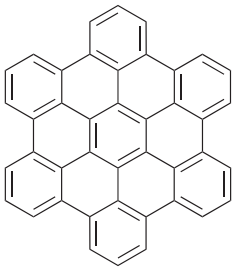

17

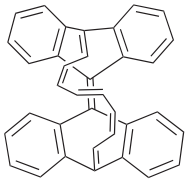

18

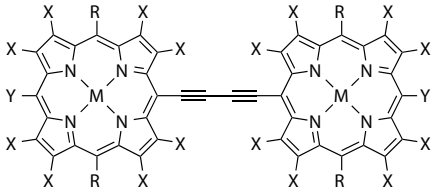

19

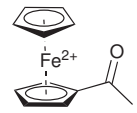

20

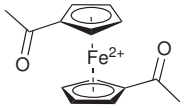

20

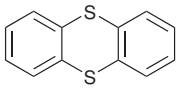

21

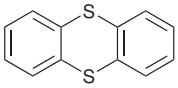

22

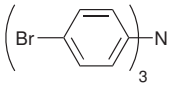

23

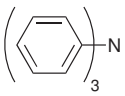

24

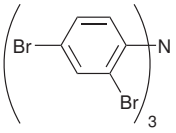

25

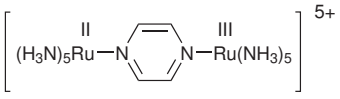

26

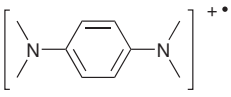

27

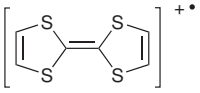	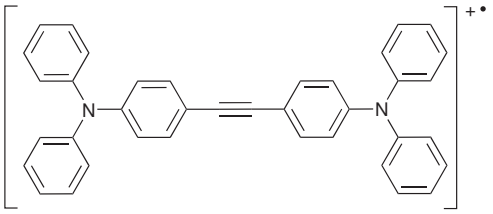
28	**29**

List of Abbreviations

Abbreviations

2PA	Two-photon absorption
A-B	Aharonov-Bohm
ACID/AICD	Anisotropy of the induced current density
ALS	Alternating least-squares
AR	Anti-resonance
ATR	Attenuated total reflectance
bipy	4,4′-Bipyridine
BLA	Bond-length alternation
C-T	Creutz-Taube (ion)
CBD	Cyclobutadiene
COT	Cyclooctatetraene
CPP	Cycloparaphenylene
CSGT	Continuous set of gauge transformations
CV	Cyclic voltammetry
cw	Continuous wave
DEER	Double electron-electron resonance
DFT	Density functional theory
DNA	Deoxyribonucleic acid
DP	Delocalised polaron
DPDA	Diphenyldiacetylene
DSSC	Dye-sensitised solar cell
ECL	Effective conjugation length
ECP	Effective core potential
EFA	Evolving factor analysis
ENDOR	Electron nuclear double resonance
EPR	Electron paramagnetic resonance
ES(A)A	Excited state (anti)aromaticity
FC	Franck-Condon
FT	Fourier transform
FWHM	Full width at half maximum
GGA	Generalised gradient approximation
GIAO	Gauge-independent atomic orbital
GPC	Gel permeation chromatography
HBC	Hexabenzocoronene
HF	Hartree-Fock
HLG	HOMO-LUMO gap
HOMA	Harmonic oscillator model of aromaticity
HOMO	Highest occupied MO
HT	Herzberg-Teller
IR	Infra-red
IRAV	IR active vibration
IUPAC	International Union of Pure and Applied Chemistry
IV-CT	Intervalence charge-transfer
LUMO	Lowest unoccupied MO
MALDI-TOF	Matrix assisted laser desorption ionisation-time of flight (mass spec.)
MCC	Maximum conductive chain
MCR	Multivariate curve resolution
MCT	Mercury-cadmium-telluride (IR detector)
MO	Molecular orbital
MS	Mass spectrometry
MV	Mixed valence
NICS	Nucleus-independent chemical shift
NIR	Near IR
NMR	Nuclear magnetic resonance
NTO	Natural transition orbital
OTTLE	Optically transparent thin layer electrochemistry
P3DT	Poly(3-decylthiophene-2,5-diyl)
P3HT	Poly(3-hexylthiophene-2,5-diyl)
PCM	Polarisable continuum model
PDT	Photodynamic therapy
PJT	Pseudo-Jahn-Teller
ppm	Parts per million
r.t.	Room temperature
RCM	Ring-current model
RF	Radio frequency
RMSD	Root mean squared deviation
SIE	Self-interaction error
STM	Scanning tunnelling microscopy
SVD	Singular value decomposition
SWV	Square-wave voltammetry

TBAP	Tetra-*n*-butylammonium hexafluorophosphate
TD-DFT	Time-dependent DFT
THF	Tetrahydrofuran
THS	Trihexylsilyl
TR-IR	Time-resolved IR
TTF	Tetrathiafulvalene
UV	Ultraviolet
VT	Variable temperature
XC	Exchange-correlation
XPS	X-ray photoelectron spectroscopy
ZPE	Zero-point energy

Symbols

ϵ_0	Vacuum permittivity, $8.85 \times 10^{-12}\,\mathrm{F\,m^{-1}}$
c	Speed of light, $3.00 \times 10^{8}\,\mathrm{m\,s^{-1}}$
m_e	Mass of an electron, $9.11 \times 10^{-31}\,\mathrm{kg}$
N_A	Avogadro's number, $6.022 \times 10^{23}\,\mathrm{mol^{-1}}$

Reader! Imagine a school-boy who has outgrown his clothes. Imagine the repairs made on the vestments where the enlarged frame had burst the narrow limits of its inclosure. Imagine the additions made where the projecting limbs had fairly and far emerged beyond the confines of the garment. Imagine the boy still growing, and the clothes, mended all over, now more than ever in want of mending – such is chemistry, and such its nomenclature.

— John Joseph Griffin in Chemical Recreations (7th Edition, 1834) "The Romance of Chemistry" p. 189

1 Introduction

Contents

1.1 Outline

This thesis explores electron delocalisation in porphyrin-based molecular wires, in both linear and cyclic topologies, and in neutral, cationic and excited electronic states. There is some necessity for restriction in the content of the introduction, and so only a very limited presentation of porphyrin chemistry will be made. Interested readers are referred to recent reviews,[1–4] and to other theses from the Anderson group which deliver comprehensive introductions to porphyrin chemistry.[5–7] The literature surrounding delocalisation of unpaired electrons (e.g. radical cations) on conjugated oligomers and in mixed-valence compounds is mainly dealt with in Chapter 4. For the most part, this introduction will be limited to a

discussion of aromaticity, particularly in the context of organic molecules. A brief introduction to computational techniques for the assignment and prediction of aromaticity will be given.

1.2 Porphyrins

Porphyrins, with their vivid colours, have captured chemists' imaginations since the discovery of the chemical properties of chlorophyll by Willstätter, for which he was awarded the Nobel Prize in 1915.[8,9] Chlorophyll, heme, and cytochrome proteins all contain porphyrins, and they all prove vitally important to life.

The simplest porphyrin is porphine **1** (Figure 1.1), comprising four pyrroles and four methines, arranged to form a tetrapyrrolic macrocycle with an aromatic 18 π-electron circuit. The 18 π-electron circuit can be represented by simplifying the porphyrin to an [18]-annulene (shown in red for tetraphenylporphyrin, TPP, **2** in Figure 1.1) or to a [16]-annulene dianion.[10,11] The atomic positions of porphine can be identified by the IUPAC systematic numbering (**1**) or by the common nomenclature. In the common nomenclature the methines are referred to as the *meso* positions, the pyrrole C−Hs are referred to as the β positions, and the quaternary pyrrole carbons are the α positions, as illustrated on TPP **2**.

Porphyrins are typically synthesised by condensation of an aldehyde and pyrrole, perhaps via a dipyrromethane (**3**, see for example Figure 1.1).[12,13] The resulting porphyrin monomers can be elaborated by oligomerisation, or by the introduction of substituents. In the former case, discrete porphyrin oligomers in diverse morphologies, with different linker groups, can be readily prepared (see later).[2,3] As an example of the latter case, dyads (e.g. **4**) and triads can be prepared for exploring photoinduced charge separation.[14,15]

The introduction of a central metal ion into a porphyrin, which acts as a square planar tetradentate ligand, allows further modulation of the porphyrin's properties. For example, a nickel(II) porphyrin **5** has been used as a photochemical spin switch, where the action of the azobenzene photoswitch causes an axial pyridine to coordinate to the Ni(II), changing it from low spin ($S = 0$) to high spin ($S = 1$) (Figure 1.2).[16] Copper(II) porphyrins are paramagnetic; they have been explored for their applications as biochemical distance rulers by double electron-electron resonance (DEER).[17] Axial coordination of ligands to metalloporphyrins, yielding square pyramidal or octahedral coordination geometries, is useful for the synthesis of supramolecular assemblies (Figure 1.3), as has been recently reviewed.[3]

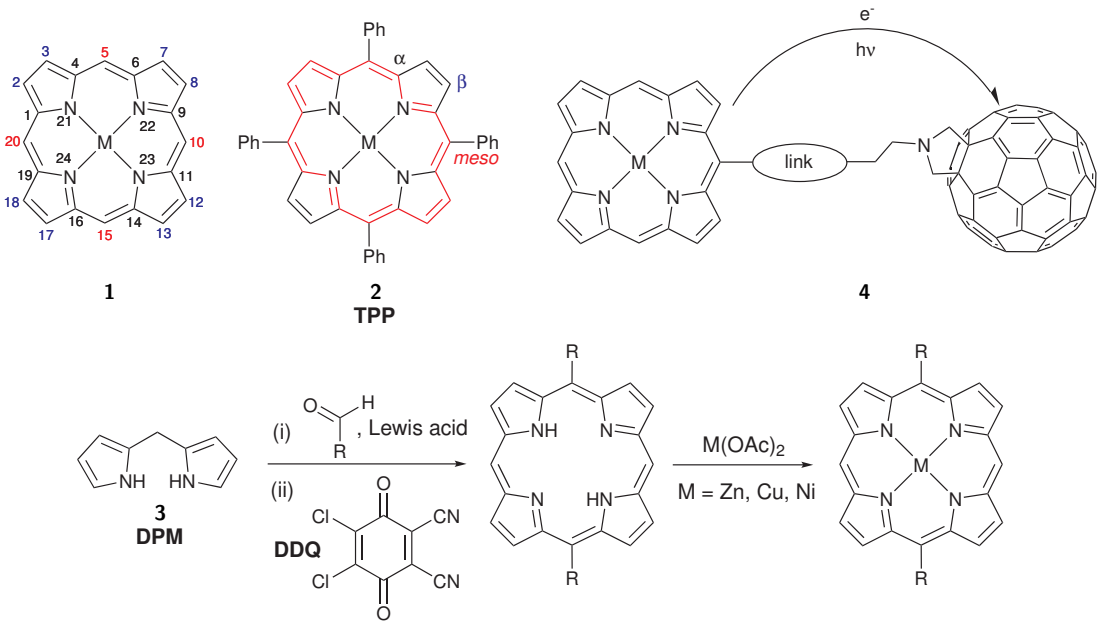

Figure 1.1: (top) Examples of porphyrins: **1** is porphine, with IUPAC atom numbering indicated; **2** is tetraphenylporphyrin (TPP), with the [18]-annulene aromatic circuit indicated in red, and with the 'common names' for the atomic positions; **4** is a schematic example of a C_{60}–porphyrin dyad, in which absorption of a photon of light can result in charge separation. (bottom) Example of porphyrin synthesis by condensation of an aldehyde with DPM **3**, followed by oxidation with DDQ. Metal insertion then follows.

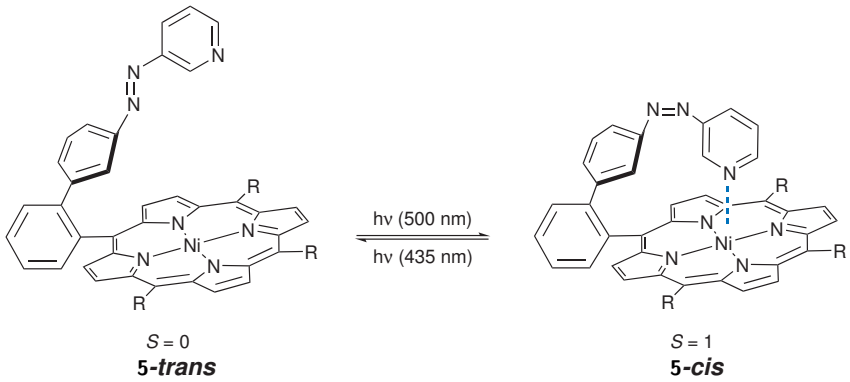

Figure 1.2: A photochemically mediated spin switch employing an azobenzene link which, upon irradiation with 500 nm light, undergoes a *trans–cis* isomerism, causing a pyridine ligand to axially coordinate the Ni(II) and switching the spin state from low spin (***trans***) to high spin (***cis***).[16]

This thesis concerns the chemistry of butadiyne-linked zinc-porphyrin oligomers. This class of oligomer was first prepared by Arnold in 1978,[18] and has since been the subject of intense study, mainly by his group and that of Anderson.[19–22] Historically, Arnold focused primarily on the physical properties of short oligomers (e.g. porphyrin dimers),[20] whilst Anderson explored the supramolecular chemistry of porphyrins. The Anderson group has prepared spectacular structures such as porphyrin ladders,[23] the nanoring-template complex ***c*-P6•T6**,[24] the Vernier-templated figure-of-eight ***c*-P12•T6$_2$**,[25] ring-in-ring complexes,[26] and an axially elongated nanoring tube ***t*-P12•T6$_2$** (Figure 1.3).[27] The preparation of these

structures has relied on the binding of nitrogenous ligands – typically pyridine – to the axial coordination site of the Zn-porphyrin. The Zn-porphyrin–pyridine binding constant is weak ($K = 10^4$ M^{-1}),[28] but chelate cooperativity diminishes the entropic cost for multiple-binding, leading to huge binding constants.[29] For example, **T6** in ***c*-P6•T6** has a binding constant of $K = 10^{36}$ M^{-1}.[24] The butadiyne link ensures good conjugation between the porphyrin units, which can readily adopt a coplanar conformation without steric hindrance, in contrast to the steric clash between porphyrin β-protons in a planar monoalkyne-linked dimer. However, as we will see in Chapter 2, there is little thermodynamic preference for planarity: the barrier to torsional rotation in a butadiyne-linked porphyrin dimer is about 2 kJ mol^{-1}.[30,31] As such, butadiyne-linked porphyrin oligomers are prone to the introduction of conjugation-breaking defects in the form of non-planarity of adjacent porphyrin units.

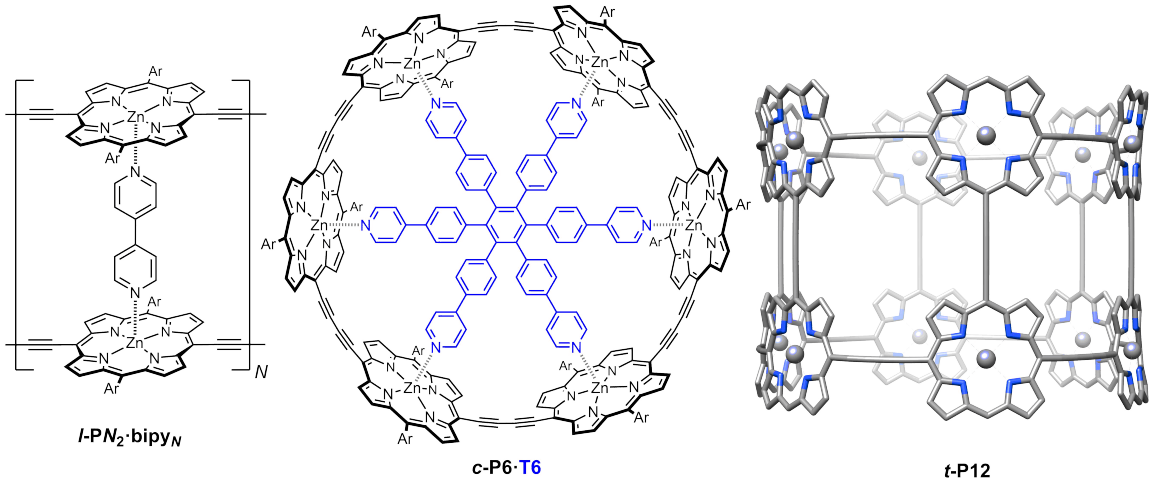

Figure 1.3: A double-stranded porphyrin ladder formed by coordination of 4,4′-bipyridine (bipy),[23] a [6]-porphyrin nanoring ***c*-P6•T6**,[24] and a [12]-porphyrin nanotube (BLYP/6-31G*) ***t*-P12**.[27]

The high absorption coefficients of porphyrins and their oligomers often motivate comparisons to the light harvesting complexes in green plants, which comprise circular arrays of chlorophyll molecules.[32,33] Efforts continue to use porphyrins in high-efficiency dye-sensitised solar cells (DSSCs), through both the design of new materials and investigations into electron transport properties.[15,34] To date, the power conversion efficiency of synthetic DSSCs has reached 12%, compared to 22% for leading perovskite materials and 26% for silicon cells.[35] The theoretical limit for a single-junction cell, the Shockley-Queisser limit, is 34%.[36] Porphyrins have found more application in medicine, where they are employed for photodynamic therapy (PDT). In this treatment for cancer, a sensitiser molecule (porphyrin)

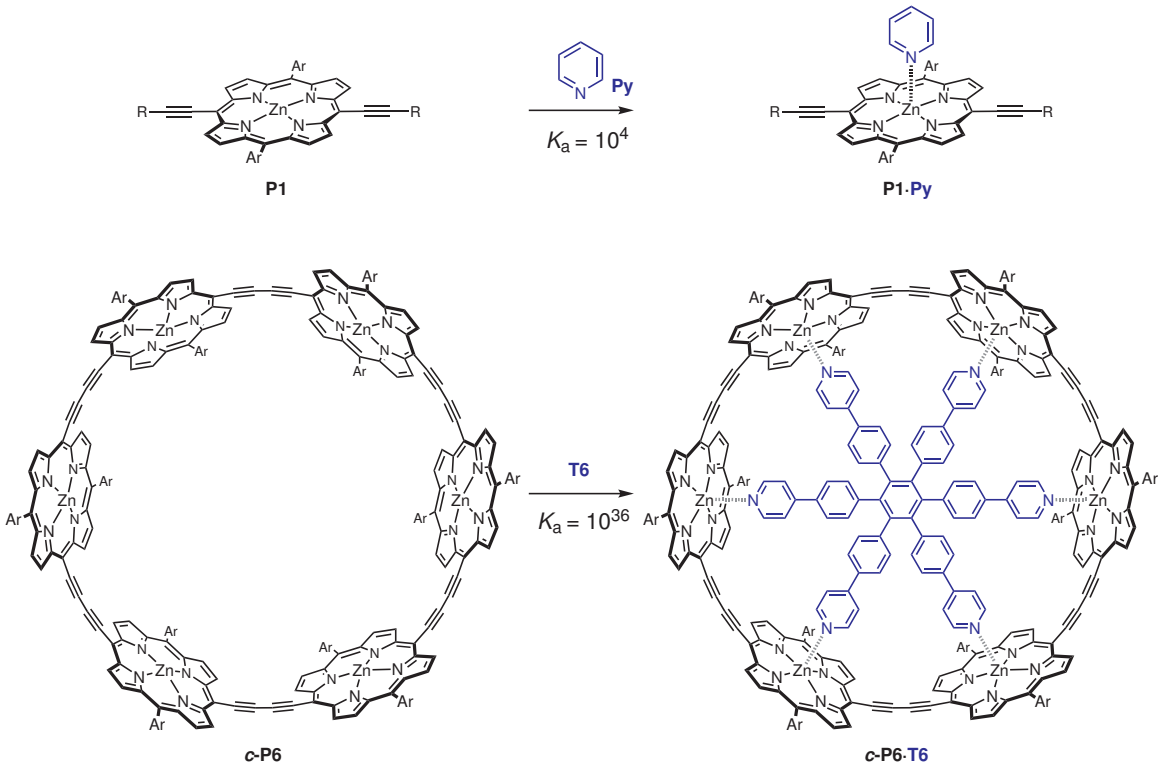

Figure 1.4: Comparison of binding constants for a porphyrin monomer to pyridine and for a [6]-porphyrin nanoring ***c*-P6** to a hexadentate template **T6**, demonstrating significant cooperativity in the latter.

accumulates in a tumour and is then irradiated with light. Intersystem crossing to the triplet manifold occurs, resulting in sensitisation of oxygen and oxidative destruction of tissue.[37,38]

The field of porphyrin chemistry is broadened by the introduction of the porphyrinoids and the expanded and contracted porphyrins.[39,40] These molecules are essentially variations upon the theme of the porphyrin: for example, diverse porphyrinoids can be generated by replacing the pyrroles of the macrocycle with other 5-membered aromatic rings, like furan or thiophene.[41,42] Expanded porphyrins (e.g. **6**, Figure 1.5) are simply large porphyrinoids, with at least 17 atoms in their 'internal ring pathway'.[43,44] The diversity of porphyrinoids has proven extremely useful for dissecting concepts in aromaticity,[39,45–47] including excited state and Möbius aromaticity, as we shall see in the next section.

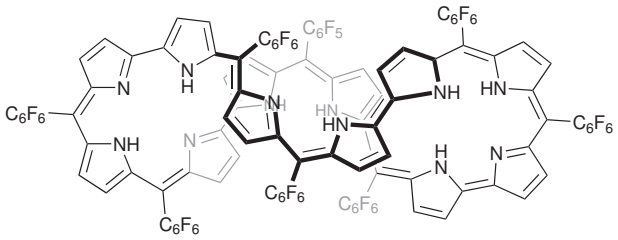

6

Figure 1.5: Osuka's Hückel aromatic [50]-π expanded porphyrin **6**.[48]

1.3 Aromaticity

Aromaticity is a heavily-reviewed topic, and was the subject of entire issues of *Chem. Rev.* in 2001 and 2005,[49,50] and of *Chem. Soc. Rev.* in 2015.[51] In this section, a brief historical account of aromaticity will be given, illustrated by prominent examples.

A simple bibliometric analysis using Google Books[52] shows that, although benzene was widely written about from the late 1800s, the concept of 'aromaticity' only gained prominence with the appearance of molecular orbital theory, ring current theories, and NMR (Figure 1.6a, nuclear magnetic resonance). This correlation describes the development of aromatic chemistry, from the study of compounds with particular olfactory properties to the broad-ranging subject of aromaticity, facilitated by synthetic, spectroscopic, and computational advances.

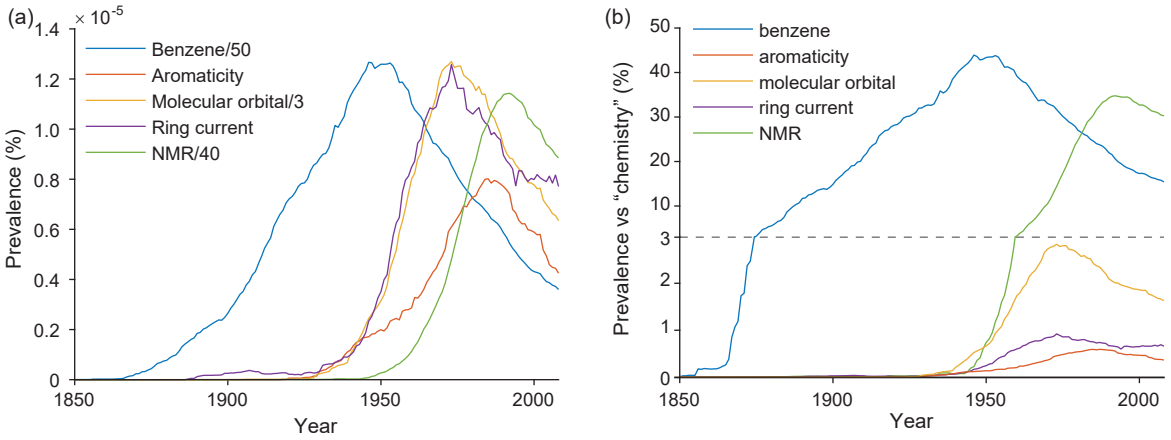

Figure 1.6: Bibliometric analysis (ngrams)[52] showing the use of benzene, aromaticity, molecular orbital, ring current and NMR in the English language corpus of Google Books.[52] In (a) the prevalence of each phrase, case insensitive, is shown. The numbers in the legends denote a scale factor applied to the specified term. In (b) the prevalence of the (case sensitive) terms relative to the prevalence of the word 'chemistry' are shown. All data are smoothed with a 10-point (21-year) moving average.

The decline in frequency in all of these terms since the mid-1900s is partly a consequence of chemistry forming a smaller part of the English language corpus in modern times. In

Figure 1.6b, the frequencies of several terms relating to aromaticity are normalised by the frequency of the word 'chemistry'. The results show that relative to chemistry, interest in ring currents and aromaticity has remained fairly steady since the 1980s. It is reflective of benzene's importance that in the 1940s, the word 'benzene' was mentioned almost half as many times as the word 'chemistry'!

1.3.1 Early aromaticity

Benzene (**7**, Figure 1.7) was isolated by Faraday in 1825, but its structure remained unknown until the 1860s. After Kekulé and Coupers' independent realisations that carbon is tetravalent,[53,54] the former deduced (through the famous, perhaps apocryphal, day-dream of a snake biting its own tail) that benzene is cyclic.[55] Kekulé proposed a benzene structure with alternating single and double bonds, which he later refined by the suggestion that the single and double bonds rapidly interconverted.[56] Benzene and the other aromatic molecules became defined by reactivity, most notably by the fact that they underwent a substitution reaction with bromine, as opposed to the addition expected for alkenes (Figure 1.8).

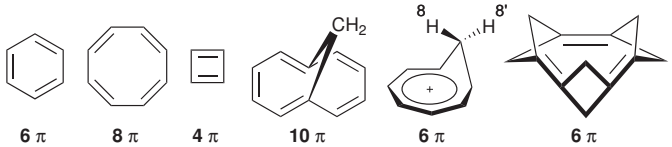

Figure 1.7: Examples of aromatic, non-aromatic, and antiaromatic compounds.

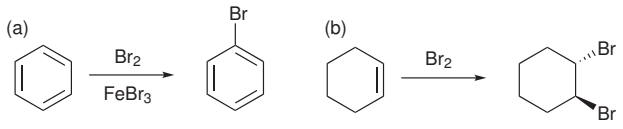

Figure 1.8: (a) Benzene undergoes a substitution reaction with bromine, in the presence of $FeBr_3$ as an activating Lewis Acid; (b) cyclohexene undergoes an addition reaction with benzene.

Thiele proposed a theory to account for this reactivity, namely that unsaturated carbons had a 'partial valence', which was especially reactive.[57] Adjacent pairs of partial valences could interact with (saturate) each other, provided neither was at a terminal position (hence, the partial valences in ethylene could not saturate). Reactivity was thus found at the unsaturated partial valences, explaining the reactivity at the 1,4-positions of 1,3-butadiene and the stability of benzene (Figure 1.9). However, Thiele's theory was proven wrong by our earlier hero of chlorophyll chemistry, Willstätter, who isolated cyclooctatetraene

(COT, **8**) in 1911,[58] and found that it reacted with bromine as an alkene, without any hint of partial valence stabilisation.

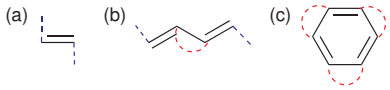

Figure 1.9: Thiele's theory of partial valences applied to (a) ethylene, (b) 1,3-butadiene and (c) benzene. Partial valences are indicated by dotted lines: blue dotted lines are unsatisfied partial valences, and thus sites of high reactivity. Saturated partial valences are denoted by red dotted semicircles: these positions are unreactive.

Although much research into aromatic compounds continued in the latter part of the 19$^{\text{th}}$ century, heavily motivated by their application in dyestuffs, the notion of aromaticity as a distinct chemical property did not really exist until the 1930s, with the development of molecular orbital theory, and only became ascendant as late as the 1950s (Figure 1.6).

1.3.2 The aromatic sextet and Hückel's theory

Crocker, Armit and Robinson presented the idea of the *aromatic sextet* in the 1920s, proposing that benzene's aromatic stability arose from the favourability of a sextet of valence electrons.[59–61] Pauling and Wheland soon developed valence bond (VB) theory and the accompanying notion of resonance was quickly adopted by organic chemists. Benzene's aromatic stabilisation was explained by the presence of multiple resonance structures, in which the delocalised π-electrons are represented by different VB representations: more resonance structures confer more stability.[62] Although Erich Hückel's molecular orbital (MO) theory was developed in the 1930s, and was able to quantitatively explain the stability of aromatic molecules, his explanations struggled to displace the pervasive and simple resonance theory.[63,64] It was really only with the development of mnemonics, such as Doering's presentation of the $[4n+2]$ rule[65] (bringing the theory back to aromatic sextets) and Frost and Musulin's graphical presentation of Hückel's orbital energies[66] that Hückel's MO theory entered the mainstream.[64] The familiar $[4n+2]$ rule states that a molecule with $[4n+2]$ conjugated π-electrons is aromatic, while a molecule with $[4n]$ π-electrons is antiaromatic, where n is a non-negative integer.

By constructing the Frost-Musulin diagrams for benzene and cyclobutadiene (CBD, antiaromatic, **9**) we can immediately see that benzene, in a D_{6h} model, has a filled degenerate pair of orbitals as its highest-occupied MO (HOMO), whereas CBD, with only $[4n]$ π-electrons, adopts a triplet configuration in its D_{4h} symmetric structure (Figure 1.10).

Further calculations reveal that CBD is better described as a D_{2h} rectangle, with increased double-bond and single-bond character (i.e. bond length alternation, BLA) compared to benzene.[67] This pseudo-Jahn-Teller (PJT)[68] distortion is common to the [4*n*]-π antiaromatic molecules, and lifts the HOMO degeneracy as shown in Figure 1.10, leading to a closed shell antiaromatic configuration with a small HOMO–LUMO (lowest unoccupied MO) gap.

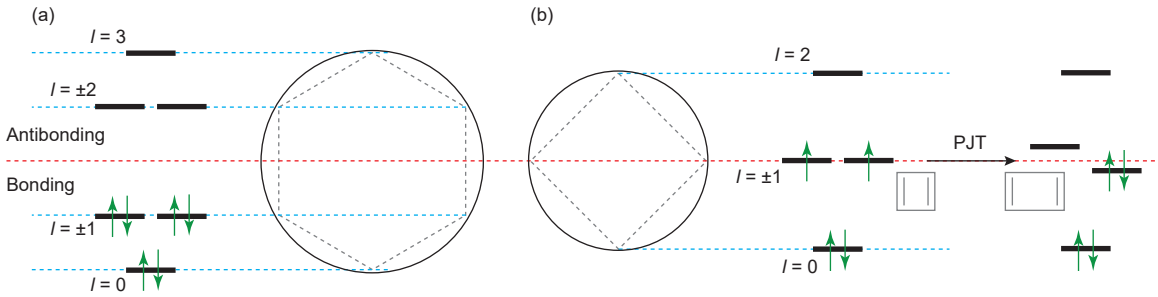

Figure 1.10: Frost-Musulin diagrams for (a) benzene and (b) CBD. In (a), all of the bonding orbitals (below the horizontal red line) of benzene are filled. In (b), the half-occupied degenerate pair is non-bonding. A pseudo-Jahn-Teller (PJT) distortion breaks the degeneracy and leads to a bonding character for one electron pair.

1.3.3 Ring currents

In addition to advances in theory, the early part of the 20th century saw a development of experimental methods for the quantification of aromaticity. Pascal noted that aromatic molecules were more diamagnetic (χ_M) than expected on the basis of additive substituent contributions (χ'_M),[69] and Pacault termed this excess of diamagnetic susceptibility the 'exaltation' (Λ).[70,71]

$$\Lambda = \chi_M - \chi'_M \tag{1.1}$$

The utility of exaltation measurements for the assignment of aromaticity was demonstrated by Dauben et al. in 1969,[72] but by this time there was a more experimentally informative, and appealing, method of measuring magnetic properties: NMR. Nowadays, susceptibility measurements have almost entirely fallen out of favour,[73] despite the fact that they were once described as the 'only' unambiguous assignor of aromaticity.[74]

NMR is a particularly helpful descriptor of aromaticity because of the effect of so-called aromatic ring-currents on NMR chemical shifts. The resonances of nuclei inside an aromatic ring are shielded; those outside are deshielded. For example, the protons of

benzene are deshielded from an olefinic chemical shift (5 ppm) to what is now colloquially called 'the aromatic region', around 7 ppm. In the ring-current model (RCM) the delocalised π-electrons in an aromatic ring precess about the ring centre in the presence of an external magnetic field B_{ext} (typically defined along the z axis, perpendicular to the molecular plane). This precession is a *diatropic* current of electrons which flows clockwise around the ring, when viewed from the z axis (looking towards $-z$) (Figure 1.11). Consistent with Ampère's right hand screw rule, this induced ring-current J_{ind} has an associated magnetic field B_{ind}, which opposes B_{ext} inside the ring (hence has a shielding effect) and reinforces B_{ext} outside the ring (hence deshielding). Examples of the shielding and deshielding effects arising from the RCM will be discussed shortly, but first we must give a surprisingly late introduction to antiaromaticity, via the annulenes.

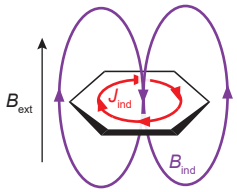

Figure 1.11: Representation of the induced ring current (J_{ind}) in benzene in the presence of an applied magnetic field (B_{ext}). The induced current generates its own magnetic field, B_{ind} which opposes B_{ext} inside the ring, and reinforces it outside.

Benzene, COT and CBD are all members of the class of molecules termed the *annulenes* by Sondheimer.[75] Annulenes are ring systems of general formula C_mH_m comprising alternating single and double C–C bonds. Sondheimer prepared a spectacular array of annulenes and dehydroannulenes, in which some C=C bonds are replaced with C≡C bonds.[76–78] He made the remarkable discovery that while the $[4n + 2]$-annulenes exhibited NMR spectra similar to that of benzene: i.e. shielded inner resonances and deshielded outer resonances, the $[4n]$-annulenes had reversed spectra: inner resonances were deshielded and outer resonances shielded.[77]

The term *antiaromatic* was first applied by Breslow in 1965 to describe the instability exhibited by some molecules with $[4n]$ π-electrons, antithetical to the established aromatic stabilisation of $[4n + 2]$-π molecules.[79] In antiaromatic molecules, the ring current flows in the opposite direction (*paratropic*) to that in aromatic molecules,[80] which accounts for the opposite effects on chemical shifts.

It is important to note that both aromatic and antiaromatic molecules simultaneously possess counter-rotating diatropic and paratropic ring current character to different extents. The diatropic ring current (and the diamagnetic susceptibility) is a ground state property; paratropic currents (and temperature-independent paramagnetic susceptibility) arise from interactions with excited states.[81] It is easy to see why the paratropic currents can dominate for antiaromatic molecules due to the smaller HOMO-LUMO gap.

In a Hückel theory approximation, a symmetric annulene has a manifold of π-orbitals with angular momentum values $l = 0, \pm1, \pm2 \ldots$. For aromatic molecules with $[4n + 2]$ π-electrons, these orbitals are filled to $l = \pm n$. In the antiaromatic case, the degenerate pair $l = \pm n$ is only half-filled, and can undergo distortions to lift the $l = \pm n$ degeneracy and afford a HOMO with $l = n$ and LUMO with $l = -n$. The HOMO–LUMO gap is small in this case, compared to that for an aromatic molecule (Figure 1.10), so the excited state transition (and accompanying change in angular momentum) which induces the paratropic ring currents is more accessible.[81,82]

Fowler and Steiner have presented an alternative model in which the ring current direction is predicted by the symmetry of the dominant frontier-orbital transitions – in this model, both diatropic and paratropic ring currents arise from transitions to excited states. A rotationally allowed transition (as between a Jahn-Teller distorted angular-momentum pair) leads to a paratropic current, while a translationally allowed transition (as between $l = \pm n$ and $l = \pm[n + 1]$) leads to diatropicity.[80,83] More thorough introductions to the quantum mechanical origin of ring currents and magnetic susceptibilities can be found in the cited reviews and references therein.[84,85]

The NMR shielding effect inside an aromatic ring can be probed by molecules where an NMR-active nucleus is located inside the ring. Vogel and coworkers were able to synthesise a [10]-annulene derivative with a methylene bridge above the annulene plane (1,6-methanocyclodecapentaene, **10**): as expected from the RCM, this methylene is shielded by about 2–3 ppm to -0.5 ppm.[86] The propensity of Li^+ to coordinate to the π-systems of aromatic molecules can also be exploited, allowing the use of ^{7}Li NMR to measure the ring-current shielding effect.[74]

Porphyrin chemistry provides many examples of the ring current shielding effects for aromatic and antiaromatic derivatives. The porphine ligand is formally in a $2-$ oxidation

state with an aromatic set of 18 π-electrons. Typically, a 2+ metal binds to the porphyrin to give a net zero charge, as is the case for M = Zn, Mg, Ni, 2H, etc. In the latter case, M = 2H, the protons are characteristically shielded from a pyrrolic 8 ppm to -2 ppm. Vaid and coworkers have prepared a TPP complex of Si, where the TPP ligand has a -4 (20π) oxidation state. ^{29}Si NMR shows that the central Si is deshielded by 125 ppm on account of the antiaromatic ring-current.[87]

1.3.4 Other experimental signs of aromaticity

There are other properties available by which to assign aromaticity. The most traditional of these is based on aromatic reactivity: a propensity to undergo electrophilic aromatic substitution rather than addition. A related aspect is the energetic stability of aromatic systems, arising from a large resonance stabilisation energy (contrast to zero, or negative, stabilisation for antiaromatic systems). Finally, structural properties can support an assignment of aromaticity: aromatic compounds exhibit a low BLA, whereas the pseudo-Jahn-Teller distortion for antiaromatic compounds leads to a higher BLA. Such data can come from infra-red (IR) or Raman spectroscopies, X-ray diffraction, or from calculation.

1.3.5 Predicting aromaticity

There is a multitude of methods available to computationally predict and characterise aromaticity in molecules. Their utility is facilitated by the availability of computing power and the applicability of density functional theory (DFT), which scales well for small molecules (systems with a few hundred atoms are routine) with generally accurate results.

1.3.5.1 Ring currents

Perhaps the most popular methods for predicting aromaticity are those which measure the properties of the aromatic ring current. The first of these techniques was the nucleus independent chemical shift (NICS), which evaluates the NMR shielding at a point in space around a molecule. This is achieved by placing a 'ghost' atom (in Gaussian, 'Bq', after the character (latterly a ghost) Banquo[88] in *Macbeth*) at the desired probe position(s). In the first reported NICS calculations, the ghost atoms were placed at the geometric centres of rings.[89] For some inorganic ring systems, it was noted that the in-plane NICS was prone to contamination by σ and in-plane π bonds, motivating the dissection of π and σ components

to give $NICS_{\pi}$ and $NICS_{\sigma}$.[90] The measurement of NICS(X) at some position X Å above the ring plane was also used for these inorganic systems, to avoid in-plane contributions.[90] Indeed, it had been earlier noted that NICS values were higher above the ring plane than in the plane for small π-aromatic systems, reflecting the toroidal distribution of π-electrons and the presence of σ bond anisotropy contamination for in-plane measurements.[89]

In addition to choosing a suitable z-axis height, the selection of the correct tensor component to describe aromaticity is also important: the original report used the isotropic (iso) shielding ($NICS_{iso}$),[89] but later studies have placed increased emphasis on the zz shielding tensor component ($NICS_{zz}$) as being more reflective of aromaticity effects. Of the myriad combinations of 'dissected NICS' (i.e. π contributions only), distances above the ring plane, and tensor components, it was found that $NICS(0)_{\pi zz}$ gave the best correlation to aromatic stabilisation energy, and that the non-dissected $NICS(1)_{zz}$ was a suitable alternative, since shifting the ghost atom 1 Å above the ring plane has the effect of removing most in-plane contamination.

Since its invention in the late 1990s the NICS method has been extended to the calculation of shielding isosurfaces[91] and NICS-scans[92] which reveal the variation in aromaticity in different parts of a molecule.[92,93] Examples of the utility of NICS and its derivatives have been thoroughly reviewed.[73,94]

NICS evaluates the effects of the ring current: the magnetic shielding and deshielding. It is also possible to computationally predict and visualise the ring current. The anisotropy of the induced current density (ACID) method depicts the induced current as an isosurface around the molecule.[95] By examining this anisotropy property, rather than just the current density field, it is possible to subtract out local diamagnetic (isotropic) atomic ring currents, which otherwise dominate. As a result, electron delocalisation can be visualised as a three-dimensional isosurface around the molecule (Figure 1.12).

ACID was first applied by Wallenborn et al. to assess transition state aromaticity,[96] and the utility of the technique was significantly broadened from aromaticity to other examples of conjugation, including hyperconjugation and spiroconjugation, by Herges et al.[95,97] An illustrative example of ACID's application to porphyrin ring currents shows the utility of the technique in dissecting electron delocalisation pathways.[46] The additional calculation of induced current vectors shows the direction of electron flow in the presence of an applied field, and thus the assignment of diatropic and paratropic ring currents.[97]

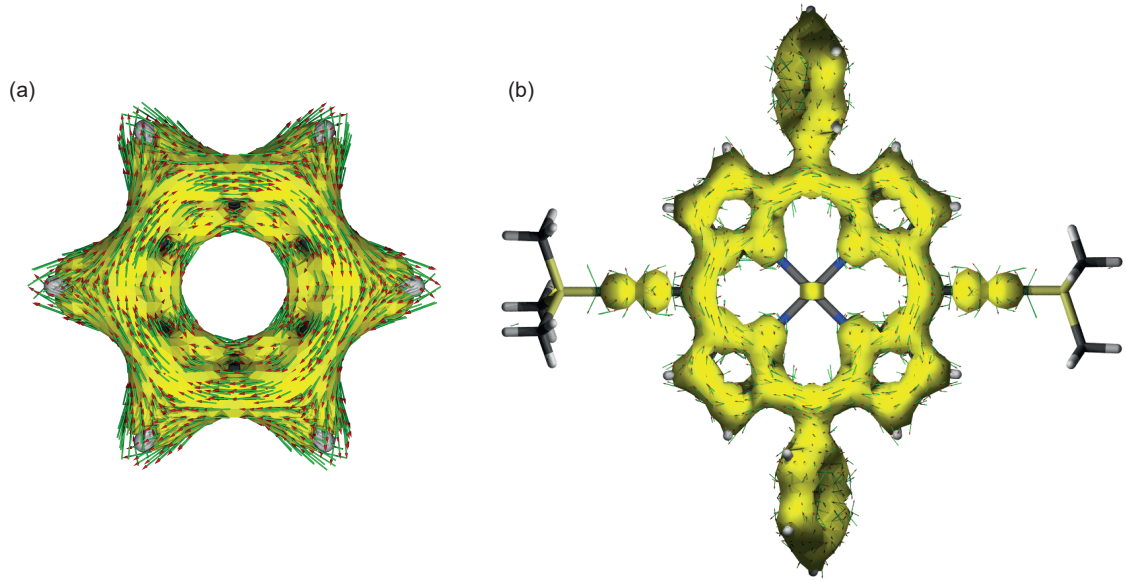

Figure 1.12: ACID isosurfaces (yellow, isovalue = 0.05) and current vectors (green/red) for (a) benzene and (b) a zinc porphyrin monomer. The monomer is substituted with trimethylsilylacetylenes. B3LYP/6-31G* (LANL2DZ ECP for Zn). The current vectors are calculated for an applied magnetic field perpendicular to the aromatic ring planes (i.e. out of the page).

It is also possible to directly calculate the magnitude of the ring current passing through a given bond. The Gauge-Including Magnetically Induced Currents (GIMIC) technique is popular for this calculation, and several examples of its use have been reported.[98–100]

1.3.5.2 Structural

In benzene, all of the C−C bonds are of equal length: there is no BLA, indicating complete electron delocalisation. The extent of BLA in a molecule can be quantified using the harmonic oscillator model of aromaticity (HOMA)[101]

$$\text{HOMA} = 1 - \left[\frac{\alpha}{N}\sum_{i}^{N}(R_{\text{opt}} - R_{\text{i}})^2\right] \tag{1.2}$$

$$= 1 - \alpha(R_{\text{opt}} - R_{\text{av}})^2 - \frac{\alpha}{N}\sum_{i}^{N}(R_{\text{av}} - R_{\text{i}})^2 \tag{1.3}$$

$$= 1 - \text{EN} - \text{GEO} \tag{1.4}$$

where HOMA is a quantity from 0 (complete localisation) to 1 (complete delocalisation), α is an empirical scaling constant, N is the number of bonds over which the sums run, R_{i} is the length of the i$^{\text{th}}$ bond, R_{av} is the average bond length, and R_{opt} is the optimum bond length for a fully delocalised bond (e.g. 1.388 Å for C−C).[101] In other words, the first term

(EN) relates to an increase (vs. the optimum) in mean bond length in the system, and the second term (GEO) relates to the amount of BLA. Both of these parameters indicate non-aromaticity, and hence a decrease in HOMA towards zero.[102]

The theory and application of structural descriptors of aromaticity have been reviewed by Krysowski and Cyrański.[103] Although BLA is a good metric for aromaticity in small molecules, it has been shown computationally that [30]-annulene exhibits the magnetic characteristics of aromaticity despite the presence of significant BLA, and even larger annulenes (up to [66]-annulene) are aromatic if high symmetry (D_{6h}) is retained.[104,105]

1.3.5.3 Energetic

The increased thermodynamic stability conferred by aromaticity is often termed the aromatic stabilisation energy (ASE), and can be calculated explicitly. The forerunners of the ASE methods were estimations of resonance energy, either by experiment or calculation.[71,106]

In calculations of resonance energy, the additional stabilisation of aromaticity is taken as the difference between the aromatic molecule's energy and the energies of the substituent 'localised' components. For example, the resonance energy of benzene can be estimated by the difference of benzene's electron energy and the sum of its bond contributions: three C=C, three C−C and six C−H. These approaches require the energy of the aromatic molecule, and reliable energies for the localised substituents.

The calculation of ASE depends on devising, and calculating, a suitable reaction scheme which directly reports on the aromaticity of the molecule, whilst avoiding contributions to the reaction energy from changes in hybridisation or atom numbers. The two primary methods are the homodesmotic stabilisation energy (HSE) and its improved form: the isomerisation stabilisation energy (ISE) (Figure 1.13).[107] In the former, starting materials and products have the same number of atoms with the same hybridisation. In the latter, the aromatic molecule is optimised with a methyl substituent: the ISE comes from the difference in energy when the methyl is converted into an exocyclic double bond with accompanying loss of aromaticity.

The ISE has been evaluated for the annulenes from benzene ([6]-annulene) to [66]-annulene (Figure 1.14).[104] As ring size increases, ISE-per-electron becomes vanishingly small: for example, [42]-annulene has an ISE-per-electron of 2.3 kJ mol^{-1}. Put into context, this is about the same as the entropic cost, at room temperature, of freezing a sp^2–sp^2 torsion.[108] This comparison implies that, for large annulenes, the aromatic stabilisation

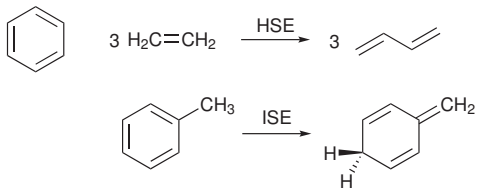

Figure 1.13: (top) A homodesmotic reaction for calculating the HSE of benzene; (bottom) the reaction scheme for calculating the ISE of benzene.

energy becomes vanishingly small compared to the entropic cost of maintaining a regular cyclic geometry necessary for aromaticity.

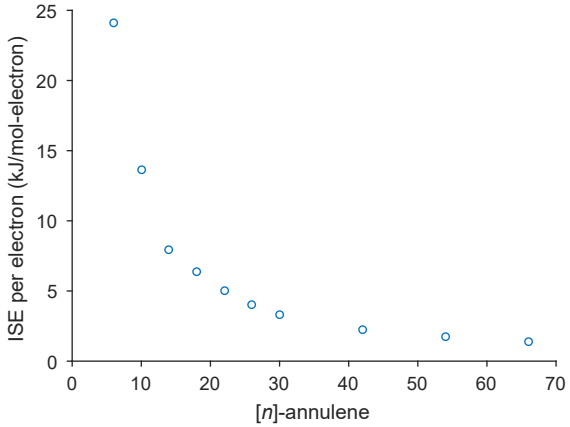

Figure 1.14: Isomerisation stabilisation energy (ISE) per electron for the annulenes, B3LYP/6-31G*. Data from Wannere and Schleyer.[104]

1.3.5.4 Electronic

There has been a recent adoption of computational aromaticity metrics which describe electron delocalisation directly, rather than a physical observable such as BLA, or magnetic properties. These metrics have recently been reviewed.[109] Indeed, the ACID method (see Section 1.3.5.1) also falls into this category. Without going into too much detail, many electron-delocalisation measures are calculated by evaluating the nature of the electron density at bond critical points and ring critical points (i.e. at the centres of bonds and rings), within the framework of the Quantum Theory of Atoms in Molecules.[110] In contrast to the other methods presented above, wavefunction analysis is perhaps the most remote from an experimental observable (cf. NMR for NICS, crystallography for structural properties, and calorimetry for stabilisation energies).

1.3.6 Topological effects on aromaticity

The annulenes are all monocyclic carbocycles, but molecules can exhibit much broader topological diversity, which has implications for the assignment of aromaticity. In this section we discuss, roughly in order of their appearance in the literature, polycyclic aromaticity and Clar's rule, homoaromaticity, and Möbius aromaticity.

1.3.6.1 Polycyclic aromaticity

Some of the earliest identified aromatic compounds, on the basis of smell, were those comprising fused benzene rings. These molecules exhibit some non-aromatic character in their reactivity: anthracene (**13**), comprising three linearly fused benzene rings, undergoes Diels-Alder reaction at the 9,10-positions of the central benzene ring. Phenanthrene (**14**) has distinctly olefinic chemistry at its 9,10-positions. These observations were rationalised by Clar, who noted that the aromaticity of a polybenzenoid molecule depends on the number, and location, of discrete aromatic sextets of six π-electrons.[111] In anthracene, three resonance structures, each with one sextet, can be drawn; Diels-Alder chemistry at the 9,10-positions offers a product with two Clar sextets (**15**), while reaction at either of the terminal benzene rings gives just one Clar sextet (**16**). Hence reactivity is exclusively at the 9,10-positions. For phenanthrene (**14**), the maximum possible number of sextets is two, for the terminal rings, leaving olefinic character in the central ring (Figure 1.15).[112]

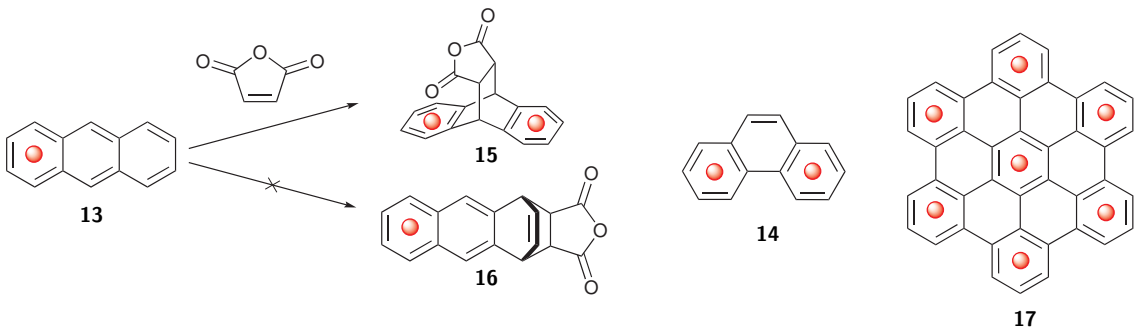

Figure 1.15: Examples of polycyclic aromatic hydrocarbons, and the application of Clar's rule to predict and rationalise aromatic character. The red dots denote aromatic sextets.

This idea has been extended to hexabenzocoronene (HBC), which has a maximum of seven aromatic sextets. Spectacularly, the different aromatic and single bond character predicted by Clar's rule is measurable by atomic force microscopy (AFM).[113]

Porphyrins present another example of polycyclic aromaticity: they essentially comprise an [18]-annulene $[4n+2]$ π-electron pathway appended by two (spectator) ethylene bridges and two aromatic 6 π-electron pyrroles. Both of these aromatic ring current paths are important to the porphyrin aromaticity, though on an atom-weighted basis the pyrroles contribute more aromatic stabilisation energy.[46] The aromatic stabilisation energy (ASE) calculated by the block-localised wavefunction method to isolate the π-electron effects shows that the ASE from the macrocyclic [18] π-electron circuit in the porphyrin is the same as that of an individual 6 π-electron pyrrole ($\sim$80 kJ mol^{-1}).[46]

1.3.6.2 Homoaromaticity

The homoaromatics comprise a different sort of topological perturbation of the monocyclic π-framework of the annulenes: introduction of an insulating (e.g. CH_2) interruption. Remarkably, aromaticity and conjugation can persist in charged species despite this disruption. So, the homotropylium cation **11** ($C_8H_9^+$, Figure 1.7) is distinctly aromatic, as revealed by the different chemical shifts of protons 8 (inside, -0.6 ppm) and 8′ (outside, 5.2 ppm).[71,114]

Homoaromaticity is much rarer for neutral species,[71] and seems to arise only when the π-orbitals on either side of the conjugation defect are close enough to effect delocalisation, such as in the theoretical trishomoaromatic molecule **12** (Figure 1.7).[115]

1.3.6.3 Möbius aromaticity

Heilbronner (1964) predicted that the introduction of a 180° phase shift into the aromatic π-system would reverse Hückel's law: such a molecule with $[4n]$ π-electrons is then aromatic, and $[4n+2]$ π-electrons becomes antiaromatic.[116] Such molecules are known as Möbius aromatic molecules, for their resemblance to the topological Möbius strip (Figure 1.16).

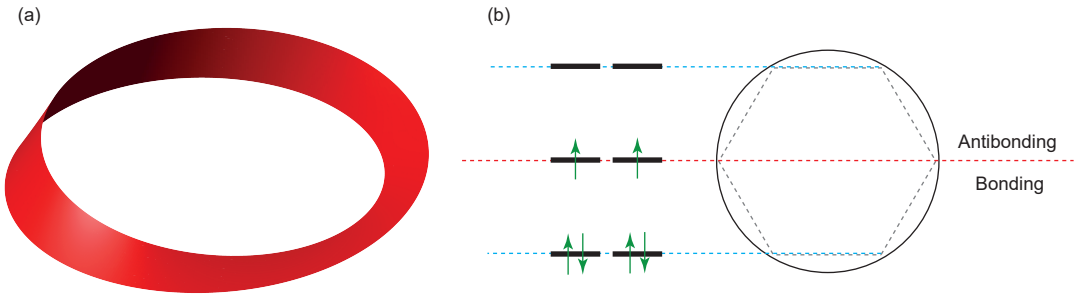

Figure 1.16: (a) A Möbius strip. (b) A Frost-Musulin diagram for a hypothetical 6 π-electron Möbius molecule.

The first synthetic example of a Möbius aromatic molecule was given by Herges and coworkers: the twisted [16]-annulene **18** (Figure 1.17) is aromatic.[117] It is possible to introduce two Möbius twists into a molecule, at which point it reverts back to Hückel's aromaticity rules.[118,119] Several examples of expanded porphyrins which exhibit Möbius aromaticity have been reported by Osuka and co-workers.[120]

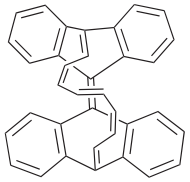

18

Figure 1.17: Example of Möbius aromatic compound **18**.[117]

1.3.6.4 Excited state aromaticity

In molecules which exhibit excited state (anti)aromaticity (ES(A)A), the electron-counting rules are once again reversed (Table 1.1).[121,122] The effect has been reported in expanded porphyrins by Osuka and co-workers, and was assigned on the basis of the structure of excited state absorption spectra.[123,124] In their case, an excited state aromatic compound has an absorption spectrum similar to a ground state aromatic analogue, and vice versa for excited state antiaromaticity. A further introduction to excited state aromaticity is given in Chapter 5.

Table 1.1: Effect of topology, π-electron count and electronic state on (anti)aromatic character.

	Ground state		Excited state	
	$4n$	$4n+2$	$4n$	$4n+2$
Hückel	Antiaromatic	Aromatic	Aromatic	Antiaromatic
Möbius	Aromatic	Antiaromatic	Antiaromatic	Aromatic

1.4 The limits of electron delocalisation

Aromaticity can be considered the limit of electron delocalisation in molecules: the ring-current model leads us to imagine that the π-electrons are freely circulating around the entire conjugation path. However, cyclic conjugation is not the sole requirement for aromaticity: the cycloparaphenylenes (CPP) and cycloparaphenyleneacetylenes (CPPA) do not exhibit

measurable macrocyclic aromaticity around their peripheries,* as evidenced by their benzeniod NMR spectra.[126–128] Indeed, it is only upon oxidation to the dication that a ring current is observed in [8]-CPP.[129] Similarly to homoaromaticity in charged molecules, it seems that oxidation disrupts the ground state electronic character (8 isolated benzene rings) and permits enhanced delocalisation (a [32]-annulene dication with 30 π-electrons).

We are led to the inevitable question: if CPP does not exhibit macrocyclic aromaticity, how can porphine be aromatic? Porphine has three sources of aromatic stabilisation, all calculated to be of roughly equal weight ($\sim$80 kJ mol^{-1} BLW-ASE (block-localised wavefunction)): the [18]-annulene pathway and two pyrroles.[46] The pyrrole aromaticity is not entirely 'switched off' in favour of the [18]-annulene circuit, since there are still local pyrrolic ring currents. The same calculations predict a BLW-ASE for benzene of about 120 kJ mol^{-1}, and for isolated pyrrole of about 70 kJ mol^{-1}.[46]

There are two key differences between the CPP(A)s and porphine: first, there is much more ASE to be lost (about 50 kJ mol^{-1}) by (partial) disruption of the local aromaticity of benzene than of pyrrole. Second, in the absence of an [18] π-electron circulation in porphine, the 12 non-pyrrolic π-electrons of the circuit are localised: essentially, there is a Pauling resonance argument for delocalising these additional electrons through macrocyclic aromaticity. In contrast, CPP has no localised electrons, and [n]-CPPA has a $6n$:$4n$ ratio of aromatic:static electrons. If a macrocyclic ring current were to be established in [n]-CPPA, only 4 π-electrons from each benzene would be involved, immediately negating the electron-counting benefit of including $2n$ acetylene electrons in the macrocyclic aromatic circuit.[130]

As will be discussed in the introductions to Chapters 3, 5 and 6, large aromatic molecules are of interest because they may exhibit novel quantum effects, such as a Aharonov-Bohm oscillations of the ring current direction as a function of magnetic field.[130,131] Such oscillations, introduced in more detail in Chapter 3, could result in magnetic field control of conductance through a molecular junction.[132,133] Intriguingly, at high magnetic fields it has been calculated that molecular ring currents will reverse direction,[134,135] just like the experimental observations in metal rings.[136]

*Taubert et al. have calculated the magnitude of macrocyclic ring currents in [6]-CPP to [11]-CPP and report paratropic and diatropic currents for [6]-CPP and [7]-CPP, respectively. These ring-currents do not significantly affect NICS(0) at the CPP ring centres (-2.1 ppm and -1.9 ppm for [6]- and [7]-CPP, respectively). The reversal of the calculated current direction between [6]- and [7]-CPP is surprising because both CPPs are, formally, [$4n$] all-*cis* annulenes. In contrast, the dianions ([$4n+2$] π-electrons) of all the CPPs studied are aromatic according to NICS(0).[125]

Aromaticity and antiaromaticity are predominantly features of molecules with even numbers of electrons. For those with odd-numbers of electrons, such as radical cations and anions, the focus for studies of electron delocalisation is the radical electron/hole, or polaron. As we shall introduce more thoroughly in Chapter 4, the extent of charge (or spin) delocalisation is an important predictor of molecular properties in a device: with long delocalisation lengths, coherent transport becomes possible, preserving the quantum state of an injected electron or hole.[137] In contrast, shorter delocalisation lengths can still transmit charge over long distances along a molecular wire, through a stepwise hopping process.[137] Charge delocalisation has been reported to be 'extreme' (across up to seven porphyrin units, 7.5 nm) in monoalkyne-linked linear porphyrin oligomer radical cations and anions.[138,139] Polyfluorenes (**PF**) have been extensively studied, and seem to have a radical anion delocalisation length of 3–5 fluorene units.[140–142] For poly(3-decylthiophene) (**P3DT**), the polaron delocalisation length is remarkably long: 11.5 units for an anion, or 8.7 units for a cation,[143] though in terms of spatial extent (4–5 nm) these distances are similar to those for **PF**. In contrast, the polaron delocalisation length is limited to 2–3 monomer units in a poly(phenylenevinylene) (**PPV**) radical anion.[142,144]

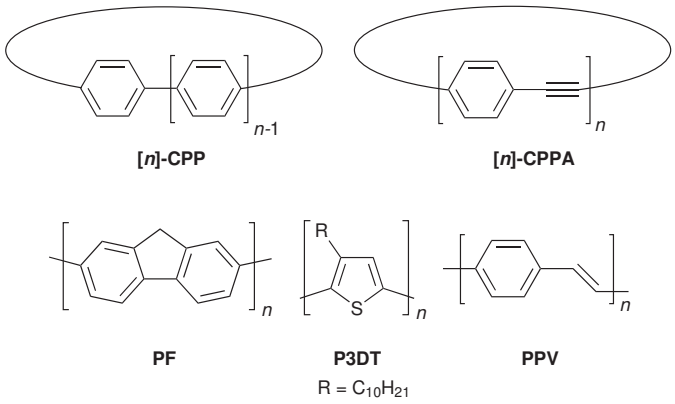

Figure 1.18: Examples of conjugated polymers.

Charge delocalisation is controlled by two competing effects: the conjugated π-system efficiently delocalises charge, but its efforts are frustrated by the presence of conjugation breaking defects. These defects can be kinks and twists in the oligomer chain,[145] or can arise from a more dynamic vibrational relaxation following polaron formation: electron-phonon coupling. In this second case, a short segment of the oligomer chain becomes more strongly conjugated (lower BLA) and thus encourages charge localisation within this region.[143] Overall, polaron delocalisation depends on π-conjugation, oligomer flexibility, and the absence of charge-localising vibrations.

1.5 Prospective

The remainder of this thesis starts by considering perhaps the simplest case of delocalisation in butadiyne-linked porphyrin oligomers: the resonance energy of the neutral dimer ***l*-P2** (Chapter 2). The resonance energy is determined from the experimentally determined height of the torsion barrier for rotation of porphyrins around the butadiyne link. Chapter 2 also serves to introduce some of the photochemistry of porphyrins.

Next, we explore the chemistry of the even π-cations of the [6]-porphyrin nanoring ***c*-P6** and its template complex ***c*-P6•T6** (Chapter 3). Although the nanoring does not exhibit global aromaticity (i.e. around the nanoring circumference) in its neutral oxidation state, after oxidation it is shown to obey Hückel's law. ***c*-P6** exhibits aromaticity and antiaromaticity in its 6+ and 4+ oxidation states, respectively. It is even possible to generate the 12+ cation of the nanoring: this oxidation state corresponds to six antiaromatic ([16]-π) porphyrin subunits, and global (anti)aromaticity is not prominent. These conclusions are developed from DFT and experiment.

We next turn to an exploration of charge and spin delocalisation in the radical cations of a series of linear (***l*-P1** to ***l*-P6**), cyclic (***c*-P6** and ***c*-P6•T6**) and tubular (***t*-P12•T6$_2$**) porphyrin oligomers (Chapter 4). By using spectroelectrochemistry, DFT, and EPR, we show that the cation is delocalised over just two or three porphyrin units.

The thesis concludes with two short chapters which each extend the study of aromaticity in porphyrin nanorings. In Chapter 5 we ask whether porphyrin nanorings exhibit ES(A)A. Although DFT suggests that nanorings smaller than ***c*-P8** do have ES(A)A, initial photophysical experiments do not reveal any physical manifestations. In the final chapter (Chapter 6) we use DFT to calculate the effect of removing a single acetylene (C_2) unit from ***c*-P6** – does the nanoring still obey Hückel's rules when two π-electrons are removed, with an accompanying reduction in symmetry? The resulting molecule, with asymmetric conjugation paths, is interesting for studies on quantum interference. This chapter is entirely computational: synthetic efforts towards the truncated nanoring are under way independently.

I do not know what I may appear to the world, but to myself I seem to have been only like a boy playing on the sea-shore, and diverting myself in now and then finding a smoother pebble or a prettier shell than ordinary, whilst the great ocean of truth lay all undiscovered before me.

— Isaac Newton, as quoted in Memoirs of the Life, Writings, and Discoveries of Sir Isaac Newton (1855) by David Brewster (Volume II. Ch. 27)

2

Experimental and computational evaluation of the barrier to torsional rotation in a butadiyne-linked porphyrin dimer

Contents

Parts of this chapter were published in: M. D. Peeks, P. Neuhaus and H. L. Anderson, 'Experimental and Computational Evaluation of the Barrier to Torsional Rotation in a Butadiyne-Linked Porphyrin Dimer', *Phys. Chem. Chem. Phys.*, 2016, **18**, 5264–5274.

2.1 Abstract

The barrier to torsional rotation in a butadiyne-linked porphyrin dimer in solution has been determined by variable temperature UV-Vis-NIR spectroscopy: $\Delta H = (5.27 \pm 0.03)\,\mathrm{kJ\,mol^{-1}}$, $\Delta S = (10.69 \pm 0.14)\,\mathrm{J\,K^{-1}\,mol^{-1}}$. The value of ΔH agrees well with theoretical predictions. Quantum chemical calculations (DFT) were used to predict the torsion angle dependence of the absorption spectrum, and to calculate the vibronic fine structure of the $S_0 \rightarrow S_1$ absorption for the planar dimer, showing that the absorption band of the planar conformer has a vibronic component overlapping with the $\langle 0|0\rangle$ absorption of the perpendicular conformer. The torsion barrier in the porphyrin dimer is higher than that of 1,4-diphenylbutadiyne (calculated $\Delta H = 1.1\,\mathrm{kJ\,mol^{-1}}$). Crystallographic bond lengths and IR vibrational frequencies confirm that there is a greater contribution of the cumulenic resonance form in butadiyne-linked porphyrin dimers than in 1,4-diphenylbutadiyne. The DFT frontier orbitals of the twisted conformer of the porphyrin dimer are helical, when calculated in the absence of symmetry. The helical character of these orbitals disappears when D_{2d} symmetry is enforced in the 90° twisted conformer. Helical representations of the frontier orbitals can be generated by linear combinations of the more localised orbitals from a symmetry-constrained calculation but they do not indicate π-conjugation. This work provides insights into the relationship between electronic structure and conformation in alkyne-linked conjugated oligomers.

2.2 Introduction

Molecules with extended π-conjugation are of wide interest, both as ingredients in molecular electronic and optical materials,[146,147] and as molecular wires for creating nanoscale electronic devices.[148–151] Conjugated oligomers and polymers have been constructed by linking aromatic monomer units with a wide variety of π-conjugated bridges.[152] The properties of these oligomers are critically dependent on the molecular conformation because any twist in the π-system can dramatically reduce the coherent electronic coupling through the bridge. Conformational heterogeneity can thus attenuate the ability of a conjugated molecule to transport charge or electronic excitation. Several workers have explored the relationship between conformation and function in different types of molecular wire.[15,152–159] Conjugated butadiyne-linked porphyrin oligomers have been actively investigated for more than twenty

years,[18,19,21,160,161] but the barrier to torsional rotation around the butadiyne link has yet to be determined experimentally. In this chapter, we present a time-dependent density functional theory (TD-DFT) evaluation of the electronic excitations of the porphyrin dimer as a function of inter-porphyrin torsion angle, and use variable temperature (VT) UV-Vis-NIR spectroscopy to determine the torsion barrier. Our experimental results permit the accurate simulation of conformational dynamics in this, and similar, systems. Our (TD-)DFT results provide insights into the nature of bonding and electronic excitations in butadiyne-linked oligomers.

Porphyrin-based molecular wires have been widely investigated for their potential applications in functional materials,[2] as dyes for two-photon absorption,[162,163] as models for biological photosystems (e.g. light-harvesting photosystem 2)[164] and as wires for single-molecule charge transport.[165–167] The Anderson group, and others, have prepared a wide variety of *meso–meso* butadiyne-linked porphyrin architectures, including linear oligomers,[21,22,161,168] nanorings[25,169] and supramolecular complexes.[21,23,170] Other linking groups have also been explored: *meso–meso* alkynylene,[160] vinylene,[171] phenylenes,[172–174] and direct porphyrin connection via oxidative coupling at the β and *meso* positions,[175] among many others.

The *meso–meso* butadiyne link permits strong inter-porphyrin electronic coupling and the extension of conjugation upon oligomer homologation is most apparent in the progressive bathochromic shift of the lowest energy optical transition ($S_0 \rightarrow S_1$, 625–850 nm, Q-band, Figure 2.1). However, the butadiyne link also permits torsional heterogeneity, with a continuous range of torsion angles (θ) between the porphyrin chromophores. The length of the butadiyne bridge is sufficient to avoid any steric repulsion between the opposing β hydrogens of the porphyrins (denoted "X" in Table 2.1), thus the lowest energy conformer is planar ($\theta = 0°$). The energy difference between the perpendicular and planar conformers reflects the bridge-mediated resonance stabilisation energy between the porphyrins. The torsional heterogeneity contributes towards the increasing width of the Q-band absorption with increasing oligomer length (Figure 2.1).

Previous semi-empirical and DFT calculations have predicted that the lowest energy conformation of **P2** is planar ($\theta = 0°$). These calculations gave a torsional energy barrier (ΔE) of about 3–4 kJ mol^{-1} (Table 2.2, Figure 2.2) between $\theta = 0$ and 90°,[30,161,176] which is in the range of $k_B T$ at room temperature (2.48 kJ mol^{-1}), thus it is anticipated

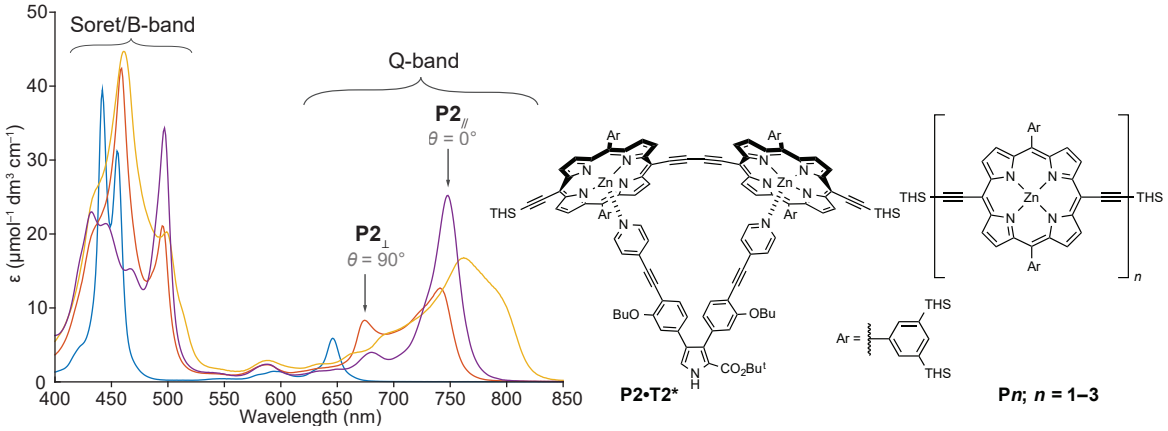

Figure 2.1: Absorption spectra of linear oligomers: monomer **P1** (blue), dimer **P2** (red), trimer **P3** (yellow) and planar dimer complex **P2** • **T2** (purple). (Solvent: CH_2Cl_2:THF:pyridine 10:10:1, except **P2•T2**: CH_2Cl_2. THS = trihexylsilyl.)

that all torsion angles are populated at room temperature. The barrier height was not significantly affected by the use of a range-separated DFT functional (CAM-B3LYP),[177] an effective core potential, or a solvent model (Table 2.2). The torsion profile for the butadiyne linked dimer **P2** contrasts with that for the corresponding monoalkyne linked dimer:[160] in that case, coplanarity is disfavoured by the steric clash between porphyrin β protons, and the DFT equilibrium torsion angle is about 34° (Figure 2.2). The ΔE between the equilibrium geometry and the perpendicular 90° conformer is around 5 kJ mol^{-1}, greater than that in butadiyne linked **P2**, and indicating increased conjugation across the linker. These computational results on **C_2-P2** are in agreement with those found in several other studies, reviewed and contributed to by Rintoul et al.,[178] who note that the computational equilibrium torsion angle (~35°) is much greater than that expected from the narrow, redshifted absorption spectrum and than the angles observed in crystal structures (0–20°).

Computational work[30] (TD-DFT calculations, reproduced in this work, Figure 2.5) has shown that the visible electronic transitions of the butadiyne-linked porphyrin dimer exhibit a strong dependence on interporphyrin torsion angle θ; as θ increases from 0 to 90° the Q-band transition is hypsochromically shifted. Torsion angle-dependence is also apparent in the B-band, albeit in the presence of several overlapping transitions.

The torsion-dependence of the Q-band absorption wavelength has been exploited to selectively excite populations of molecules with different conformations. The wavelength of fluorescence emission is also dependent on the torsion angle. Analysis of fluorescence emission and excitation spectra shows that the S_1 state has a much higher torsion barrier

Table 2.1: Molecular structures referred to in Table 2.2 and in the present study

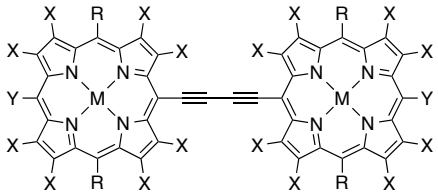

#	M	R	X	Y
19a	Ni	H	Et	H
19b	Zn	H	H	H
19c	Zn	Ph	H	C_2H
19d	Zn	Ph	H	C_2SiMe_3
19e	Zn	H	H	C_2H
P2	Zn	Ar†	H	C_2THS‡

† Ar = 3,5-bis(trihexylsilyl) as defined in Figure 2.1.
‡ THS = trihexylsilyl.

Table 2.2: Calculated barriers, ΔE, to torsional rotation in butadiyne-linked porphyrin dimers

Molecule	Method	ΔE (kJ mol^{-1})	Ref
19a	VWN and BP86	∼63	[176]
19b	AM1	∼4	[161]
19c	B3LYP/6-31G*	2.8	[30]
19d	B3LYP/6-31G*/LANL2DZ	3.1†	This work
19d	TPSSh/6-31G*/LANL2DZ	3.7†	This work
19d	CAM-B3LYP/6-31G*	1.3†	This work
19d	CAM-B3LYP/6-31G* ‡	2.3†	This work
19d	B3LYP/def2-SV(P)	2.8†	This work
19e	B3LYP/6-31G*	2.6†	This work

† No zero-point energy (ZPE) correction applied.
‡ PCM THF solvent model.

(16 kJ mol^{-1}) than the electronic ground state (S_0).[30] Perpendicular conformers which are excited to S_1 tend to planarise prior to emission, unless solvent viscosity retards the rotation.[30,179–181] The torsion angle has also been found to influence the two-photon absorption (2PA) cross-section and the singlet oxygen ($^1O_2$) yield. Planar conformers have stronger two-photon absorption,[163] larger third-order optical non-linearities[182] and higher charge-mobilities,[183,184] and they are more efficient oxygen sensitizers because intersystem crossing ($S_1 \rightarrow T_1$) is faster than in twisted conformers.[179]

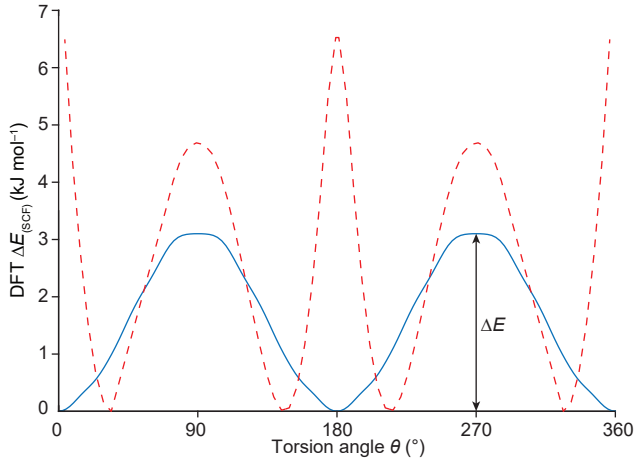

Figure 2.2: Calculated (B3LYP/6-31G*/LANL2DZ) energy profile for butadiyne torsion in **P2**, model **19d** (blue). The red dashed line shows the torsion profile (B3LYP/6-31G*) for a monoalkyne linked analogue of **P2** (substitution pattern corresponding to model **19b**). θ is the angle between the mean planes of each porphyrin, defined by the 24 non-hydrogen atoms in each macrocycle. The indicated ΔE is the torsional barrier for **P2** which is under discussion in this chapter.

The torsion angle can be constrained to enforce coplanarity by the preparation of supramolecular complexes, such as ladder complexes with a bidentate ligand (e.g. DABCO or 4,4′-bipyridine),[23] or simple 1:1 complexes between oligomers and designed templates, such as **T2** (Figure 2.1).[30,184] Fixing the torsion angle results in the expected bathochromic shift and sharpening of the Q-band (Figure 2.1), as the conformation is restricted to a librational range of angles around $\theta \approx 0°$.

Interestingly, Aida et al. prepared tetrameric cages from *meso*-pyridyl substituted butadiyne-linked porphyrin dimers.[185] They found that the cage composed of dimer units with perpendicular porphyrins was favoured, due to the resulting cancellation of the pyridine dipole moments. This result showed that the torsion barrier in the butadiyne-linked dimer is low enough to be overcome by a dipole-based conformational preference.[185]

The aim of this chapter is to experimentally determine the barrier to torsion in porphyrin dimer **P2** using VT UV-Vis-NIR spectroscopy and to understand how torsional rotation alters the electronic structure of this molecule. After presenting the VT UV-Vis-NIR results, we will discuss our theoretical analysis of the electronic excitations. With the help of this theoretical analysis, we will extract thermodynamic parameters using a van't Hoff analysis. We will use evidence from IR spectroscopy and bond-length alternation to discuss the resonance stabilisation of the planar conformer. Finally, we discuss our observation of helical frontier orbitals and natural transition orbitals in DFT calculations.

2.3 Methods

2.3.1 Synthesis and spectroscopy

Porphyrin compounds were prepared as described previously.[183,186] Oligomers **P*N*** with trihexylsilyl (THS) solubilising groups on the *meso*-aryls were used throughout this study, since THS porphyrins exhibit excellent solubility and a low propensity towards aggregation. Room temperature UV-Vis-NIR spectra were recorded using a Perkin-Elmer Lambda 20 with a 1 cm quartz cuvette. Variable temperature UV-Vis-NIR spectra were recorded using a Perkin-Elmer Lambda 1050 and an Oxford Instruments LN_2 optical cryostat, with 1 cm and 1 mm Infrasil Quartz cuvettes (Starna). In all cases, freshly mixed CH_2Cl_2:THF:pyridine (10:10:1) was used as the solvent mixture. CH_2Cl_2 and THF were dried over activated alumina before use. CH_2Cl_2 contained amylene (50–150 ppm) as a stabiliser; THF was unstabilised. Variable temperature UV-Vis-NIR experiments were performed across a wide concentration range (0.8 µM, 1.6 µM and 58.5 µM) to confirm the absence of thermally-induced aggregation. Absorbances were not corrected for concentration change due to thermal contraction of the solvent, since the ratio of absorbances is not affected by concentration. Emission spectra were collected using an ISA Fluoromax-2 Fluorimeter. Infrared spectra were collected using a Bruker Tensor 27 FT-IR spectrometer in ATR mode with neat sample, with 2 cm^{-1} resolution at 293 K.

2.3.2 Computational methods

All (TD-)DFT calculations were conducted using Gaussian09/D.01.[187] The B3LYP density functional[188] was used in conjunction with the 6-31G* basis set,[189–192] with the LANL2DZ ECP[193,194] on Zn as indicated. For computational tractability, truncated model compounds were used. The potential-energy surface scan and TD-DFT calculations used a model of **P2** with phenyl substituents in place of the *meso*-aryls, and trimethylsilyl protecting groups as the acetylene end-groups, and C_1 symmetry, **19d**. Further truncated models were used for the calculation of the vibronic fine structure of the Q-band transitions and vibrational frequencies: the *meso*-aryls and the trimethylsilyl acetylene protecting groups were replaced by hydrogens, **19e**. These calculations were then conducted in D_{2h} and D_{2d} symmetry for planar and perpendicular conformers respectively.

The potential energy surface was calculated by varying the interporphyrin torsion angle in 2.5° increments and, while holding the torsion coordinate fixed, relaxing the remainder of the structure. The resulting ΔE_{SCF} is used for comparison: the zero-point vibrational contribution to the energy has been neglected unless indicated otherwise. Vibrational frequencies (calculated analytically, with the harmonic oscillator model) were scaled by a multiplicative factor of 0.96.

Unless otherwise specified, orbital isosurfaces are depicted using the default threshold settings in the Chimera[195] program. Namely, the thresholds are placed symmetrically about zero, at a value which encompasses 99% of the voxels on either side of zero.

2.4 Results and discussion

2.4.1 Experimental VT UV-Vis-NIR spectroscopy

Since the calculated torsion barrier ΔE is of the order of $k_B T$ at room temperature, we envisioned that VT UV-Vis-NIR spectroscopy would probe the equilibrium between twisted and planar conformers. Indeed, dramatic changes in the UV-Vis-NIR spectrum of **P2** (∼59 µM, CH_2Cl_2:THF:pyridine 10:10:1) were observed upon cooling within the solvent liquid range (298–173 K, Figure 2.3). Below 180 K, discontinuous changes in the spectra are observed, which we attribute to changes in bulk solvent properties at temperatures close to the glass transition temperature.[196]

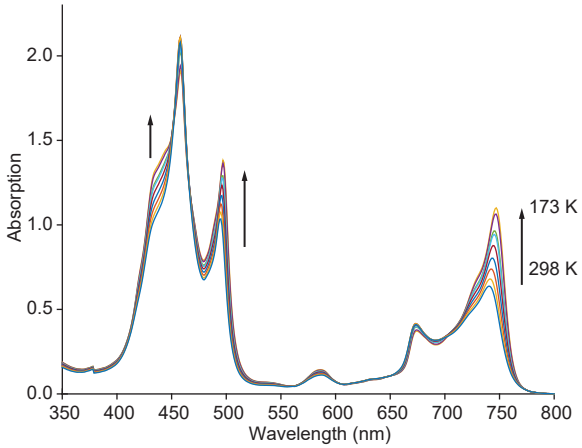

Figure 2.3: Variable temperature (298–173 K) absorption spectra of porphyrin dimer **P2** in CH_2Cl_2:THF:pyridine (10:10:1), concentration ca. 59 µM, path length 1 mm.

Previous work has shown that temperature-dependent changes in the absorption spectra of butadiyne-linked porphyrin oligomers can be caused by aggregation,[197,198] but as noted in

the Methods, we were able to exclude the presence of aggregation by selection of appropriate solvent and solubilising side-chains. VT experiments performed on the porphyrin monomer **P1** in the same solvent mixture showed that, within the temperature range 298–163 K, there is no thermochromic shift of the Q-band absorption λ_{max} (Figure 2.4).

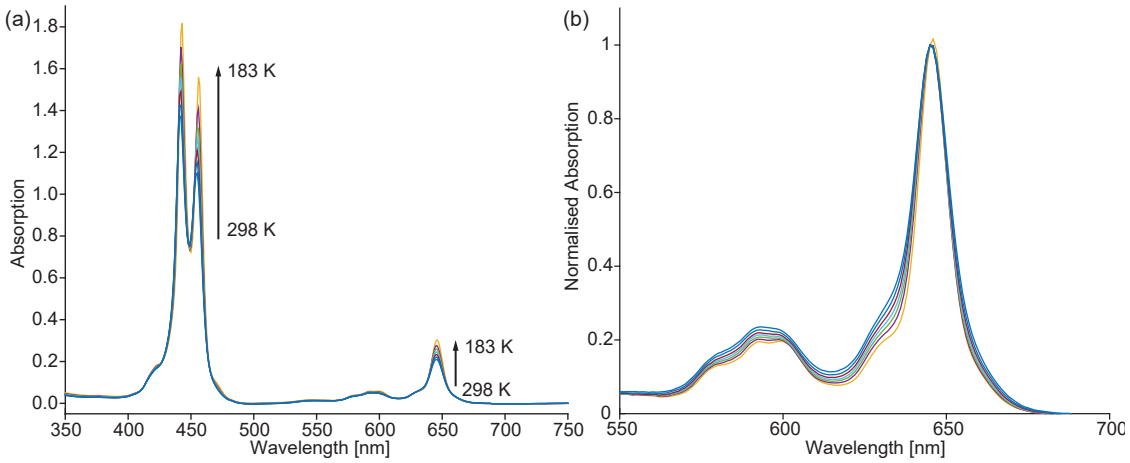

Figure 2.4: VT UV-Vis spectra of monomer **P1** in CH_2Cl_2:THF:pyridine 10:10:1, (a) full spectrum in temperature range 298–77 K (b) expansion of Q-band region in temperature range 298–163 K.

When a solution of **P2** is cooled, its UV-Vis-NIR spectrum exhibits several changes (Figure 2.3): the red edge of the Q-band becomes more intense (~740 nm; planar conformations, $\theta \approx 0°$), at the expense of a slight decrease in intensity on the blue edge (675 nm; perpendicular conformations, $\theta \approx 90°$). We can be confident in our assignment of the absorbance at 675 nm to perpendicular conformers thanks to measurements of the emission of twisted dimer conformers in viscous solution by Kuimova et al.,[180] who found that highly viscous solvents inhibited excited state planarisation. The resulting emission, predominantly from twisted conformers, occurred bathochromically to the "shoulder" on the high-energy side of the Q-band absorption.

The absorption at 570 nm, assigned with the help of TD-DFT to near-planar conformers (see later), increases intensity on cooling. In the Soret/B-band, a sharpening and intensification of the absorption on the red edge is observed (~490 nm). This band can thus also be assigned to near-planar conformers. Before discussing the van't Hoff analysis of the VT UV-Vis-NIR of **P2**, we will further develop our understanding of the absorption spectra using TD-DFT.

2.4.2 Calculated electronic transitions as a function of torsion angle

We computed the electronic excitations for different torsion angles using TD-DFT (B3LYP/6-31G*/LANL2DZ) (Figure 2.5). The results agree with earlier published work.[30] The transition dipole moments for the lowest energy part of the Q-band are polarised along the butadiyne (long, x) axis, as observed experimentally.[199,200] Analysis of the angle dependence of the Q-band excitation energy reveals a relationship to $\cos\theta$: i.e., the projection of the porphyrin planes (Figure 2.6), as given by equation (2.1):

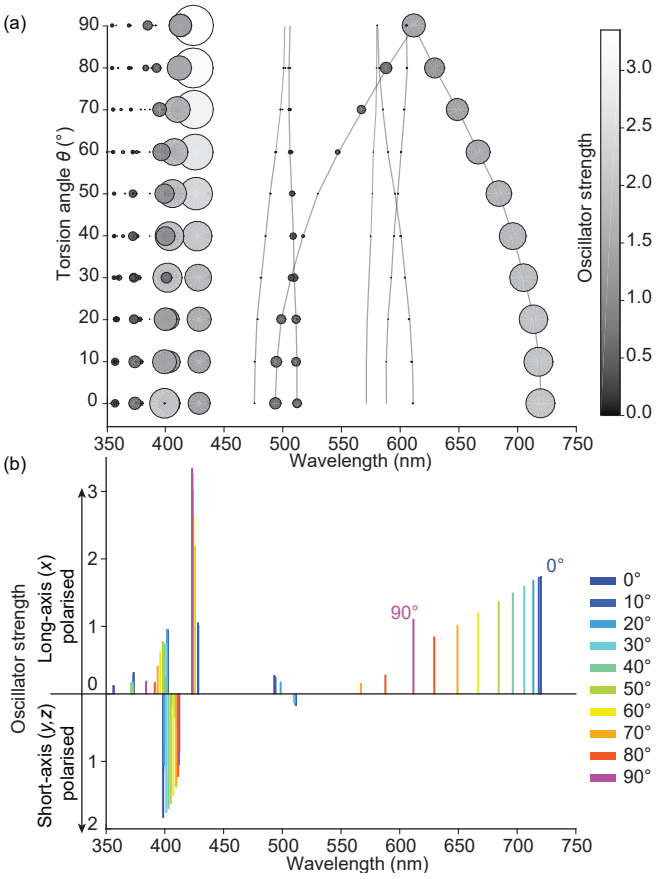

Figure 2.5: Calculated (TD-B3LYP/6-31G*/LANL2DZ) vertical excitation energies in the UV-Vis-NIR region for different torsion angles in a model **P2** (**19d**). (a) Calculated wavelength vs. torsion angle. Faint grey lines (only shown for the Q-bands) connect corresponding states, comprising a Walsh diagram; circle size is proportional to oscillator strength, as is the circle shading. (b) Calculated wavelength vs. oscillator strength. Transitions with oscillator strength <0.1 are not included. Bars above the x-axis correspond to transitions polarised along the long molecular axis (x, butadiyne axis) of the molecules. Bars below the x-axis correspond to transitions polarised along either the y or z (short) molecular axes.

$$E_Q \approx E_\perp - (E_\perp - E_\parallel) \cdot \cos\theta \tag{2.1}$$

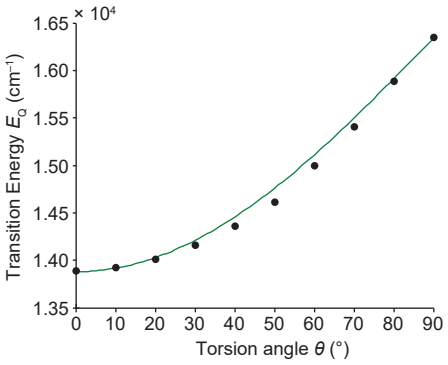

Figure 2.6: Comparison of TD-DFT calculated $S_0 \rightarrow S_1$ vertical excitation energy (blue) vs. a predictive model based on the projection of the porphyrin planes (green) (Eqn. (2.1)).

where E_Q is the Q-band absorption energy for a conformer with inter-porphyrin torsion angle θ. $E_{\parallel}$ and $E_{\perp}$ are the limiting energies for planar (low energy) and perpendicular (high energy) conformers, respectively. This function readily relates absorption energy to the overlap of the porphyrin π-systems along the butadiyne and shows that E_Q is most sensitive to θ when $\theta \approx 90°$.

The calculated oscillator strength of the lowest energy transition is surprisingly high for the 90° conformer (Figure 2.5b), contrasting its gradual decrease with increasing θ between 0–80°. This result does not appear to be a simple computational artefact: the increase of oscillator strength is gradual from 85–90° (Figure 2.7). Close examination of the TD-DFT results reveals that, on twisting from 0–90°, the second-lowest energy x-axis (long axis) polarised transition is progressively redshifted until it becomes degenerate with the lowest energy transition (Figure 2.5a). This analysis further reveals that the weak absorption centred at ~580 nm in the experimental spectrum (Figure 2.1) arises predominantly from planar conformers, and contains components polarised along both the long (x) and short (y) molecular axes. A detailed discussion of TD-DFT results and orbital/state correlations as a function of torsion angle has been published previously by Winters et al., and our computational results are in complete agreement with theirs.[30]

The high oscillator strength of the Q band of the perpendicular conformer ($\theta = 90°$) provides a partial explanation for the peak observed in the absorption spectrum at 675 nm (Figures 2.1 and 2.3). However, a further contribution appears likely because the peak at 675 nm persists at low temperature, with similar relative intensity to the planar conformer as at room temperature. Even at 78 K, at which temperature occupation of the perpendicular state should be thermally inhibited, there is a discrete absorption at ~675 nm (Figure 2.8).

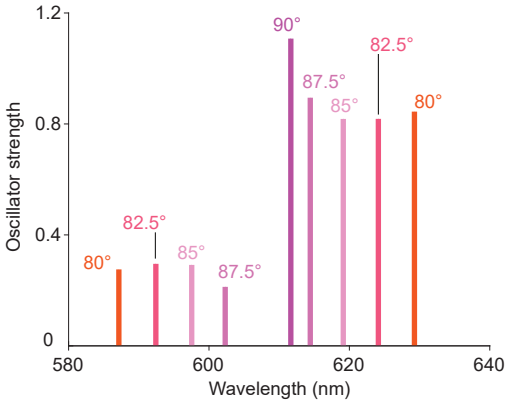

Figure 2.7: TD-DFT (B3LYP/6-31G*/LANL2DZ) calculated excitation energies and oscillator strengths for **P2** (model **19d**) as a function of inter-porphyrin torsion angle

Room temperature emission spectra of **P2** and **P2•T2** (Figures 2.9a and 2.9b) show a similar shoulder on the red edge of the main emission band. Therefore we assign this shoulder to a vibronic contribution of the planar conformer, with the support of computational results described in the next section.

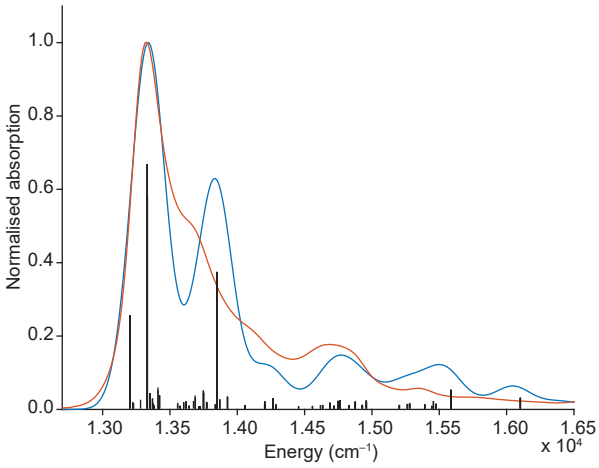

Figure 2.8: (red) Absorption spectrum of Q-band region (600–800 nm) of **P2** in frozen solution (CH_2Cl_2:THF:pyridine 10:10:1) at 78 K; (blue) calculated (B3LYP/6-31G* Franck-Condon/Herzberg-Teller approximation) vibronic structure of Q-band absorption for planar **P2**, model **19e**; (sticks) vibronic transitions; transitions with low relative intensity are not plotted. The $\langle 0|0 \rangle$ transition in the computational result was shifted in energy to match the low-energy peak in the experimental spectrum (red).

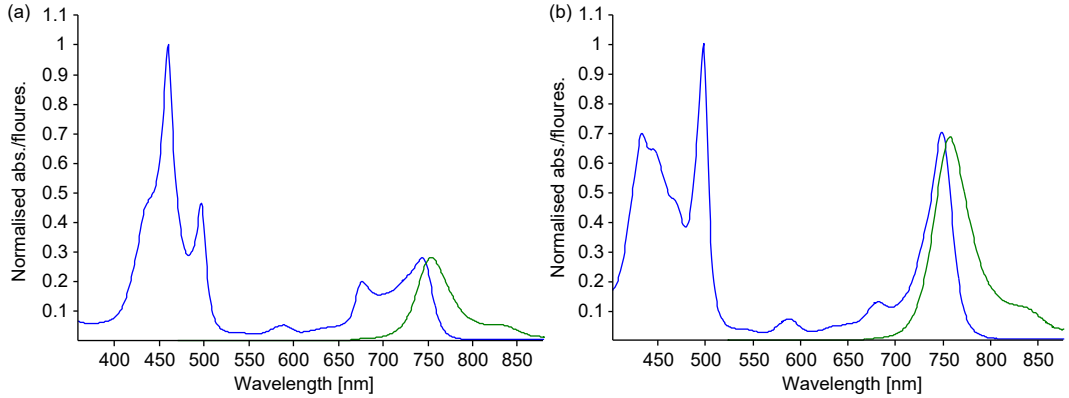

Figure 2.9: Absorption (blue) and fluorescence (green) of (a) **P2** ($CHCl_3$ + 1% pyridine), $\lambda_{ex} = 450$ nm and (b) **P2•T2** ($CHCl_3$), $\lambda_{ex} = 450$ nm, $\lambda_{max}(\log_{10}\epsilon)$: 749 (5.297), 682 (4.574), 588 (4.324), 498 (5.452), 434 (5.295).

2.4.3 Vibronic contribution to the Q-band electronic transition

We used the Franck-Condon (FC) and Herzberg-Teller (HT) approximations as implemented in Gaussian09/D.01 to calculate the vibronic absorption spectrum for the $S_0 \rightarrow S_1$ transition in planar **P2**.[201,202] The calculation was restricted to excitations originating from the vibrational ground state of S_0, thus treating the vibronic spectrum as temperature independent. This calculation gave a predicted spectrum which is in remarkably close agreement to the experimental spectrum of **P2** recorded at 78 K (Figure 2.8). At this temperature the near-planar conformers of **P2** are expected to be dominantly populated. The major vibronic bands arise from intra-porphyrin collective stretching modes, and do not appear to involve nuclear displacements on the butadiyne link (see Figure 2.10). The vibronic band which we calculate at $\sim$390 cm^{-1} from the $\langle 0|0\rangle$ transition has also been experimentally characterised by Camargo et al. in **P1**, at 380 cm^{-1}.[203] We used the computational vibronic spectrum to firmly assign the absorption at 675 nm in (planar) **P2•T2** (Figure 2.1) to a vibronic contribution. Similarly, the anomalously increased intensity at the blue edge of the Q-band ($\sim$675 nm) in the experimental spectra of **P2** at room temperature (Figure 2.1) is partially attributed to this vibronic contribution, in addition to the relatively high oscillator strength of the overlapping perpendicular absorption. The significant overlap between the absorption of the twisted conformer and that of a vibronic band of the planar conformer rationalises previous results where wavelength-selective excitation of the twisted conformer appeared to result, additionally, in excitation of the planar conformer.[30,163]

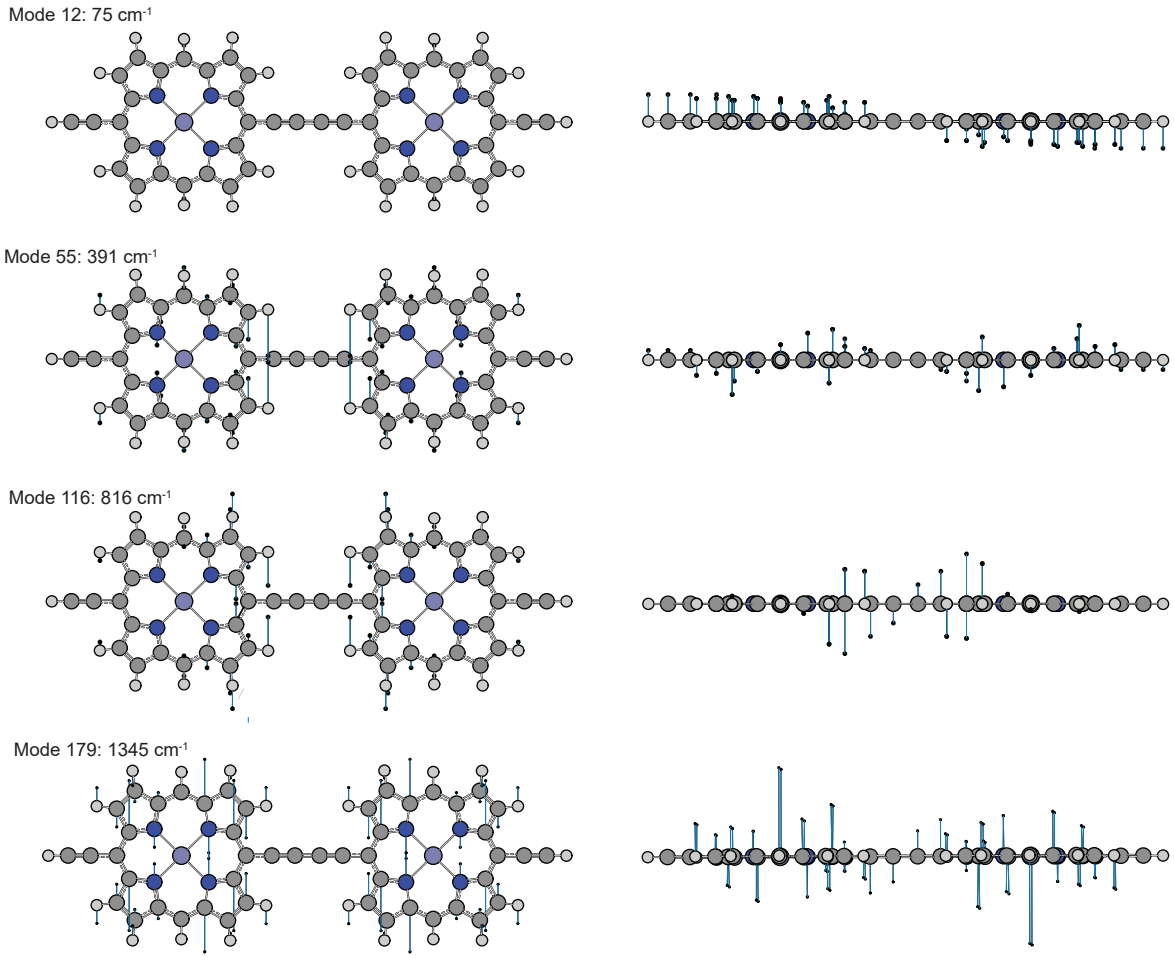

Figure 2.10: Normal modes of S_1 state of **P2** (model **19e**) associated with major vibronic bands.

2.4.4 van't Hoff analysis of experimental VT UV-Vis-NIR data

The experimental VT UV-Vis-NIR data were subject to a van't Hoff analysis of the equilibrium constant for a simple two-state model comprising near-planar and near-perpendicular conformers, $\mathbf{P2}_{\parallel}$ ($\theta \approx 0°$) and $\mathbf{P2}_{\perp}$ ($\theta \approx 90°$) with concentrations proportional to the absorbances at 750 and 675 nm, respectively, weighted by the TD-DFT oscillator strengths for the 0° and 90° transitions.[‡] The vibronic contribution of the planar conformer to the absorption at 675 nm (mostly perpendicular conformer) was subtracted. The relative magnitude of this vibronic contribution was assumed to be temperature-invariant and was calculated from the ratio of peak heights in the spectrum of **P2** at 78 K.

[‡]We also used the van't Hoff equation without weighting the absorbances at 750 and 675 nm to the calculated oscillator strengths. This approach does not change the resulting value of ΔH ($(5.27 \pm 0.03)\,\mathrm{kJ\,mol^{-1}}$), but it gives a higher value of ΔS ($(14.42 \pm 0.14)\,\mathrm{J\,K^{-1}\,mol^{-1}}$); thus, $\Delta G_{298\,\mathrm{K}}$ becomes $(0.98 \pm 0.05)\,\mathrm{kJ\,mol^{-1}}$

The equilibrium constant at each temperature was thus calculated according to equation (2.2):

$$K = \frac{f_{\parallel}}{f_{\perp}} \cdot \frac{A_{\perp}}{A_{\parallel}} = \frac{f_{\parallel}}{f_{\perp}} \cdot \frac{A_{675} - A_{750} \cdot x_{vibr}}{A_{750}} \tag{2.2}$$

where K is the equilibrium constant for:

$$\mathbf{P2}_{\parallel} \rightleftharpoons^{K} \mathbf{P2}_{\perp}$$

$A_{\parallel}$ and $A_{\perp}$ are the absorbances for planar and perpendicular conformers, respectively. $f_{\parallel}$ and $f_{\perp}$ are the TD-DFT oscillator strengths for planar and perpendicular conformers, respectively ($\frac{f_{\parallel}}{f_{\perp}} = 1.574$). x_{vibr} is the ratio of the intensities of the planar $\langle 0|0 \rangle$ absorption and its vibronic contribution (at $\sim$1350 cm^{-1} separation) in the experimental 78 K spectrum of **P2** ($x_{vibr} = 0.186$). The ratio of TD-DFT oscillator strengths (1.574) is consistent with the ratio of estimated experimental extinction coefficients for the planar and perpendicular conformers. The experimental ratio of extinction coefficients for planar and perpendicular conformers ($\frac{\epsilon_{\parallel}}{\epsilon_{\perp}}$) was estimated by comparing the absorption coefficients of free **P2** (in the presence of pyridine) and complexed **P2•T2** at 750 nm (planar, $\epsilon_{\parallel}$) and 675 nm (perpendicular, $\epsilon_{\perp}$), after subtraction of the vibronic contribution at 675 nm in free **P2**. The vibronic contribution in liquid solution at room temperature is given by the following equation, assuming that in **P2•T2**, there is no perpendicular **P2** (i.e., all absorption at 675 nm arises from the vibronic contribution).

$$x_{vibr} = \frac{\epsilon_{675\,\mathrm{nm},\mathbf{T2}}}{\epsilon_{750\,\mathrm{nm},\mathbf{T2}}} = 0.171 \tag{2.3}$$

Thus $\epsilon_{\perp}$ can be estimated by subtracting this vibronic contribution:

$$\epsilon_{\perp,py} = x_{vibr} \times \epsilon_{675\,\mathrm{nm},py} = 60{,}960\,\mathrm{M}^{-1}\,\mathrm{cm}^{-1} \tag{2.4}$$

Where ϵ_{py} corresponds to spectra recorded in the presence of pyridine, and $\epsilon_{\mathbf{T2}}$ to the complex **P2•T2**. Next we calculate $\Delta\epsilon_{\parallel}$. $\Delta\epsilon_{\perp}$ was found in the previous step (60,960 $\mathrm{M}^{-1}\,\mathrm{cm}^{-1}$) assuming all **P2** has been planarised.

$$\Delta\epsilon_{\parallel} = \epsilon_{750\,\mathrm{nm},\mathbf{T2}} = \epsilon_{750\,\mathrm{nm},py} = 103{,}990\,\mathrm{M}^{-1}\,\mathrm{cm}^{-1} \tag{2.5}$$

Thus:

$$\frac{\Delta\epsilon_{\parallel}}{\Delta\epsilon_{\perp}} = \frac{103{,}990}{60{,}960} = 1.7059 \tag{2.6}$$

Within the temperature range 298–198 K, the van't Hoff plot (Figure 2.11) of the extracted equilibrium constants shows an excellent straight-line fit, and is concentration independent across the range measured (0.8–59 μM), thus excluding the presence of aggregation. Thermodynamic parameters were extracted: $\Delta H = (5.27 \pm 0.03)\,\mathrm{kJ\,mol^{-1}}$ (in reasonable agreement with most computational estimates, Table 2.2), $\Delta S = (10.69 \pm 0.14)\,\mathrm{J\,K^{-1}\,mol^{-1}}$. The large value of ΔS demonstrates an important temperature dependence for the rotational barrier: $\Delta G_{298\,\mathrm{K}} = (2.08 \pm 0.05)\,\mathrm{kJ\,mol^{-1}}$; $\Delta G_{180\,\mathrm{K}} = (3.35 \pm 0.04)\,\mathrm{kJ\,mol^{-1}}$ – in other words, the barrier rises as the temperature falls.

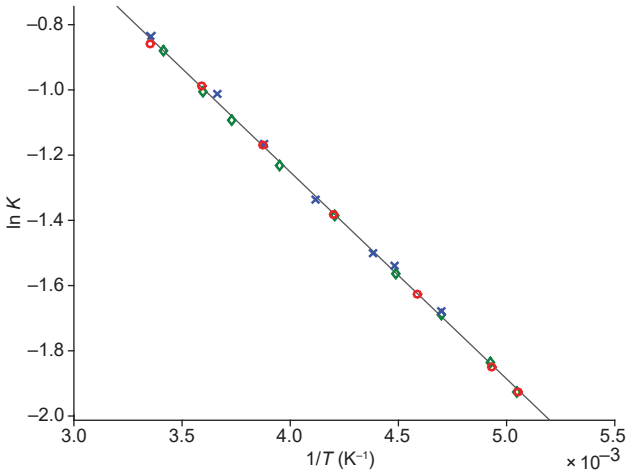

Figure 2.11: van't Hoff plot and fit line for VT experiments at three different concentrations: 0.8 μM (blue crosses), 1.6 μM (green diamonds), 58.5 μM (red circles). $R^2 = 0.999$.

There are few previous reports of the determination of both ΔH and ΔS for a torsional equilibrium. Our thermodynamic parameters for **P2** are similar to those reported for *trans-skew* isomerism in 1,1-dihalo-3-fluoro-buta-1,3-dienes from solution-phase IR spectroscopy (halo = Br: $\Delta H = 3.53\,\mathrm{kJ\,mol^{-1}}$, $\Delta S = 3.5\,\mathrm{J\,K^{-1}\,mol^{-1}}$; halo = Cl: $\Delta H = 2.95\,\mathrm{kJ\,mol^{-1}}$, $\Delta S = 2.3\,\mathrm{J\,K^{-1}\,mol^{-1}}$).[204] ΔS for oxalyl chloride (*trans-gauche* isomerism) has been calculated from the experimental vibrational modes (excluding the torsion mode) as $\sim$13 $\mathrm{J\,K^{-1}\,mol^{-1}}$,[205] and from gas-phase electron diffraction as $10\,\mathrm{J\,K^{-1}\,mol^{-1}}$.[206] We attribute our positive value of ΔS to changes in the frequencies of large-amplitude (low frequency) motions between the planar and twisted states, including the pertinent torsion mode and butadiyne bending modes.

The potential energy surface from DFT calculations (Figure 2.2) was scaled based on the experimentally determined thermodynamic parameters (ΔH and ΔS), and the Boltzmann equation (Equation 2.7) was used to determine the temperature dependence of the mole fraction of each conformer (Figure 2.12). Inclusion of the entropic factor in this manner permits a more accurate simulation of temperature-dependent populations than simply using a temperature-independent barrier height, which would overestimate conformational heterogeneity at low temperature, and underestimate it at high temperatures.

$$p_i = \frac{e^{-\frac{E_i}{k_B T}}}{\sum_{j=1}^{M} e^{-\frac{E_j}{k_B T}}} \tag{2.7}$$

where p_i is the population of the i^{th} state, $k_B T$ is the Boltzmann constant, and E_i is the relative energy of the i^{th} state.

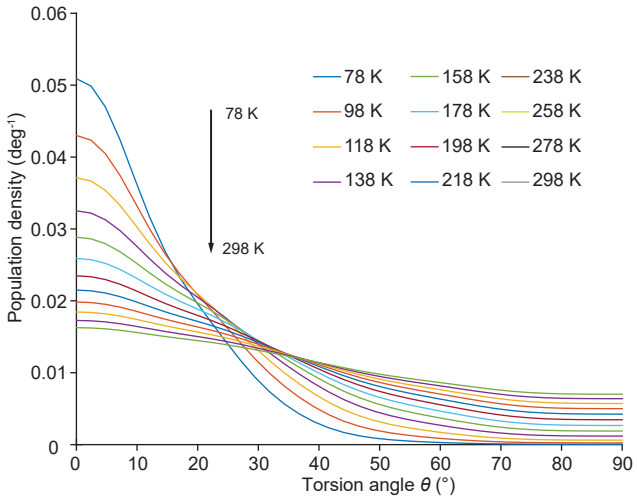

Figure 2.12: Temperature dependence of the population density for different torsion angles, based on the experimentally determined ΔH and ΔS.

The stated error in our thermodynamic parameters is the error in the fit of the experimental data to the van't Hoff equation, and must be taken in the context of the approximation of the two-state model. Our analysis presents a lower bound for the torsion barrier height, because the model evaluates the barrier between near-planar and near-perpendicular conformers. Spectral overlap between angles in a small range (estimated 0–20°) around 0° and 90° means that the absorptions at 750 nm and 675 nm capture some contributions from nearby angles.

2.4.5 Evidence for enhanced conjugation in the planar conformer from C≡C bond length and vibrational frequencies

The torsion barrier for **P2**, $\Delta H = 5.27\,\mathrm{kJ\,mol^{-1}}$, can be compared to that for other alkyne- and butadiyne-linked molecules. The experimental torsion barrier of tolane (Ph–C≡C–Ph) is $2.42\,\mathrm{kJ\,mol^{-1}}$,[207] compared to the near-barrierless ($0.05\,\mathrm{kJ\,mol^{-1}}$) torsion of dimethylacetylene (Me–≡–Me).[208] Calculations have indicated that the barrier for diphenyldiacetylene (DPDA, Ph–C≡C–C≡C–Ph) is around $1.1\,\mathrm{kJ\,mol^{-1}}$ (PBE0/6-31+G*//6-31G* and B3LYP/6-31+G**).[209,210]

1,4-Bis(phenylethynyl)benzene (Ph–C≡C–C_6H_4–C≡C–Ph) has an experimental barrier of $2.75\,\mathrm{kJ\,mol^{-1}}$, similar to that for tolane, but DFT (B3LYP/6-31G**) dramatically overestimates the barrier at $8.75\,\mathrm{kJ\,mol^{-1}}$.[211]

To ensure comparability of computational results, we have calculated the torsion barrier of tolane and DPDA at the B3LYP/6-31G* level of theory, by performing constrained geometry optimisations of planar and perpendicular conformers. At this level of theory, the barrier for DPDA is $1.1\,\mathrm{kJ\,mol^{-1}}$, while that for tolane is $3.8\,\mathrm{kJ\,mol^{-1}}$ (calculated in this work, and in agreement with previously published data[212]).

One might expect the torsion barrier to increase with the ability of the π-system at each end of the butadiyne to stabilise radical or anionic/cationic character, as a consequence of contributions from cumulenic resonance forms in the ground state (Figure 2.13a). Such contributions should be reflected in a decrease in the bond length alternation (BLA) in the butadiyne link (Figure 2.13b). This hypothesis is supported by our computational studies: the BLA in planar **P2** (**19d**, 0.151 Å) is smaller than that in DPDA (0.158 Å) as shown in Table 2.3. We used the range-separated CAM-B3LYP[177] functional in this part of the study: CAM-B3LYP gave BLAs in closer agreement to crystal structures than B3LYP. The more accurate estimation of BLA in polyynes when using DFT functionals with increased exact exchange (BHHLYP and CAM-B3LYP vs. B3LYP) has been reported.[213]

The calculated BLA for perpendicular **P2** (0.163 Å) is higher than for planar **P2** (0.151 Å), and is even higher than both conformations of DPDA (0.158 Å). This change in the nature of bonding between perpendicular and planar **P2** further supports the hypothesis that resonance delocalisation via a cumulenic canonical form is important in the planar conformer. The resonance stabilisation in DPDA is demonstrably lower – the calculated BLA is the same in perpendicular and planar conformers.

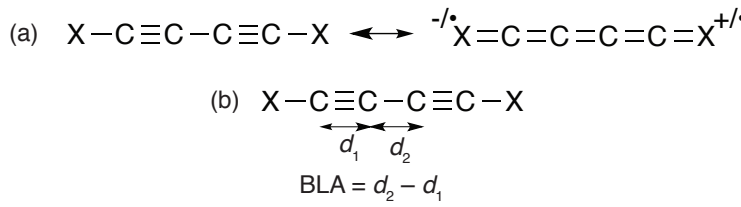

Figure 2.13: (a) A butadiyne-linked conjugated compound can be considered a combination of both alternant and cumulenic forms. The alternant form is dominant. (b) The relative contributions of these resonance structures can be estimated from the bond length alternation.

Table 2.3: Calculated and crystallographic bond length alternation (BLA) in **19d** and DPDA

Molecule	Method	Conformer	BLA(Å)
19d	CAM-B3LYP/6-31G*	$\theta = 90°$	0.163
		$\theta = 0°$	0.151
	crystal structure[168,214,215]	$\theta = 0°$	0.165 ± 0.007
DPDA	CAM-B3LYP/6-31G*	$\theta = 90°$	0.158
		$\theta = 0°$	0.158
	crystal structure[216–221]	$\theta = 0°$	0.178 ± 0.011

We have also compared BLA in crystal structures of **P2** vs. DPDA. We used ConQuest[222] to search the Cambridge Crystallographic Structure Database.[223] After rejection of one DPDA structure with a high R-value (9.2%),[224] we did indeed find that the mean BLA in butadiyne-linked porphyrin dimers (average of 3 structures) is less than that in unsubstituted DPDA (average of 6 structures, Table 2.3). However, the difference has low statistical significance ($p = 0.067$, Welch's t-statistic) and the sample sizes are too small to permit an unequivocal conclusion. Thus, we consider the evidence for resonance stabilisation from BLA analyses of crystal structures provisional: as more accurate crystallographic data become available, it may be possible to perform a more definitive analysis.

A contribution from cumulenic resonance forms should also be apparent in the frequency of the butadiyne $\nu_{C\equiv C}$ asymmetric stretch, observable by IR spectroscopy (2100–2200 cm^{-1}). We,[225] and others,[226] have previously used IR spectroscopy to explore cumulenic character in electronic excited states of polyynes. Increasing cumulenic character results in a lower frequency vibration. Experimentally, we see a 13 cm^{-1} difference for the $\nu_{C\equiv C}$ in experimental ATR FT-IR spectra of DPDA (2147 cm^{-1}) compared with **P2** (2134 cm^{-1}) (Table 2.4). These results are in reasonable agreement with calculation (Table 2.4). It is clear from the IR and crystallographic BLA that the contribution of cumulenic resonance structures

to the bonding in **P2** is very small, as reflected in the low barrier to torsional rotation, but that it is greater than in DPDA.

Table 2.4: Experimental and calculated acetylene stretch frequencies $\nu_{C\equiv C}$

Molecule	Method	$\nu_{C\equiv C}$ cm^{-1}
19e (S_0)	Expt.	2134
	B3LYP/6-31G* †	2132 (2120)‡
19e (S_1)	TD-B3LYP/6-31G* †	2078 (2109)‡
DPDA	Expt.	2147
	B3LYP/6-31G* †	2156

†Planar conformer, frequencies scaled by a multiplicative factor 0.96.
‡Terminal alkyne stretch

The calculated vibrational frequencies of **P2** in its S_1 excited state show far more cumulenic character with a lower $\nu_{C\equiv C}$ (2078 cm^{-1}, Table 2.4), correlating with the increased torsion barrier (16 kJ mol^{-1}) in S_1.[30] This result suggests that time-resolved IR spectroscopy could be used to probe the extent and dynamics of conjugation in the excited states of butadiyne-linked oligomers. We have previously used this technique to show cumulenic character in the first singlet and triplet excited states of a hexayne chain.[225]

2.4.6 Helical molecular orbitals in twisted conformers

To offer further insight into the nature of the Q-band ($S_0 \rightarrow S_1$) excitations, we have calculated the natural transition orbitals (NTOs)[227] for both planar and perpendicular **P2** (Figure 2.14). The NTOs provide an intuitive picture of the natural orbital origin of the hole and electron involved in a transition. Multiple electron/hole NTO pairs may be used to describe a single transition: the relative contribution of each electron/hole pair representation to the TD-DFT transition density is denoted by an eigenvalue (λ). The NTO pair describing the $S_0 \rightarrow S_1$ (Q-band) transition in planar **P2**, ($\theta = 0°$, Figure 2.14a) shows, as expected, the absence of charge transfer character in the excitation. Both hole and electron are delocalised over both porphyrin units.

Interestingly, the first two NTOs of perpendicular **P2** ($\theta = 90°$, Figure 2.14b) show that this excitation can be largely described (~85%) with both hole and electron delocalised over both porphyrin units through apparent helical orbital character on the butadiyne link, arising

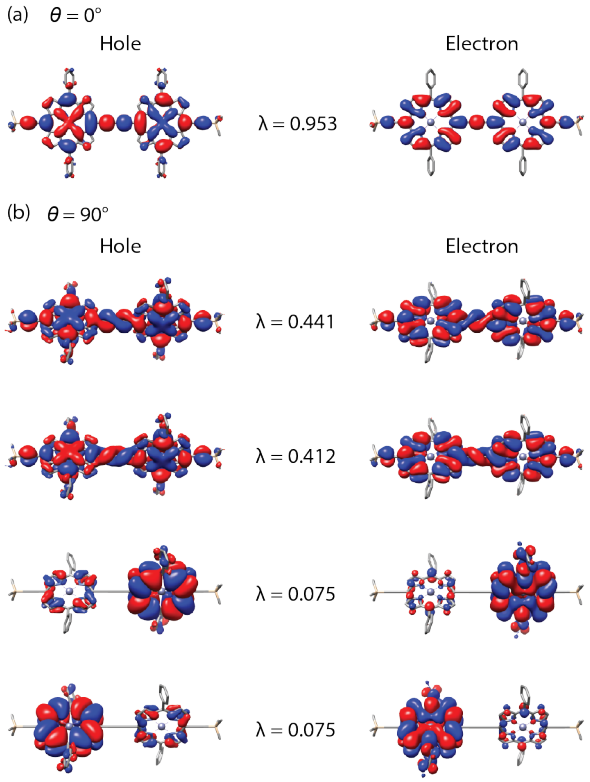

Figure 2.14: Natural transition orbitals (NTOs) calculated at the B3LYP/6-31G* level of theory for (a) planar and (b) perpendicular conformers of **19d**. The eigenvalue associated with each NTO hole/electron pair is shown as λ. The default isovalues are depicted (for $\theta = 0°$, ~0.01ã.u.; for $\theta = 90°$, ~0.008ã.u. and ~0.005ã.u. for $\lambda \approx 0.4$ and $\lambda \approx 0.08$, respectively.)

from admixture of the perpendicular π_x and π_y butadiyne orbitals. The NTOs for **P2** are similar to the HOMO and LUMO for the planar and perpendicular conformers (Figure 2.15), reflecting the predominantly HOMO–LUMO nature of the $S_0 \rightarrow S_1$ transition. Helical butadiyne orbitals are also observed for the HOMO and LUMO of twisted conformers of **P2**, with increasing admixture of π_x and π_y orbitals upon twisting (Figure 2.15). Similar effects have been observed in calculations on the much simpler DPDA.[209] The reported effects of endgroup torsion on the DFT frontier orbital energies in DPDA[209] are similar to those reported in our previous work for **P2**.[30] Helical orbitals have previously been calculated by DFT for some cumulene/polyyne molecules.[228,229] However, we are reluctant to attach much significance to the helicity in the NTOs and frontier orbitals of **P2**: the first two NTOs are pseudo-enantiomeric and near degenerate ($\lambda = 0.441$ and $\lambda = 0.412$), and their structures differ only in the phase of localised orbitals on the left hand porphyrin, and in the handedness of the helical portion of the MO. Degeneracy is broken due to the lack of symmetry in this model: the *meso*-aryl groups and terminal trimethylsilylacetylenes result

in C_1 symmetry. A similar calculation performed with a truncated model (D_{2d} symmetry) gave a degenerate pair of orthogonal NTOs, with no orbital helicity (Figure 2.16). Similarly, the frontier orbitals in this symmetric model show no helical orbital character (Figure 2.17).

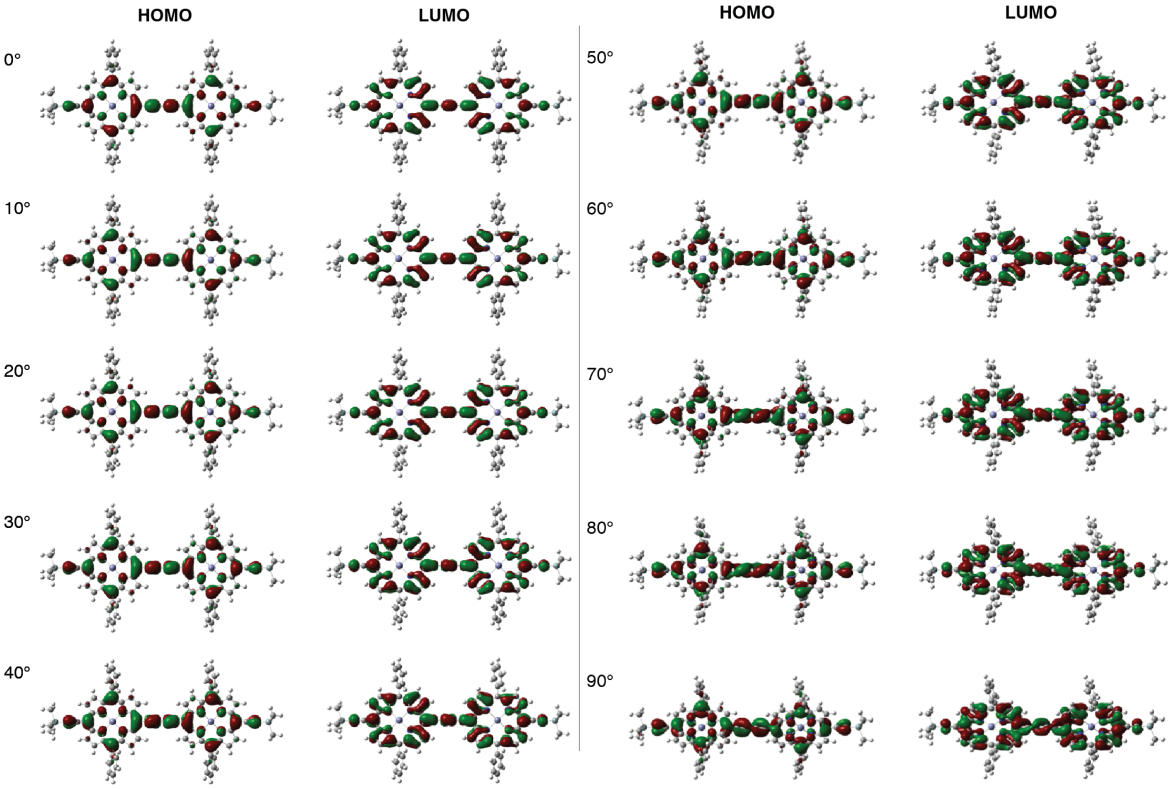

Figure 2.15: DFT (B3LYP/6-31G*/LANL2DZ) HOMO and LUMO for **P2** (model **19d**) as a function of interporphyrin torsion angle, 0–90°. The default isovalues are used, which are typically 0.08 to 0.15ã.u.

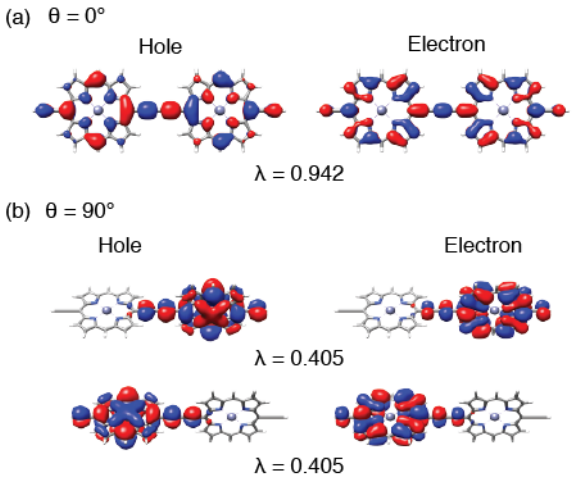

Figure 2.16: Natural transition orbitals (NTOs) for $S_0 \rightarrow S_1$ transition calculated (TD-B3LYP/6-31G*) for model **19e**. The eigenvalue associated with each NTO hole/electron pair is shown as λ. The default isovalues are used, which for all parts of the figure are ∼0.15ã.u.

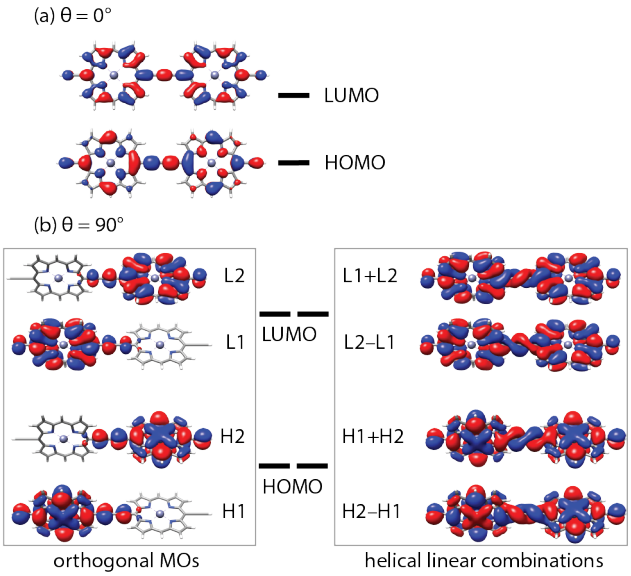

Figure 2.17: (a) Degenerate HOMO and LUMO of planar (D_{2h}) **P2** (model **19e**); (b) degenerate HOMO and LUMO of perpendicular (D_{2d}) **19e** (left) and linear combinations of the same orbitals (right), showing helical character. The default isovalues are used, which for all parts of the figure are ∼0.15ã.u.

The equivalence of helical and localised MO representations is demonstrated by taking linear combinations of the (originally orthogonal) degenerate HOMO and LUMO of a twisted conformer (D_{2d} symmetry, B3LYP/6-31G*, Figure 2.17), giving non-orthogonal but degenerate helical orbitals. For example, in the $\theta = 90°$ conformation of **19e**, there are two degenerate HOMOs, H1 and H2, each localised on one porphyrin unit; the sum and difference of these orbitals (H1 + H2 and H2 – H1) are helical, enantiomeric and degenerate. In the present study, we have found that helical orbitals occur where there is a deviation from D_{2d} symmetry (and hence frontier orbital degeneracy) in twisted conformers, either due to non-symmetric molecular structures (disordered sidegroups) or due to geometry relaxation to a minimum with a value of θ close to, but not exactly 90°.

2.5 Conclusions

The barrier to torsion about the butadiyne link in a porphyrin dimer has been determined experimentally by VT UV-Vis-NIR absorption spectroscopy. The planarisation of a twisted dimer was analysed with a van't Hoff treatment to yield the following thermodynamic parameters for planarisation: $\Delta H = (5.27 \pm 0.03)\,\mathrm{kJ\,mol^{-1}}$ and $\Delta S = (10.69 \pm 0.14)\,\mathrm{J\,K^{-1}\,mol^{-1}}$.

(TD-)DFT calculations were used on model systems to explore the suitability of computational methods for the study of these chromophores. Gratifyingly, an affordable DFT

functional/basis set combination (B3LYP/6-31G*) provided a barrier height in reasonable agreement with experiment, and TD-DFT results permitted clear characterisation of the dimer Q-band, in agreement with previous work.[30] In particular, the use of TD-DFT to assign vibronic structure in the Q-band absorption was essential for the deconvolution of overlapping spectral features for the van't Hoff analysis and afforded theoretical insight into previous wavelength-selective excitation studies.

The torsion barrier in **P2** is higher than that calculated for 1,4-diphenylbutadiyne, suggesting that the increase in the size of the conjugated endcapping π-system increases the barrier height, owing to increased resonance stabilisation. Examination of the experimental $\nu_{C\equiv C}$ IR stretch and calculated BLAs offer some support to this rationale.

Your assumptions are your windows on the world. Scrub them off every once in a while, or the light won't come in.

— Isaac Newton

3

Aromaticity and antiaromaticity in a 2.4 nm molecular nanoring

Contents

Parts of this chapter were published in: M. D. Peeks, T. D. W. Claridge and H. L. Anderson, 'Aromatic and antiaromatic ring currents in a molecular nanoring', *Nature*, 2017, **541**, 200–203.

3.1 Abstract

Aromatic and antiaromatic molecules exhibit ring currents around their perimeters.[71,102] Similar persistent currents are observed in metal rings, when the coherence length of the electrons is longer than the circumference of the ring.[130,231] The relationship between these quantum mechanical phenomena is poorly understood, partly because they are studied in different size regimes: the largest aromatic molecules have diameters of about 1 nm, whereas persistent currents are found in rings with diameters of 20–1000 nm. It is not clear whether aromaticity and antiaromaticity are confined to small molecules, or whether the necessary quantum coherence can be achieved in large macrocycles. Here we show, using ^{1}H NMR spectroscopy and DFT, that a six-porphyrin nanoring template complex ***c*-P6•T6**, with a diameter of 2.4 nm, is antiaromatic in its 4+ oxidation state and aromatic in its 6+ oxidation state. These species have circuits of 80 and 78 π electrons, respectively, and they are the largest aromatic and antiaromatic systems yet reported. The antiaromatic state has a huge paramagnetic susceptibility, despite having no unpaired electrons. This work demonstrates that a global ring current can be promoted in a macrocycle by adjusting its oxidation state to suppress the local ring currents of its components. The discovery of ring currents around a molecule with a circumference of 7.5 nm, at room temperature, shows that quantum coherence can persist in surprisingly large molecular frameworks, and implies that it will be possible to exploit quantum interference effects, such as Aharonov-Bohm oscillations, in molecular electronic devices.

3.2 Introduction

Chemists have been fascinated by aromatic compounds ever since Faraday isolated benzene in the 1820s, and aromaticity has become an important concept for understanding molecules with delocalised electronic structures.[71,102] Hückel's rule predicts that a molecule will be aromatic or antiaromatic if it has a delocalised circuit of $[4n+2]$ or $[4n]$ electrons, respectively, where n is an integer. These ideas were developed by studying cyclic hydrocarbons known as annulenes, with the general formula $C_m H_m$ (where m is even),[232] and the prototypical aromatic and antiaromatic molecules are benzene (C_6H_6) and cyclobutadiene (C_4H_4), respectively.

3. Aromaticity and antiaromaticity in a 2.4 nm molecular nanoring

The most characteristic feature of aromatic and antiaromatic molecules is their ability to sustain an induced ring current in a magnetic field. Molecular ring currents are quantum mechanical phenomena and their main manifestation is induced magnetisation.[84] In aromatic molecules, the direction of the ring current is such as to generate a magnetic field that opposes the external field inside the ring (a 'diatropic' current), while ring currents in antiaromatic molecules flow in the reverse direction ('paratropic').[85] These ring currents give rise to diagnostic NMR chemical shifts,[85] and are accompanied by diamagnetic and paramagnetic susceptibility exaltations, for aromatic and antiaromatic molecules respectively, and large out-of-plane magnetic anisotropies.[72] The persistent currents observed in metal and semiconductor rings resemble aromatic ring currents,[130,231] and in direct analogy to Hückel's rule, the direction of the persistent current depends on the number of electrons in the system.[233] Persistent currents in non-molecular rings switch direction as a function of the magnetic flux passing through the ring, so that they can be changed from diatropic ('aromatic') to paratropic ('antiaromatic') simply by changing the strength of the external magnetic field. The magnetic field required for one such Aharonov-Bohm oscillation is inversely proportional to the area of the ring and absurdly high fields would be needed to test this effect in small molecules (e.g. a benzene molecule, with a diameter of 0.3 nm, would require a field of 6×10^4 T for one cycle). Understanding the connection between aromaticity and the persistent currents in mesoscopic rings provides a strong motivation for investigating ring currents in molecules of an intermediate size.[131]

Studies on annulenes have led to the conclusion that aromaticity decreases with increasing ring size and vanishes for systems with more than about 30 π electrons (corresponding to a diameter of around 1.3 nm),[104,105] but it seems likely that aromaticity can be preserved in larger systems if geometrical disorder is suppressed.[134] The previous record for the largest aromatic molecule is held by a 50π dodecaphyrin with a diameter of about 1.3 nm.[48] The dication of [8]cycloparaphenylene ([8]CPP, 30π, diameter 1.1 nm) is also aromatic.[129] The Anderson group recently reported the synthesis of π-conjugated macrocycles consisting of 5–50 porphyrin units, with diameters of 2–20 nm, (***c*-PN**, $N = 5 - 50$, Figure 3.1), as well as the corresponding linear oligomers ***l*-PN**.[234–236] The ***c*-PN** rings might all be expected to exhibit diatropic or paratropic ring currents around the whole nanoring because they all have circumferential circuits of $[4n + 2]$ or $[4n]$ π electrons (e.g. ***c*-P6** 84π; ***c*-P7** 98π), yet, as in [8]CPP, the neutral molecules exhibit no signs of global aromaticity or antiaromaticity.

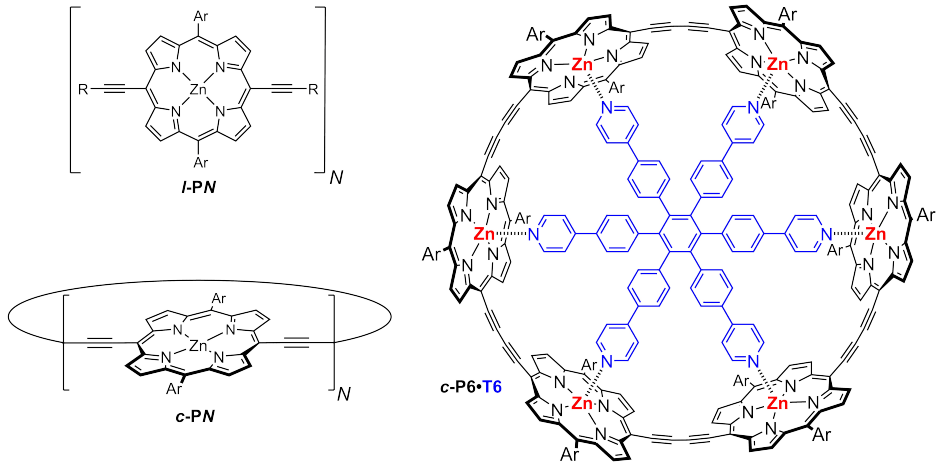

Figure 3.1: Molecular structures of the butadiyne-linked porphyrin oligomers used in this study: ***l*-P*N***, ***c*-P*N*** and ***c*-P6•T6**. Ar = (3,5-bis(trihexylsilyl))phenyl as shown for ***l*-P*N***. The template **T6** in ***c*-P6•T6** is shown in blue.

3.3 Methods

3.3.1 Synthetic chemistry

I synthesised the oxidants and porphyrin nanorings as described below. General experimental details can be found in the Appendix. The syntheses of linear porphyrin oligomers, ***c*-P6•T6** and ***c*-P6** have been reported previously.[186] Bulky 3,5-bis(trihexylsilyl)phenyl solubilising sidegroups were chosen to permit high-concentration NMR experiments, and to inhibit aggregation. ***c*-P6•T6** was synthesised from 200 mg of monomer **P1**. Small amounts of larger rings (***c*-P8** to ***c*-P16**) were isolated as side products, characterised by gel permeation chromatography (GPC), NMR, MALDI-TOF MS and UV-Vis-NIR spectroscopy. It is notable that the yield of ***c*-P10** (2.3%) was much higher than that of ***c*-P12** (0.1%), presumably because the bulky THS sidechains disfavour the formation of the ***c*-P12•T6$_2$** figure-of-eight complex,[25] instead favouring a less crowded ***c*-P10•T6$_2$** complex in which two template 'legs' are unbound.[237]

For the synthesis of oxidants, all solvents were dried. Exposure of reaction mixtures or pure solvents to rubber septa was carefully avoided. CH_2Cl_2 was purchased unstabilised, and was purified by washing with conc. H_2SO_4 followed by distillation from CaH_2.

3.3.1.1 Acetylferrocenium hexafluoroantimonate (AcFc)

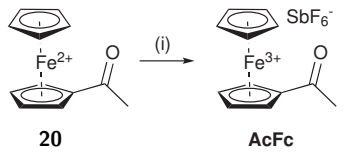

Scheme 3.1: (i) $AgSbF_6$, $MeNO_2$, r.t., 30 min, 57%.

Acetylferrocene (395 mg, 1.73 mmol) and silver hexafluoroantimonate ($AgSbF_6$, 578 mg, 1.73 mmol) were combined and dried *in vacuo*. The mixture was dissolved in $MeNO_2$ (5 mL) and stirred at r.t. for 30 min. The mixture was filtered to remove colloidal Ag. Et_2O (20–100 mL) was then added to precipitate the product as a blue-green solid (454 mg, 57%), used without further characterisation.

3.3.1.2 Diacetylferrocenium hexafluoroantimonate (diAcFc)[238]

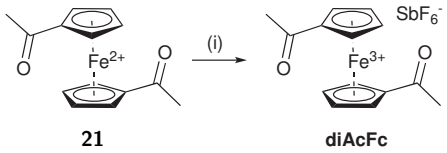

Scheme 3.2: (i) $AgSbF_6$, CH_2Cl_2 and $MeNO_2$, r.t., 30 min, 44%.

Diacetylferrocene (360 mg, 1.33 mmol) and silver hexafluoroantimonate ($AgSbF_6$, 445 mg, 1.33 mmol) were combined and dried *in vacuo*. The mixture was dissolved in CH_2Cl_2 (5 mL) and $MeNO_2$ (2 mL) and stirred at r.t. for 30 min. The mixture was filtered to remove colloidal Ag. Et_2O (50 mL) was then added to precipitate the product as a blue-green solid (294 mg, 44%), used without further characterisation.

3.3.1.3 Thianthrenium hexafluoroantimonate (Thn)

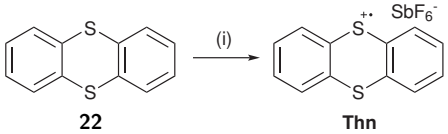

Scheme 3.3: Method one: (i) $NOSbF_6$, $MeNO_2$, r.t., 60 min, 25%. Method two: (i) SbF_5, CH_2Cl_2, 0 °C, 30 min, 96%.

The compound was prepared by two strategies. First, by oxidation of thianthrene with $NOSbF_6$ (25% yield); second, by oxidation with SbF_5 (96% yield).

Warning: SbF_5 is extremely corrosive and evolves HF in the contact with water. Calcium gluconate gel should be available for first-aid when this reagent is in use.

Strategy 1: Thianthrene (100 mg, 0.46 mmol) and $NOSbF_6$ (128 mg, 0.48 mmol) were combined as dry solids. Dry $MeNO_2$ (8 mL) was then added and the mixture was stirred at r.t. for 60 min. Dry Et_2O was then added to precipitate the product, which was collected by cannula filtration. The precipitate was washed with Et_2O. The product was a purple solid (51 mg, 25%).

Strategy 2: SbF_5 (167 µL, 502 mg, 2.31 mmol) was added to a cooled (ice bath) suspension of thianthrene (500 mg, 2.31 mmol) in CH_2Cl_2 (5 mL). The mixture was then warmed to r.t. and stirred for 30 min. Dry Et_2O was added to precipitate the product, which was collected by cannula filtration under an inert atmosphere and washed with further Et_2O. The product was a purple solid and was dried *in vacuo* (1.00 g, 96%).

3.3.1.4 Tris(4-bromophenyl)aminium hexafluoroantimonate ($BAHA_F$)

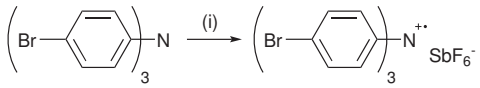

Scheme 3.4: (i) $AgSbF_6$, I_2, CH_2Cl_2, r.t., 15 min, 56%.

Tris(4-bromophenyl)amine (0.75 g, 1.56 mmol) and silver hexafluoroantimonate ($AgSbF_6$, 778 mg, 2.33 mmol) were combined and dried *in vacuo*. Dry CH_2Cl_2 (10 mL) was added whereupon the solution turned blue. I_2 (396 mg, 1.56 mmol) was added as neat solid and the mixture was stirred at r.t. for 15 min. The mixture was filtered under an inert atmosphere, using a cannula, to remove colloidal Ag. Dry Et_2O was then added to the filtrate to precipitate the product, which was collected by further cannula filtration and washed with Et_2O. The precipitate was dried *in vacuo* and the product was a fine dark blue powder (627 mg, 56%). The product was used without further characterisation.

3.3.1.5 Tris(2,4-dibromophenyl)amine (24)[239]

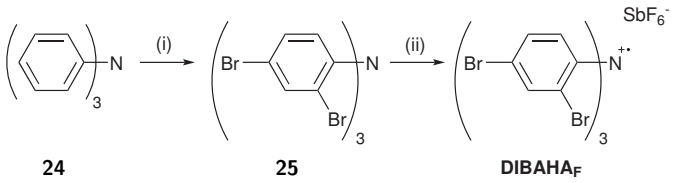

Scheme 3.5: (i) Br_2, $CHCl_3$, r.t., 64 h, 72%; (ii) $AgSbF_6$, I_2, CH_2Cl_2, r.t., 30 min, 52%.

Triphenylamine **24** (5.05 g, 20.6 mmol) was mixed with $CHCl_3$ (20 mL). Br_2 (7 mL, 138 mmol) in $CHCl_3$ (7 mL) was added dropwise, at r.t., over the course of one hour. The mixture was then stirred at r.t. for 64 h. The product was precipitated by the addition of EtOH, then recrystallised twice from $CHCl_3$/EtOH to afford the product **25** as a mixture of colourless, small crystals and large hexagonal faintly yellow crystals (10.73 g, 72%). ^{1}H NMR (400 MHz, $CDCl_3$) δ_H, ppm: 7.74 (d, $J = 2.2$ Hz, 3H), 7.35 (dd, $J = 8.5, 2.2$ Hz, 3H), 6.68 (d, $J = 8.5$ Hz, 3H).

3.3.1.6 Tris(2,4-dibromophenyl)aminium hexafluoroantimonate (DIBAHA$_F$)

Tris(2,4-dibromophenyl)amine **25** (1 g, 1.39 mmol) and silver hexafluoroantimonate ($AgSbF_6$, 701 mg, 2.10 mmol) were combined and dried *in vacuo*. I_2 (356 mg, 1.40 mmol) was added followed by dry CH_2Cl_2 (10 mL), with stirring. The solution immediately became dark green. The mixture was stirred at r.t. for 30 min, then filtered by cannula in an inert atmosphere. Dry pentane was added to the filtrate to precipitate the product, which was collected by further cannula filtration in an inert atmosphere, washing with dry Et_2O. The product was dried *in vacuo* to afford a blue-green water-sensitive powder (692 mg, 52%), which had a UV-Vis spectrum in accordance with literature.[240] The product was used without further characterisation.

3.3.1.7 *c*-P6•T6

The overall route to ***c*-P6•T6** is shown in Scheme 3.6. Steps (i) to (v) are described elsewhere.[186]

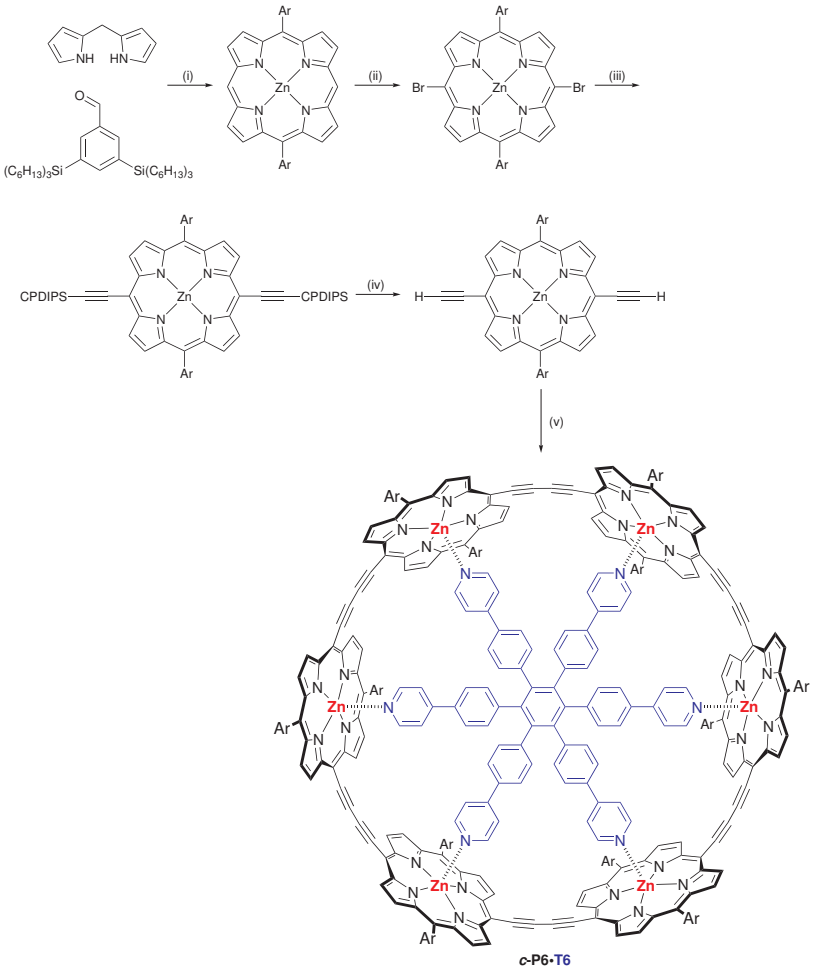

Scheme 3.6: (i) TFA, CH_2Cl_2, then DDQ, then Et_3N; (ii) $Zn(OAc)_2 \cdot 2\,H_2O$, $CHCl_3$, MeOH; (iii) *N*-bromosuccinimide, CH_2Cl_2; (iv) CPDIPS-acetylene, $Pd(PPh_3)_2Cl_2$, CuI, THF, DIPA; (v) TBAF, CH_2Cl_2; (vi) **T6**, $Pd(PPh_3)_2Cl_2$, CuI, 1,4-benzoquinone, $CHCl_3$, DIPA, r.t., 16 h, 20–36%. Yields and full experimental for steps (i)–(v) reported in ref. [186].

{H,H}-P1 (200 mg, 0.12 mmol) and template **T6** (26 mg, 29 µmol) were dissolved in $CHCl_3$ (133 mL) by sonication for 2 h. A solution of $Pd(PPh_3)_2Cl_2$ (27 mg, 39 µmol), copper(I) iodide (37 mg, 0.19 mmol) and 1,4-benzoquinone (89 mg, 0.80 mmol) in $CHCl_3$ (18 mL) and DIPA (0.25 mL) was added to the porphyrin mixture at r.t. The mixture was stirred at r.t. overnight, open to air. The reaction mixture was partially concentrated and passed over a plug of alumina ($CHCl_3$). Purification by SEC (toluene) and preparative recycling GPC (toluene + 1% pyridine) afforded ***c*-P6•T6** (78 mg, 36%) as a brown solid. On a larger scale (800 mg **{H,H}-P1**), the yield was only 20% due to apparent co-absorption of polymer and product to alumina and glass frits during purification, and due to mechanical losses. ^{1}H NMR (500 MHz, $CDCl_3$) δ_H, ppm: 9.54 (d, J = 4.2 Hz, 24H), 8.72 (d, J = 4.2 Hz, 24H), 8.30 (bs, 12H), 7.98 (bs, 12H), 7.97 (bs, 12H), 5.52 (d, J = 8.5 Hz,

12H), 5.45 (d, $J = 8.5$ Hz, 12H), 4.98 (d, $J = 6.1$ Hz, 12H), 2.41 (d, $J = 5.8$ Hz, 12H), 1.54–1.41 (m, 144H), 1.41–1.17 (m, 432H), 0.98–0.77 (m, 360H); MS (MALDI-TOF) m/z: calcd. M^+ for $C_{720}H_{1068}N_{30}Si_{24}Zn_6$: 11211; found: 11207. UV-vis (CH_2Cl_2) λ_{max} [nm] (log ϵ [$M^{-1}\,cm^{-1}$]): 850 (5.61), 808 (5.70), 772 (5.57), 612 (4.59), 482 (5.76).

3.3.1.8 Free-base *c*-P6 $[H_2]_6$-*c*-P6

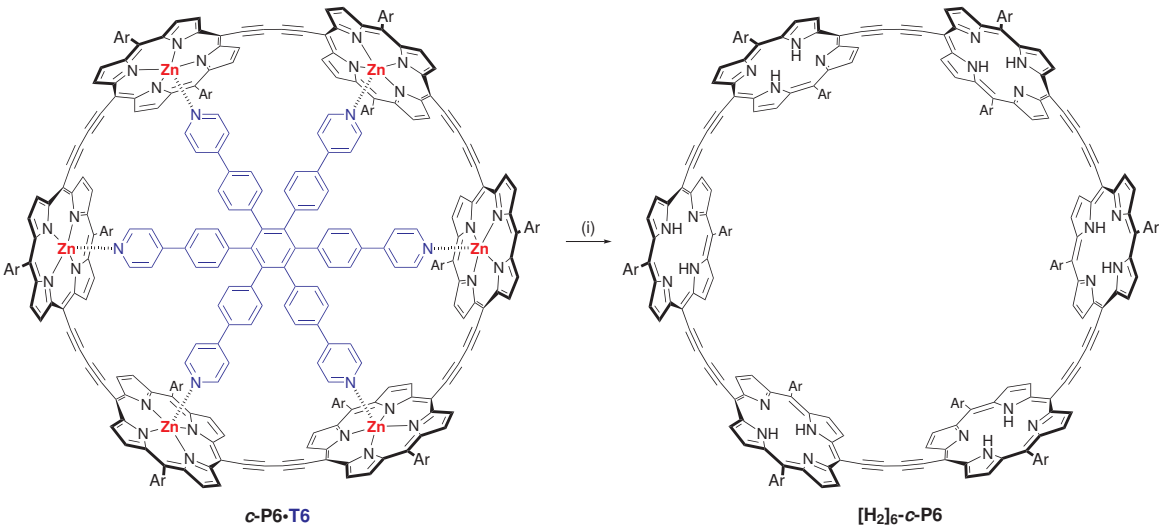

Scheme 3.7: (i) TFA, $CHCl_3$, r.t., 5 min, 79–100%.

Trifluoroacetic acid (95 µL, 1.24 mmol) was added to a solution of ***c*-P6•T6** (23 mg, 2.078 µmol) in $CHCl_3$ (2 mL). The mixture was stirred at r.t. until UV-Vis indicated complete conversion of starting material (typically 5 min), then pyridine (0.2 mL) was added and the mixture was immediately filtered over a short column of silica gel ($CHCl_3$ + 1% pyridine). Removing the solvent yielded **FB-*c*-P6** (16 mg, 79%) as a green solid. Yields varied from 79% to 100%. ^1H (400 MHz, $CDCl_3$) δ_H, ppm: 9.56 (d, $J = 4.7$ Hz, 24H), 8.71 (d, $J = 4.7$ Hz, 24H), 8.15 (bs, 24H), 7.96 (bs, 12H), 1.52–1.36 (m, 144H), 1.36–1.14 (m, 432H), 1.07–0.94 (m, 144H), 0.94–0.85 (m, 216H), −1.29 (s, 12H); MS (MALDI-TOF) m/z: calcd. M^+ for $C_{648}H_{1032}N_{24}Si_{24}$: 9834; found: 9836; UV-vis (CH_2Cl_2) λ_{max} [nm] (log ϵ [$M^{-1}\,cm^{-1}$]): 791 (5.47), 771 (5.49), 659 (5.30), 466 (5.72).

3.3.1.9 *c*-P6

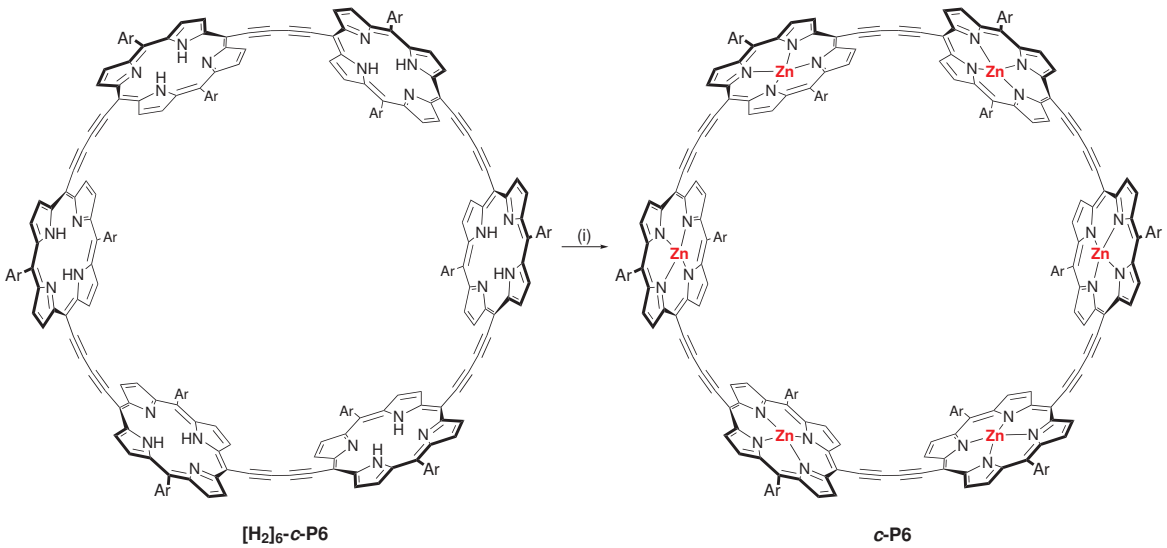

Scheme 3.8: (i) $Zn(OAc)_2 \cdot 2\,H_2O$, $CHCl_3$, MeOH, 40 °C, 70 min, quant. Over two steps (with Scheme 3.7), 73%.

$[H_2]_6$-*c*-P6 (43.9 mg, 4.5 µmol) was dissolved in $CHCl_3$ (6 mL) and a solution of $Zn(OAc)_2 \cdot 2\,H_2O$ (8.8 mg, 219 µmol) in methanol (0.6 mL) was added. The mixture was stirred at 40 °C for 70 min, at which time UV-Vis indicated reaction completion. The mixture was then filtered through a short column of silica gel (CH_2Cl_2 + 1% pyridine) to afford ***c*-P6** (46 mg, quant.) as a brown solid. ^{1}H (400 MHz, $CDCl_3$) δ_H, ppm: 9.67 (d, J = 4.6 Hz, 24H), 8.81 (d, J = 4.6 Hz, 24H), 8.16 (m, 24H), 7.91 (m, 12H), 1.50–1.37 (m, 144H), 1.37–1.12 (m, 432H), 0.94–0.84 (m, 144H), 0.84–0.72 (m, 216H); MS (MALDI-TOF) m/z: calcd. M^+ for $C_{648}H_{1020}N_{24}Si_{24}Zn_6$: 10214; found: 10211; UV-vis (CH_2Cl_2) λ_{max} [nm] ($\log \epsilon$ [$M^{-1}\,cm^{-1}$]): 772 (5.45), 748 (5.49), 593 (4.62), 473 (5.71).

In another example, the two-step preparation of ***c*-P6** from ***c*-P6•T6** had an overall yield of 73%.

3.3.1.10 Removal of templates from larger rings

The template, **T6**, was removed from larger rings by displacement with pyridine. A sample of ring was dissolved in $CHCl_3$ + 20% pyridine, and passed through a SEC column. The absence of template was confirmed by NMR. Residual pyridine could be removed by washing with a saturated aqueous solution of potassium hydrogen phthalate (three times), then with water (twice) before passage over a SiO_2 plug to remove water and

phthalate residues. An alternative method of removing pyridine is to repeatedly dissolve the sample in tetrahydrofuran, then remove the solvents by evaporation. The phthalate wash is much more reliable.

3.3.1.11 *c*-P8

***c*-P8** was isolated as a by-product in the synthesis of ***c*-P6•T6** (from 0.8 g **{H,H}-P1**) as a brown solid (3.2 mg, 0.4%). ^{1}H (400 MHz, $CDCl_3$) δ_H, ppm: 9.74 (d, $J = 4.5$ Hz, 32H), 8.85 (d, $J = 4.5$ Hz, 32H), 8.21 (s, 32H), 7.97 (s, 16H), 1.76–0.72 (m, 1248H); MS (MALDI-TOF) m/z: calcd. M^+ for $C_{864}H_{1360}N_{32}Si_{32}Zn_8$: 13615; found: 13786; UV-vis (CH_2Cl_2) λ_{max} [nm] ($\log \epsilon$ [$M^{-1}\,cm^{-1}$]): 818 (5.54), 597 (4.62), 495 (5.74), 469 (5.68).

3.3.1.12 *c*-P9

***c*-P9** was isolated as a by-product in the synthesis of ***c*-P6•T6** (from 0.8 g **{H,H}-P1**) as a brown solid (2.9 mg, 0.4%). ^{1}H (400 MHz, $CDCl_3$) δ_H, ppm: 9.83 (d, $J = 4.6$ Hz, 36H), 8.93 (d, $J = 4.6$ Hz, 36H), 8.26 (s, 36H), 8.00 (s, 18H), 1.52–0.80 (m, 1404H); MS (MALDI-TOF) m/z: calcd. M^+ for $C_{972}H_{1530}N_{36}Si_{36}Zn_9$: 15317; found: 15550; UV-vis (CH_2Cl_2) λ_{max} [nm] ($\log \epsilon$ [$M^{-1}\,cm^{-1}$]): 821 (5.60), 600 (4.66), 487 (5.78), 472 (5.77).

3.3.1.13 *c*-P10

***c*-P10** was isolated as a by-product in the synthesis of ***c*-P6•T6** (from 0.8 g **{H,H}-P1**) as a brown solid (19.2 mg, 2.3%). ^{1}H (400 MHz, $CDCl_3$) δ_H, ppm: 9.80 (d, $J = 4.6$ Hz, 40H), 8.88 (d, $J = 4.6$ Hz, 40H), 8.25 (s, 40H), 7.99 (s, 20H), 1.60–0.79 (m, 1560H); MS (MALDI-TOF) m/z: calcd. M^+ for $C_{1080}H_{1700}N_{40}Si_{40}Zn_{10}$: 17019; found: 17241; UV-vis (CH_2Cl_2) λ_{max} [nm] ($\log \epsilon$ [$M^{-1}\,cm^{-1}$]): 821 (5.73), 598 (4.81), 495 (5.89, sh.), 471 (5.92).

3.3.1.14 *c*-P11

***c*-P11** was isolated as a by-product in the synthesis of ***c*-P6•T6** (from 0.8 g **{H,H}-P1**) as a brown solid (2.1 mg, 0.3%). ^{1}H (400 MHz, $CDCl_3$) δ_H, ppm: 9.90 (d, $J = 4.7$ Hz, 44H), 8.98 (d, $J = 4.6$ Hz, 40H), 8.31 (s, 40H) 8.02 (s, 20H), 1.60–0.80 (m, 1716H); MS (MALDI-TOF) m/z: calcd. M^+ for $C_{1188}H_{1870}N_{44}Si_{44}Zn_{11}$: 18721; found: 19016; UV-vis (CH_2Cl_2) λ_{max} [nm] ($\log \epsilon$ [$M^{-1}\,cm^{-1}$]): 820 (5.70), 596 (4.79), 493 (5.88), 471 (5.89).

3.3.1.15 *c*-P12

***c*-P12** was isolated as a by-product in the synthesis of ***c*-P6•T6** (from 0.8 g **{H,H}-P1**) as a brown solid (1.2 mg, 0.1%). ^{1}H (400 MHz, $CDCl_3$) δ_H, ppm: 9.68 (d, $J = 4.5$ Hz, 48H), 8.80 (d, $J = 4.5$ Hz, 48H), 8.17 (s, 48H), 7.95 (s, 24H), 1.74–0.63 (m, 1872H); MS (MALDI-TOF) m/z: calcd. M^+ for $C_{1296}H_{2040}N_{48}Si_{48}Zn_{12}$: 20423; found: 20657; UV-vis (CH_2Cl_2) λ_{max} [nm] ($\log \epsilon$ [M^{-1} cm^{-1}]): 821 (5.88), 596 (4.88), 488 (6.06), 472 (6.07).

3.3.1.16 *c*-P13

***c*-P13** was isolated as a by-product in the synthesis of ***c*-P6•T6** (from 0.8 g **{H,H}-P1**) as a brown solid (1.9 mg, 0.2%). ^{1}H (400 MHz, $CDCl_3$) δ_H, ppm: 9.93 (d, $J = 0.45$ Hz, 52H), 9.00 (d, $J = 0.45$ Hz, 52H), 8.33 (s, 52H), 8.04 (s, 52H), 1.62–0.82 (m, 2028H); MS (MALDI-TOF) m/z: calcd. M^+ for $C_{1404}H_{2210}N_{52}Si_{52}Zn_{13}$: 22125; found: 22530; UV-vis (CH_2Cl_2) λ_{max} [nm] ($\log \epsilon$ [M^{-1} cm^{-1}]): 821 (5.75), 595 (4.83), 490 (5.91), 472 (5.93).

3.3.1.17 *c*-P16

***c*-P16** was isolated as a by-product in the synthesis of ***c*-P6•T6** (from 0.8 g **{H,H}-P1**) as a brown solid (2.4 mg, 0.3%). ^{1}H (400 MHz, $CDCl_3$) δ_H, ppm: 10.00 (d, $J = 4.4$ Hz, 64H), 9.07 (d, $J = 4.4$ Hz, 64H), 8.39 (s, 64H), 8.08 (s, 32H), 1.60–0.86 (m, 2496H); MS (MALDI-TOF) m/z: calcd. M^+ for $C_{1728}H_{2720}N_{64}Si_{64}Zn_{16}$: 27230; found: 27686; UV-vis (CH_2Cl_2) λ_{max} [nm] ($\log \epsilon$ [M^{-1} cm^{-1}]): 829 (5.89), 594 (4.97), 491 (6.03), 473 (6.05).

3.3.2 Computational chemistry

DFT calculations were all performed using a model of ***c*-P6** in which solubilising aryl groups had been replaced with hydrogens (D_{6h} initial symmetry). Geometries were optimised using Gaussian09/D.01[187] and the B3LYP/6-31G* functional/basis set combination.[188,190–192] The neutral and 6+ rings converged to D_{6h} symmetry, while the 4+ and 12+ rings lost symmetry (C_1). The 2+ ring was optimised with both unrestricted and restricted DFT, and the stability of triplet and singlet wavefunctions were checked in the former case. The 2+ oxidation state optimised to C_{2h} symmetry and a singlet ground state with spin contamination $\langle S^2 \rangle = 0.7342$ (0.2022 after annihilation). The converged geometry optimised structures were confirmed as minima by performing frequency calculations, which showed no imaginary frequencies.

NICS/susceptibility and ACID calculations were conducted using the GIAO and CSGT methods, respectively, as implemented in Gaussian09/D.01. NICS grids were calculated with 1 Å resolution on a 20×20 Å grid. Version 2.0 of the ACID program[97] (external to Gaussian) was used to generate the ACID results, and they were visualised using POV-Ray. Application of Grimme's zero-damped D3 (GD3) dispersion correction[241] to geometry optimisations did not affect the conclusions of subsequent NICS calculations. The D3 correction caused small changes in the geometries (RMSD 0.018–0.025 Å) and this affected the NICS by 0–5% of their B3LYP values. The M06-2X and ωB97X-D functionals[242,243] were tested on the 0+, 4+, 6+ and 12+ oxidation states and gave similar NICS values to B3LYP (Table 3.2). M06-2X is a highly parametrised hybrid meta GGA (generalised gradient approximation) functional with good performance for main group thermochemistry and non-covalent interactions. ωB97X-D is a long-range corrected hybrid GGA functional with an empirical dispersion correction term, and similar areas of applicability as M06-2X with the addition of good treatment of the self-interaction error. The magnitude of NICS(0) for the antiaromatic 4+ oxidation state decreases according to B3LYP $>$ M06-2X $>$ ωB97X-D due to a corresponding increase in ellipticity ($f = 0.049, 0.088$ and 0.166 for B3LYP, M06-2X and ωB97X-D, respectively). For ωB97X-D, this elliptical distortion results in predicted non-aromaticity of the 4+ state. The presence of template (**T6**) in the experimental studies maintains an approximately circular geometry by limiting such distortion, ensuring antiaromaticity.

3.3.3 Spectroscopy

All oxidation experiments were conducted in J. Young tap NMR tubes using CD_2Cl_2 stored over molecular sieves, employing standard Schlenk line techniques. For titrations, a solution of oxidant (40–50 mM) was added to a solution of porphyrin compound (ca. 4 mg/mL) in the NMR tube, cooled to $-78\,^{\circ}C$ and kept under a flow of argon. For single point oxidations, an excess of an oxidant as a solution or suspension was added to the porphyrin solution in the same manner. Tubes were then closed and quickly transferred to an NMR spectrometer pre-cooled to the appropriate temperature. Exposure to water is immediately deleterious to porphyrin polycations, but they are stable to oxygen (O_2). The use of rubber septa was avoided: we found that the introduction of small quantities of rubber (even by non-coring needles) has an immediate quenching effect on the cations.

NMR measurements were performed on a Bruker AVII 500 (5 mm TXI probe) or a Bruker AVIII 700 (5 mm TCI cryoprobe). Chemical shifts are reported in ppm vs. the residual solvent peak. The ^{1}H NMR spectra of ***c*-P6•T6^{4+}** and ***c*-P6•T6^{6+}** are unchanged on warming from 213 K to 278 K. In contrast, the spectrum of ***c*-P6•T6^{12+}** broadens upon warming, and this change becomes irreversible if the sample is kept at 20 °C for more than a few minutes, due to decomposition. Neutral ***c*-P6•T6** is insoluble in CD_2Cl_2 at low temperatures (<233 K), but solubility improves upon oxidation. The ^{1}H NMR spectra of all species are field-independent, from 500 MHz (11.7 T) to 700 MHz (16.4 T).

Voltammetric measurements were made using an Autolab PGSTAT 12 with a glassy-carbon working electrode, platinum wire counter electrode and Ag/AgCl quasi-reference electrode. Voltammograms were referenced to the Fc/Fc^+ couple (0.0 V) as an internal reference after each measurement. Square wave voltammograms (SWV) were acquired with a 5 mV step potential, 50 mV modulation amplitude and 5 Hz frequency. Exclusion of water was essential for the acquisition of clean voltammograms. The supporting electrolyte salt (tetra-*n*-butylammonium hexafluorophosphate, TBAP, Bu_4NPF_6) was dried by melting in vacuo. CH_2Cl_2 (dried over alumina (MBraun SPS), distilled from CaH_2, and stored over 4 Å molecular sieves) was added to the dry electrolyte to a concentration of 0.1 M electrolyte. Analyte solutions were prepared by addition of this electrolyte solution to porphyrin oligomer (2–10 mg), and measurements were performed over 4 Å molecular sieves.

3.4 Results and discussion

3.4.1 Computational assignment of aromaticity

DFT was used to calculate NICS[89,94] as a measure of aromaticity.

For our purposes, we chose to calculate NICS(0) on grids in the *xy* plane, since ***c*-P6** is sufficiently large that negligible in-plane contamination would be expected at the ring centre (c.f. the limited extent of in-plane anisotropy presented in[91]). The $NICS(0)_{zz}$ indicate aromaticity for the 6+ oxidation state, while 0 (neutral) and 12+ are non-aromatic, and 4+ is antiaromatic. The $NICS(0)_{iso}$ calculated on a grid in the *xy* plane (the plane of the six Zn atoms) for ***c*-P6**, ***c*-P6^{4+}**, ***c*-P6^{6+}** and ***c*-P6^{12+}** clearly demonstrates the nature of the ring current in each oxidation state (Figure 3.2 and Figure 3.3).

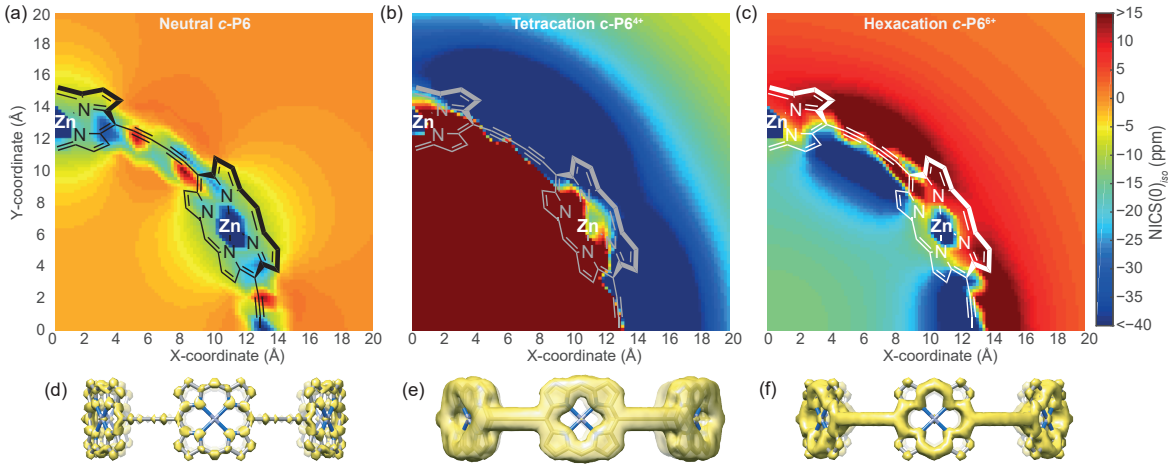

Figure 3.2: Computational data supporting aromaticity and anti-aromaticity. $NICS(0)_{iso}$ grids in the *xy* plane of (a) ***c*-P6**, (b) ***c*-P6^{4+}** and (c) ***c*-P6^{6+}**. The colour axis has been truncated to compare the grids on the same scale; see Figure 3.3 for grids with individual scales. (d–f) show ACID plots for each oxidation state. The yellow iso-surface depicts the anisotropy of the induced current density, with an isovalue of 0.1 a.u. The neutral oxidation state (a) shows ring current effects local to each porphyrin subunit. In contrast, the 4+ and 6+ oxidation states (b and c) show global ring current effects, manifest by sign-reversal of the NICS inside and outside the ring.

Table 3.1: Calculated (NICS, ppm) and experimental ($\Delta\delta$, ppm) parameters for the description of aromaticity in different oxidation states of ***c*-P6** (calculations were performed on a ***c*-P6** model). Negative NICS/$\Delta\delta$ values correspond to aromaticity, and positive NICS/$\Delta\delta$ values to antiaromaticity. The NICS(0) values were calculated at the centre of the ring. The NICS and magnetic susceptibility for the dication were calculated using unrestricted DFT.

	0+	2+	4+	6+	12+
$n\ \pi\ e^-$	84	82	80	78	72
Hückel classification	$4n\ \pi$	$4n+2\pi$	$4n\ \pi$	$4n+2\pi$	$4n\ \pi$
$NICS(0)_{zz}$ (ppm)	1	−10	304	−41	1
$NICS(0)_{iso}$ (ppm)	−1	−5	101	−13	1
χ_{mol} $cm^3\ mol^{-1}$ (cgs)	-2.0×10^{-3}	-4.2×10^{-3}	6.8×10^{-2}	-1.0×10^{-2}	1.1×10^{-4}
$\Delta\delta_{o',o}$	0.26	—	—	−1.87	−0.74
$\Delta\delta_{THS',THS}$	0.14	—	3.45	−0.70	−0.18

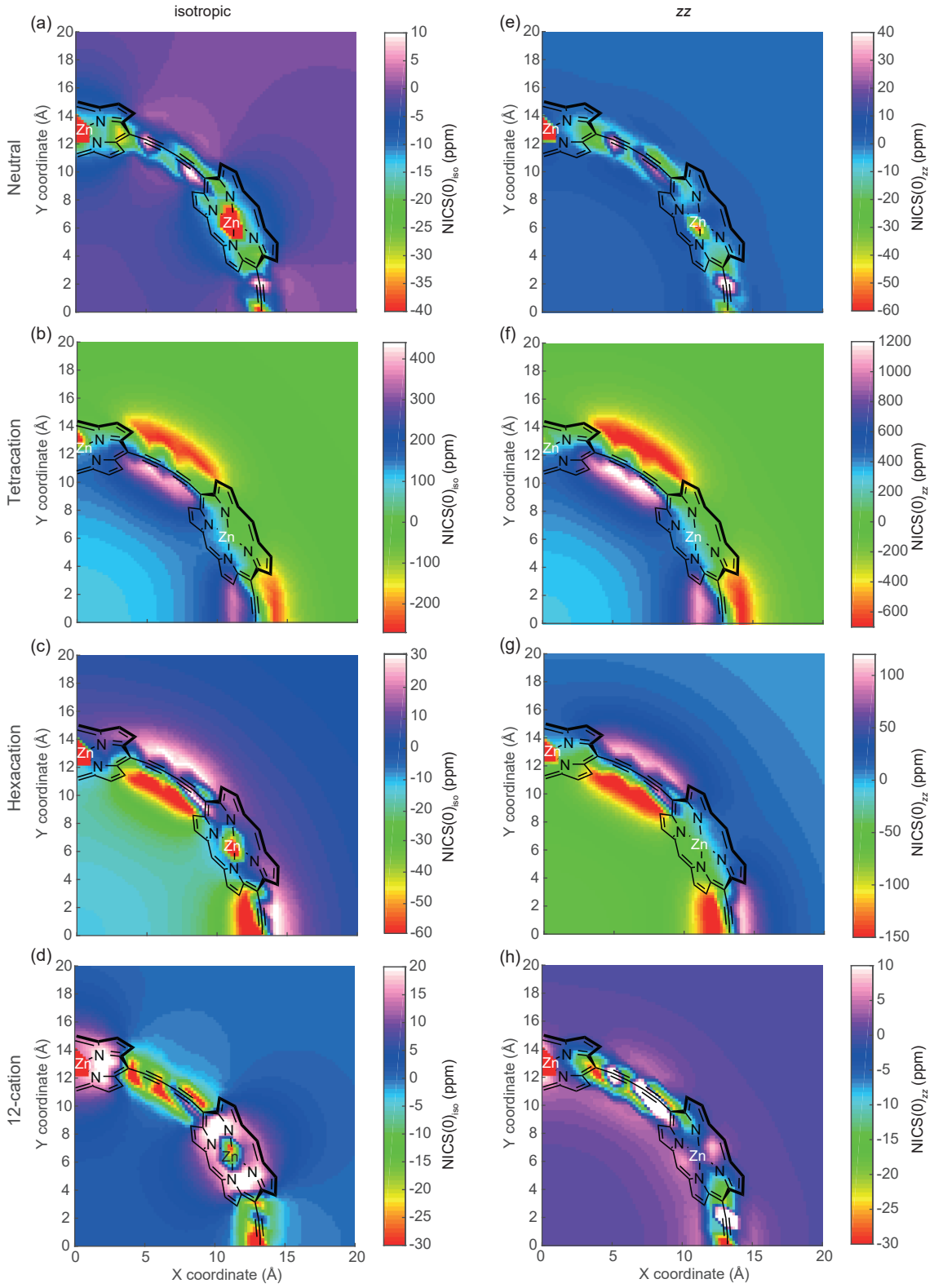

Figure 3.3: NICS(0)$_{iso}$ grids for neutral, 4+, 6+ and 12+ ***c*-P6**. (e–h): corresponding NICS(0)$_{zz}$ grids. Level of theory B3LYP/6-31G*.

Table 3.2: $NICS(0)_{iso}$ and (in brackets) $NICS(0)_{zz}$ values (ppm) for ***c*-P6** in different oxidation states, with different DFT functionals. The 6-31G* basis set was used throughout.

	0+	2+	4+	6+	12+
B3LYP//B3LYP	−1 (1)	−5 (−10)	101 (304)	−13 (−41)	1 (1)
B3LYP//B3LYP-D3	−1 (1)	−5 (−10)	106 (320)	−13 (−41)	1 (1)
M06-2X//M06-2X	−2 (1)	n.d.	3 (12)	−15 (−45)	0 (1)
ωB97X/ωB97X-D	−2 (1)	n.d.	0 (1)	−16 (−46)	0 (1)

For the neutral ***c*-P6**, the ring current effects are localised above and below the plane of each porphyrin unit, with no net global ring current (Figure 3.2a). This result is in stark contrast to ***c*-P6^{4+}**, where the NICS is positive (NMR deshielding) inside the macrocycle, and negative (shielding) outside, characteristic of paratropicity (Figure 3.2b). This effect is reversed in the aromatic ***c*-P6^{6+}**, with shielding inside the macrocycle, and deshielding outside (Figure 3.2c).

The $NICS(0)_{iso}$ grid for the 12+ (Figure 3.3) shows local porphyrin antiaromaticity, with no global aromaticity, consistent with six local 16π antiaromatic porphyrin ring-currents. For the 6+, we also calculated $NICS_{zz}$ in the orthogonal *xz* and *yz* planes (Figures 3.4 and 3.5), showing that the shielding anisotropy of the nanoring extends as a double cone above and below the plane of the ring.

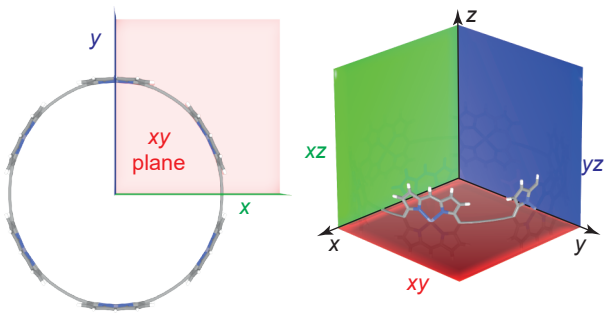

Figure 3.4: Representations of ***c*-P6** describing the *xy*, *xz* and *yz* planes in which NICS grids have been calculated.

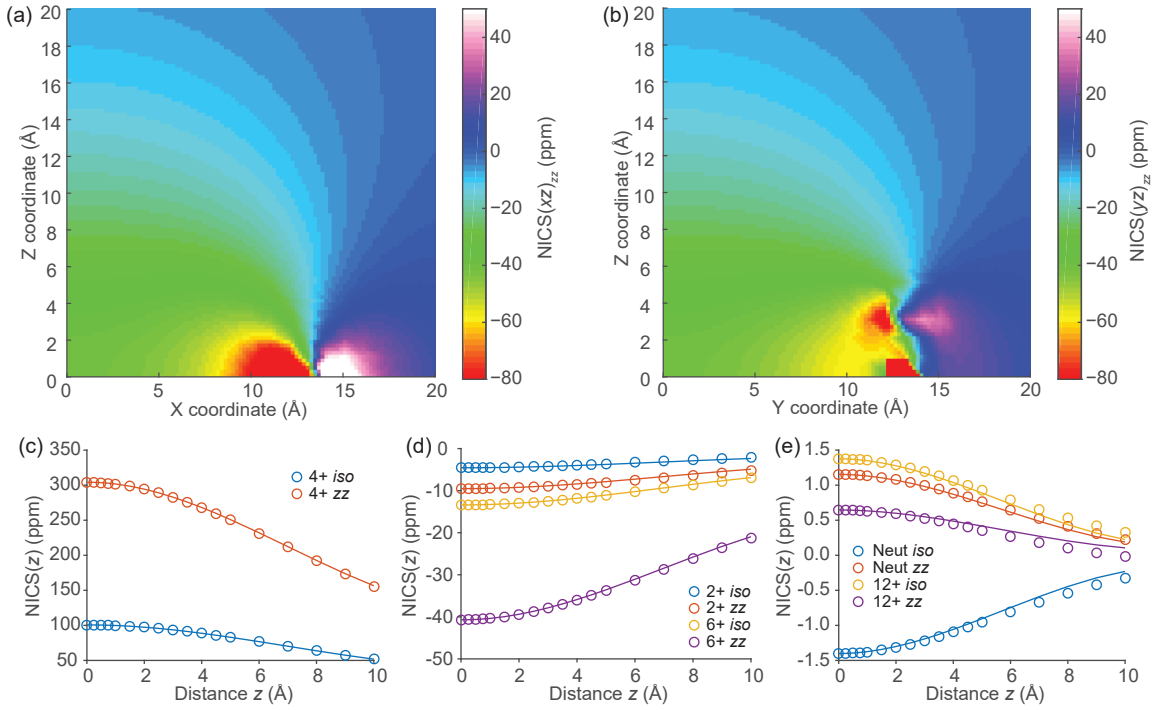

Figure 3.5: $NICS_{zz}$ grids for ***c*-P6^{6+}** in (a) the *xz* plane and (b) the *yz* plane of the molecule. In (a), the view bisects a butadiyne and in (b) the view bisects a porphyrin. (c–e) show NICS(z) scans along the z axis of the molecule (see Figure 3.4). The fitting lines are described below. Level of theory: B3LYP/6-31G*.

These calculated NICS(z) values (Figure 3.5c-e) fit well to a cubic polynomial:

$$\mathrm{NICS}(z) = \frac{\mathrm{NICS}(0)}{100}(az^3 + bz^2 + cz + 100) \tag{3.1}$$

Where a, b and c are defined by fitting, according to aromaticity status, as identified in Table 3.3.

Table 3.3: Fitting parameters for NICS(z) scans to a cubic polynomial. The shape of the polynomial is consistent for all (anti)aromatic states, and distinct from that for non-aromatic states.

	Ox. states	a	b	c
(Anti)aromatic	2+, 4+, 6+	4.50×10^{-2}	-9.46×10^{-1}	1.10×10^{-1}
Non-aromatic	0, 12+	1.13×10^{-1}	-1.96	-1.30×10^{-1}

Models of ACID on ***c*-P6** support the conclusions from NICS, demonstrating a coherent current ACID isosurface for ***c*-P6^{4+}** and ***c*-P6^{6+}** (with paratropic and diatropic current directions, respectively; current vectors shown in Figure 3.6), in contrast to an interrupted isosurface for ***c*-P6** and ***c*-P6^{12+}** (Figure 3.2d–f and Figure 3.6).

Many antiaromatic systems, including cyclobutadiene, undergo a Jahn-Teller distortion to favour a low-symmetry conformation, and this effect is evident in ***c*-P6^{4+}**. The geometries

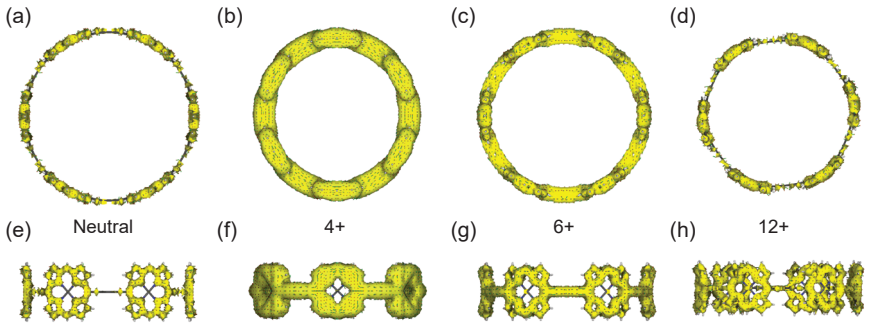

Figure 3.6: ACID plots, viewing the molecule along the $-z$ axis, for an applied magnetic field along the $+z$ axis, for (a) ***c*-P6**, (b) ***c*-P6^{4+}** (c) ***c*-P6^{6+}** and (d) ***c*-P6^{12+}**. (e–h) show the corresponding views along the y axis. The ACID isosurface corresponds to an isovalue of 0.06 a.u.

of ***c*-P6** and ***c*-P6^{6+}** converge in D_{6h} symmetry whereas ***c*-P6^{4+}** has C_1 symmetry with an elliptical flattening factor of $f = 0.049$ (defined as $1 - b/a$, where a and b are the major and minor radii of the Zn_6 ellipse). ***c*-P6^{12+}** also has C_1 symmetry but in this case there is almost no ellipticity ($f < 10^{-3}$).

3.4.2 Experimental measurement of aromaticity and antiaromaticity

The nanoring cations can be generated in solution by chemical or electrochemical oxidation. Square-wave voltammetry (SWV) of ***c*-P6•T6** reveals six reversible porphyrin-centred oxidations in a first manifold, at +0.1 to +0.7 V (vs. Fc/Fc^+) (Figure 3.7; Chapter 4 for spectroelectrochemistry). The second manifold comprises a single six-electron oxidation to generate ***c*-P6•T6^{12+}**, in which each porphyrin unit is in its 2+ oxidation state.

All of the oxidation states are accessible by titration with tris(2,4-dibromophenyl)aminium hexafluoroantimonate ($DIBAHA_F$, $E_{red} = 1.14$ V), and specific oxidation states can be targeted with diacetylferrocenium hexafluoroantimonate (diAcFc, $E_{red} = 0.50$ V), tris(4-bromophenyl)aminium hexafluoroantimonate ($BAHA_F$, $E_{red} = 0.70$ V) and thianthrenium hexafluoroantimonate (Thn, $E_{red} = 0.86$ V) (all vs. Fc/Fc^+, Figure 3.7, Figure 3.8 for structures).[244]

The magnetic effects of molecular ring currents are particularly apparent in NMR spectra.[85] Titration of $DIBAHA_F$ into a solution of ***c*-P6•T6** at 223 K in CD_2Cl_2 gives a sequence of three resolved ^1H NMR spectra (Figure 3.9), assigned to the 4+ (red-brown solution), 6+ (burgundy solution) and 12+ (grey/black solution) oxidation states (see later). There is no further change in the NMR spectrum upon addition of excess $DIBAHA_F$: the

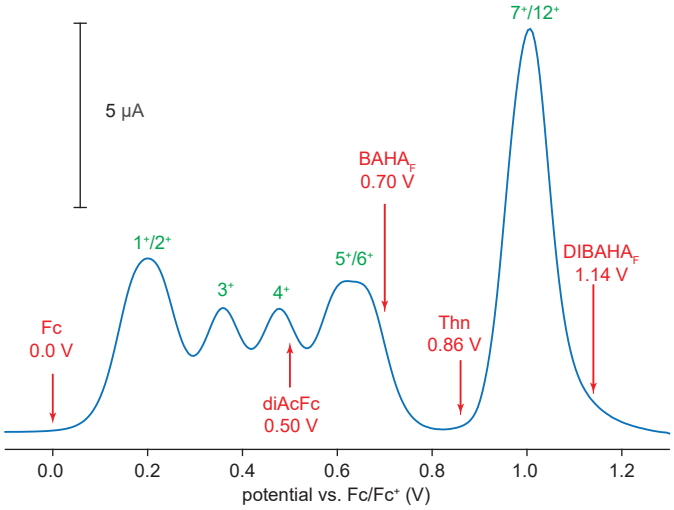

Figure 3.7: Square-wave voltammetry of *c*-P6•T6. The solvent was CH_2Cl_2 (0.1 M Bu_4NPF_6). Red arrows show the first reduction potential of each oxidant:[244] ferrocene (Fc), diacetylferrocene (diAcFc), tris(4-bromophenyl)aminium hexafluoroantimonate ($BAHA_F$), thianthrenium hexafluoroantimonate (Thn) and tris(2,4-dibromophenyl)aminium hexafluoroantimonate ($DIBAHA_F$). There are six oxidations in a first manifold, generating oxidation states up to the hexacation (6+). A second manifold contains only a single oxidation wave generating the dodecacation (12+).

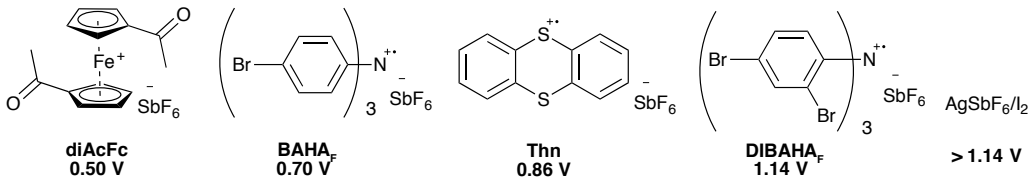

Figure 3.8: Chemical structures of oxidants used in this study. Abbreviations are expanded in the text. The potentials underneath each structure refer to the E_{red} for the first reduction of each oxidant.

12+ state is the endpoint. Identical spectra are obtained using $AgSbF_6/I_2$ (4:1 or 2:1) as the oxidant. Intermediates with odd numbers of electrons are not observed during these NMR titrations, presumably because their spectra are extremely broad. The spectrum for the 2+ oxidation state (i.e. after addition of 2 eq. oxidant) is also too broad to observe, indicating that ***c*-P6•T6^{2+}** is open-shell and paramagnetic. We confirmed the oxidation state of the first two resolved products (4+ and 6+) by single-point oxidations with diAcFc (4+), $BAHA_F$ (6+) and Thn (6+). These single-point oxidation NMR spectra are reproducible in the presence of supporting electrolyte (0.1 M Bu_4NPF_6).

Before presenting the NMR evidence for global nanoring (anti)aromaticity in the 4+ and 6+ oxidation states, we calibrate discussion of the ^{1}H NMR spectra on the well-studied[245] neutral ***c*-P6•T6**. The porphyrin β-pyrrole protons resonate at the characteristic chemical shifts for neutral porphyrins (a: 9.56 ppm, b: 8.75 ppm, Figure 3.9a; Table 3.4).

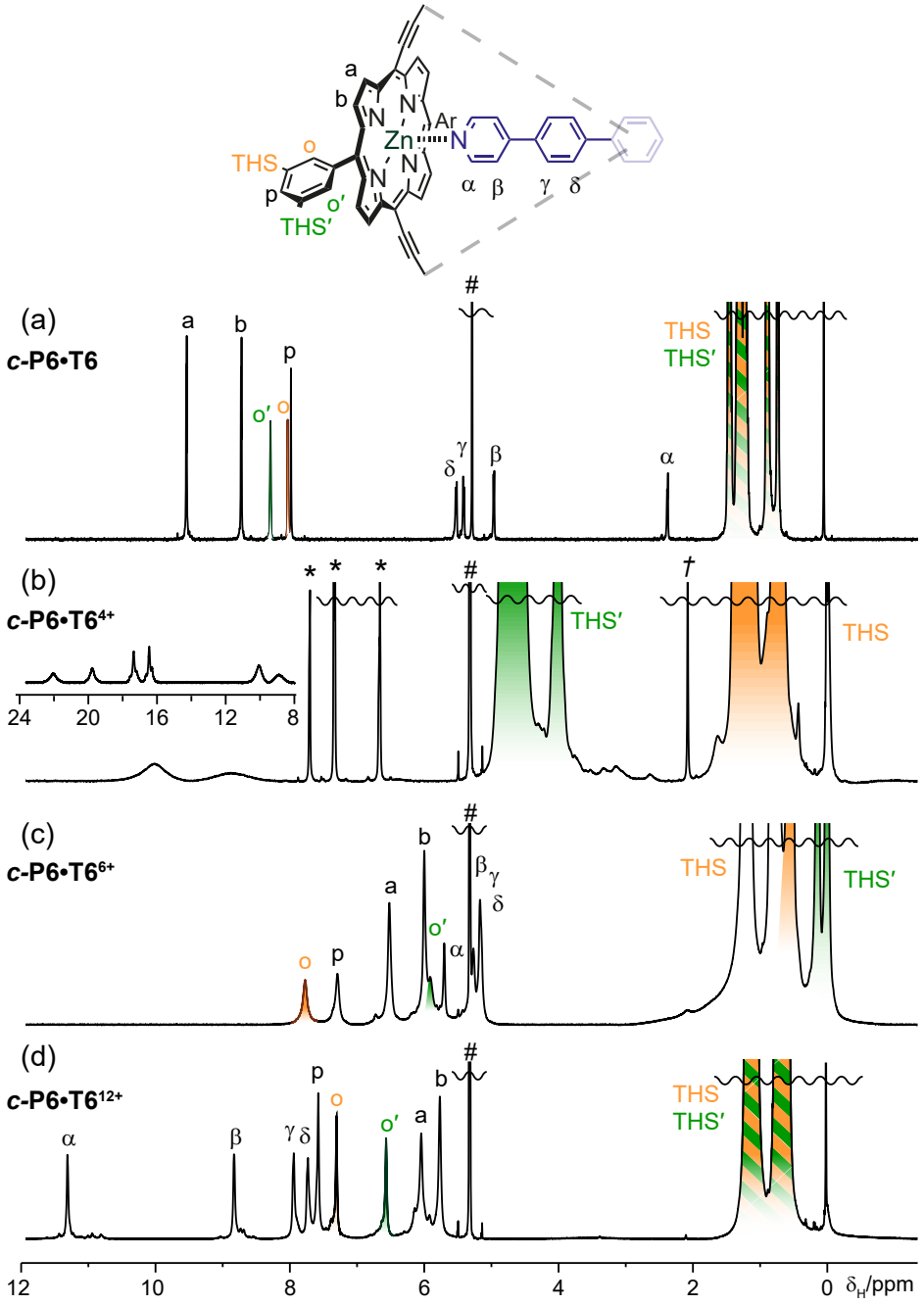

Figure 3.9: NMR spectra of neutral and oxidised *c*-P6•T6. ^{1}H NMR (500 MHz, CD_2Cl_2) of (a) neutral ***c*-P6•T6** (298 K); (b) ***c*-P6•T6^{4+}** generated by titration with $DIBAHA_F$, 223 K; (c) ***c*-P6•T6^{6+}** generated during titration with $AgSbF_6/I_2$, 223 K; (d) ***c*-P6•T6^{12+}** generated by oxidation with excess $DIBAHA_F$, 223 K. The inset shows the molecular structure of the repeat unit of the 6-fold symmetric ***c*-P6•T6**. The peaks labelled # and ∗ arise from $CHDCl_2$ and neutral oxidant (tris(2,4-dibromophenyl)amine), respectively. Unlabelled resonances are not assigned. † is an unknown impurity. In the neutral state (a), the template resonances (α–δ) probe the local aromaticity of each porphyrin. This aromaticity is reversed in the dodecacation (d), where the template protons report local antiaromaticity. The global aromaticity and antiaromaticity of the tetracation (b) and hexacation (c) are revealed by the large chemical shift difference between similar protons inside and outside the ring. The full spectra, without truncated peaks, are shown in Figure 3.20.

Table 3.4: ^{1}H and ^{13}C NMR chemical shifts for ***c*-P6•T6**, ***c*-P6•T6^{4+}**, ***c*-P6•T6^{6+}** and ***c*-P6•T6^{12+}**. 'THS CH_3' refers to the terminal methyl in the hexyl chain of the trihexylsilyl group (determined by multiplicity edited HSQC), and 'THS CH_2' refers to the methylene proximal (α) to the silicon atom, determined by chemical shift. The inner (′) and outer THS manifolds could be readily distinguished by COSY, TOCSY and NOESY. All chemical shifts are given in ppm.

	Neutral		4+		6+		12+	
	^{1}H	^{13}C	^{1}H	^{13}C	^{1}H	^{13}C	^{1}H	^{13}C
α	2.41	143.4	—	—	5.71	145.9	11.31	151.0
β	4.99	119.9	—	—	5.27	—	8.83	125.6
γ	5.45	124.3	—	—	~5.17	—	7.94	126.3
δ	5.56	131.2	—	—	~5.17	—	7.73	131.8
a	9.56	130.6	—	—	6.52	128.2	6.05	133.6
b	8.75	133.3	—	—	5.99	133.4	5.77	136.5
o	8.06	141.6	—	—	7.78	—	7.31	128.2
o′	8.32	140.8	—	—	5.91	—	6.57	134.4
p	8.02	139.9	—	—	7.92	—	7.58	144.6
THS CH_3	0.77	14.4	0.69	13.9	0.84	14.2	0.83	13.7
THS′ CH_3	0.91	14.4	4.14	17.3	0.14	13.6	0.65	14.1
THS CH_2	0.92	13.0	0.80	11.7	0.73	11.6	0.75	~13
THS′ CH_2	0.92	13.0	4.73	14.9	0	10.8	0.59	~13
$\Delta\delta_{o',o}$	0.26	−0.8	—	—	−1.87	—	−0.74	6.2
$\Delta\delta_{\text{THS}',\text{THS CH}_3}$	0.14	0	3.45	3.4	−0.70	−0.6	−0.18	0.4
$\Delta\delta_{\text{THS}',\text{THS CH}_2}$	0	0	3.93	3.2	−0.73	−0.8	−0.16	~0

Rotation of *meso*-aryl groups is slow on the NMR timescale (see Supplementary Section for details), so that the inner and outer ortho protons (o′ and o) and trihexylsilyl resonances (THS′ and THS) can be confidently distinguished. A global aromatic ring current would shield the inner protons (o′ and THS′) and deshield the outer protons (o and THS) causing large differences in chemical shift ($\Delta\delta = \delta_{inner} - \delta_{outer}$). It is observed that these signals give small chemical shift differences ($\Delta\delta_{o'/o} = 0.26$ ppm; $\Delta\delta_{THS'/THS} = 0.14$ ppm) in the neutral ring, implying that there is no global ring current. The ring current of each aromatic 18π porphyrin unit is apparent from the ^{1}H chemical shifts of the template protons α, β, γ and δ, which are shielded by the porphyrin; the shielding is attenuated with increasing distance from the porphyrin: $\alpha \gg \beta > \gamma > \delta$ (Figure 3.9a and Table 3.5).

The ^{1}H NMR spectrum of ***c*-P6•T6^{4+}** is very broad (Figure 3.9b), precluding detailed assignment of the resonances. However, a clear splitting of the THS groups is apparent in the aliphatic region (Figure 3.10a).

Table 3.5: Chemical shift differences ($\Delta\delta_{X+} = \delta_{\textbf{T6, free}} - \delta_{\textbf{T6 in c-P6•T6}^{X+}}$) for the template protons (α, β, γ and δ) in ***c*-P6•T6**, ***c*-P6•T6^{6+}** and ***c*-P6•T6^{12+}**, vs. unbound template (**T6**, 400 MHz, $CDCl_3$). All values are given in ppm.

	T6	$\Delta\delta_0$	$\Delta\delta_{6+}$	$\Delta\delta_{12+}$
α	8.54	6.13	2.83	−2.77
β	7.33	2.34	2.06	−1.50
γ	7.24	1.79	2.07	−0.70
δ	7.02	1.46	1.85	−0.71

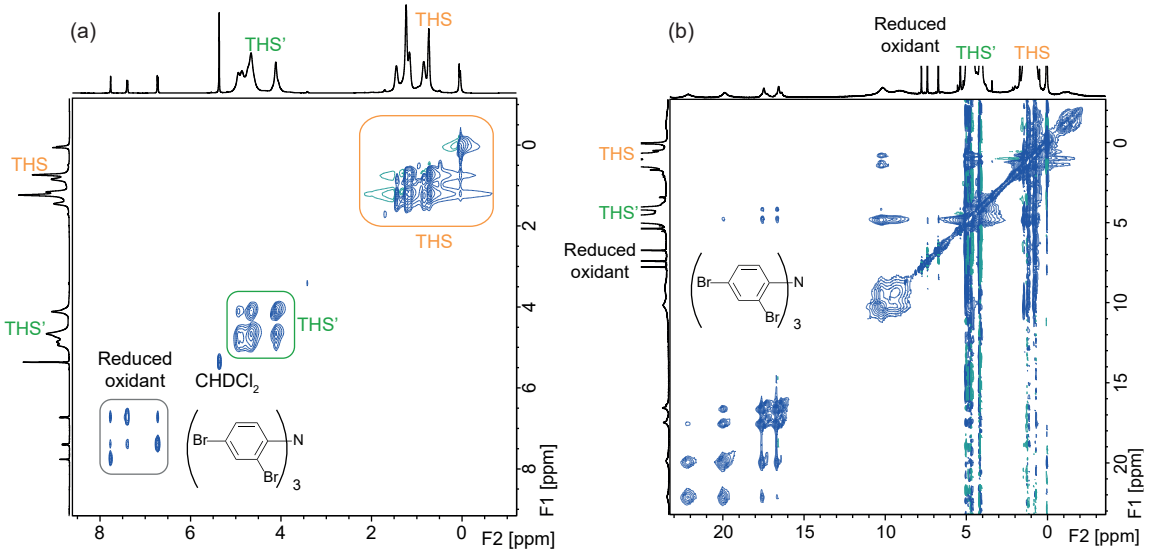

Figure 3.10: (a) TOCSY (t_{mix} = 60 ms, MLEV17 sequence) and (b) NOESY (t_{mix} = 250 ms) of ***c*-P6•T6^{4+}** (500 MHz, 223 K). This sample was prepared by titration with $DIBAHA_F$.

The less shielded set of THS resonances shows multiple NOEs to resonances at high chemical shift (8–24 ppm), and is thus assigned to the inner THS′ group Figure 3.10b). The large positive $\Delta\delta_{THS/THS'}$ (3.45 ppm) implies a strong macrocyclic paratropic ring current. Antiaromaticity is further supported by an extremely high paramagnetic susceptibility exaltation for ***c*-P6•T6^{4+}** measured by Evans' NMR method (see subsection 3.5.1)[246] and corroborated by DFT calculations; χ_{mol} (experimental) = 21,000 ppm $cm^3\,mol^{-1}$ ($\mu_{eff} = 6.5\mu_B$), χ_{mol} (calc.) = 68,000 ppm $cm^3\,mol^{-1}$, (μ_{eff} = 11.5 μB), compared to χ_{mol} = 1480 ppm $cm^3\,mol^{-1}$ (μ_{eff} = 1.7 μ_B) expected for a single unpaired electron (all units c.g.s.; see Figure 3.18, Table 3.1). Despite many predictions of paramagnetism in closed-shell antiaromatic compounds,[135] to the best of our knowledge, this is the first time that the effect has been observed experimentally, though diamagnetic susceptibility exaltation is a well-recognised characteristic of aromatic systems.[72] Experimental studies of

other antiaromatic systems have found a reduction in the diamagnetism rather than outright paramagnetism.[72] 'Giant orbital paramagnetism' has been predicted, but not observed, for carbon-based nanostructures such as carbon nanotube tori.[247]

In contrast to ***c*-P6•T6^{4+}**, the NMR spectrum of ***c*-P6•T6^{6+}** is well resolved and fully assigned by 2D techniques (see Figures 3.11a (NOESY) and 3.11b,c (COSY)).

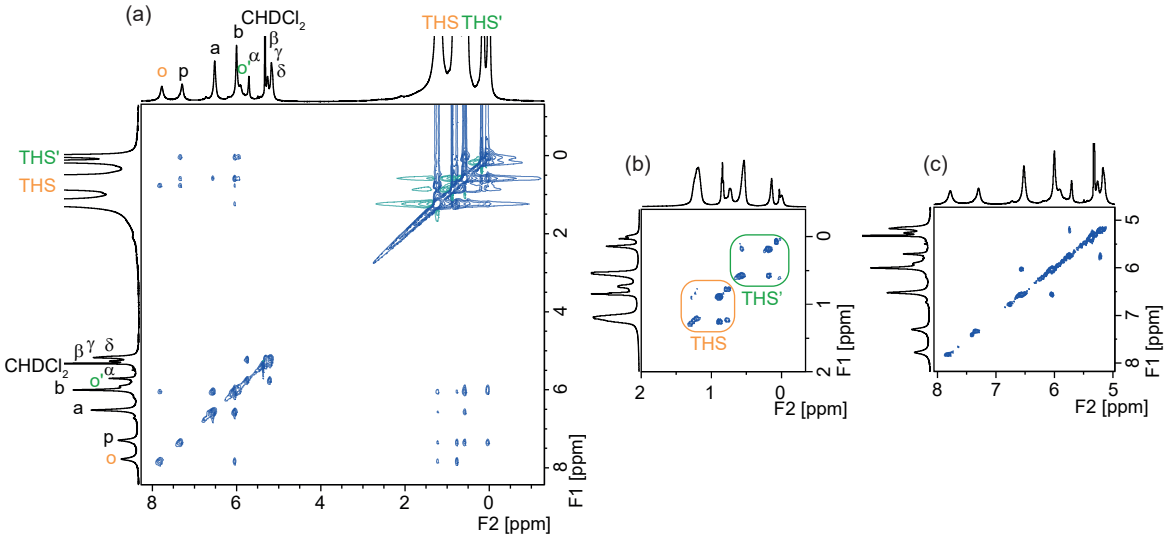

Figure 3.11: (a) NOESY (t_{mix} = 250 ms) (b) COSY (aliphatic expansion) and (c) COSY (aromatic expansion) of ***c*-P6•T6^{6+}** (500 MHz, 223 K). This sample was prepared by titration with $AgSbF_6/I_2$.

A large $\Delta\delta$ is observed between the o′/o (−1.87 ppm) and THS′/THS (−0.70 ppm) resonances. NOEs to the template were used to assign the inner vs. outer resonances. The inner o′ and THS′ are more shielded than their external counterparts (negative $\Delta\delta$) in ***c*-P6•T6^{6+}**, confirming the presence of a global diatropic ring current. The template protons α–δ are all nearly equally shielded with respect to unbound **T6** (Table 3.5), revealing a uniform shielding effect within the macrocycle, as predicted by the NICS grids (Figure 3.2c), and indicating the absence of local porphyrin aromaticity.

The ^{1}H NMR spectrum of ***c*-P6•T6^{12+}** is well resolved and was fully characterised by 2D NMR techniques (Figures 3.12a (NOESY), 3.12b (COSY) and 3.13 (NOE build-ups)). In ***c*-P6•T6^{12+}**, every porphyrin unit is in the antiaromatic 16π dicationic oxidation state.[248] The antiaromatic porphyrin centres deshield the template protons (with respect to unbound template, Table 3.5); the extent of deshielding decreases with distance from the porphyrin plane, $\alpha >> \beta > \gamma > \delta$ (Figure 3.9d). This behaviour is entirely local to the 16π porphyrin unit, as demonstrated by the similarity between the ^{1}H NMR spectra of the porphyrin monomer ***l*-P1^{2+}**, dimer ***l*-P2^{4+}**, tetramer ***l*-P4^{8+}**, and cyclic oligomers

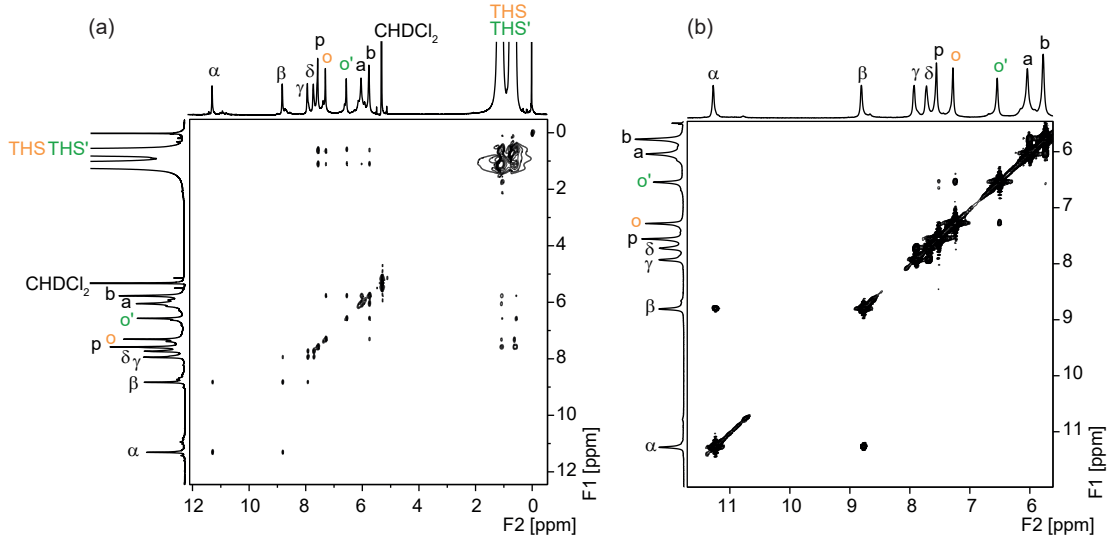

Figure 3.12: (a) NOESY of ***c*-P6•T6**$^{12+}$ (500 MHz, 223 K). t_{mix} = 200 ms. This sample was prepared by titration with excess $DIBAHA_F$. (b) COSY of ***c*-P6**$^{12+}$ (500 MHz, 213 K). This sample was prepared by oxidation with excess $DIBAHA_F$.

***c*-P6•T6**$^{12+}$, ***c*-P6**$^{12+}$, ***c*-P8**$^{16+}$, ***c*-P10**$^{20+}$, ***c*-P11**$^{22+}$ and ***c*-P12**$^{24+}$ (all recorded in the presence of excess $DIBAHA_F$; Figure 3.14).

Comparison of the SWV of ***l*-P1** and ***l*-P2** shows that the first oxidation wave of ***l*-P1** is split upon oligomer homologation, while the second oxidation wave is not split (Figure 3.15a). This lack of electronic communication is reflected in the highest occupied molecular orbital (HOMO) of ***l*-P2**$^{4+}$, corresponding to the Gouterman a_{1u} orbital,[249] which exhibits no density at the porphyrin *meso* positions (Figure 3.15b). In contrast, the HOMOs of neutral oligomers exhibit high density at the *meso* positions (Gouterman a_{2u}), leading to strong electronic communication in *meso–meso* linked porphyrin oligomers.[161]

The ^{1}H NMR spectra of ***c*-P6**$^{6+}$ and ***c*-P6**$^{12+}$ with no bound template are very similar to those of the template complexes, except for the absence of template signals (Figure 3.16).

We were unable to observe a ^{1}H NMR spectrum of ***c*-P6**$^{4+}$ without the bound template, and the conformational lock provided by the template seems to be essential for creating a well-defined antiaromatic system.

Neutral butadiyne-linked porphyrin oligomers have a very low barrier to torsional rotation about the alkyne axis[31] (Chapter 2) and fast exchange occurs between the ortho (o and o′) resonances in ***c*-P6**, even at low temperature, due to this free rotation. In contrast, the o and o′ resonances are split at low temperature for ***c*-P6**$^{6+}$ ($T < 263$ K; Figure 3.17a) and ***c*-P6**$^{12+}$ ($T < 243$ K; Figure 3.17b), indicating increased conjugation between porphyrin subunits in these oxidation states.

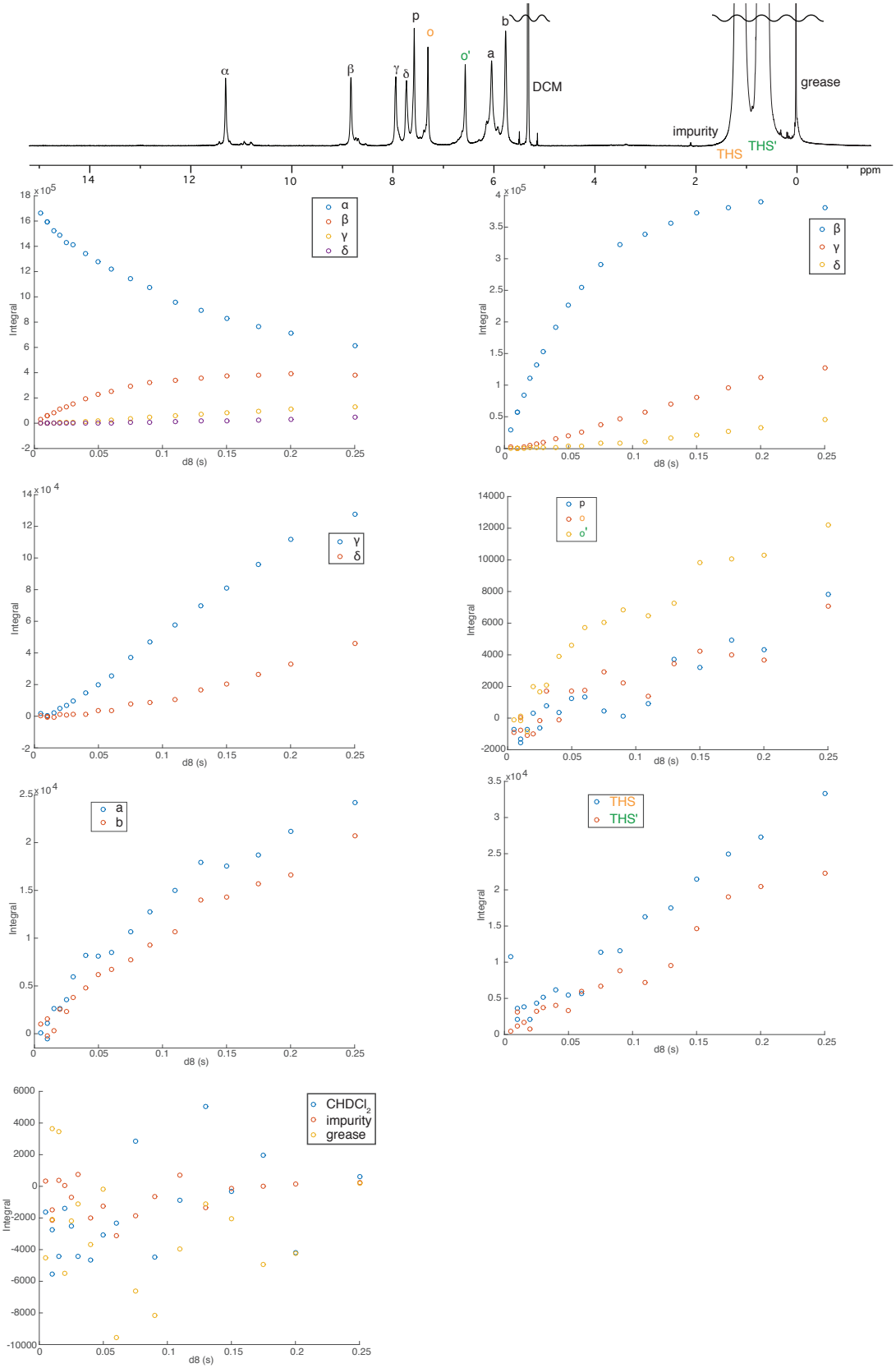

Figure 3.13: Transient ^{1}H NOE (500 MHz, CD_2Cl_2, 223 K) buildup/decay curves for ***c*-P6•T6^{12+}**, with NOE transfer following selective excitation ($t_{mix} = d_8$) of the template α proton. The sample was prepared by oxidation with excess $DIBAHA_F$.

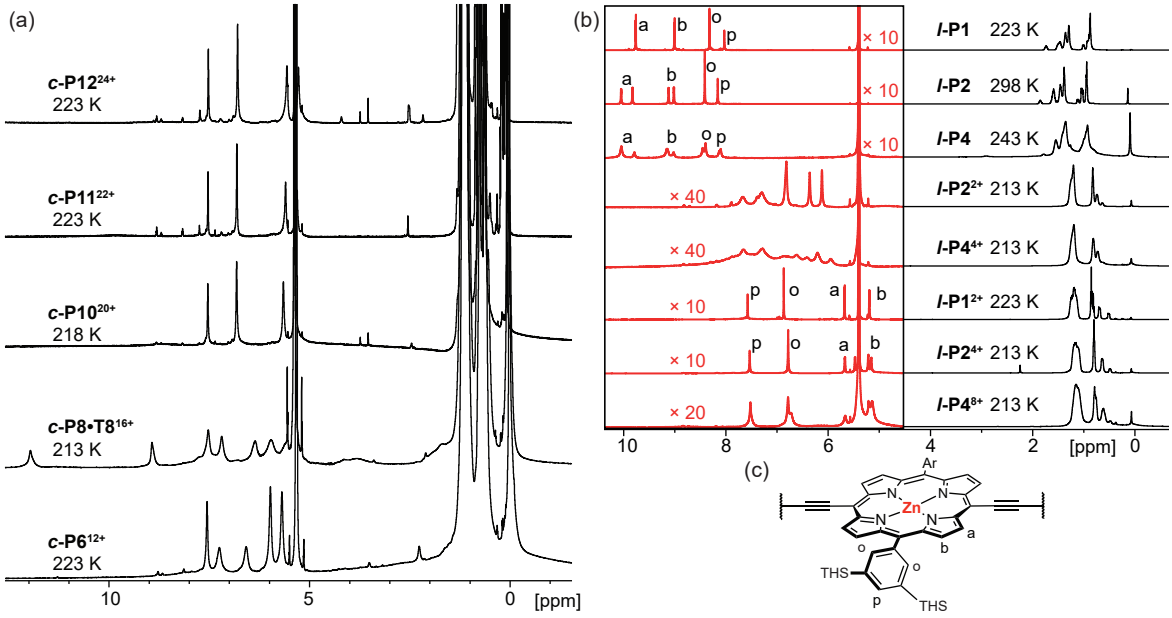

Figure 3.14: (a) ^{1}H NMR spectra (500 MHz, CD_2Cl_2) of the $2N+$ oxidation states of ***c*-P6**, ***c*-P8•T8**, ***c*-P10**, ***c*-P11** and ***c*-P12**, generated by oxidation with excess $DIBAHA_F$. (b) ^{1}H NMR spectra (500 MHz, CD_2Cl_2) of ***l*-P1**, ***l*-P2** and ***l*-P4** in their diamagnetic neutral, $N+$ and $2N+$ oxidation states (excluding paramagnetic ***l*-P1$^{+\bullet}$**). Atom labels for linear oligomers are described in (c).

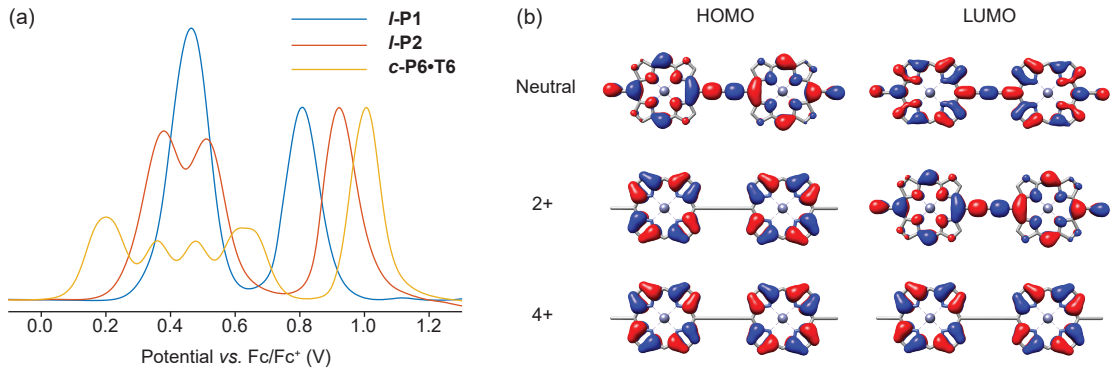

Figure 3.15: (a) Square wave voltammetry of ***l*-P1** (blue), ***l*-P2** (red) and ***c*-P6•T6** (orange), in CH_2Cl_2 (0.1 M Bu_4NPF_6). The abscissa (current) is normalised to the height of the highest oxidation peak (~1 V). (b) Frontier orbitals of ***l*-P2** in its neutral, 2+ and 4+ oxidation states. A truncated model of ***l*-P2** was used, with aryl sidegroups and terminal trialkylsilyl alkyne protecting groups truncated to H (overall D_{2h} symmetry). Level of theory: B3LYP/6-31G*. The isosurfaces are plotted at an isovalue of ~0.18ã.u.

EXSY[250] NMR experiments at 213 K revealed $\Delta G^{\ddagger}$ of 49.5 ± 0.4 kJ mol^{-1} and 42.6 ± 0.4 kJ mol^{-1} for 6+ and 12+ respectively (see Supplementary Section 3.5.2, Figure 3.19 and Table 3.6, for details). The ***c*-P6^{6+}** hexacation is aromatic with or without the bound **T6** template, but the template has two important roles in this system: it holds the nanoring in a regular geometry, resulting in sharper NMR spectra, and it provides a set of protons to probe the magnetic effects of the ring current at well-defined positions inside the nanoring.

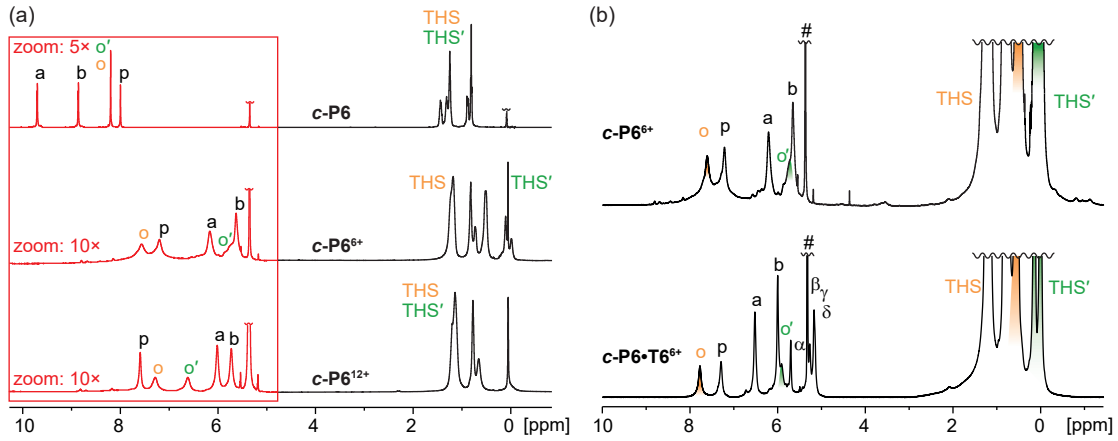

Figure 3.16: (a) Comparison of ^{1}H NMR spectra (500 MHz, 223 K, CD_2Cl_2) of template-free ***c*-P6** in its neutral, 6+ and 12+ oxidation states. The 6+ oxidation state was generated by oxidation with excess Thn, and the 12+ oxidation state was generated by oxidation with excess $DIBAHA_F$. (b) Comparison of ^{1}H NMR spectra (500 MHz, 223 K, CD_2Cl_2) of ***c*-P6** in its 6+ oxidation state, with and without template. The samples were prepared by oxidation with excess Thn and by titration with $AgSbF_6/I_2$, respectively.

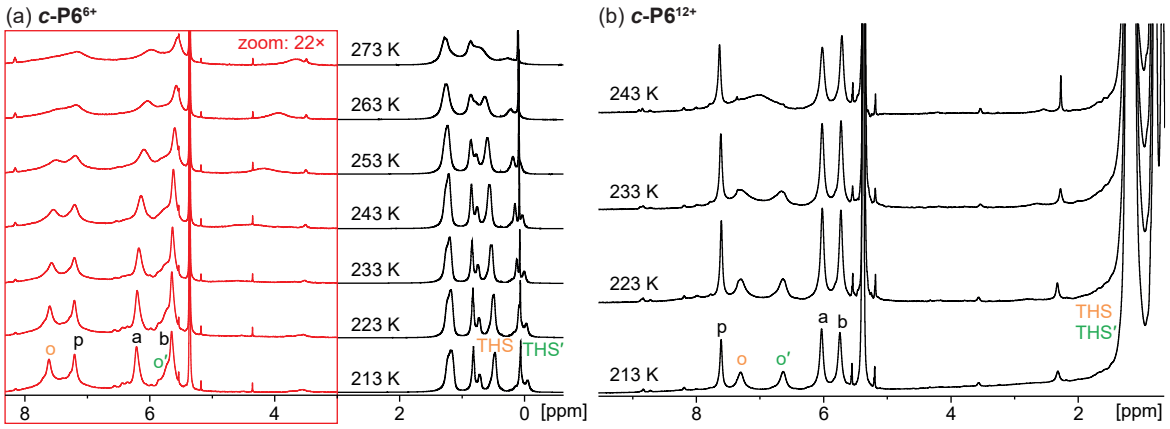

Figure 3.17: VT ^{1}H NMR (500 MHz, CD_2Cl_2) of (a) ***c*-P6^{6+}** and (b) ***c*-P6^{12+}**, generated by oxidation with excess Thn and excess $DIBAHA_F$, respectively.

3.5 Supplementary details

3.5.1 Paramagnetic susceptibility by Evans' Method

We applied the principles of Evans' method[246,251–253] for the determination of magnetic susceptibility by NMR to determine the approximate magnetic susceptibilities of the [6]-porphyrin nanoring oxidation states. At the outset, we expected to observe increases in paramagnetic susceptibility for the odd oxidation states (1+, 3+, 5+) and for the free oxidant, with near-zero relative magnetic susceptibility for the closed-shell oxidation states.

The Evans' method involves separating an analyte and a reference solution by placing one in an isolated coaxial chamber within the other. In our case, we placed a flame-sealed capillary of $CFCl_3$ in d_8-toluene into a standard 5 mm J. Young NMR tube containing the

analyte solution, $CFCl_3$ and CD_2Cl_2. The reference capillary was supported with custom-made PTFE spacers. With this assembly, we were able to conduct titrations of oxidant into ***c*-P6•T6** solutions, and measure the frequency shift between the $CFCl_3$ resonances in the ^{19}F domain. We chose to use $CFCl_3$ since the ^1H domain was too crowded to permit reliable measurement of a chemical shift difference between analyte and reference probe resonances for the commonly used references. However, the ^{19}F resonance for $CFCl_3$ is split into a complicated multiplet pattern owing to different isotopic chemical shift effects from $^{35/37}Cl$ (the resonance resembles the mass spectrum isotope pattern for $CFCl_3$, Figure 3.18b). For this reason, we use d_8-toluene as the solvent in our reference capillary, to provide an appreciable initial frequency difference between analyte and reference chamber $CFCl_3$ resonances, and make subsequent measurements of $\Delta\nu$ (calculated relative to the $\Delta\nu$ between $CFCl_3$ resonances in the reference and analyte compartments in otherwise pure solvent (without ***c*-P6•T6**)) more reliable.

Attempts to use Evans' method without an explicit reference compound, instead monitoring the ^2H solvent resonances, failed due to the broad line-width and low signal to noise of the ^2H spectrum. Control experiments indicated that, in the absence of analyte, $\Delta\nu$ with $CFCl_3$ varied by about 1 Hz/K temperature variation. In the context of a titration, this implies an error of at least ± 2 Hz in each $\Delta\nu$.

A titration of $DIBAHA_F$ (ca. 44.5 mM, in 21 µL increments) into ***c*-P6•T6** (ca. 2.0 mM, 450 µL in CD_2Cl_2) was conducted at 243 K. At this concentration and field, one equivalent of oxidant (2.0 mM, i.e. $2.0 \times 10^{-6}\,\mathrm{mol\,cm^{-3}}$) with a magnetic moment of 1 μ_B (Bohr magneton) would give an imperceptible (1–2 Hz) frequency difference $\Delta\nu$. However, our experimental results (Figure 3.18) show a huge $\Delta\nu$ (66 Hz) for the antiaromatic tetracation ***c*-P6•T6^{4+}**. This surprising result corresponds to a large paramagnetic susceptibility and is supported by DFT calculations for ***c*-P6** (Figure 3.18 and Figure 3.19).

The magnetic susceptibility χ_{mol} is related to the chemical shift difference $\Delta\nu$ by:

$$\chi_{mol} = -\frac{3\Delta\nu}{4\pi\nu_0 c} \tag{3.2}$$

where ν_0 is the spectrometer frequency (470 MHz) and c is the concentration of ***c*-P6**, in $\mathrm{mol\,cm^{-1}}$. An explicit diamagnetic solvent correction has been neglected from this analysis, since it is already factored in the susceptibility of the neutral nanoring solution from which all other relative susceptibilities are calculated.

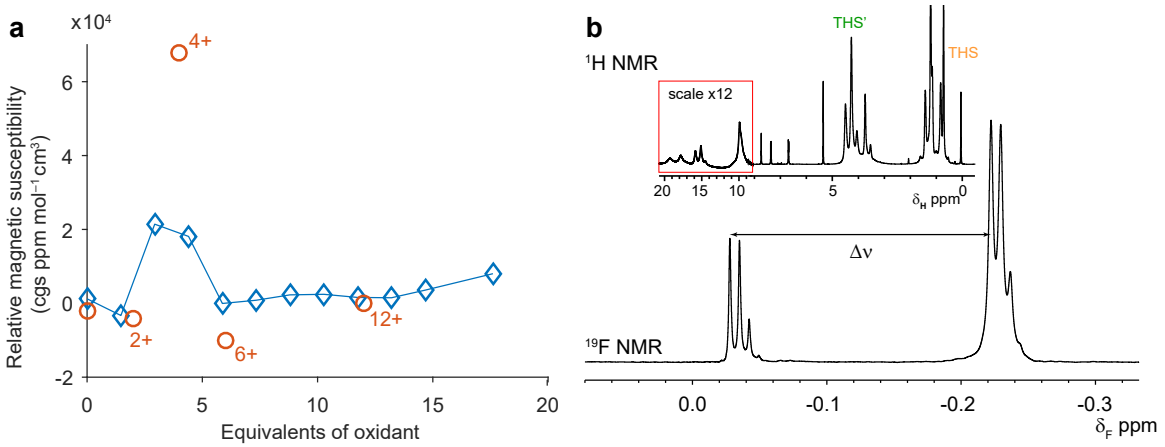

Figure 3.18: (a) Experimental magnetic susceptibility during an NMR (243 K, 470 MHz (^{19}F)) titration of DIBAHA$_F$ into ***c*-P6•T6** in CD_2Cl_2 (blue diamonds). The molar susceptibility was calculated based on the approximate concentration of ***c*-P6•T6**, and the concentration of oxidant has been corrected by a factor of 1.3 to account for error in the concentrations of oxidant and porphyrin. The red points show the DFT (B3LYP/6-31G*) calculated magnetic susceptibility. (b) Example ^{19}F (470 MHz) NMR spectrum showing the measurement of $\Delta\nu$, and the corresponding ^{1}H (500 MHz) spectrum, inset. These spectra correspond to the third data point (~4 eq. oxidant) in (a).

3.5.2 The interporphyrin torsion barriers in *c*-P6 6+ and 12+

In template-free neutral ***c*-P6**, the barrier to inter-porphyrin torsion about the butadiyne linkers is likely to be similar to that in ***l*-P2**, ca. 2.1 kJ mol^{-1},[31] (Chapter 2) thus the porphyrins are rapidly rotating at room temperature ($k_B T = 2.5$ kJ mol^{-1}). Consequently, only one resonance is observed in ^{1}H NMR for the o and o′ (ortho) protons in fast exchange. No broadening is apparent when reducing temperature to 223 K in CD_2Cl_2, below which solubility becomes limiting. In contrast, the o/o′ resonances in oxidised nanorings ***c*-P6^{6+}** and ***c*-P6^{12+}** are in slow exchange at 223 K.

VT NMR can be used to determine the coalescence temperature T_c between the o and o′ resonances and hence the exchange activation barrier at T_c (via the Eyring equation). Estimates of T_c from VT NMR are >278 K and ~233 K for 6+ and 12+, respectively. Estimation of T_c is confounded by broadening of the entire spectrum of oxidised species at elevated temperatures, perhaps owing to paramagnetic exchange with residual oxidant. To avoid this problem, we used 2D-EXSY NMR to measure the exchange rate constant k at 213 K for ***c*-P6^{6+}** and ***c*-P6^{12+}**.

A phase-sensitive NOESY (EXSY) pulse sequence with gradient enhancement (noesygpph) was employed with variable mixing times t_{mix} from 5 ms to 125 ms. The recycle delay (d_1) was 1 s. The Fourier-transformed (with a squared sine bell window function applied

to the FID) spectra were phase-corrected and a 2D baseline of 5th order was subtracted. The intensities of peaks of interest were determined by volume integration.

The pertinent o/o′ exchange was modelled as a simple two-spin system, with spins labelled A and B. An equal population of sites A and B was assumed, leading to the following equalities for the intensities I of on-diagonal peaks (I_{AA} and I_{BB}) and off-diagonal crosspeaks (I_{AB} and I_{BA}).[250,254] These equalities are not experimental facts due to spectral overlap, but this does not affect the analysis.

$$I_{AA} = I_{BB} \tag{3.3}$$

$$I_{AB} = I_{BA} \tag{3.4}$$

The intensities I can be defined as follows:

$$I_{AA} = \frac{1}{4} e^{\frac{-t_{\text{mix}}}{T_1}} [1 + e^{-kt_{\text{mix}}}] M^0 \tag{3.5}$$

$$I_{AB} = \frac{1}{4} e^{\frac{-t_{\text{mix}}}{T_1}} [1 - e^{-kt_{\text{mix}}}] M^0 \tag{3.6}$$

where t_{mix} is exchange mixing time, $T1$ is the spin-lattice relaxation time (assumed equal for A and B), k is the exchange rate constant and M^0 is the initial magnetisation. If we take the ratio of intensities r, the equations simplify, removing the dependencies on M^0 and T_1:

$$r = \frac{I_{AB} + I_{BA}}{I_{AA} + I_{BB}} \tag{3.7}$$

$$r = \frac{1 - e^{-kt_{\text{mix}}}}{1 + e^{-kt_{\text{mix}}}} \tag{3.8}$$

The experimental data points and fit for 6+ and 12+ are shown in Figure 3.19 respectively. The equations for I_{AA} and I_{AB} are based on the following chemical system:

$$\text{A} \underset{k_{BA}}{\overset{k_{AB}}{\rightleftharpoons}} \text{B}$$

which, given the equal populations of A and B, leads to the following definition of k.[254]

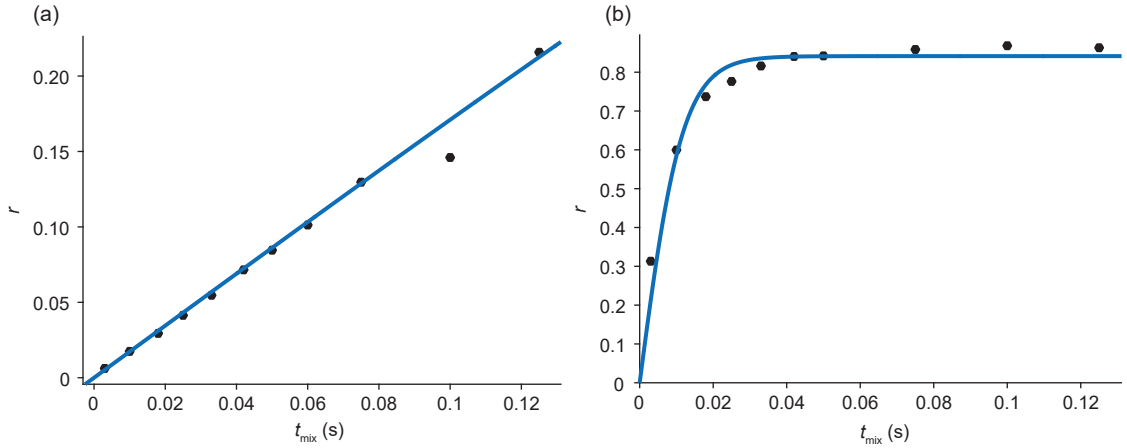

Figure 3.19: Fit of ^{1}H EXSY data (500 MHz, CD_2Cl_2, 213 K) for o/o′ exchange in (a) ***c*-P6^{6+}** and (b) ***c*-P6^{12+}**, as a function of t_{mix}.

$$p_A = p_B = 0.5 \tag{3.9}$$

$$k_{AB} = p_B k \tag{3.10}$$

$$k_{BA} = p_A k \tag{3.11}$$

$$k = 2k_{AB} = 2k_{BA} = k_{AB} + k_{BA} \tag{3.12}$$

In 1992, Green et al. noted that a multiplicative factor of two must be applied to k_{obs} ($= k_{AB}$) determined by magnetisation transfer experiments for equally populated two-site exchange in order to deliver a k_{chem} suitable for the calculation of $\Delta G^{\ddagger}$.[255] The rationale is that a species at the midpoint of a symmetric reaction profile will only decay in such a way that gives rise to magnetisation transfer 50% of the time. This notion is the direct analogue of the transmission coefficient κ in the Eyring equation:

$$k = \kappa \frac{k_B T}{h} e^{-\frac{\Delta G^{\ddagger}}{RT}} \tag{3.13}$$

In words, if we denote labelling with an asterisk, the species A*B will form a transition state in which the label is no longer well-defined: [AB]*. This transition state can decay with 50% probability (owing to the symmetric nature of the reaction profile) to give A*B and AB*. A rate constant k_{AB} only describes those transition states which result in magnetisation transfer from A to B, thus a value of $\kappa = 0.5$ must be used, analogous to Green's multiplicative factor of two for k_{chem} (i.e., $k_{chem} = 2k_{obs} = \frac{k_{AB}}{\kappa}$).

Table 3.6: Kinetic parameters for porphyrin torsional rotation in ***c*-P6^{6+}** and ***c*-P6^{12+}** from ^{1}H EXSY measurements (500 MHz, CD_2Cl_2, 213 K).

	$k_{213\ \mathrm{K}}$ (s^{-1})	$\Delta G^{\ddagger}_{213\ \mathrm{K}}$ kJ mol^{-1}	k_{chem,T_c} (s^{-1})	T_c (K)
***c*-P6^{6+}**	3.45 ± 0.86	49.48 ± 0.44	4154	282 ± 2
***c*-P6^{12+}**	172 ± 43	42.56 ± 0.44	1644	234 ± 2

In our case the formulations of k, I_{AA} and I_{AB} give us k_{chem} directly,[254] such that we use a transmission coefficient $\kappa = 1$ to determine $\Delta G^{\ddagger}$. The results are shown in Table 3.6.

The chemical exchange rate constant at the coalescence temperature (T_c) can be determined by taking an estimate for $\Delta\nu$ between o/o′ in slow exchange from the templated nanoring spectra (Table 3.1 and Table 3.4), and thus T_c can be estimated using $\Delta G^{\ddagger}$ from the above analysis. The quantitative analysis of errors in this EXSY experiment is difficult – rather than relying on the 95% confidence interval of the fit (0.07 s^{-1} and 35 s^{-1} for 6+ and 12+, respectively), we have adopted an empirical error of 25%.

Based on the absence of exchange broadening in neutral ***c*-P6** at 223 K (hence $T_c \ll$ 223 K, and $k_{ex} = 578$ s^{-1} at T_c), an upper bound of $\Delta G^{\ddagger} \ll 42.3$ kJ mol^{-1} can be assigned for the neutral oxidation state.

The value of the exchange rate constant k at 213 K for ***c*-P6^{6+}** is of the same order as that measured for o/o′ exchange due to aryl rotation about the *meso*–aryl bond in a similar complex (a templated [10]-porphyrin nanoring), at 298 K: 4 s^{-1} and 0.4 s^{-1} for two inequivalent porphyrin sites.[237] These values of k correspond to $\Delta G^{\ddagger}$ of 70 kJ mol^{-1} and 263 kJ mol^{-1}, respectively, and are thus unlikely to contribute to the EXSY spectra at 213 K. Furthermore, no o/o′ exchange is observed in the 223 K NOESY spectra of ***c*-P6•T6^{6+}** and ***c*-P6•T6^{12+}** with $t_{\mathrm{mix}} = 250$ ms.

3.5.3 Additional figures

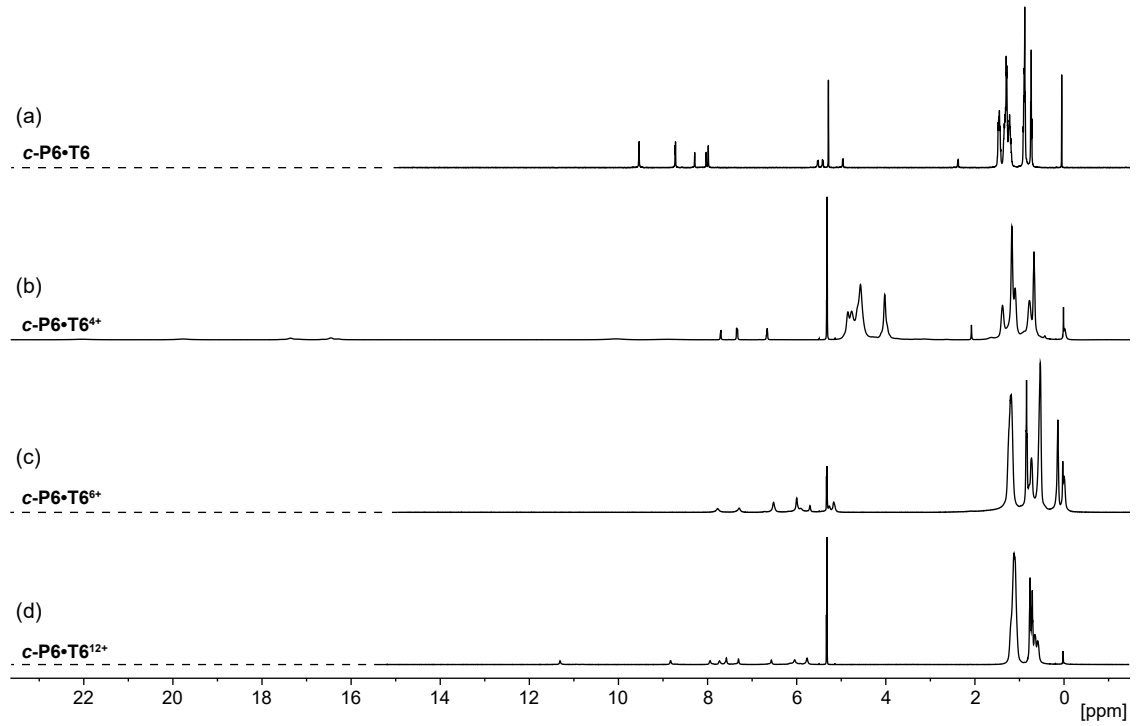

Figure 3.20: Full ^{1}H NMR spectra (500 MHz) of (a) neutral ***c*-P6•T6** (298 K); (b) ***c*-P6•T6^{4+}** generated during titration with DIBAHA$_F$, 223 K; (c) ***c*-P6•T6^{6+}** generated during titration with AgSbF$_6$/I$_2$, 223 K; (d) ***c*-P6•T6^{12+}** generated by oxidation with excess DIBAHA$_F$, 223 K. (cf. expanded extract in Figure 3.9).

We must not forget that when radium was discovered no one knew that it would prove useful in hospitals. The work was one of pure science. And this is a proof that scientific work must not be considered from the point of view of the direct usefulness of it. It must be done for itself, for the beauty of science, and then there is always the chance that a scientific discovery may become like the radium a benefit for humanity.

— Marie Skłodowska Curie (1921), Lecture at Vassar College New York

4

Charge and spin delocalisation in butadiyne-linked porphyrin oligomers

Contents

4.1 Abstract

The charge and spin delocalisation lengths in doped organic polymers are important parameters for the design of functional materials and for understanding the mechanisms of long-range charge transport. Here we thoroughly investigate the extent of charge

delocalisation in the radical cations of butadiyne-linked porphyrin oligomers, using optical (Vis-NIR-IR) and EPR (ENDOR) spectroscopies. Our results reveal charge/spin delocalisation over 2–3 porphyrin units in linear oligomers, and over a similar or greater distance in cyclic and tubular arrays. We observe strongly intensified IR signals for the radical cations and, for the cyclic systems, Fano-like anti-resonance interferences between a low-lying electronic transition and the butadiyne vibration. Our room temperature continuous-wave EPR results show that, in these conditions, the radical cation spin is rapidly hopping and manifests as complete delocalisation on the EPR timescale. In the low temperature (100 K) ENDOR, spin localisation becomes apparent. We believe that the charge localisation in these cations arises from a combination of electrostatic pinning by a counterion, end-group effects, and vibronic localisation.

4.2 Introduction

4.2.1 Molecular wires

The phenomenological connection between conjugated π-systems, in which electrons are fully delocalised along the oligomer, and wires, in which electrons and holes can flow freely in a conduction band, has aroused great interest towards the prospective application of molecules as wires and components in electronic devices.[148–150,256] The recent rapid growth of computational power has been enabled by miniaturisation of silicon-based transistors, from ~10 µm (1960s) to 10 nm (2017).[257] Although a miniaturisation limit has not yet been realised, molecular components may offer an alternative approach for the preparation of sub-5 nm devices.[257] There is a fundamental interest in understanding the nature of molecular conductance, and the exploitation of molecular properties and quantum mechanical effects to deliver new device function. For example, quantum interference can result in a second-order dependence of the conductance upon the number of parallel paths available in a parallel circuit:[258] a quantum circuit with two parallel paths exhibits a four-fold conductance compared to the one path analogue.[259]

Molecular conductance can arise by two mechanisms. In the first, the whole electrode|molecule|electrode junction is treated as a single potential, so at sufficient bias voltage, current flows.[159,258,260–265] In this regime, the rate of electron transfer (k_e) has

an exponential dependence on the distance (r), according to $k_e(r) = Ae^{-\beta r}$. Alternatively, an incoherent hopping process can occur, involving tunnelling events between neighbouring sections of the wire,[266,267] such as bases in a DNA chain[268] or monomers in a *p*-phenylenevinylene oligomer.[269] The hopping process has a much lower distance dependence than single-step tunnelling.

Conductances in molecular wires are related to the extent of radical anion or cation (in general: polaron) delocalisation. Delocalisation is also crucial for semiconductor band-like structures in bulk organic polymers,[270,271] which is important for their applicability in devices such as OLEDs and OFETs.[147]

4.2.2 Mixed valence

Mixed valence (MV) systems are those which comprise two redox centres across which some charge is spread, evenly or otherwise.[137,272] Classical examples of MV systems are inorganic coordination complexes, such as the archetypal Creutz-Taube (C-T) ion **26**, comprising a $Ru^{II/III}$ complex.[273] In general, an MV complex with a net 1+ charge, comprising two redox active centres R and a bridge b $[R-b-R]^+$, can exist between the extremes of complete localisation: R^+-b-R and complete delocalisation: $R^{0.5+}-b-R^{0.5+}$. The C-T ion **26** exists in the latter category, and each Ru centre has a 2.5+ oxidation state.

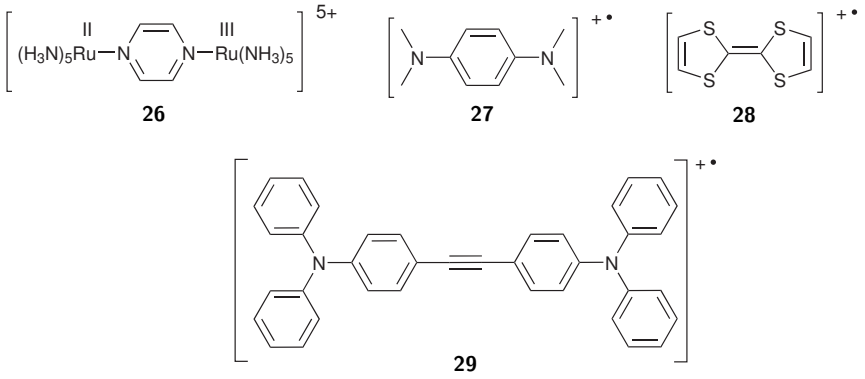

26 **27** **28** **29**

Figure 4.1: Examples of mixed-valence compounds.

Although it is easy to imagine myriad examples of MV metal coordination compounds, the category does not restrict itself to metal redox centres. Wurster's blue[274] (**27**) is an early example of a fully delocalised organic MV compound. Wudl's tetrathiafulvalene (TTF) radical cation **28**, which is also fully delocalised, is generally considered to have initiated contemporary MV study.[137,275] It is instructive to make a quick attempt to categorise **27**

and **28** into redox moieties (R) and bridges (b). The effort reveals a fundamental challenge for organic MV: with inherently delocalised (not metal-centred) radical cations and anions, it is difficult to distinguish between bridges and redox centres. The assignment is easier for **29**,[276] where the triarylamine moieties are readily recognisable as redox centres, but the situation becomes confused again when a redox system is strongly conjugated into its bridge, such that the [R−b] moiety behaves as an extended chromophore.

MV systems can be classified into three main categories, using the Robin-Day classification system.[137,272,277] In Class I, the redox moieties do not interact with each other in a measurable way, and charge is fully localised on one redox centre. In Class II, the charge is localised at one centre, but the redox centres do interact and thus the charge transfer between them can be interrogated spectroscopically, manifest as NIR intervalence charge-transfer (IV-CT) absorptions. Finally, Class III includes systems where the charge is fully delocalised between redox centres. Similar NIR bands appear in Class III systems and they are often empirically referred to as IV-CT absorptions. It is important to note that these NIR bands do not, and cannot, effect charge transfer in fully delocalised Class III systems, and it has been suggested that the 'intervalence charge resonance' label ought to be applied in preference.[278] We will use IV-CT to refer to all broad NIR bands in porphyrin oligomer radical cations.

Marcus-Hush theory can be applied to the analysis of the IV-CT bands to extract the critical factors which control charge delocalisation: the interaction energy (H_{AB}) and the reorganisation energy (λ).[137,272] In Marcus-Hush theory a MV complex is described by two interacting (adiabatic) potential energy surfaces, with the degree of electronic coupling described by the parameter H_{AB} (Figure 4.2). For $H_{AB} = 0$, the system is Class I; for non-zero H_{AB} the system moves into Class II. When $2H_{AB} \geqslant \lambda$, the system is Class III (Figure 4.2).

The reorganisation energy λ collects all of the energetic terms involved in the charge-transfer process, such as bond length reorganisation and solvent redistribution. Thus λ can be highly medium-dependent. The reaction coordinate x describes the charge-transfer process: hence the left parabola (for Figure 4.2a and b) describes the state where all of the charge is localised on one unit (x_A), and the right parabola where it is localised on the other (x_B). At the Class III limit there is no distinction between the two redox units, thus the most stable point on the reaction coordinate is at $x_{A,B} = 0.5$, where the charge is shared between both units.

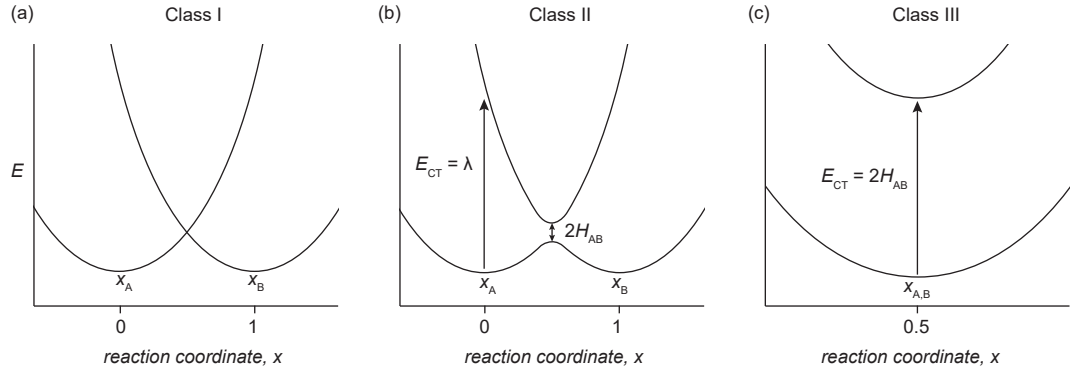

Figure 4.2: Schematic energy surfaces for (a) Class I, (b) Class II and (c) Class III MV systems. λ is the reorganisation energy; H_{AB} is the electronic coupling between the MV centres.[272]

In the high-temperature limit (i.e. where $h\nu \ll k_B T$ for vibrations), there is a Boltzmann weighted population of vibrational states. Optical transitions from the vibrational manifold of the lower potential to the upper potential can thus clearly be seen to give rise to a Gaussian band shape, with the centre energy $\nu_{max} = \lambda$. However, there is a lower limit to ν_{max}; $2H$ is the minimum energy transition possible in this picture, effecting a low-energy cut-off at $\nu_{max} = 2H$, characteristic of the Class II/III borderline.[279] The cut-off is not as pronounced in experiment as in theory (consider that at room temperature, $\frac{k_B T}{hc} \approx 200\,\mathrm{cm}^{-1}$), but the effect is that an IV-CT band becomes increasingly asymmetric with increasing H. For a system firmly within Class II, with a symmetric Gaussian-shaped IV-CT band, the band width at half height (FWHM, $\Delta\nu_{\frac{1}{2}}$) can be described as follows:[137]

$$\Delta\nu_{\frac{1}{2}} = \sqrt{16 k_B T \nu_{max} \ln 2} \tag{4.1}$$

For ν_{max} in cm^{-1}, the constant terms collect to $2310\,\mathrm{cm}^{-1}$. The presence of a narrower band, in the Class II/III continuum, describes the shift of x_A from 0 towards 0.5 (and x_B from 1 to 0.5). Towards the highly coupled Class III limit, where $x_{A,B} = 0.5$, a relatively narrow line should result since the optical excitation now proceeds to a less sloped part of the upper potential.

The delineation of the Class II/III borderline is very difficult. The primary features controlling Class II vs. III character are solvent (or counterion) pinning and vibrational self-localisation.[280] Care must be taken when using different spectroscopies to probe MV characteristics: the timescale of EPR is 10^{-7} s whilst vibrational spectroscopy probes $< 10^{-11}$ s. Thus a Class II/III borderline compound may appear as the averaged Class III state in EPR,

whilst appearing localised in IR spectroscopy.[280] Similarly, the rate of hopping is affected by temperature, so a molecule which appears fully delocalised at room temperature may reveal a localised character at lower temperatures.[272,281] The true MV character of the compound is, of course, intrinsic to the molecule and not to the spectroscopic technique. X-ray photoelectron spectroscopy (XPS, 10^{-17}s) is the ultimate technique for confirming Class III character.[280]

4.2.3 Porphyrin molecular wires

Dyads and triads comprising porphyrins, fullerenes, and ferrocene have shown that porphyrin-based molecular wires mediate efficient charge transport following photoinduced charge separation, over distances up to 50 Å for butadiyne linked oligomers.[15,183,184,282–285] The conductance of alkyne-linked porphyrin oligomers has been measured in an STM break-junction device. The conductance through these oligomers exhibits a remarkably shallow attenuation (β) with increasing molecule length,[165–167,286] possibly indicating a hopping mechanism.

The steady-state properties of mono-alkyne linked porphyrin oligomer radical cations and anions have been studied extensively by Therien and coworkers.[138,139,287] Continuous wave (cw) EPR spectroscopy showed that, on the timescale of the technique at room temperature ($\sim$100 ns), the radical cations sample the hyperfine interaction along the whole oligomer length, from dimer to linear heptamer (7.5 nm).[138] These results could be explained by coherent electron/hole delocalisation, or by an incoherent rapid hopping process. Similar EPR results were obtained for the radical anions of these mono-alkyne linked oligomers.[139]

Wasielewski and coworkers reported rapid hopping, on the EPR timescale at room temperature, in *meta*-phenylene-linked, and directly *meso–meso*-linked porphyrin oligomer radical cations.[288] This result indicates that hopping between porphyrins can be extremely rapid even when electronic conjugation is 'turned off' by a *meta*-phenyl link, or by near-orthogonality of porphyrin planes in the *meso–meso*-linked dimer.

Here we present a detailed analysis of the electronic delocalisation in a series of linear and cyclic butadiyne-linked porphyrin oligomers, for linear oligomers from monomer to hexamer (***l*-P*N*** for $N = 1$–6),[168] a six-porphyrin nanoring with (***c*-P6•T6**) and without (***c*-P6**) a hexapyridyl rigidifying template,[24,236] and a 12-unit porphyrin nanotube with two bound templates ***t*-P12•T6$_2$**.[27]

4.3 Methods

4.3.1 Synthesis

The oligomers ***l*-P1** to ***l*-P6**, ***c*-P6**, ***c*-P6•T6** and ***t*-P12•T6$_2$** were prepared as described previously.[27,186] Dr P. Neuhaus, Dr A. Cnossen and Ms R. Haver are thanked for gifts of linear oligomers and ***t*-P12•T6$_2$**. Solution studies of zinc-porphyrin oligomers often employ pyridine as a solvent additive to suppress aggregation. Unfortunately, pyridine reacts with porphyrin radical cations.[289] Our preferred strategy to avoid aggregation was to use bulky solubilising 3,5-bis(trihexylsilyl)phenyl (THS) substituents at the porphyrin *meso* positions.[183]

4.3.2 Chemical oxidation

Solutions of radical cations were prepared by addition of up to one equivalent of an oxidant to a solution of the porphyrin oligomer. Two oxidising agents were used in this study: tris(4-bromophenyl)hexachloroantimonate (BAHA, $E_{1/2} = 0.70\,\mathrm{V}$ vs. Fc/Fc^+) and thianthrenium hexachloroantimonate (Thn, $E_{1/2} = 0.86\,\mathrm{V}$ vs. Fc/Fc^+).[244] Note that the counterion is $SbCl_6^-$, not SbF_6^- as in Chapter 3. These oxidising agents are strong enough to effect stoichiometric oxidation of the porphyrin oligomers to their radical cations (for ***l*-P1**, $E_{1/2} = 0.44\,\mathrm{V}$ vs. Fc/Fc^+), but not to oxidise porphyrin units to their 2+ states (hence a $2N+$ overall charge on the oligomer ***l*-PN**). Radical cations prepared with different oxidants gave identical spectra. Liquid solutions of porphyrin radical cations are stable for several hours under ambient conditions without precaution to water or air, and they can be cleanly reduced back to the neutral porphyrin oligomers by addition of ferrocene. EPR experiments were carried out in a glass-forming solvent mixture of toluene-d_8:THF-d_8:CD_2Cl_2 1:1:1.

4.3.3 Spectroelectrochemistry

4.3.3.1 Experimental details

Spectroelectrochemical experiments were performed in an optically transparent thin layer electrochemistry (OTTLE) cell comprising platinum gauze working and counter electrodes, and a Ag/AgCl quasireference electrode. The electrolyte solution was CH_2Cl_2 with 0.1 M tetra-*n*-butylammonium hexafluorophosphate (TBAP). Optical data were collected using a Bruker Vertex 80 FT-IR spectrometer with a HeNe laser probe. Vis spectra were collected with a UV-CaF_2 beamsplitter, tungsten source and RT-Si diode detector; NIR spectra with

a CaF_2 beamsplitter, tungsten source and RT-DLaTGS detector, and IR spectra with a KBr beamsplitter, Globar source and LN_2-MCT detector. Attempts to use the (faster) MCT detector in the NIR region failed because the detector was significantly non-linear in this energy range. Spectra were collected every ~1.2 s whilst a cyclic voltammetry (CV) experiment was performed in the OTTLE cell. A slow scan rate ($5\,mV\,s^{-1}$) was used for the CV to promote equilibrium conditions for each potential step.

4.3.3.2 Curve-fitting

For each oligomer, the spectroelectrochemical data comprised six parts: $[m \times n]$ (m time-separated measurements at n wavelengths) matrices $\mathbf{D}_i$ of optical spectra for each of the Vis, NIR and IR spectral regions and their corresponding cyclic voltammograms. The overall goal was to extract the unique spectra for as many oxidation states as possible from these datasets, by decomposing $\mathbf{D}$ into $\mathbf{C}$ and $\mathbf{S}$.

$$\mathbf{D} = \mathbf{C} \cdot \mathbf{S} + \mathbf{E} \tag{4.2}$$

where, for k species, $\mathbf{C}$ is a $m \times k$ matrix of speciation (concentration) profiles; $\mathbf{S}$ is a $k \times n$ matrix of spectra, and $\mathbf{E}$ is a matrix of residuals.

The curve-fitting problem is only solvable if all spectra are sufficiently different and, in some respect, non-overlapping. The data must also be high quality and relatively free of spectral artefacts. The raw experimental data were subject to some pre-processing using home-made Python and MATLAB scripts, before fitting using multivariate curve resolution (MCR), with the MCR-ALS project in MATLAB.[290] The individual steps involved in the data processing will be described, with a brief introduction to the underlying theory.

Pre-processing The pre-processing comprised three steps: truncation of datasets $\mathbf{D}_i$, their concatenation into one matrix $\mathbf{D}$ for each oligomer, and then a background subtraction. These steps are explained and illustrated for ***I*-P3**.

Surface plots for the raw data are shown in Fig. 4.3. The vertical axis shows time, and there is a clear mirror symmetry at ~250–300 s in each surface plot. This time point corresponds to the switch between anodic and cathodic sweeps in the cyclic voltammogram, and the symmetry demonstrates good reversibility of the oxidations. For fitting, only the anodic linear sweep is required, so the data are truncated in the time axis by visual inspection.

Similarly, the signal at the high and low energy limits of the spectra is noisy, so truncation in the energy axis is also appropriate to afford the spectra in Fig. 4.4

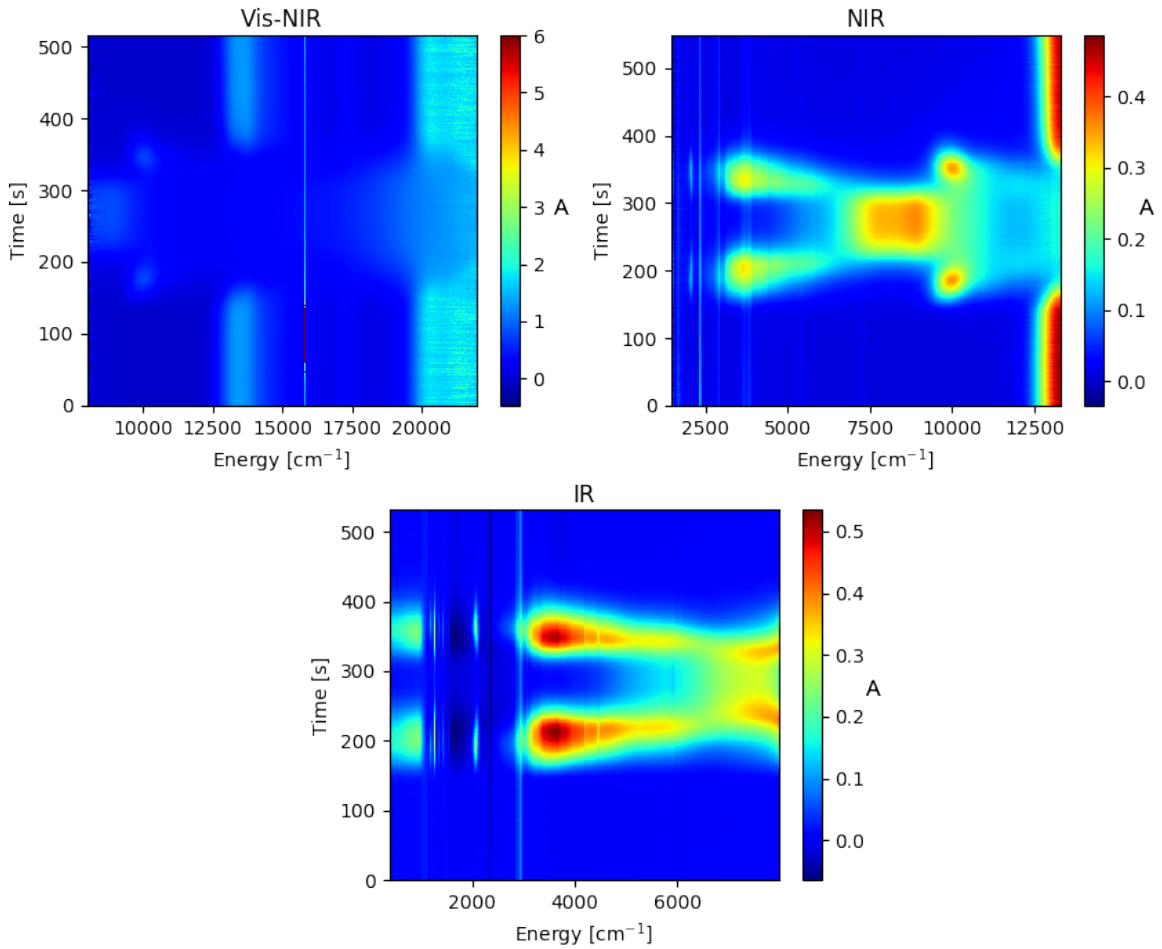

Figure 4.3: Raw spectroelectrochemical data for ***I*-P3**, measured in CH_2Cl_2/0.1 M TBAP at room temperature.

For **P3**, we expect four oxidation states to be accessible with the oxidants used here, and within our electrochemical potential range: neutral, 1+, 2+ and 3+. From each individual subfigure in Fig. 4.4, taken in isolation, it is only possible to confidently identify three spectra. However, juxtaposition of the Vis and NIR contour plots reveals four clearly distinct spectra. Thus a clear prerequisite for the computational deconvolution of the matrix **D** into **C** and **S** is the construction of a merged spectrum, spanning the Vis to IR regions.

2D traces of absorbance vs. time can be extracted from each of $\mathbf{D}_f$ and $\mathbf{D}_g$ (where f and g are neighbouring regions) for each wavelength in the region of spectral overlap between the two matrices. Each trace is a function of time and they can be denoted $g(t)$ and $f(t)$. The overlap of a pair of traces, g and f, depends on three parameters:

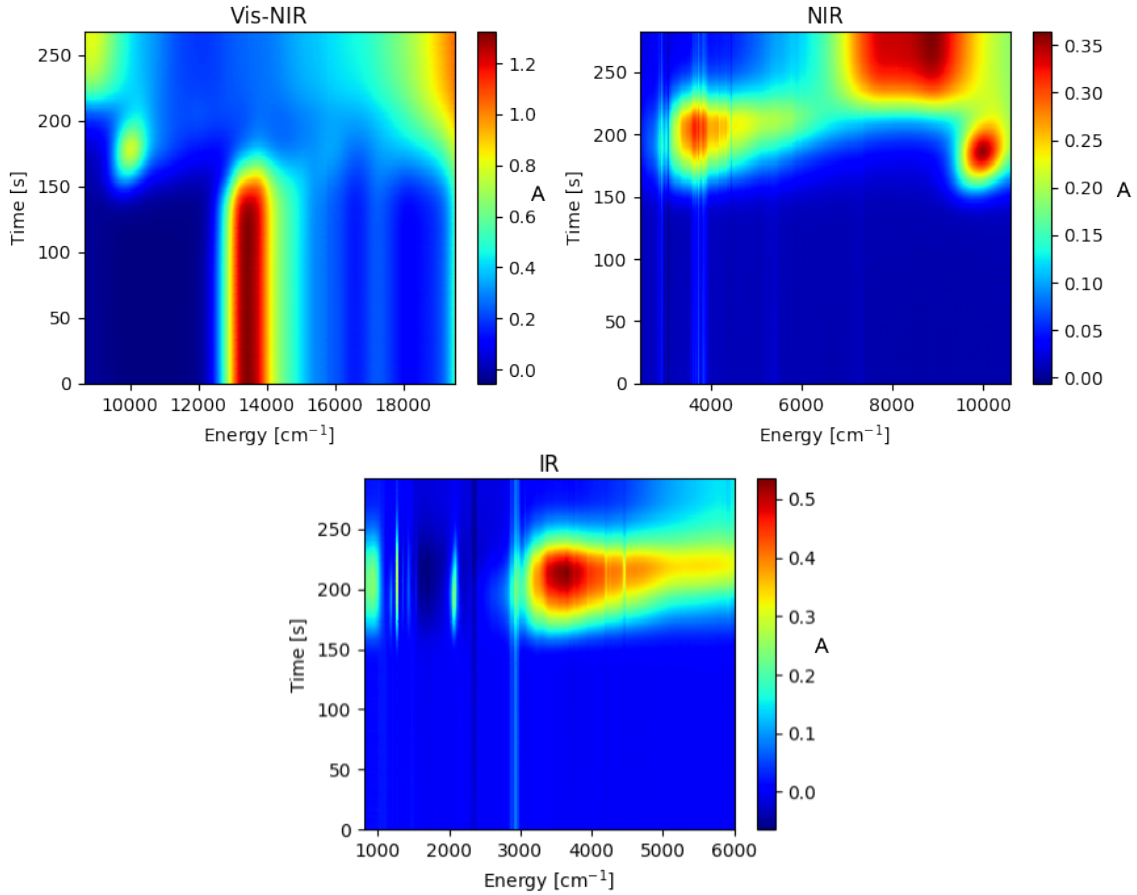

Figure 4.4: Spectroelectrochemical data from Fig. 4.3, after removal of noisy edges and truncation of the time axis to show only the anodic (oxidation) sweep of the CV.

a scaling factor (m), a time offset (c) and a baseline offset (d). The spectra can be fit by least-squares optimisation of m, c and d according to:

$$f(t) = m \cdot g(t + c) + d \tag{4.3}$$

The original time axes for f and g may be different: inconsistency can be resolved by interpolation. With m, c and d in hand, these parameters can be applied to the full matrix $\mathbf{D}_g$ to concatenate it with $\mathbf{D}_f$. In a final step, the mean absorbances for the first ten spectra in each $\mathbf{D}$, for wavelengths >1000 nm were subtracted from the remainder of the matrix, to eliminate most residual solvent/electrolyte absorbances. This process formally converts the presented IR spectra into difference spectra, but this fact is of no consequence because the neutral state IR modes are so weak as to be in the noise.

When this procedure (implemented in Python) was applied to ***I*-P3**, the merged spectra in Fig. 4.5 resulted. Now four clearly distinct spectra can be resolved, denoted by the arrows

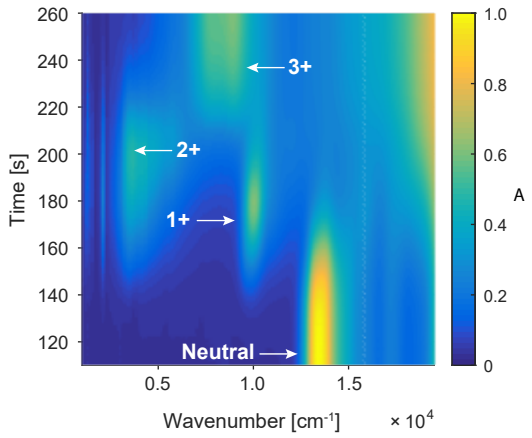

Figure 4.5: Merged spectroelectrochemical data for ***I*-P3**, revealing four clearly identifiable distinct component spectra.

on the time axis, at ~130 s (neutral), ~170 s (1+), ~210 s (2+) and ~250 s (3+).

MCR With a complete matrix **D** in hand, we would like to determine **C** and **S**. There are a number of solutions to this matrix factorisation (or multivariate curve resolution, MCR) problem. The method most commonly used in the chemometric community is alternating least squares (ALS).[291] Here, **C** and **S** are optimised iteratively. An initial guess of the concentration vs. time profiles **C** is used to generate a test matrix of spectra **S** by left division or non-negative least squares. Constraints can then be enforced on **S**, such as equality or closure constraints, if appropriate. **D** is then divided into **S** to generate a new test matrix **C**, to which constraints are applied before the process repeats. A typical termination condition arises when the reduction in fitting error ($\|\mathbf{E}\|$) between the product of factorised matrices **CS** and the original data matrix **A** falls below a tolerance.

The inclusion of sensible constraints in the MCR-ALS procedure is essential. In their absence, it is impossible to obtain a unique solution: solutions will be rotationally ambiguous – in other words, there are infinite combinations of component spectra (such combinations described by **C**) which can equally well describe **D**.

Suitable constraints include non-negativity in **C** and **S** (spectra and concentrations cannot be negative), closure in **C** (the sum of all normalised concentrations at each time point should be unity) and unimodality in **C** (the concentration of each component should have a single maximum). All of these constraints are applied in this work.

There are two remaining questions: first, how can we confidently decide on the number of components (k) necessary to describe **D**, and second, how can we generate an initial guess for **C**?

For oligomers **PN** with $N \leqslant 4$, it is sufficient to use a model-based estimate: $k = N + 1$ (i.e. 0, 1+, ..., N+). Beyond tetramer, we must be careful to ensure that **A** actually contains enough resolvable components to permit a reliable curve resolution. In this case it is sensible to turn to a model-free analysis.

Singular value decomposition (SVD) is a technique which factorises a matrix **M** according to $\mathbf{M} = \mathbf{U\Sigma V}^{\mathsf{T}}$.[292] Importantly, the diagonal values of $\mathbf{\Sigma}$ (the *singular values* of **M**) describe the 'most important' components in **M** (alternatively, the rank of **M**). Large singular values correspond to important components, while low values correspond to noise. A suitable cutoff applied to $\log(\mathbf{\Sigma}_{ii})$ can be used to determine the 'model-free' number of components.

The SVD technique can also be applied to the generation of an initial guess for **C**. In evolving factor analysis (EFA), SVD is applied incrementally to submatrices of **D**, starting with the first row (measurement) and growing the submatrix by inclusion of later rows.[293] The application of SVD to each submatrix recovers the $\mathbf{\Sigma}_{ii}$ singular values. Plotting the value of each i^{th} singular value as a function of number of rows included in the submatrix gives a picture of how many components are present at each measurement. The procedure can be repeated as 'backwards EFA' by starting with the last measurement of **D** and growing by addition of earlier rows. The combined EFA results permit the estimation of when species appear and disappear during the course of the experiment, and thus the generation of concentration profile guesses.

For ***I*-P5** and ***I*-P6**, an additional constraint was employed: the matrix **D** was augmented with the electrochemical data. The forward sweep of the CV was baseline corrected and numerically integrated using the trapezoid method to afford a vector describing the charge (in Coulombs) transferred as a function of time, normalised to the oligomer length (i.e. 5 or 6). The final row of the spectra matrix **S** was then constrained with a vector describing the oxidation states of the species predicted (e.g. six components in ***I*-P5**, [0 1 2 3 4 5]; five components in ***I*-P6**, [0 1 3 5 6]). The time offset between electrochemical data and spectroscopic data, and the number of components and their oxidation states, were assessed by sampling different values for these parameters. Candidate spectra which were chemically meaningful (i.e. no sharp spikes in the Vis-NIR spectra) were considered and their residual errors compared. Although there were multiple candidate solutions in each case, the positions of ν_{max} for the 1+ radical cations were relatively consistent.

4.3.4 Raman spectroscopy

Resonance Raman spectra were collected following chemical oxidation of ***c*-P6•T6** with BAHA in CH_2Cl_2 solution, $\sim$1 µM. The spectra were collected on a Bruker FT-Raman MultiRAM with a 1064 nm Raman probe. Data were baseline corrected with a 5th order polynomial and the background solvent was subtracted. The absence of non-linearity was confirmed by power-dependence measurements. The Raman measurements were performed at the Central Laser Facility, Harwell, with the kind support of Prof. Tony W. Parker.

4.3.5 EPR spectroscopy

Continuous wave (cw) EPR spectra were collected at X-band (Bruker EMX) at room temperature and at 100 K. Pulsed ENDOR measurements were made at W-band (Bruker Elexsys 680) between 6 K and 100 K. Mims ENDOR spectra were recorded using the pulse sequence $\frac{\pi}{2} - \tau - \frac{\pi}{2} - T - \frac{\pi}{2} - \tau -$ echo with $t_{\frac{\pi}{2}} = 44$ ns, $\tau = 200$ ns and a radio-frequency (RF) pulse length T of 18 µs, with the RF power adjusted to deliver a π pulse. Spectra recorded with different τ values, or using the Davies ENDOR pulse sequence, did not reveal any distortion arising from τ-dependent blind spots. All EPR and ENDOR measurements and analyses were performed by Dr C. E. Tait.

4.3.6 Density functional theory

There are two essential issues with the use of DFT for calculating the properties of open-shell molecules. The first of these is the self-interaction error (SIE), which arises from the Coulomb term:

$$V[\rho] = \frac{1}{2} \int \int \frac{\rho(\mathbf{r}_1)\rho(\mathbf{r}_2)}{r_{12}} d\mathbf{r}_1 d\mathbf{r}_2 \tag{4.4}$$

where $\rho(\mathbf{r})$ is the density at a point $\mathbf{r}$ in space.

Even with just one electron in the system, neither density term on the numerator of the integral is zero, thus an electron experiences a Coulomb interaction with itself. The exact exchange-correlation functional would cancel this error, but it is not known. In Hartree-Fock theory, the SIE in the Coulomb term is explicitly cancelled by an equivalent exchange interaction. Thus, the natural solution to avoid SIE in DFT, in the absence of the exact

functional, is to introduce some portion of exact (or Hartree-Fock, HF) exchange. Thus, for example, B3LYP (20% exact exchange) suffers less SIE than pure functionals like BLYP.

The second problem is the incorrect long-range behaviour of the exchange-correlation (XC) potential: semi-local potentials decay too quickly with the density, with an exponential decay rather than the physical decay following $\frac{1}{r}$. Thus for short distances r standard XC functionals behave well, but long-range exchange can be poorly described. An attractive method to deal with this poor description of non-locality is to partition the exchange component into a 'local' component, described by approximate DFT exchange (e.g. GGA), and a 'long range' component described by exact exchange. HF (or exact) exchange is explicitly calculated from the DFT Kohn-Sham orbitals analogously to the calculation of Fock exchange from HF orbitals. These partitioning functionals are called 'range separated' hybrids.

In this work we tested three functionals: B3LYP,[188] ωB97X-D,[243] and LC-ωPBE.[294] All three are hybrid functionals. ωB97X-D is range-separated and incorporates a dispersion correction (Grimme's D2), while the XC functional is B97. LC-ωPBE is another range separated functional based on the hybrid HSEh1PBE. The ω parameter defines 'long range'. Small values of ω lead to the use of DFT exchange over long distances (the 'short range regime' extends over a longer range of interatomic distances), whereas large values of ω incorporate more exact exchange at shorter distances. The asymptotic behaviour at the long-range limit is 100% exact exchange. Where erf is the error function, the $\frac{1}{r}$ decay,with r as distance, is partitioned as follows:

$$\frac{1}{r} = \frac{1 - \mathrm{erf}(\omega r)}{r} + \frac{\mathrm{erf}(\omega r)}{r} \tag{4.5}$$

The 6-31G* all-electron basis set and the Gaussian09/D.01 program were used throughout.[187,189–192] We compared the ability of the above functionals to describe charge (de-)localisation by calculating the excitation energies of electronic transitions, focusing on the NIR transition at $\sim$1000 nm (defined as 'band 2', see later). Spin contamination in the TD-DFT results was moderate ($\langle S^2 \rangle \approx 1$ to 1.6). We initially benchmarked using gas-phase geometries, with excitations calculated in a PCM solvent model of dichloromethane.[295] We found that B3LYP, as expected, completely overestimated the extent of delocalisation and thus underestimated transition energies for longer oligomers (Figure 4.6). LC-ωPBE

also failed for $\omega = 0.1\,\text{bohr}^{-1}$, but a good fit to the experimental trend was observed with $\omega = 0.2\,\text{bohr}^{-1}$ (Figure 4.6). The fit of ωB97X-D was similarly good (Figure 4.6), perhaps because the default ω is $0.2\,\text{bohr}^{-1}$ for this functional.[243] Vibrational frequencies were scaled by a multiplicative factor of 0.951, as appropriate for the (non-range-separated) HSEh1PBE functional.[296] Raman intensities were calculated (off-resonance) using ωB97X-D at the LC-ωPBE geometries, since the implementation of the latter functional in Gaussian09 does not permit Raman calculations.

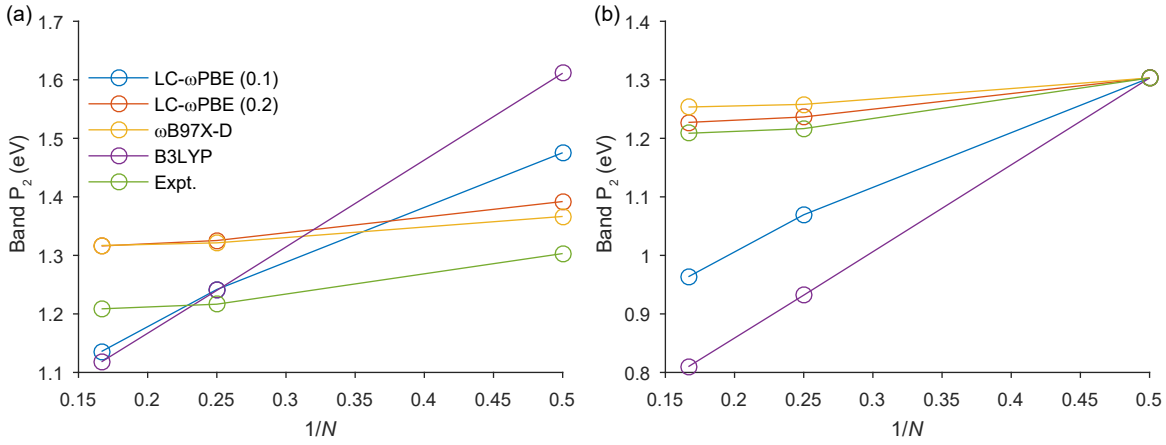

Figure 4.6: Comparison of calculated excitation energies for band P_2 compared to experiment. In (b), an equal energy offset has been subtracted for each functional such that the excitation energy for **P2**$^{+\bullet}$ is equal to experiment. Lines are a guide to the eye. N is oligomer length.

4.4 Results and discussion

4.4.1 NIR-IR spectroscopy of radical cations

Multivariate curve resolution permitted us to resolve all $N + 1$ oxidation state spectra for ***l*-P1** to ***l*-P5**, ***c*-P6** and ***c*-P6•T6** (Figure 4.7). For ***t*-P12•T6$_2$**, it was only possible to resolve seven components, presumably due to near-degeneracy of pairs of oxidation states. For ***l*-P6** the spectra of the 2+ and 3+ oxidation states are degenerate and unresolvable, as are those for the 4+ and 5+ states. Although encouraged by the fact that the speciation profiles correspond to chemical intuition and to the resolved electrochemical voltammograms,[230,236] we cannot exclude the presence of rotational ambiguities in the extracted spectra for oligomers longer than ***l*-P3**. In other words, the extracted spectra for some adjacent oxidation states may be linear combinations of the true spectra of those oxidation states. For this reason we do not discuss the higher oxidation states in detail, and

primarily restrict ourselves to the radical cation and $N+$ oxidation states. We were able to confirm the ν_{max} and relative intensities of NIR bands in the radical cations by comparing the MCR-resolved spectra to the raw spectra recorded at low potentials, where a mixture of only monocation radical and neutral species would be expected.

In this section we will discuss a qualitative characterisation of the radical cation (1+ oxidation state) NIR electronic absorption bands, before considering the strongly amplified IR modes and the presence of unusual anti-resonances in the nanoring IR spectra. We will progress to a quantitative analysis of the radical cation Vis-NIR-IR spectra to estimate the effective conjugation length (N_{ECL}) and the ground state charge delocalisation extent, according to a Robin-Day Class II model. Finally, we will compare experimental features to those obtained from (TD-)DFT calculations.

4.4.1.1 Qualitative description

The NIR spectra of porphyrin oligomer radical cations are dramatically changed from their neutral states, with the appearance of strong absorption bands at ~1000 nm and ~3000 nm. In their studies on the radical cations of butadiyne-linked porphyrin dimers, Arnold and coworkers observed similar bands and assigned them to SOMO→LUMO ('band 2') and HOMO→SOMO ('band 1') transitions, respectively (Figure 4.8b).[297,298] These bands, and their assignments, are similar to those used more widely to describe conjugated polymer polaron excitations: P_1 and P_2.[299]

The emergence of P_1 and P_2 can be described either in molecular orbital theory (Figure 4.8c) or in terms of an electron–phonon (or Su-Schrieffer-Heeger) model (Figure 4.8d), in which two polaron levels appear inside the valence-conduction band gap.[303] It has recently been argued that this latter model is illogical, since the newly created intra-gap polaron level implies that the remaining unpaired electron has a lower ionisation potential than was experienced by the (former) valence-band electron in the preceding ionisation event.[301] The suggested remedy to this inconsistency is shown in Figure 4.8e, in which a localised hole polaron results in a 'dip' in the valence band (corresponding to an easier reduction in this region), and changes to transitions P_1 and P_2.[301] We will refer to the bands in our spectra by the general P_n notation.* In addition, the Q-band and the C≡C IR stretching vibration ($\nu_{C\equiv C}$) are labelled in Figure 4.9.

*The polaron notation P_N is not to be confused with the (always bold-face) notation for porphyrin oligomers: **P*N*** and ***I*-P*N***.

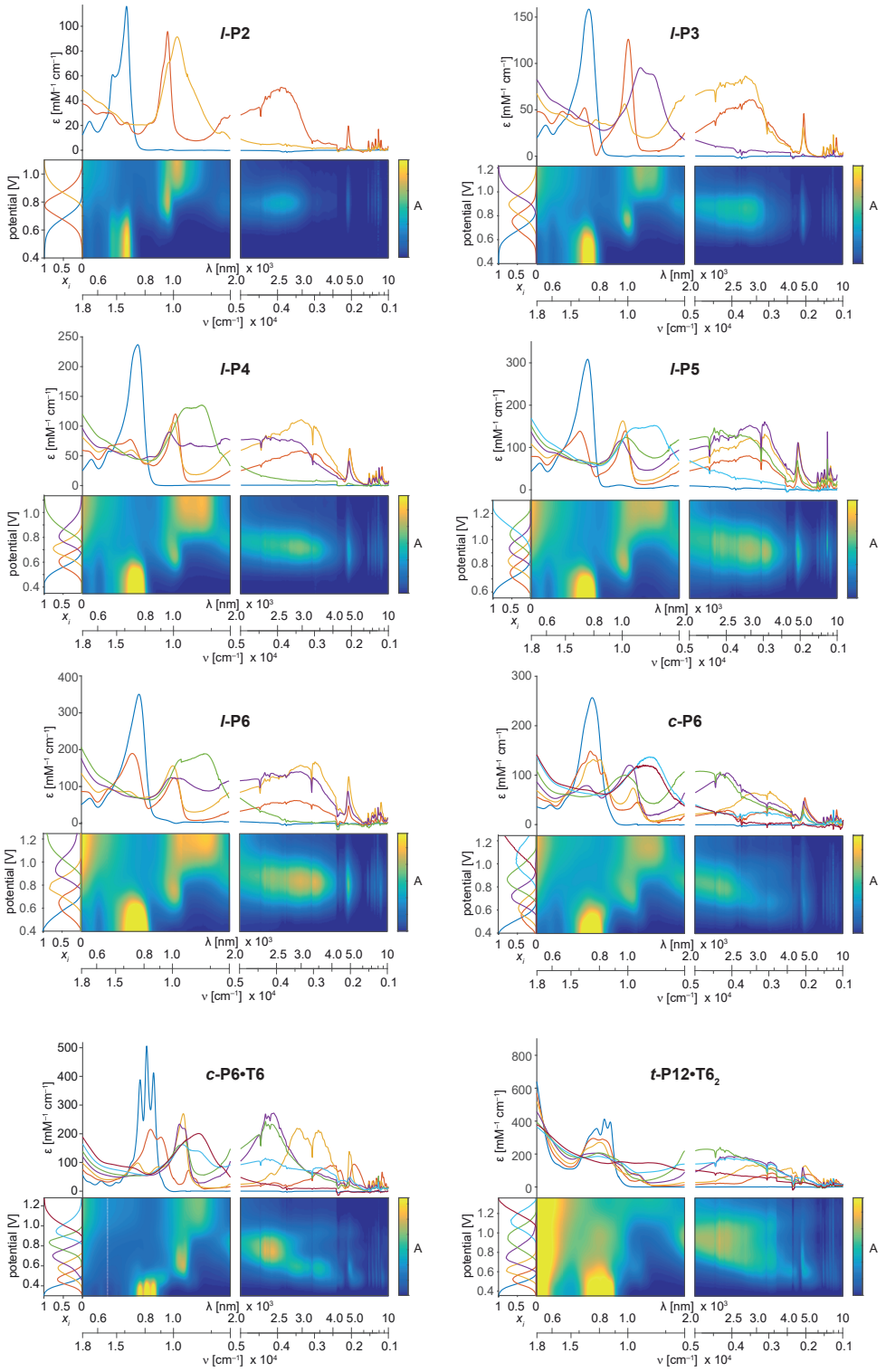

Figure 4.7: MCR resolved spectra for porphyrin oligomer oxidation states, in CH_2Cl_2 with 0.1 M TBAP. The surface plots show the pre-processed spectral data, with a normalised absorption (colour) axis. Above each mesh plot is the series of extracted spectra, with the corresponding speciation profiles shown left. The colour with which spectra are drawn correspond to colours in the speciation plots.

For oligomers longer than ***I*-P3**, the radical cation Vis-NIR spectra exhibit increasing absorption intensities in the range 600–800 nm, corresponding, approximately, to the neutral

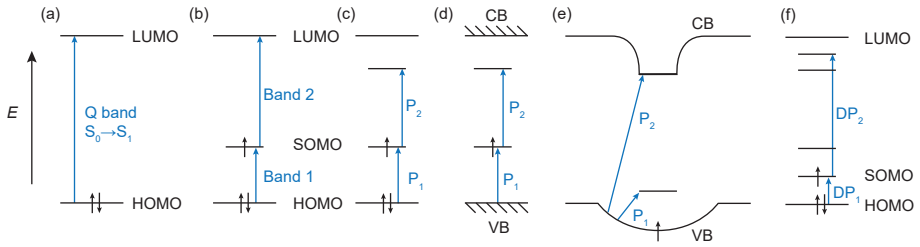

Figure 4.8: Models for electronic excitations in porphyrin polarons and, generally, in conjugated polymers. (a) shows the Q-band $S_0 \rightarrow S_1$ transition; (b) shows the model of electronic transitions for a porphyrin dimer described by Arnold et al.;[300] (c) depicts the molecular orbital picture of electronic excitations in a generic π-conjugated polymer, in which, by analogy to the electron–phonon band model (d), two polaron states develop in the band gap.[299] In (e) the recently refined form of model (d) is shown,[301] and in (f) the 'delocalised polaron' (DP) transitions are depicted. The DP transitions arise in 2D ordered lamellar structures,[302] and are additional to the P transitions shown in (c, d). VB and CB refer to the valence and conduction bands, respectively.

state Q-band absorption. This coexistence of apparent oxidised and neutral chromophores in the MCR-resolved spectra of the radical cations implies MV Class II structure for the longer oligomers. For ***I*-P2$^{+\bullet}$** there is no band in the Q-band region, implying Class III character. These tentative conclusions are supported by a quantitative analysis of oscillator strengths and band position shifts (see later).

Band P_1 of the radical cation spectra (at 3000 nm/3300 cm^{-1}) is extremely broad and, for ***I*-P3$^{+\bullet}$** and longer, featureless (Figure 4.10). The significant asymmetry of this peak may arise from conformational variations, vibronic effects, or could be a hallmark of the Class II–Class III borderline,[279] in which the IV-CT transition exhibits a low energy cutoff.

Dr P. Neuhaus has explored the solvatochromism of ***I*-P2$^{+\bullet}$** generated by chemical oxidation: the P_1 band is blueshifted in aromatic solvents (benzene, toluene and hexafluorobenzene), but is unchanged in other solvents (CH_2Cl_2, THF, CCl_4 or 1,1,2-trichloro-1,2,2-trifluoroethane). The positions of bands P_1 and P_2 are largely unchanged between chemical oxidation in neat CH_2Cl_2 and electrochemical oxidation in the presence of 0.1 M TBAP. These results suggest the absence of a simple solvent dipole induced charge localisation (in which case aromatic apolar solvents would reduce localisation and lead to a redshift of P_1).

In the IR part of the spectrum (1000–2400 cm^{-1}), vibrational modes are significantly increased in intensity compared to the neutral oligomers (Figure 4.10). The intensification of so-called infra-red active vibrations (IRAVs) has been reported in polaron-containing states of several conjugated organic polymers and oligomers following their first discovery in the 1970s. The canonical first example of IRAVs is in doped polyacetylene, reported by

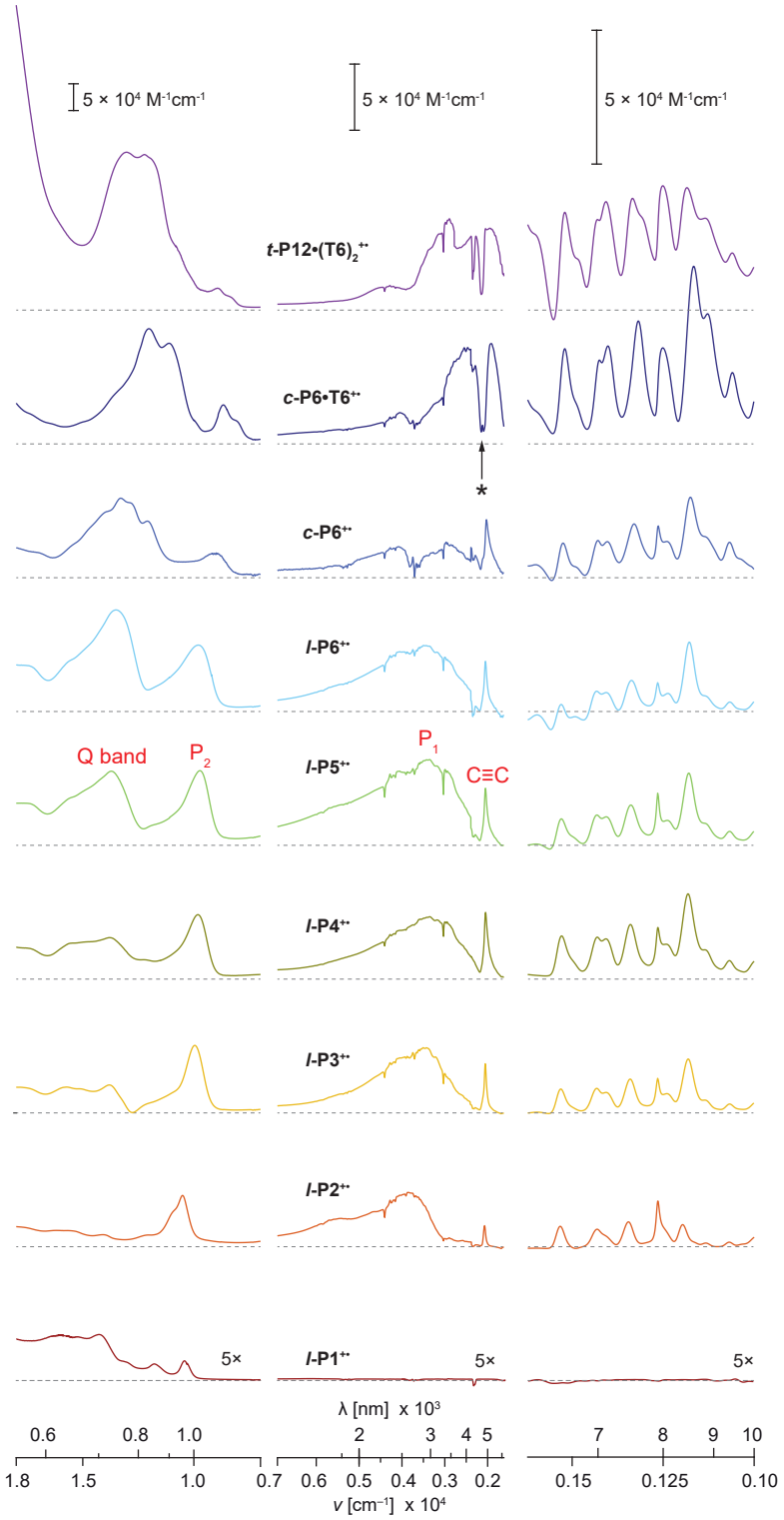

Figure 4.9: Vis-NIR-IR spectra for porphyrin oligomer radical cations measured by spectroelectrochemistry (CH_2Cl_2, 0.1 M TBAP), with the monocation spectra extracted by multivariate curve resolution. Bands P_1 and P_2 are described in Figure 4.8. C≡C denotes the acetylene stretch mode. ∗ denotes an anti-resonance (AR) acetylene stretch mode, apparent for ***c*-P6•T6** and ***t*-P12•T6$_2$**.

Fincher et al. in 1979.[304] However, the same phenomenon was, apparently, reported in 1972 by Kaplunov et al., in the form of strong vibrations in TCNQ radical anion complexes.[305]

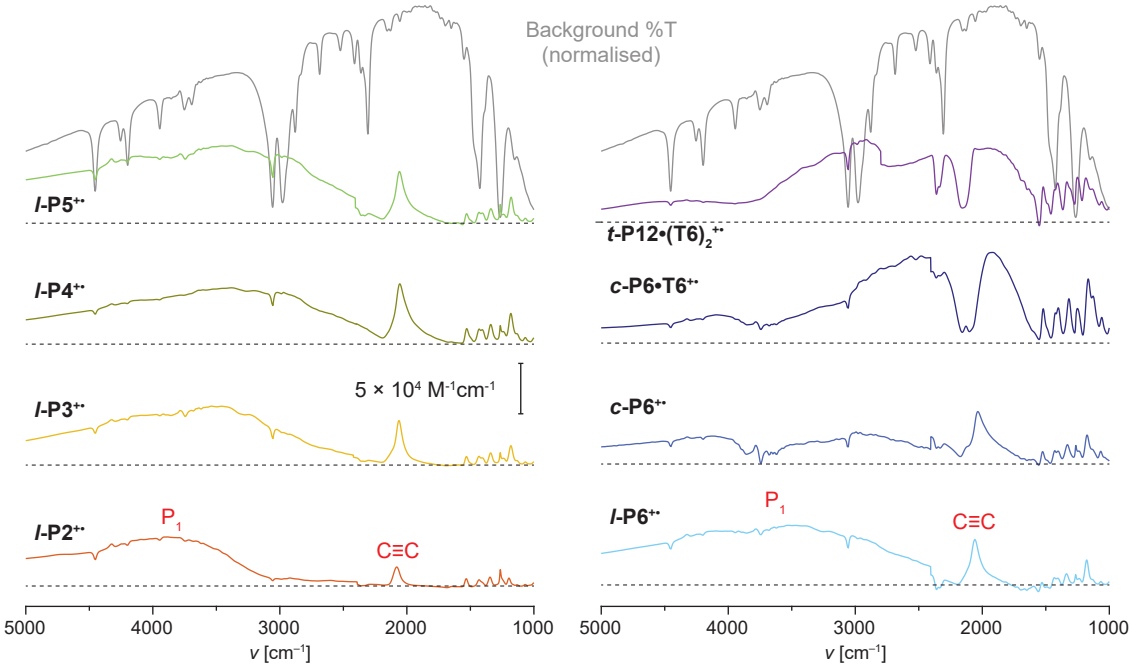

Figure 4.10: MIR-IR region of porphyrin oligomer radical cation spectra, showing the broad P_1 band, IRAVs and, for ***c*-P6•T6** and ***t*-P12•T6$_2$**, prominent Fano-like ARs. The background transmission spectrum (for the OTTLE cell, solvent and supporting electrolyte) is shown at the top of the figure, to demonstrate that the AR signals do not correspond to background correction anomalies.

The literature then diverged: most conjugated polymer research refers to IRAVs, while most mixed valence studies (including those on the photosynthetic special pair)[306] refer to *phase phonon* modes,[306–311] which trace their way back to Kaplunov's discovery.[305] Phenomenologically at least, these spectral features are identical.

IRAVs are a hallmark of solitons: self-localised charges,[303] which can arise as a result of chemical doping[312–315] or transiently, in photoinduced spectroscopies.[302,316–319] The appearance of IRAVs is generally attributed to symmetry breaking as a result of charge localisation, and their huge intensities are related to the increased dipole derivatives of charge-coupled modes upon doping. Pure Raman modes in pristine polymers can contribute to the IRAV bands, again as a result of the symmetry breaking phenomenon.[320,321]

IRAVs may also have a more capricious origin. Strong IRAVs are present in the bacteriorhodopsin special pair radical cation, despite significant charge delocalisation between its two component chlorophyll moieties (charge density: ~0.64:0.36).[306] In contrast, a firmly Class II (and thus charge-asymmetric) bis-ferrocenyl compound reported by Speck et al. exhibits no IRAVs: (neutral) electronic ground state vibrations are of equal, or greater, intensity to those in the radical cation MV system.[322] It is therefore important to distinguish

between intensity enhancement as a result of charge-induced symmetry breaking between mixed valence monomers in an MV dimer, and as a result of vibronic coupling. The activation of a symmetric (Raman active) bridge-centred vibrational mode is a strong indicator of Class II character,[280] but does not appear unequivocal. In particular, studies on pyrazine linked MV dimers have revealed intensification of the symmetric pyrazine stretch beyond expectations,[323] conflicting with evidence for delocalisation from broad asymmetric IRAVs (indicative of rapid delocalisation on the IR timescale, fs).[310] A proposed solution to this conflict is to invoke vibronic coupling between the low lying IVCT transition (P_1) and IRAVs, which leads to a strong IR activity.[323]

The observation of a strongly intensified acetylene stretch in the radical cation of a butadiyne-linked MV Ru−Ru complex was attributed to increased intensity from cumulenic bridge character, with complete charge delocalisation (Robin Day Class III).[324]

If the IRAVs result purely from symmetry breaking, then their presence in ***I*-P2$^{+\bullet}$** implies that there is a charge localisation process even in this, the shortest oligomer of the series. The absence of IRAVs in the $N+$ oxidation states of all the oligomers (Figure 4.7) appears consistent with a symmetry-breaking origin for IRAVs in lower oxidation states.

However, the alternative vibronic origin remains feasible: for the $1 < x < N+$ oxidation states of ***I*-PN^{x+}** there is a strong P_1 band, which disappears (or is blue shifted) in the $N+$ oxidation states. The coupling of this very low energy electronic transition to vibrational modes at the breakdown of the Born-Oppenheimer approximation may contribute to the large IR intensities. Published examples indicate that DFT is capable of reproducing IRAV intensities,[314,315] but the match between experimental and calculated frequencies seems poor.

The IR spectra for ***I*-P3$^{+\bullet}$** to ***I*-P6$^{+\bullet}$** are almost identical in shape, and there is no obvious correlation between oligomer length and peak intensities. This invariance suggests that the extent of radical cation delocalisation (and hence polaron-phonon coupling) is similar in this series of oligomers. In contrast, the IR spectrum of ***I*-P2$^{+\bullet}$** is different: the band found at 1175 cm^{-1} for longer oligomers is much smaller and shifted to 1195 cm^{-1} in the dimer. For the rigid cyclic systems, ***c*-P6•T6** and ***t*-P12•T6$_2$**, the IR spectrum is much more intense than for the linear systems or the untemplated nanoring ***c*-P6**, and the shape of the spectrum is also changed, with softening of some bands. The increased IRAV intensity in the rings may indicate a greater extent of charge delocalisation,[321] or stronger vibronic (electron-phonon) coupling.

The C≡C stretching modes are useful probes of delocalisation in conjugated systems containing alkynes, softening towards 2000 cm^{-1} with increasing bond-length equalised cumulenic character. For the linear oligomer radical cations, there is a subtle (~20 cm^{-1}) softening of the IR band as a function of *N* from ***l*-P2$^{+\bullet}$** until it saturates at ***l*-P4$^{+\bullet}$** (Figure 4.13b and Table 4.3). Increased cumulenicity could account for the strength of this vibrational mode, since cumulene stretch bands are typically more intense than those for acetylenes.[324,325] The C≡C stretch becomes broader with increasing oligomer length, due to overlap with the progressively red-shifted electronic band P_1.

For ***c*-P6•T6** and ***t*-P12•T6$_2$** the C≡C stretches are prominent as Fano-type anti-resonances (AR) on the overlapping broad electronic excitation. It is important to distinguish the 'negative' peaks from background subtraction artefacts: in Figure 4.10, the background transmission spectrum of the OTTLE cell, solvent, and supporting electrolyte, is shown. There is no solvent absorption at 2000 cm^{-1}. In contrast, the feature at 2350 cm^{-1} in ***l*-P4$^{+\bullet}$**–***l*-P6$^{+\bullet}$** is not an AR – it is a carbon dioxide subtraction artefact. A more subtle AR is visible in the ***c*-P6$^{+\bullet}$** spectrum, reduced in intensity commensurate with a weaker P_1 band. It must be noted that the C≡C AR in the rings is not in any way affected by the additional background subtraction process employed for the NIR–IR regions (see Methods).

Comparison of the resonance Raman spectra of samples of ***c*-P6•T6$^{+\bullet}$** (Figure 4.11) reveals a striking similarity, suggesting that some of the IRAV character arises from intensification of Raman modes. It is clear that the Fano-type AR at 2180 cm^{-1} corresponds directly to a Raman mode at the same energy.

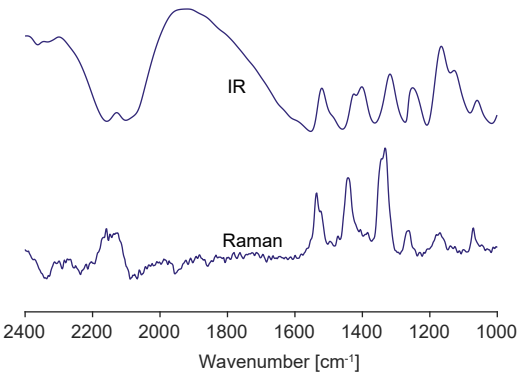

Figure 4.11: Comparison of solution Raman (CH_2Cl_2) and SEC IR spectra of ***c*-P6•T6$^{+\bullet}$**.

Fano-type ARs are well known in ordered polymer films where the low-lying polaron band P_1 overlaps with the vibrational manifold.[318] The presence of ARs in these systems

seems to be attributed to increased planarisation as a result of 2D lamellar order,[326] leading to a red-shift of the P_1 band and subsequent coincidence with IRAVs. This red-shift arises from interchain 2D delocalisation of the polaron, generating a 'delocalised polaron' (DP, Figure 4.8f).[326] The Fano effect describes the coupling between overlapping discrete and continuous transitions, and is manifest as anomalous lineshapes. Fano's original theory relating to intra-atomic transitions on an ionisation background[327] was extended to the vibronic case by Sturge et al.,[328] to explain Fano-like interference effects in transition metal doped crystals, where the transition metal acts as a discrete defect centre. Essentially, the scattered wavefunction undergoes, at the extreme, a π phase shift in the vicinity of a discrete resonant transition, yielding destructive interference.[329]

There are several examples of Fano-like ARs in conjugated organic polymer films including, most famously, in the photoinduced absorption spectra (TR-IR) of regio-regular P3HT reported by Österbacka et al.[302] In that case the appearance of AR bands for both IR and Raman modes, at similar frequencies to those for ground state absorptions, was attributed to 2D order in the polymer film.[302] ARs were later reported, by the same authors,[318] and others,[315,316,319,329] in a range of different polymers. There is a weak AR at 2200 cm^{-1} in poly(phenylene-acetylene) films.[318] This AR and nearby IRAVs were simulated using a current density wave model,[330] permitting the conclusion that there is a continuous electronic band above the polaron state, and hence supporting a characterisation of such films as semiconductors.[318]

In general, most examples of ARs on thin films are in the photoinduced absorption spectra, because photoexcitation tends to afford increased polaron delocalisation due to the absence of counterion pinning, and hence an electronic band with sufficiently low energy to interact with the vibrational manifold. However, there are also a few examples for p-doped polymer thin films.[312,313]

The supposed importance of 2D order to the appearance of Fano ARs is challenged by their appearance in polymer blends.[331] There are a handful of mentions of Fano ARs in discrete molecules, including the oxidised photosynthetic bacterial reaction centre special pair (comprising two bacteriochlorophylls offset and separated by about 3.3 Å)[317] and a mixed-valence ferrocene dimer.[311] Fano-type ARs and IRAVs have been observed in liquid solution measurements of long fluorene oligomer radical anions and cations ($N = 8$ and 30), and P3DT (poly(3-decylthiophene-2,5-diyl)) polymer radical cations.[314]

Thus, in general, it appears that Fano-type ARs in organic molecules emerge from overlap between coupled electronic and vibrational modes of similar energy (Figure 4.12), without the requirement for 2D order.

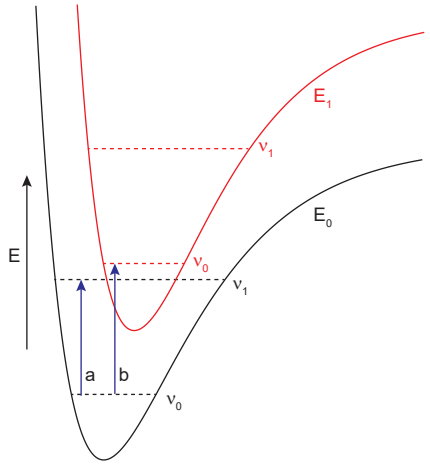

Figure 4.12: A simple depiction of the possible transitions describing band P_1 for ***c*-P6**, ***c*-P6•T6** and ***t*-P12•T6$_2$**. In this model there are two possible transitions: a vibrational transition (a), purely within the manifold of the E_0 state, and an electronic transition between E_0 and E_1 (b). This picture fails to describe the anti-resonance character, but does depict the unusual overlap between electronic and vibrational modes, and necessitates a breakdown of the Born-Oppenheimer approximation.

Having exhaustively discussed the appearance of the radical cation spectra we now turn to a more quantitative analysis of the peak positions and heights.

4.4.1.2 Quantitative analysis

The 'effective conjugation length' N_{ECL} in π-conjugated oligomers reflects the degree of exciton delocalisation, measured from the saturation of the electronic absorption (ν_∞) energy as a function of oligomer length. There are several approaches to the extrapolation of ν_∞, from the empirical relationship between wavelength and $\frac{1}{N}$ to Hückel MO theory.[332] In general, the Kuhn method[333] performs well for neutral oligomers,[332] but it gave a poor fit to our data for P_1 and P_2.

We therefore use Meier's approach[334] to empirically evaluate the saturation energy ν_∞ and to quantify the deviation from linearity (α) by fitting the experimental $\nu_{max}(N)$ according to

$$\nu_{max}(N) = \nu_{max}(\infty) + [\nu_{max}(1) - \nu_{max}(\infty)]e^{-\alpha(N-1)} \quad (4.6)$$

Where the $\nu_{max}(N)$ is determined from the experimental spectra and all other parameters, except N, are fit.

N_{ECL} is often evaluated from a plot of ν_{max} vs. the reciprocal of the oligomer length, and is defined as N for which there is no measurable difference (typically, 1 nm) between $\nu_{max}(N)$ and $\nu_{max}(\infty)$. Using this analysis for the neutral linear oligomers, $N_{ECL} = 20$.[335] However, for the radical cations, with electronic absorptions at 1 µm and 3 µm, a 1 nm shift is arbitrary. We instead favour the 'maximum conductive chain length' approach of Gierschner et al.,[336] in which N_{MCC} is determined from the intersection between an extrapolation of the linear part of the Meier fit corresponding to short oligomers, and the horizontal line describing the saturation energy $\nu_{max}(\infty)$.

Using this approach we have determined, for linear butadiyne-linked porphyrin oligomer radical cations, N_{MCC} of 3.3, 3.5 and 2.8 for bands P_1, P_2 and $\nu_{C\equiv C}$ respectively (Figure 4.13). We excluded the data for ***l*-P1**$^{+\bullet}$ from our analysis because the electronic structure of the monomer is very different to that of the oligomers. Similarly, we did not include the cyclic oligomers in our fitting efforts, but their band positions are plotted as non-circular symbols in Figure 4.13. Although we would need to examine a homologous series to establish N_{MCC} for ring radical cations, it is clear that they behave differently from the linear oligomers, presumably due, in part, to the absence of end-group effects. For P_1, we determined the peak maximum by fitting one Gaussian in the reciprocal energy (wavelength) domain, but the width of each peak and its overlap with residual solvent peaks, and other features, introduces significant uncertainty (100–200 cm^{-1}) into their true maxima. Accordingly, the Meier fit for P_1 is poor ($R^2 = 0.75$, Figure 4.13). The fits for P_2 and $\nu_{C\equiv C}$ are reasonable (Figure 4.13).

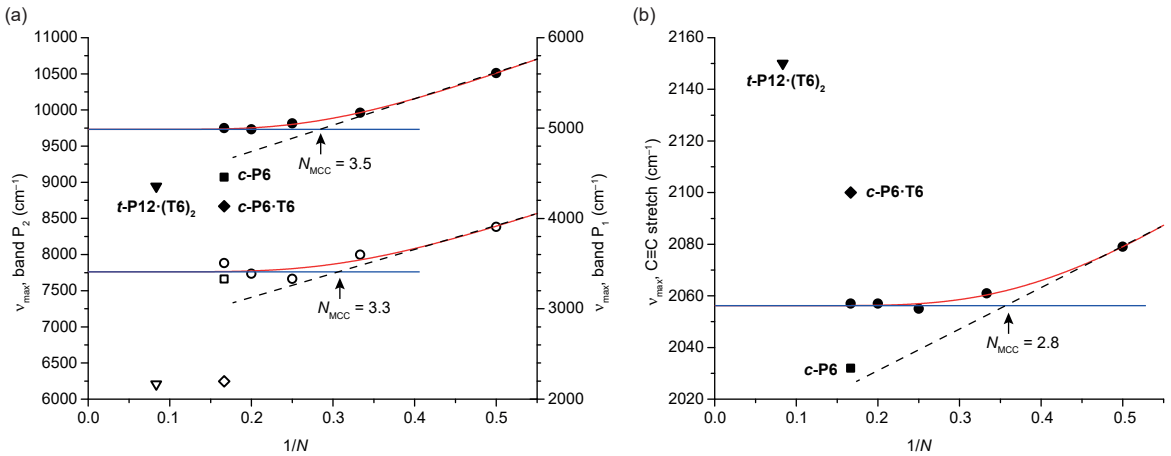

Figure 4.13: Meier plots for (a) P_1 and P_2, and (b) $\nu_{C\equiv C}$. For P_2: $\nu_{max}(1) = 12351 \pm 261$ cm^{-1}, $\nu_{max}(\infty) = 9732 \pm 15$ cm^{-1} and $\alpha = 1.2 \pm 0.1$ ($R^2 = 0.9969$); for P_1: $\nu_{max}(1) = 5353 \pm 2118$ cm^{-1}, $\nu_{max}(\infty) = 3410 \pm 86$ cm^{-1} and $\alpha = 1.34 \pm 1.1$ ($R^2 = 0.75$); for $\nu_{C\equiv C}$: $\nu_{max}(1) = 2182 \pm 60$ cm^{-1}, $\nu_{max}(\infty) = 2056 \pm 1$ cm^{-1} and $\alpha = 1.71 \pm 0.49$ ($R^2 = 0.9728$).

Table 4.1: Fit results for band P_1. ν_{max} and ϵ_{max} were determined by fitting the peaks with one Gaussian, with a reciprocal energy scale (nm). The area of the peaks, and thus f, were determined by fitting 2–3 Gaussians in the linear energy (cm^{-1}) regime.

	ν_{max} (cm^{-1})	ϵ_{max} ($M^{-1}\,cm^{-1}$)	f
***l*-P2$^{+\bullet}$**	3907	51326	0.53
***l*-P3$^{+\bullet}$**	3599	59359	0.54
***l*-P4$^{+\bullet}$**	3332	56582	0.61
***l*-P5$^{+\bullet}$**	3387	77342	1.01
***l*-P6$^{+\bullet}$**	3506	58800	0.70
***c*-P6$^{+\bullet}$**	3330	35573	0.32
***c*-P6•T6$^{+\bullet}$**	2197	118770	0.54
***t*-P12•T6$_2$$^{+\bullet}$**	2165	76121	0.62

Table 4.2: Fit results for band P_2. ν_{max} and ϵ_{max} were determined by inspection; the area (and thus f) was determined by fitting to 2–3 Gaussians.

	ν_{max} (cm^{-1})	ϵ_{max} ($M^{-1}\,cm^{-1}$)	f
***l*-P2$^{+\bullet}$**	10511	93052	0.37
***l*-P3$^{+\bullet}$**	9961	126963	0.61
***l*-P4$^{+\bullet}$**	9813	120535	0.50
***l*-P5$^{+\bullet}$**	9733	140900	0.68
***l*-P6$^{+\bullet}$**	9749	124000	0.69
***c*-P6$^{+\bullet}$**	9071	46201	0.26
***c*-P6•T6$^{+\bullet}$**	8669	72961	0.35
***t*-P12•T6$_2$$^{+\bullet}$**	8944	41228	0.17

The spectrum of a Class II MV compound has characteristics of its component parts: the neutral and oxidised parts of the molecule. An absorption resembling the Q-band of neutral porphyrin oligomers is apparent for longer oligomers ($N \geqslant 3$) at ~700 nm (Figure 4.9). We can thus determine the polaron delocalisation length using an approach similar to that introduced by Takeda for polyfluorene oligomers.[140]

We find that the sum of the extinction coefficients of the Q-band and P_2 ($\epsilon_Q + \epsilon_2$) is approximately proportional to the oligomer length, suggesting that intensity (and oscillator strength) is effectively partitioned between Q-band and P_2 absorptions. Thus the extent of ground-state cation delocalisation can be determined from the percentage of extinction coefficient in ϵ_2:

Table 4.3: Fit results for band 3 ($\nu_{C\equiv C}$). ν_{max} and ϵ_{max} were determined by inspection; the area (and thus f) were determined by fitting the C≡C peak to a Gaussian, with the background described using a further 1–2 Gaussians.

	ν_{max} (cm^{-1})	ϵ_{max} ($M^{-1}\,cm^{-1}$)	$f(10^{-2})$
***l*-P2$^{+\bullet}$**	2079	19202	0.41
***l*-P3$^{+\bullet}$**	2061	45774	0.72
***l*-P4$^{+\bullet}$**	2055	62476	1.32
***l*-P5$^{+\bullet}$**	2057	53300	1.14
***l*-P6$^{+\bullet}$**	2057	46400	0.99
***c*-P6$^{+\bullet}$**	2032	54513	2.20
***c*-P6•T6$^{+\bullet}$**	2100	n.d.	n.d.
***t*-P12•T6$_2$$^{+\bullet}$**	2150	n.d.	n.d.

$$N_{deloc} = N \cdot \frac{\epsilon_2}{\epsilon_Q + \epsilon_2} \tag{4.7}$$

This analysis gives $N_{deloc} \approx 2.0$ to 2.5 (Table 4.4 and Figure 4.14). For the second resolved oxidation state of each oligomer (2+ for ***l*-P3** to ***l*-P5**, and 3+ for ***l*-P6**), the ratio $\frac{\epsilon_2}{\epsilon_Q+\epsilon_2}$ is about 0.65 for ***l*-P3** to ***l*-P6**, supporting the notion of equal delocalisation in all of these states, and consistent with a cation delocalisation length of 2.5 porphyrin units (i.e. according to this ratio, ***l*-P5^{2+}** is delocalised to a similar extent as ***l*-P3^{2+}**, suggesting delocalisation over at least 2.5 porphyrin units). For ***l*-P2^{2+}** the ratio is 0.81.

The use of peak extinction coefficients as a proxy for oscillator strength is a crude approximation, given that the oscillator strength is proportional to the *integrated* extinction coefficient according to:[337]

$$f = \left(\frac{4\epsilon_0 m_e c^2 \ln(10)}{N_A e^2}\right) \cdot \int \epsilon(\nu)\, d\nu \tag{4.8}$$

$$f = 4.319 \times 10^{-9} mol\,dm^{-3}\,cm^2 \cdot \int \epsilon(\nu)\, d\nu \tag{4.9}$$

where the physical constants are defined as normal (see List of Abbreviations). We now use an elaborated form of Equation 4.7 in which we assume that, for ***l*-P2$^{+\bullet}$**, all of the intensity in the Q-band region arises from overlap with other transitions, as opposed to neutral-like absorption, since it is clear from visual inspection that ***l*-P2$^{+\bullet}$** has no neutral-like Q-band (compare to neutral spectrum in Figure 4.7). As a basic approximation we also

assume that the background absorption in this region scales linearly with oligomer length N. Thus N_{deloc} is determined according to:

$$N_{\text{deloc}} = N \cdot \frac{\mathcal{A}_2}{\mathcal{A}_2 + \mathcal{A}_Q - \frac{N}{2}\mathcal{A}_{Q,\textit{I}\text{-P2}}} \tag{4.10}$$

where $\mathcal{A}$ is the integrated absorption coefficient of the band indicated by the subscript. This analysis agrees with the simple peak extinction coefficient based approach, giving $N_{\text{deloc}} \approx 2.0$ to 2.5 (Table 4.4 and Figure 4.14).

Table 4.4: Calculations of N_{deloc} from extinction coefficients (ϵ) and integrated areas ($\mathcal{A}$) of the P_2 and Q bands for porphyrin oligomer radical monocations.

	ϵ_Q†	ϵ_2†	N_{deloc}§	$\mathcal{A}_Q$‡	$\mathcal{A}_2$‡	N_{deloc}‖
***I*-P2$^{+\bullet}$**	0.22	0.93	1.62	0.11	0.85	2.00
***I*-P3$^{+\bullet}$**	0.52	1.27	2.13	0.45	1.42	2.50
***I*-P4$^{+\bullet}$**	0.77	1.21	2.44	0.90	1.17	2.53
***I*-P5$^{+\bullet}$**	1.40	1.41	2.51	1.98	1.58	2.40
***I*-P6$^{+\bullet}$**	1.90	1.24	2.37	3.10	1.60	2.20

† units $M^{-1}\,cm^{-1}$ ($\times 10^{-5}$); ‡ units $M^{-1}\,cm^{-2}$ ($\times 10^{-8}$)
§: calculated with Equation 4.7; ‖: calculated with Equation 4.10

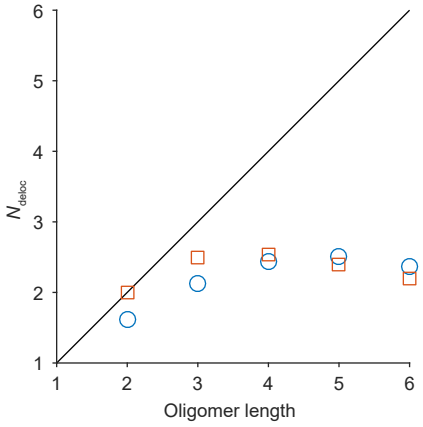

Figure 4.14: N_{deloc} calculated from extinction coefficients of P_2 and the Q-band using Equation 4.7 (blue circles) and calculated from integrated areas using Equation 4.10 (red squares). The diagonal line is a guide for the eye showing the limit of 'complete delocalisation' within the model used for analysis.

4.4.2 Computational chemistry

DFT calculations using the LC-ωPBE functional and the 6-31G* basis set revealed spin delocalisation in the radical cations over ca. 2–3 porphyrin units in linear oligomers

(Figure 4.15). The change in bonding towards cumulenic character (lower BLA) in cationic states closely follows the spin density (Figure 4.15). TD-DFT (LC-ωPBE/PCM/6-31G*) was able to reproduce the experimental trends in absorption energies (Figure 4.16) for the linear oligomers calculated: ***l*-P2**$^{+\bullet}$, ***l*-P4**$^{+\bullet}$ and ***l*-P6**$^{+\bullet}$. The stick spectra shown in Figure 4.16 exclude transitions with excessive expectation values for the spin ($\langle S^2 \rangle > 2$).

We do not present results for the odd oligomers, ***l*-P3**$^{+\bullet}$ and ***l*-P5**$^{+\bullet}$. We found that TD-DFT on ***l*-P3**$^{+\bullet}$ gave an erroneous transition energy for the band expected at $\sim$1000 nm, accompanied by a $\langle S^2 \rangle > 2$.

Frequency calculations showed strongly intensified IR modes (modes were 10–100 times more intense than in calculations of the neutral), but exhibit a poor resemblance to the experimental spectra (Figure 4.17). For ***l*-P2**$^{+\bullet}$, the Raman spectrum calculated using ωB97X-D is in remarkable agreement with the experimental IRAVs. As discussed earlier, this IR activation of Raman modes is consistent with either symmetry breaking phenomena, or vibronic (electron-phonon) coupling.[338] The fit for ***l*-P4**$^{+\bullet}$ is worse, perhaps suggesting the presence of more complicated vibronic coupling mechanisms for IRAV intensification in this apparently Class II compound.

For ***c*-P6**$^{+\bullet}$, the spin is delocalised over a similar number of porphyrin units as in the linear oligomers: 2–3. We did not attempt TD-DFT on ***c*-P6**$^{+\bullet}$, since we have noticed that straightforward TD-DFT on neutral ***c*-P6** fails to reproduce the complex vibronic splitting in the Q-band. In ***c*-P6**, the $S_0 \rightarrow S_1$ transition is symmetry forbidden, and it is argued that most intensity arises from Herzberg-Teller coupling.[236] It would thus be prohibitively expensive to accurately simulate the absorption spectrum of ***c*-P6**$^{+\bullet}$.

Figure 4.15: (a-c) The change in bond lengths between porphyrin oligomer (***l*-P2**, ***l*-P4** and ***l*-P6**) radical cations and their neutral precursors, $\Delta r = r_{\text{cation}} - r_{\text{neutral}}$. (d-f) Spin density ($\alpha - \beta$) isosurfaces for an isovalue 0.001 a.u. Calculations performed at the LC-ωPBE/6-31G* level of theory, $\omega = 0.2\,\text{bohr}^{-1}$. The colours in the spin density plots do not relate to those in the parts (a-c).

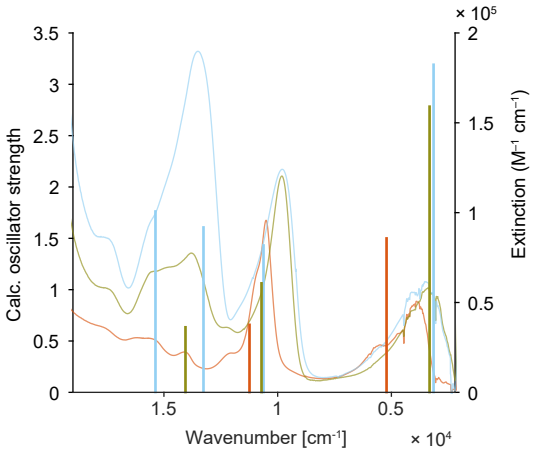

Figure 4.16: Calculated (sticks) vs. experimental Vis-NIR spectra for ***l*-P2**$^{+\bullet}$ (red), ***l*-P4**$^{+\bullet}$ (gold) and ***l*-P6**$^{+\bullet}$ (blue). Level of theory: LC-ωPBE/6-31G* with a CH_2Cl_2 PCM solvent model.

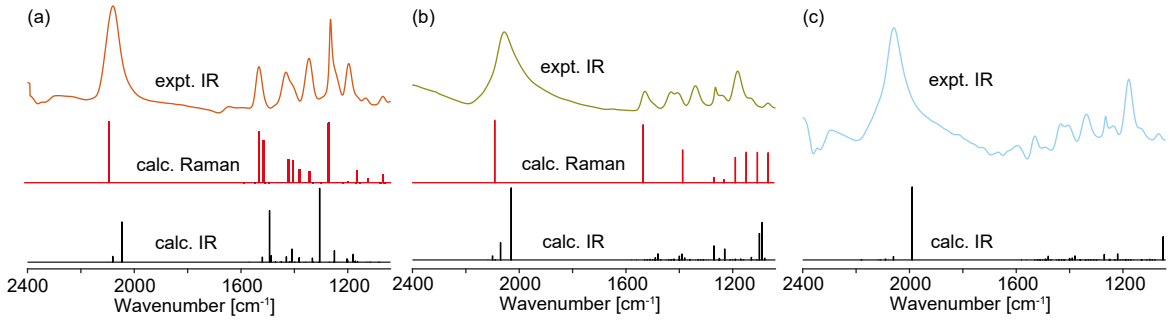

Figure 4.17: Calculated and experimental IR and Raman spectra for ***l*-P2**$^{+\bullet}$, ***l*-P4**$^{+\bullet}$ and ***l*-P6**$^{+\bullet}$. The level of theory for the IR spectra was LC-ωPBE/6-31G*; for the Raman it was ωB97X-D//LC-ωPBE/6-31G*.

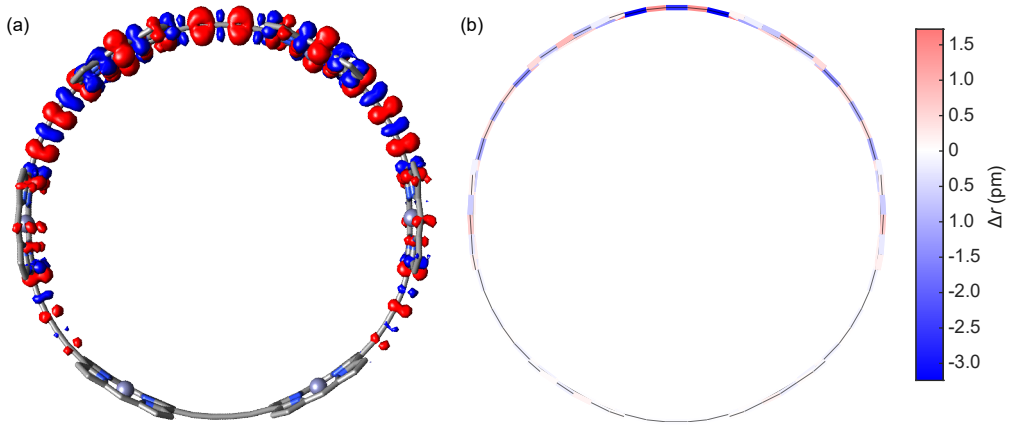

Figure 4.18: (a) Spin density in ***c*-P6**$^{+\bullet}$, the isovalue is 0.001 a.u.; (b) the change in bond lengths between ***c*-P6**$^{+\bullet}$ and its neutral analogue, $\Delta r = r_{\text{cation}} - r_{\text{neutral}}$. Level of theory: LC-$\omega$PBE/6-31G*.

4.4.3 EPR spectroscopy of radical cations

The experimental results in the section were acquired by Dr C. E. Tait, Dr P. Neuhaus and me.

4.4.3.1 Continuous wave EPR

CW EPR spectra recorded at room temperature at X-band are shown in Figure 4.19a. The spectrum for ***l*-P1**$^{+\bullet}$ shows nine hyperfine coupling lines arising from coupling to four nitrogen nuclei. Superimposed are smaller proton hyperfine couplings, which can be assigned to the *meso*-aryl *ortho* protons. The hyperfine coupling becomes less resolved for longer oligomers. The spectrum of ***c*-P6**$^{+\bullet}$ is almost identical to that of ***l*-P6**$^{+\bullet}$, but ***c*-P6•T6**$^{+\bullet}$ is slightly broader, presumably due to an additional hyperfine interaction with the axial ligand nitrogen.

Norris' equation relates the derivative peak-to-peak EPR linewidth ΔB_{pp} to the number of equivalent units over which the electron spin is delocalised (or quickly hopping) and the peak-to-peak linewidth of the monomer ($\Delta B_{\text{pp}}(N = 1)$).[339]

$$\Delta B_{\text{pp}} = \frac{1}{\sqrt{N}} \Delta B_{\text{pp}}(N = 1) \tag{4.11}$$

The experimental ΔB_{pp} fit well to Equation 4.11 (Figure 4.19b), suggesting complete delocalisation or rapid hopping of the radical cation at room temperature, across the series of oligomers considered. ***c*-P6•T6**$^{+\bullet}$ and ***t*-P12•T6$_2$**$^{+\bullet}$ show some deviation from the fit, presumably owing to the additional ligand nitrogen hyperfine coupling.

The cw spectra at low temperature (100 K) are much broader than the corresponding room temperature spectra (for example, Figure 4.19c), and are approximately identical, within signal to noise, for ***l*-P2**$^{+\bullet}$ to ***l*-P6**$^{+\bullet}$. Electron nuclear double resonance (ENDOR) experiments were used to probe the hyperfine coupling in frozen solution directly.

4.4.3.2 ^{1}H ENDOR

The hyperfine coupling (A_{iso}, Equation 4.12) gives a sensitive measurement of the extent of spin delocalisation, since it depends on the magnitude of spin density on the nucleus ($|\Psi(0)|^2$).[340] For a widely delocalised spin, each nucleus experiences a low spin density; conversely, a localised spin has high coefficients on each nucleus.

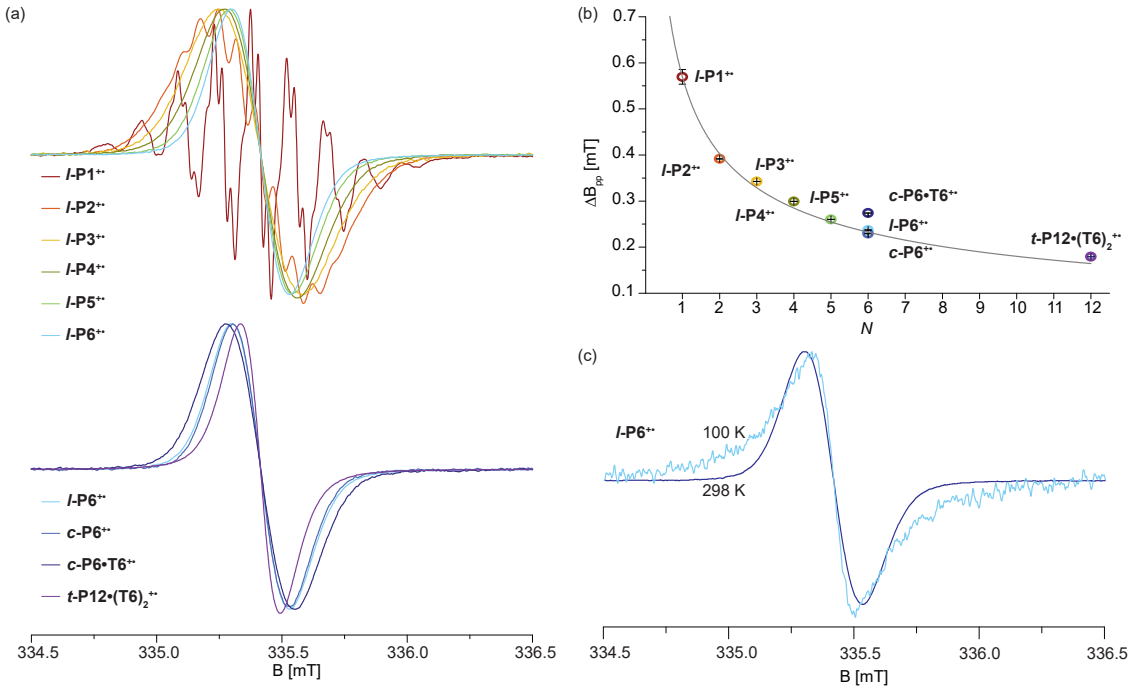

Figure 4.19: (a) CW (X-band, 298 K) EPR of porphyrin oligomer radical cations generated by chemical oxidation. (b) A fit of the peak to peak linewidths (ΔB_{pp}) to the Norris equation (Equation 4.11), showing complete radical cation delocalisation or fast hopping. (c) A comparison of cw EPR spectra of ***l*-P6**$^{+\bullet}$ at 298 K (dark blue) and 100 K (light blue). These data were collected and analysed by Dr C. E. Tait.

$$A_{iso} = \frac{2\mu_0}{3} g\beta_e\beta_n|\Psi(0)|^2 \tag{4.12}$$

where μ_0 is the vacuum permittivity ($1.257 \times 10^{-6}\,\mathrm{T^2\,J^{-1}\,m^3}$), β_e is the Bohr magneton ($9.27 \times 10^{-24}\,\mathrm{J\,T^{-1}}$) and β_n is the nuclear magneton ($5.05 \times 10^{-27}\,\mathrm{J\,T^{-1}}$).

The ENDOR technique measures the electron-nuclear hyperfine coupling by employing radio-frequency (RF) irradiation at a suitable frequency to perturb the coupled nuclear spins.[340] In this study, we used pulsed ENDOR and applied a π RF pulse at varying fields, in a range ± 2 MHz about the ^{1}H Larmor frequency, to selectively flip nuclear spins. The ENDOR response is strongest when the RF offset is on-resonance with the hyperfine coupled proton. These measurements were performed between 6–100 K at W-band, using the Mims ENDOR pulse sequence. There was no difference in the spectra over this range.

The ENDOR results reveal a large hyperfine coupling (~1 MHz) for ***l*-P1**$^{+\bullet}$, decreasing to ~0.5 MHz for ***l*-P2**$^{+\bullet}$. For linear oligomers longer than ***l*-P2** there is no further significant reduction in ^{1}H hyperfine coupling (Figure 4.20).

For ***c*-P6**$^{+\bullet}$ and ***c*-P6•T6**$^{+\bullet}$ the hyperfine coupling reduces further, consistent with delocalisation over three to four porphyrin units. The difference in ENDOR line shape

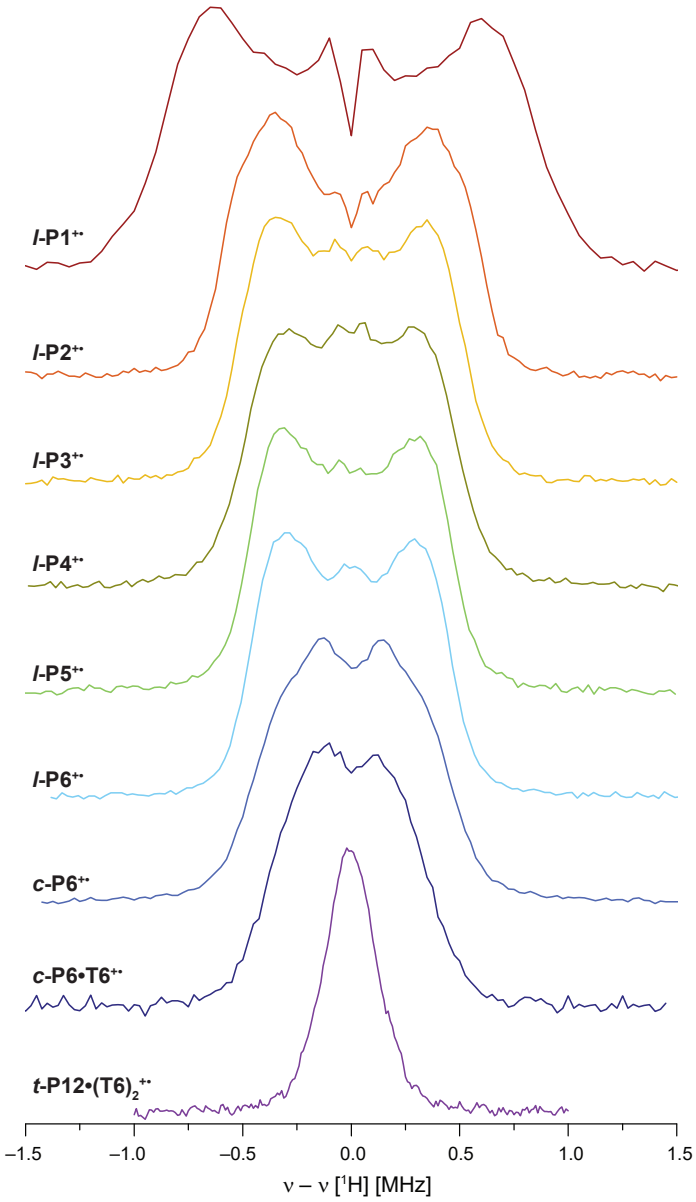

Figure 4.20: ^{1}H ENDOR (W-band, 100 K) of porphyrin oligomer radical cations generated by chemical oxidation. These data were collected by Dr C. E. Tait.

between ***c*-P6$^{+\bullet}$** and ***c*-P6•T6$^{+\bullet}$** may arise from the increased shape-persistence of the templated nanoring, or the additional hyperfine interaction with the template nitrogen. The ENDOR for the tube, ***t*-P12•T6$_2$$^{+\bullet}$**, is narrower still, suggesting increased delocalisation in this 2D analogue of ***c*-P6•T6**.

Fitting the ENDOR data to simulated spectra shows that, for ***l*-P3$^{+\bullet}$** and longer, the extent of radical cation spin delocalisation is much smaller than the whole oligomer length, and for the series ***l*-P1$^{+\bullet}$** to ***l*-P6$^{+\bullet}$** is consistent with spin delocalisation over 2–3 porphyrin units (Figure 4.21).

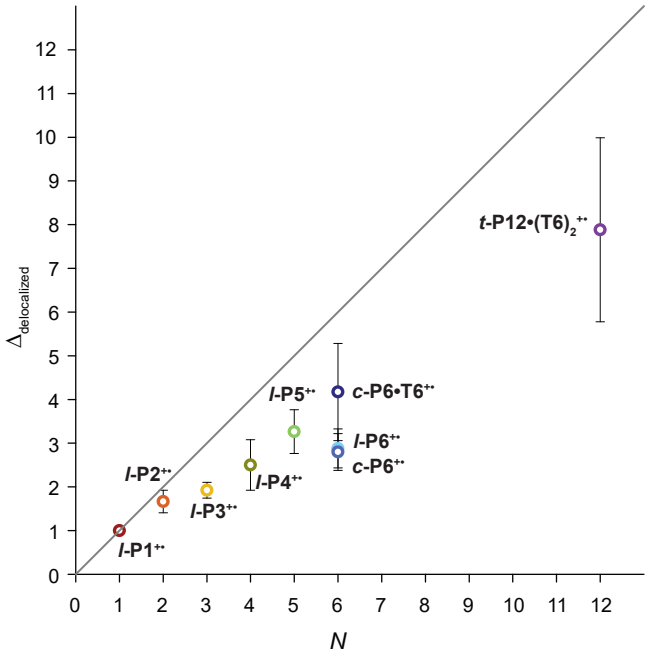

Figure 4.21: Comparison of oligomer length (N) vs. radical cation delocalisation extent, from fitting the ENDOR data. The error bars correspond to the variation in the fits. The diagonal line indicates the expected trend for complete radical cation delocalisation. This analysis was performed by Dr C. E. Tait.

4.5 Conclusions

The charge and spin delocalisation in porphyrin oligomer radical cations has been explored by optical spectroscopies and by EPR. The results indicate that the radical cation extends over 2–3 porphyrin subunits in linear oligomers. This conclusion is supported by the ratio of 'neutral' and 'cation' band (P_2) intensities for longer oligomers (***l*-P3** and longer), assuming a Robin-Day Class II model. ENDOR results further support the conclusion of delocalisation over 2–3 porphyrin units, on the EPR timescale at 100 K.

Our results must be compared to those reported by Therien and coworkers for mono-alkyne linked oligomers.[138,139,287] They concluded that the polaron delocalisation lengths are 'extreme', up to 7 porphyrin units. However, their measurements were performed with cw EPR, and we believe that the use of ENDOR and careful analysis of Vis-NIR-IR spectroscopies is necessary to distinguish between charge delocalisation and rapid hopping. Indeed, our cw results (both at room temperature and at 60 K), taken in isolation, would also be consistent with complete delocalisation. It is only when we employ low-temperature ENDOR and optical spectroscopies, that it becomes clear that rapid hopping is responsible for the cw results, perhaps with other line-broadening mechanisms at 60 K.

From Vis-NIR spectroscopy, the maximum conductive chain length (N_{MCC}) is 3–4 units. This result indicates that the excited state resulting from each transition is more delocalised than its ground state, as would be expected from the long-range delocalisation of excitation in neutral porphyrin oligomers.[335] The N_{MCC} is not expected to be the same as the radical cation charge delocalisation length, since the N_{MCC} reports on the electronic transition between states, not just the ground state delocalisation. In other words, the extent of delocalisation in both the final state, following the electronic transition, and in the ground state, are important to the N_{MCC}.

The presence of IRAVs for ***l*-P2**$^{+\bullet}$ complicates its assignment to Class II or III. If the IRAVs arise from vibronic coupling to the low lying P_1 electronic transition, or from cumulenic character, then ***l*-P2**$^{+\bullet}$ can be considered a Class III (fully delocalised) mixed-valence molecule. If, on the other hand, the IRAVs gain intensity from charge asymmetry, then the two monomer units of the dimer must not be charge-equivalent and the molecule is at the Class II/III borderline. The absence of solvatochromism suggests Class III character, which is supported by the absence of neutral-like absorbance in the Q-band. Although on a slower spectroscopic timescale, the ENDOR data are unequivocal in reporting the appearance of (perhaps averaged) Class III character.

According to EPR, spin delocalisation in the cyclic systems, ***c*-P6**$^{+\bullet}$, ***c*-P6•T6**$^{+\bullet}$ and ***t*-P12•T6$_2$**$^{+\bullet}$, is greater than in the linear oligomers. The delocalisation is greater in the templated systems, ***c*-P6•T6**$^{+\bullet}$ and ***t*-P12•T6$_2$**$^{+\bullet}$, for which the conformational lock provided by the template suppresses local disorder and thus encourages polaron delocalisation or hopping. In contrast, the DFT results suggest that spin delocalisation is similar in the cyclic and linear oligomers. The EPR and DFT results can be reconciled by recognising that the timescale of EPR is relatively slow (10^{-7} s), thus fast hopping could manifest as increased delocalisation. Hopping may be quicker in the cyclic systems due to the absence of end-group trapping effects.

The ENDOR data show that the charge in ***t*-P12•T6$_2$**$^{+\bullet}$ is significantly more delocalised than in ***c*-P6•T6**$^{+\bullet}$, consistent with the hole additionally exploring the axial dimension of the tube. We plan to measure the delocalisation length in this axial dimension by preparing longer porphyrin nanotubes.

The appearance of a Fano-like AR for the C≡C stretch in ***c*-P6•T6**$^{+\bullet}$ and ***t*-P12•T6$_2$**$^{+\bullet}$ (and to a lesser extent in ***c*-P6**$^{+\bullet}$) seems to be a feature common to systems with overlapping

coupled electronic and vibrational modes. The doped nanoring approximates a loop of semiconductor; it would be interesting to explore the effect of magnetic fields on the AR. A magnetic flux dependent frequency shift or intensity change of the AR could be evident as a result of the Aharonov-Bohm (A-B) effect. The A-B effect induces a phase shift in a circulating charge in the presence of a magnetic field,[130] and this phase could introduce a further interference into the AR, possibly affecting its intensity. The interaction of A-B and Fano effects in quantum dots has shown effects on conductance, with changing asymmetry of the transmission Fano interference as a function of magnetic field.[341–343]

The charge localisation in these systems appears to be an inner-sphere effect, as indicated by the absence of solvatochromism. Experiments with different counterions ($SbCl_6^-$ vs. BF_4^-), or the addition of supporting electrolyte (TBAP), showed no change in delocalisation length by ENDOR. In summary, it appears that internal reorganisation favours charge localisation in linear porphyrin oligomers of length greater than 3, and in all cyclic porphyrin oligomers studied here. End-group effects, resulting in different energetic properties at the termini of the oligomers, may also account for charge localisation in the linear systems.

We are presently exploring the charge delocalisation in anion radicals of these porphyrin oligomers.

Mathematics is of two kinds, Rigorous and Physical. The former is Narrow: the latter Bold and Broad. To have to stop to formulate rigorous demonstrations would put a stop to most physico-mathematical inquiries. Am I to refuse to eat because I do not fully understand the mechanism of digestion?

— Oliver Heaviside, as quoted in D. A. Edge, 'Oliver Heaviside (1850–1927) – Physical mathematician', *Teaching mathematics and its applications*, 1982, **2**, 55–61.

5

Excited state aromaticity in porphyrin nanorings

Contents

5.1 Abstract

According to Baird's rule, Hückel's aromaticity mnemonic is reversed for the triplet state of a molecule: i.e., [4*n*]-π becomes aromatic. This excited state (anti)aromaticity (ES(A)A) has been used to explain photophysical phenomena and may prove useful for the rational design of molecular photonic devices. As we have previously shown (Chapter 3), porphyrin nanorings are non-aromatic in their electronically neutral S_0 ground states. In this chapter, we begin to explore the prospect of porphyrin nanoring ES(A)A using DFT and ultrafast photophysical measurements. NICS indicates the presence of ES(A)A. However, photophysical measurements show no statistically significant difference in lifetimes or

radiative rates between nanorings predicted to exhibit excited state antiaromaticity (odd rings) and aromaticity (even rings).

5.2 Introduction

Hückel's rule famously predicts that carbocyclic π-systems with $[4n+2]$ and $[4n]$ π-electrons are aromatic and antiaromatic, respectively. This rule depends upon topology: introduction of a Möbius twist into the π-system reverses the mnemonic and $[4n]$-π becomes aromatic.[117,344] In 1972, Baird predicted a further case in which Hückel's rule is reversed: in the lowest triplet state (T_1) of a molecule.[121] Several experimental examples of T_1 aromaticity have since been presented, and the predictive power of Baird's rule has been extended to the S_1 state.[345,346]

The primary computational methods for investigating ES(A)A are analyses of bond length alternation (BLA) using the harmonic oscillator model (HOMA),[101] and calculations of aromatic stabilisation energy (ASE)[106] and nucleus independent chemical shift (NICS).[89] Experimentally, ES(A)A is difficult to unambiguously assign. With ground state aromaticity, NMR is the technique of choice for measuring magnetic shielding, but this technique is not practical for the S_1 or T_1 excited states. EPR of the T_1 state can help to assign the presence of a triplet ground state, as in the antiaromatic (4 π-electron) cyclopentadienyl cation,[347] but it has not been used to detect (anti)aromatic ring current effects.

Many assignments of ES(A)A employ photophysical methods. The HOMO–LUMO gap (HLG) for aromatic molecules is larger than that for antiaromatic molecules, and consequently the $S_0 \rightarrow S_1$ transitions are higher energy in aromatic molecules.[122] This effect arises from combination of an aromatic stabilisation of S_0 and antiaromatic destabilisation of S_1 for the $[4n+2]$-π case, and the reverse for the $[4n]$-π case. The low energy of the S_1 state can result in an avoided crossing to S_0 and thus low emission quantum yields (due to decay by an internal conversion process), as observed for highly symmetric $[4n]$-π hydrocarbons,[348] and expanded porphyrins.[349] In general, it is difficult to disentangle the effects of ground state (anti)aromaticity from ES(A)A in photophysical properties. More broadly, ES(A)A has been widely invoked to explain the photochemical reactions of $[4n]$-π and $[4n+2]$-π carbocycles,[122] with the classical example given by benzene's excited state propensity towards rearrangements.[350,351]

5. Excited state aromaticity in porphyrin nanorings

Kim and coworkers have assigned ES(A)A on the basis of the shape of the excited state absorption spectrum.[123,349] In their studies, the antiaromatic excited states of hexaphyrins exhibit broad, featureless absorption spectra, whereas the aromatic excited states are much more structured, qualitatively resembling the ground state absorption spectra of aromatic hexaphyrins.

The most convincing assignments of ES(A)A, and confirmation of Baird's rule, would come from measurements on a series of compounds which differ mainly in their π electron count. [*N*]-Porphyrin nanorings (***c*-P*N***) have conjugated circuits of $14N$ π-electrons. Thus, a [5]-porphyrin nanoring has $[4n + 2]$ π-electrons, and a [6]-porphyrin nanoring $[4n]$ π-electrons. The series continues: odd-*N* rings have $[4n + 2]$ π-electrons; even-*N* $[4n]$-π. However, in apparent opposition to Hückel's rule, the S_0 ground states of all of these species are non-aromatic, as evidenced by the similarity of their ^{1}H NMR spectra. Only aromaticity local to each porphyrin monomer is observed: there is no global macrocyclic ring current. However, as we have shown for ***c*-P6** in Chapter 3, oxidation disrupts the local porphyrin aromaticity and leads to the emergence of macrocyclic ring currents.[230]

The Anderson, Herz, and Timmel groups have thoroughly investigated the delocalisation of singlet and triplet states of linear butadiyne-linked porphyrin oligomers, ***c*-P6**, and, for photophysical measurements (Herz), larger rings.[157,186,335,352–356] The photophysical results show rapid singlet state delocalisation over the entire nanoring within 200 fs for nanorings up to ***c*-P24**. ***c*-P6** emits from a delocalised state, whereas partial localisation occurs prior to emission in ***c*-P8** and larger.[355] EPR measurements of triplet states show complete triplet delocalisation at 20 K for ***c*-P6**,[186] but show localisation over 2–3 units for linear oligomers,[186] even when planarity is enforced by coordination.[354]

In the remainder of this chapter we present DFT results which suggest excited state (T_1) aromaticity for even rings and antiaromaticity for odd rings, consistent with Baird's rule. We then present experimental measurements of the TA and fluorescence lifetimes, which are unable to offer support to the prediction of ES(A)A. Future work on this project is then outlined.

5.3 Methods

DFT calculations were carried out using the B3LYP functional and the 6-31G* all-electron basis set,[188–192] as implemented in Gaussian09/D.01.[187] The *meso*-aryl groups on the nanorings were truncated to –H. Nanorings ***c*-P5**, ***c*-P6**, ***c*-P7** and ***c*-P8** were optimised in their S_0 state with the highest possible symmetry (D_{Nh}). The geometries converged as follows: ***c*-P5** (D_{5h}), ***c*-P6** (D_{6h}), ***c*-P7** (C_{7h}) and ***c*-P8** (C_{8h}). Triplet states were then optimised and converged to non-symmetric (C_1) geometries. The stability of the triplet wavefunctions was checked. NICS shieldings[89] were calculated using the GIAO method.

We measured overall lifetimes (τ, defined below) by two methods: transient absorption (TA) spectroscopy and time correlated single-photon counting (TCSPC) fluorescence spectroscopy. The radiative rate (k_R) was determined from TCSPC by measurement of emission quantum yields (QY) in the same conditions. The TA measurements were performed in CH_2Cl_2, while the TCSPC used toluene + 1% pyridine as solvent. The sample concentrations were similar ($\sim$1 µM) in both cases. The TCSPC and QY measurements were performed by Ms. J. Q. Gong (Herz group, Oxford Physics). Ms. R. Haver and Mr. T. Kobatake are thanked for gifts of ***c*-P5** and ***c*-P7**.

$$\tau = \frac{1}{k_{tot}} \tag{5.1}$$

$$k_{tot} = k_R + k_{NR} \tag{5.2}$$

5.4 Results and discussion

5.4.1 Computational chemistry

The HLG of porphyrin nanorings in their neutral ground states show a distinct odd-even effect: the [4*n*]-π (even) rings have a smaller HLG than the [4*n* + 2]-π (odd) rings. Consistent with a simple Hückel MO picture, the odd rings have degenerate HOMO/HOMO-1 and LUMO/LUMO+1 pairs, whereas the degeneracy is lifted for the [4*n*]-π even rings, despite the retention of symmetry for both geometry and wavefunction. Aside from the retention of (for ***c*-P6**) full D_{6h} symmetry, the loss of frontier orbital degeneracy is similar to that which occurs for a pseudo-Jahn-Teller (PJT) distortion, as in cyclobutadiene (see

Chapter 1).[357] Similar results have been found in a computational study on porphyrin nanotubes of different diameters.[358]

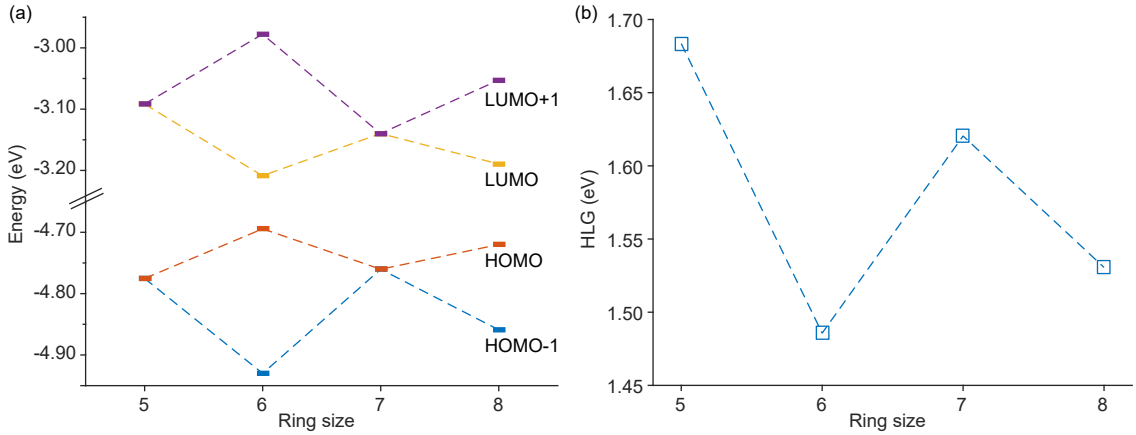

Figure 5.1: (a) Frontier molecular orbital energies for ***c*-P5**–***c*-P8** (B3LYP/6-31G*) in the S_0 state. (b) HLG for ***c*-P5**–***c*-P8** in the S_0 state.

The NICS(0) results at the centres of the rings show that, although every S_0 state is non-aromatic, the T_1 states of ***c*-P5** and ***c*-P6** are antiaromatic and aromatic, respectively (Table 5.1). For ***c*-P7** and ***c*-P8**, the T_1 states remain non-aromatic, as assessed by NICS(0) at the centres of the rings (Table 5.1). However, when NICS(0) is calculated on a grid of points through the ring plane, a difference in shielding between the inside and outside of the nanorings, consistent with global (anti)aromaticity, is present for the T_1 states of all rings (Figure 5.2). The effect is minuscule for ***c*-P7** and ***c*-P8**; the (anti)aromaticity apparent in the ***c*-P7** and ***c*-P8** T_1 states is probably so small as to be experimentally inconsequential.

Table 5.1: $NICS(0)_{iso}$ and $NICS(0)_{zz}$ (all units ppm) at the centres of porphyrin nanorings in their S_0 and T_1 states. Level of theory: B3LYP/6-31G*.

	S_0		T_1	
	$NICS(0)_{iso}$	$NICS(0)_{zz}$	$NICS(0)_{iso}$	$NICS(0)_{zz}$
***c*-P5**	−3	0	2	10
***c*-P6**	−1	1	−5	−12
***c*-P7**	−1	0	0	2
***c*-P8**	−1	0	−1	−1

Figure 5.2 shows that the triplet spin is delocalised over about five porphyrin units. The porphyrin monomer subunit which sustains most triplet spin density exhibits NICS characteristic of antiaromaticity (deshielding above and below the porphyrin plane), which

can be rationalised using valence bond theory by imagining that the two triplet electrons are significantly localised on this porphyrin moiety, giving an effective $2-$ charge, and thus a 20-π antiaromatic ring system.[122,359]

The absence of significant ES(A)A in ***c*-P7** and ***c*-P8** may arise from triplet localisation: for ***c*-P5** and ***c*-P6** the triplet is almost entirely delocalised around the ring, perhaps encouraging coherent effects like aromaticity, whereas reduced delocalisation diminishes the ES(A)A for the larger rings.

The triplet state ENDOR spectra of linear oligomers, ***c*-P6**, and ***c*-P6•T6** have revealed that the triplet is localised over roughly two porphyrin units in the linear oligomers, and over the whole nanoring in ***c*-P6** and ***c*-P6•T6**.[186] Our computational results are consistent with these experimental conclusions, since the experimental uncertainty would encompass an error of at least one porphyrin unit, or the triplet state could be 'fast hopping' on the ENDOR timescale. The ENDOR measurements were conducted at 20 K: a barrier as high as 1 kJ mol^{-1} would still allow fast hopping at this temperature and could appear as the averaged, fully delocalised structure. Variable temperature ENDOR, down to a temperature of 5 K, could help to elucidate the threshold between fast hopping and localisation in a larger ring, such as ***c*-P8**.

These computational results suggest that ***c*-P5** and ***c*-P6** are antiaromatic and aromatic in their T_1 excited states, in accordance with Baird's rule. It appears that ***c*-P7** and ***c*-P8** are practically non-aromatic, perhaps as a consequence of the poor degree of triplet delocalisation. Experiment has shown that the S_1 states of porphyrin nanorings delocalise extremely rapidly,[355] to a greater extent than the triplet states. Thus it could be speculated that ES(A)A would persist for larger rings in their S_1 states.

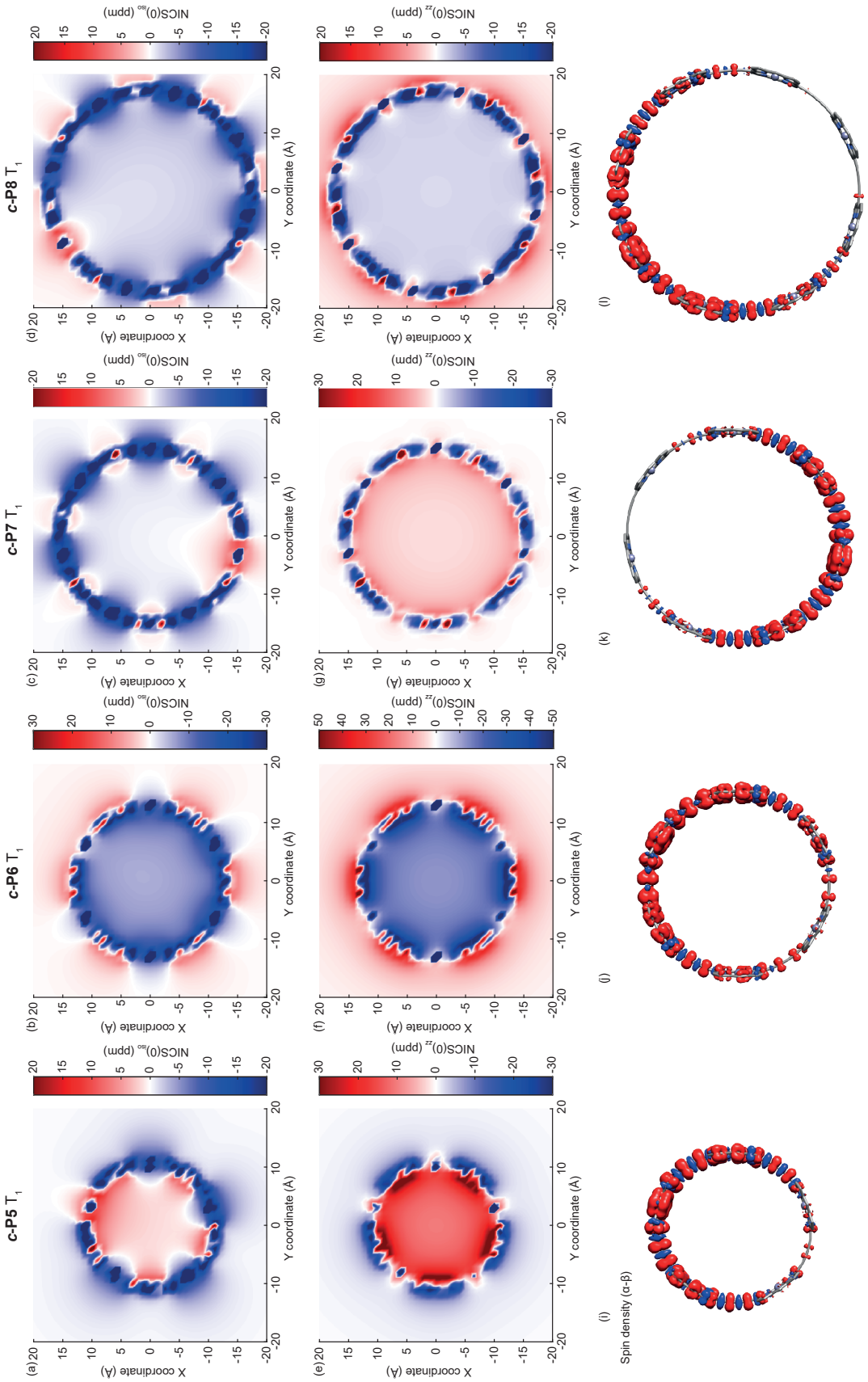

Figure 5.2: *xy*-plane NICS and spin density for ***c*-P5–*c*-P8** in their T_1 states. The top row (a-d) are $NICS(0)_{iso}$, the centre row (e-h) are $NICS(0)_{zz}$ and the bottom row (i-l) show spin densities ($\alpha - \beta$). The colour axes for a-h do not relate to i-l. The isovalues for the spin density plots are ∼0.00025ã.u.

5.4.2 Photophysics

The overall excited state lifetimes increase as a function of ring size (Figure 5.3), consistent with the trend previously observed on a different series of ring sizes.[355] The data from TCSPC show that the lifetime for ***c*-P5** is higher than those for ***c*-P6**–***c*-P8**, but this effect is not reproduced in the lifetimes determined by TA.

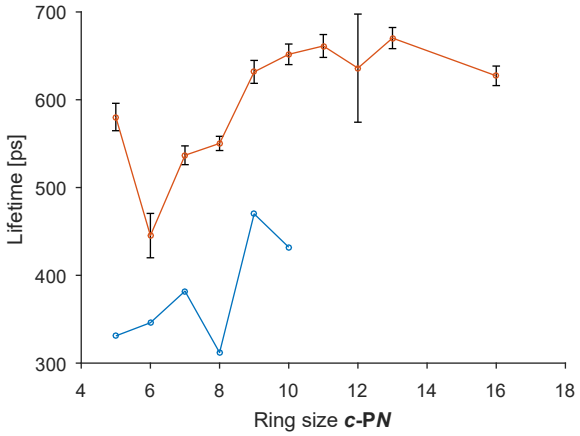

Figure 5.3: Excited state lifetimes determined by TCSPC (top, by Ms. J. Q. Gong, in toluene + 1% pyridine) and by transient absorption decay fitting (bottom, data collected and analysed by me, in CH_2Cl_2). Error bars in the TCSPC are standard errors between multiple replicates ($n = 3$–4); there are no error bars in the TA data because these come from a single measurement.

Table 5.2: Photophysical data for porphyrin nanorings from TCSPC and TA.

	TCSPC			TA	
	Φ_F (%)†	τ_{tot} (ps)†	k_R (ns^{-1})†	$\tau_{1,tot}$ (ps)‡	$\tau_{2,tot}$ (ps)‡
***c*-P5**	2.03 ± 0.40	580 ± 5	0.035 ± 0.007	2.3 (0.5)	331 (4)
***c*-P6**	1.37 ± 0.33	445 ± 6	0.031 ± 0.007	29.4 (4.0)	346 (5)
***c*-P7**	3.94 ± 0.20	537 ± 3	0.073 ± 0.004	9.7 (2.1)	382 (3)
***c*-P8**	2.74 ± 0.37	550 ± 2	0.050 ± 0.007	18.9 (2.9)	312 (6)
***c*-P9**	8.27 ± 0.73	632 ± 3	0.131 ± 0.011	3.6 (1.0)	470 (2)
***c*-P10**	12.58 ± 1.38	652 ± 3	0.193 ± 0.020	6.2 (0.31)	432 (4)
***c*-P11**	12.97 ± 1.62	661 ± 3	0.196 ± 0.024	—	—
***c*-P12**	11.23 ± 2.69	636 ± 16	0.173 ± 0.035	—	—
***c*-P13**	14.44 ± 2.30	670 ± 3	0.216 ± 0.035	—	—
***c*-P16**	22.37 ± 3.43	627 ± 3	0.356 ± 0.054	—	—

† Data recorded by Ms. J. Q. Gong. Variances are the standard error in the mean ($n = 3$ for ***c*-P5**; $n = 4$ otherwise); ‡ Data recorded by me. Parenthetical values are the standard errors in the fit, for a single experiment ($n = 1$)

By measuring the fluorescence QY (Φ_F), the radiative rate (k_R) can be calculated according to Equation 5.3.

$$k_R = \Phi k_{tot} \tag{5.3}$$

The QY of ***c*-P5** is much higher (about 3%) than that for ***c*-P6** (about 1%), as previously reported.[235,236] When k_R is plotted alongside oligomer length (Figure 5.4), using only the TCSPC data, there appears to be a subtle odd-even effect for ***c*-P5**–***c*-P8**, where the radiative rate for even rings is lower than that for odd rings. However, the odd-even effect does not reach the threshold of statistical significance, as indicated by the 95% confidence interval error bars in Figure 5.4.

The low fluorescence QY of nanorings has previously been attributed to the dipole forbidden nature of the $S_0 \rightarrow S_1$ transition.[236] In the point-dipole approximation, the transition dipoles of the six porphyrin monomers around the ***c*-P6** ring (directed along the butadiyne axis of each monomer) cancel, leading to no net transition dipole moment.[236] Similar forbiddenness of the $S_0 \rightarrow S_1$ transition has been reported in small cycloparaphenylenes.[360] When porphyrin nanorings are fixed into rigid cyclic conformations by introduction of a central template, QY reduces further due to the restriction of the Herzberg-Teller coupled symmetry breaking vibrations necessary for emission.[236] The increased QY for ***c*-P5** could arise from structural distortion in this, the smallest ring of the series, resulting in incomplete cancellation of transition dipole moments, or from ES(A)A. We might expect that a PJT distortion of the antiaromatic S_1 states of ***c*-P5** and ***c*-P7** would contribute to an increased QY since the strict molecular symmetry is broken. In contrast, aromatic stabilisation in ***c*-P6** and ***c*-P8**, though presumably weak,[104] will favour the symmetric conformer from which $S_1 \rightarrow S_0$ emission is strongly dipole forbidden.

Kim and coworkers have used the structure of TA spectra for the assignment of ES(A)A, supported by their observation that aromatic excited states resemble aromatic ground states, with sharp spectra and porphyrinoid Q- and Soret-bands. In our case, all of the TA spectra are very similar and uniformly broad and unresolved. However, this fact is relatively inconsequential for an assignment of ES(A)A, since Kim's reasoning does not apply for our molecules: the ground state, with a resolved spectrum, is non-aromatic. The cationic (anti)aromatic states for ***c*-P6**, as resolved by spectroelectrochemistry (Chapter 4, Figure 4.7), are all broad and unresolved.

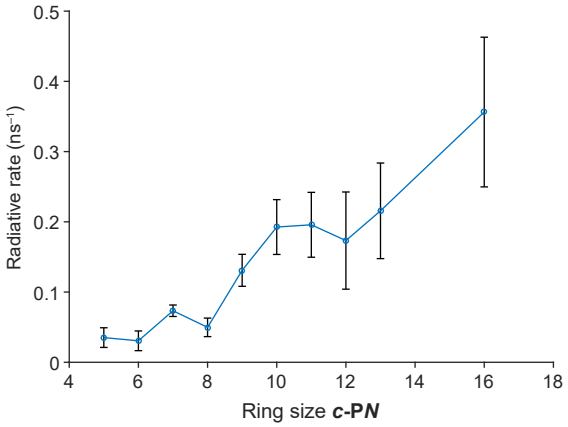

Figure 5.4: Radiative rate determined by TCSPC, in toluene + 1% pyridine. These data were collected by Ms. J. Q. Gong. The statistical analysis is my own. The error bars depict the 95% confidence interval in the mean.

5.5 Conclusions

DFT calculations demonstrate that porphyrin nanorings consisting of up to eight porphyrin units exhibit ES(A)A in their T_1 states. The triplet is delocalised over about five porphyrin subunits. The aromatic/antiaromatic character switches as a function of ring size: odd rings are antiaromatic in their excited states, and even rings are aromatic.

Notably, the electronic ground states of these nanorings are non-aromatic. This fact differentiates this work from other published examples, where ES(A)A exists as a reversal of ground state (anti)aromaticity. The ground state aromatic character is likely to affect the excited state properties. For example, antiaromatic compounds have a smaller HOMO–LUMO gap than aromatic compounds, and so may exhibit faster non-radiative decay via internal conversion.[361]

Photophysical measurements of singlet excited state lifetimes shows no significant odd-even effect. This result suggests that ES(A)A, if it is present, is beyond the capabilities of our current measurements to detect. One might expect ES(A)A to be more prominent in singlet than triplet excited states, owing to the greater inherent delocalisation of singlet states.[362]

This offers prospects for future experiments. It will be interesting to explore whether ES(A)A is apparent in the ultrafast anisotropy decay of the singlet states. The triplet state can be probed directly by transient EPR, in a continuation of previously published studies on linear oligomers and ***c*-P6**.[186] Such experiments will permit us to test the prediction of triplet state localisation over five porphyrin units by measurements on larger rings. It

may also be possible to interrogate the rate of triplet hopping by variable temperature transient-EPR and ENDOR. Further careful replication of the TCSPC and TA measurements may help to evaluate the significance of the trends observed so far.

It's still magic even if you know how it's done.

— Terry Pratchett (2004), A Hat Full of Sky

6

Aromaticity in a truncated porphyrin nanoring

Contents

6.1 Abstract

Current flowing through two equivalent paths in a molecular junction (e.g. through two halves of a cyclophane sandwiched between gold electrodes) can experience constructive interference, manifesting as a non-classical fourfold increase of the current flow compared to the singly connected mutant, whereas a phase difference between non-identical paths can reduce conductance to zero, blocking transmission. This effect is analogous to a Mach-Zehnder interferometer's effect on light. Aromaticity and antiaromaticity may offer improved and non-classical properties for molecules in molecular junctions. In this computational work we explore the effect of de-symmetrising a butadiyne [6]-porphyrin nanoring by removing a C_2 unit, truncating one butadiyne link to a monoalkyne. We show that the truncated nanoring obeys Hückel's law in a fashion entirely analogous to D_{6h} symmetric ***c*-P6**: the tetracation

is aromatic and the hexacation is antiaromatic. The hexacation exhibits a significant pseudo-Jahn-Teller distortion, which reduces the bond length alternation in the C_2 link.

6.2 Introduction

If a beam of light is split into two, and these two beams pass through different media (with different refractive indices, or path lengths), the recombined beam exhibits a phase shift as a result of interference. This principle is the basis of the Mach-Zehnder interferometer, used in light modulation and in quantum physics experiments.

There has recently been great interest in exploring the analogous effect on molecular conductance, when a molecule has two paths through which electrons can flow. Vazquez et al. provided the seminal example: a molecular junction with two equivalent paths exhibits a conductance more than twice that of one with a single path: $G_{tot} > 2G_1$.[363] In contrast, a classical circuit with two parallel paths of equal resistance obeys Kirchoff's law: $G_{tot} = 2G_1$. The greater electrical conductance in parallel molecular circuits is attributed to quantum interference effects, with a theoretical maximum $G_{tot} = 4G_1$.[258]

There are currently efforts under way in the Anderson group to determine whether constructive quantum interference is manifest in porphyrin nanorings, for example in their conductance when they are placed between two metal junctions, or in the exchange coupling between paramagnetic centres in isolated molecules. Recent results have shown that a [6]-porphyrin nanoring with copper atoms at its *para* positions (**Cu_2-*c*-P6•T6**, Figure 6.1) exhibits a fourfold enhanced exchange coupling compared to the single mutant analogue, in which one butadiyne link is broken (**Cu_2-*l*-P6•T6**, Figure 6.1).[364] There is interest in exploring the effects of ring size and external perturbations, such as magnetic fields,[132,133] on the conductivity in a molecular junction. The effect of two different electron path lengths in a nanoring junction will also be explored, such as by using a porphyrin nanoring with two inequivalent paths: **C_2-*c*-P6** (Figure 6.1). This molecule is the focus of this chapter.

In general, aromatic molecules have lower conductivity than non-aromatic molecules, and it is expected that anti-aromatic molecules will have higher conductances owing to their small HOMO–LUMO gap and large polarizability.[365–367] However, the drop in conductance in aromatic molecules is related to the resonance stabilisation energy, which is relatively

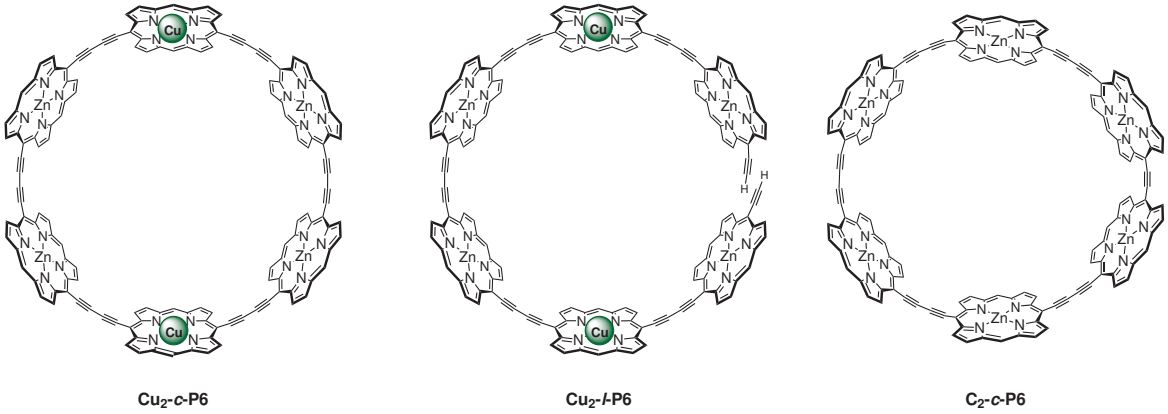

Figure 6.1: Left, centre: *para*-Cu_2 molecules for quantum interference. The exchange coupling between the Cu atoms in the doubly connected structure (left) is four times that in the singly connected structure (centre). Right: C_2 truncated ***c*-P6**.

small for large aromatic systems,[104] so the aromatic state of a [6]-porphyrin nanoring may not have an appreciably reduced conductance compared to the non-aromatic neutral ring.

Aromaticity may be important for quantum interference effects: the conceptual link to benzene substitution patterns, where *para* and *meta* substitution induce constructive and destructive interferences, respectively, is used to describe linker geometry effects on conductance.[368] It is therefore interesting to explore the effect of aromaticity and antiaromaticity on quantum interference in molecules with different substitution patterns. The results in Chapter 3 demonstrated the utility of oxidation chemistry to affect changes in nanoring aromaticity. In this chapter, we combine that principle with an asymmetric nanoring.

We wanted to test whether Hückel's law is still applicable for a nanoring with two inequivalent conjugation paths, in which we have removed 2-π electrons by truncating just one butadiyne linker to an alkyne. The computational results presented here show that this truncated nanoring, **C_2-*c*-P6**, does follow Hückel's rule, and is aromatic in its 78-π tetracationic oxidation state, and antiaromatic in its 76-π hexacationic state.

6.3 Methods

DFT calculations were all performed using a model of **C_2-*c*-P6** in which solubilising aryl groups had been truncated to –H. Geometries were optimised using Gaussian09/D.01[187] and the B3LYP/6-31G* functional/basis set combination.[188–192] The neutral state converged to C_2 symmetry whilst the 4+ and 6+ states had no symmetry (C_1). NICS calculations

were conducted using the GIAO method, as implemented in Gaussian09/D.01. NICS grids were calculated with 1 Å resolution on a 40 × 40 Å grid.

Our earlier studies on ***c*-P6** (Chapter 3) revealed that B3LYP/6-31G* was a sufficient level of theory with which to describe porphyrin nanoring (anti)aromaticity,[230] and so we did not attempt different levels of theory here.

6.4 Results and discussion

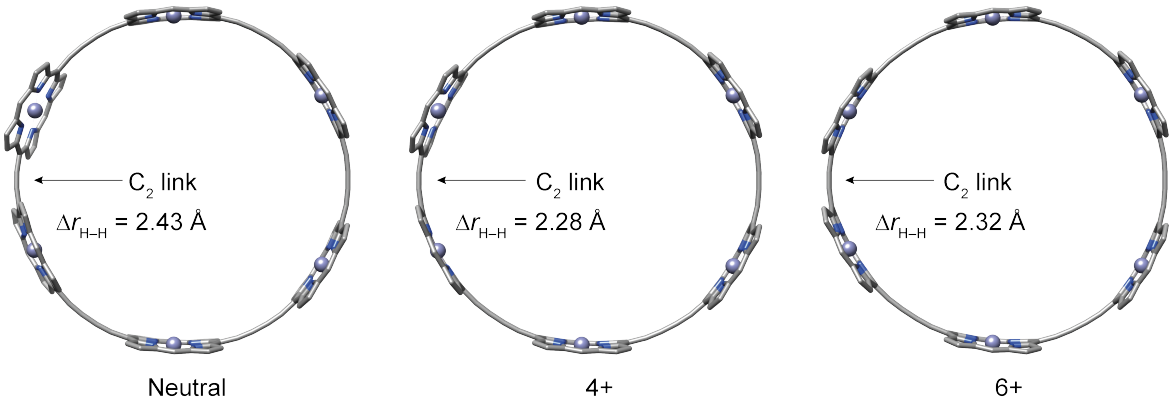

Figure 6.2: Optimised geometries (B3LYP/6-31G*) of **C_2-*c*-P6** in its neutral, tetracationic (aromatic) and hexacationic (antiaromatic) oxidation states. Δr_{H-H} refers to the distance between β protons across the C_2 link (see text).

The geometry optimised structures of **C_2-*c*-P6** in its neutral, 4+ and 6+ oxidation states are shown in Figure 6.2. In the neutral state, there is a clear torsion between the C_2 linked porphyrins, amounting to around 23°. This torsion reduces for the tetracation (9°) and further to zero for the hexacation. This huge reduction in torsion angle is surprising: in a linear monoalkyne-linked porphyrin dimer **C_2-P2** the barrier to planarity is around 6.5 kJ mol^{-1} (Chapter 2, Figure 2.2).[178] Whilst one might invoke marginal aromatic stabilisation energy[104] to explain the increased planarity in the aromatic tetracation, it is difficult to imagine why the antiaromatic hexacation does not distort away from planarity, permitting it to avoid both the high torsion barrier and antiaromaticity.

The barrier to planarity in **C_2-P2** arises from steric repulsion between the β-protons. Despite the reduction in torsion angle in **C_2-*c*-P6^{6+}**, the inter-proton distance is greater than that for the 4+ oxidation state (2.32 Å vs. 2.28 Å), due to a distortion of the porphyrin rings. The inter-proton distance in the neutral nanoring is 2.43 Å.

6. Aromaticity in a truncated porphyrin nanoring

A popular geometric criterion for aromaticity is the reduction in bond-length alternation (BLA).[101,103] Consider the equal bond lengths in benzene, compared to the localised single and double bonds of hypothetical cyclohexatriene. It is widely accepted that, for large aromatic [*n*]-annulenes ($n \geqslant 14$), there is a return of BLA even in the presence of aromaticity.[68,369] If we calculate BLA for the C_2 fragment as BLA $= r_{C-C} - r_{C\equiv C}$, then the BLA shows the surprising trend $6+ < 4+ <$ neutral (Table 6.1)! To understand this result further we plotted the bond length difference $\Delta r = r_{n+} - r_{\text{neutral}}$ for each bond (Figure 6.3). The results reveal that the decreased BLA for the C_2 link in $\mathbf{C_2}$-***c***-$\mathbf{P6^{6+}}$ arises from a pseudo-Jahn-Teller (PJT) distortion: the majority of the bond-length equalisation in the 6+ state is found in three of the linker (alkyne and butadiyne) units. In contrast, all of the linker units in the aromatic $\mathbf{C_2}$-***c***-$\mathbf{P6^{4+}}$ are bond-length equalised by roughly the same amount.

This PJT distortion is analogous to that observed in antiaromatic cyclobutadiene: that molecule distorts from a D_{4h} square to a D_{2h} rectangle, with increased BLA (Chapter 1).

Our results reveal that, although BLA is known to be significant for large annulenes,[68,369] it retains utility in describing bonding changes between aromatic and antiaromatic oxidation states of a molecule, and vividly illustrates the PJT distortion in the antiaromatic oxidation state.

We next turned to the calculation of nucleus independent chemical shifts (NICS), to assign aromaticity based on magnetic properties. The results are entirely consistent with expectations (Table 6.1 and Figure 6.4): much like we saw for ***c***-**P6** in Chapter 3, the neutral oxidation state exhibits no NICS in the *zz* component of the chemical shielding tensor, and the isotropic component reveals the local aromatic ring currents of each component porphyrin monomer (Figure 6.4d and a, respectively). In contrast, the 4+ and 6+ oxidation states exhibit a dramatic difference in NICS between the inside and outside of the nanoring. The (anti)aromaticity apparent in the *zz* tensor component clearly dominates the isotropic NICS (Figure 6.4b–f). The internal shielding (negative NICS) and external deshielding (positive NICS) of the 4+ oxidation state is diagnostic for aromaticity, and the reverse for the 6+ state is diagnostic of antiaromaticity.

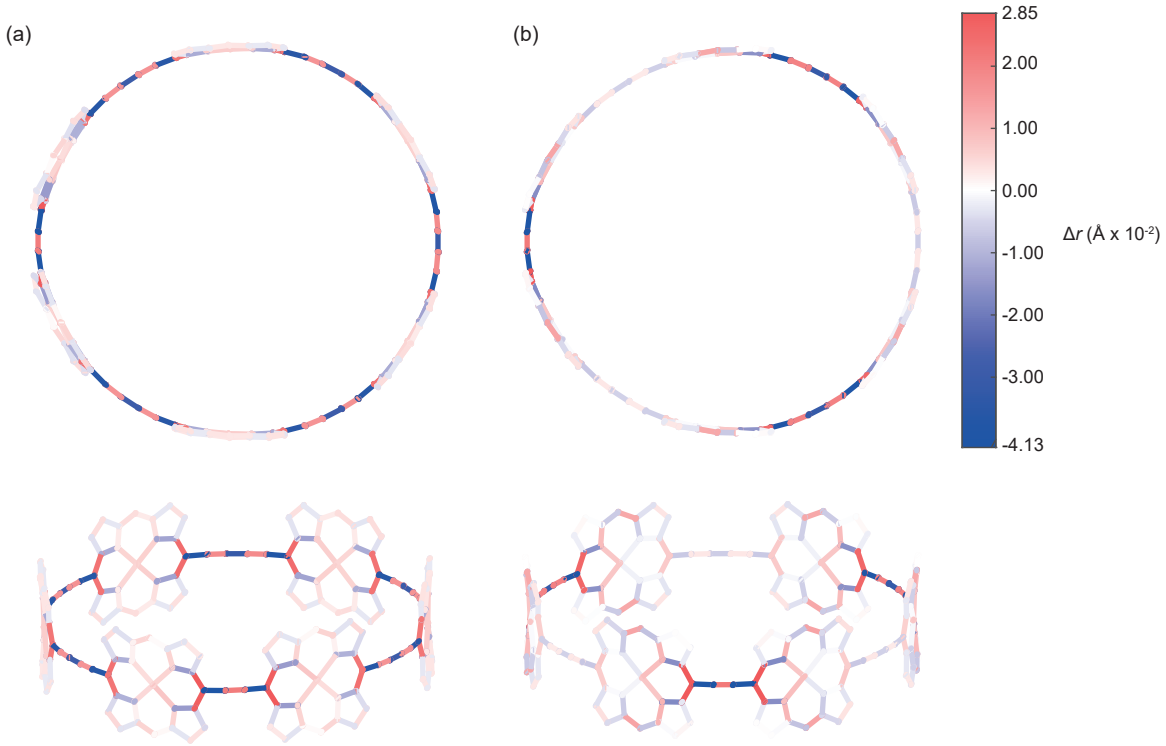

Figure 6.3: Bond length differences Δr between the neutral state and (a) the aromatic tetracation and (b) the antiaromatic hexacation of **C_2-*c*-P6**. The C_2 fragment is on the left in the upper two subplots, and at the centre-foreground in the lower two.

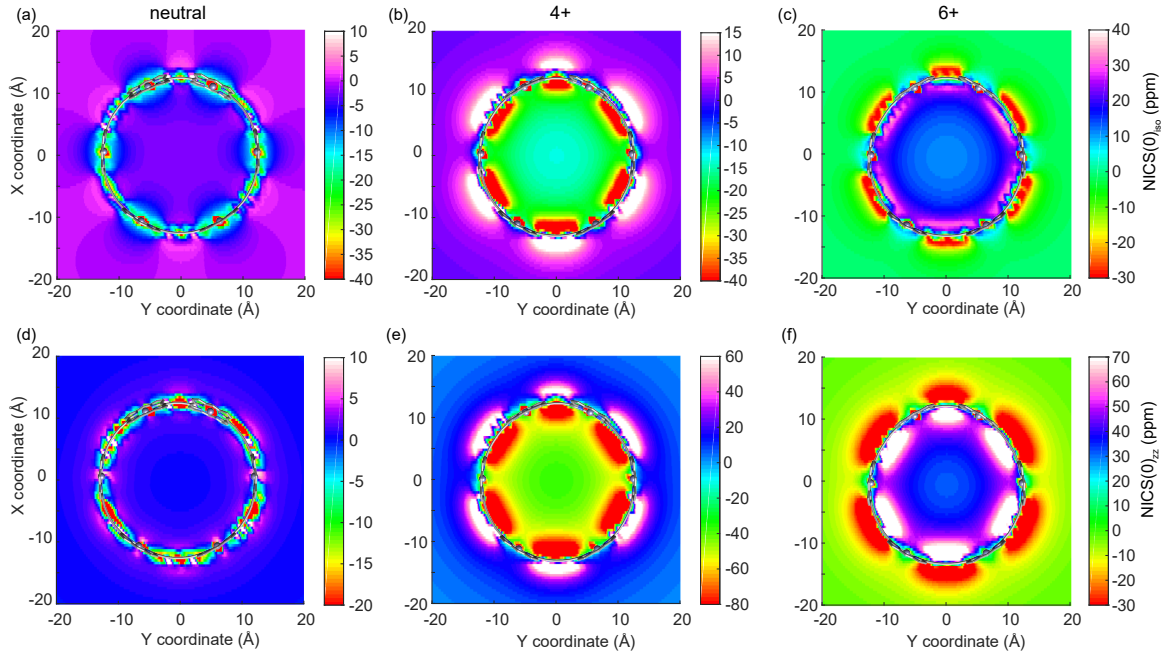

Figure 6.4: NICS grids (B3LYP/6-31G*) for **C_2-*c*-P6** showing (a-c) $NICS(0)_{iso}$ and (d-f) $NICS(0)_{zz}$. The neutral (a and d) state shows no macrocyclic aromaticity, the 4+ state (b and e) shows macrocyclic aromaticity, and the 6+ state (c and f) shows macrocyclic antiaromaticity.

Table 6.1: Theoretical aromaticity criteria for **C_2-*c*-P6**. NICS and BLA were calculated at the B3LYP/6-31G* level of theory.

	0+	4+	6+
n π e^-	82	78	76
Hückel classification	$4n+2$ π	$4n+2\pi$	$4n$ π
NICS(0)$_{zz}$ (ppm)	0	-37	32
NICS(0)$_{iso}$ (ppm)	-2	-13	11
BLA (C_2) (Å)	0.2	0.17	0.14

6.5 Conclusions

We have shown that a truncated [6]-porphyrin nanoring, **C_2-*c*-P6**, in which one butadiyne linker is replaced with a monoalkyne linker, exhibits aromaticity and antiaromaticity upon oxidation, consistent with Hückel's rule and with the results presented in Chapter 3.

Efforts are currently under way to synthesise this nanoring. The experimental measurement of aromaticity is likely to be more challenging than in the case of 'normal' ***c*-P6**. The reduction in symmetry from D_{6h} to C_{2h} will result in a more complex NMR spectrum. It may also be more difficult to directly access the aromatic oxidation state of **C_2-*c*-P6** (4+) than it was for ***c*-P6** (6+), since in the latter case there was a large electrochemical gap between the 6+ and 12+ oxidation states (Chapter 3, Figure 3.7), and there was thus negligible disproportionation to nearby oxidation states.

We also plan to use **C_2-*c*-P6** in molecular junctions, to explore the impact of unequal path lengths on quantum interference effects in conductances, by comparison to ***c*-P6**.

Appendices

A

Experimental supplement

A.1 Notes

Unless stated otherwise, all reagents were obtained from commercial sources and used as received without further purification. Diethyl ether (Et_2O), chloroform ($CHCl_3$) and toluene were dried by passing through activated alumina columns using a positive pressure of dry N_2. Diisopropylamine (DIPA) was dried by distillation from CaH_2. Analytical gel permeation chromatography (GPC) was performed on a JAIGEL H-P precolumn, a JAIGEL 3H-A (8 mm × 500 mm) and a JAIGEL 4H-A column (8 mm × 500 mm) in series with THF:pyridine 100:1 as eluent. Preparative recycling gel permeation chromatography was performed on a JAIGEL H-P precolumn, a JAIGEL 3H (20 mm × 600 mm) and a JAIGEL 4H column (20 mm × 600 mm) in series with toluene:pyridine 100:1 as eluent. Flash column chromatography was performed on Merck silica gel 60 (40–63 µm). Alumina columns were performed using aluminium oxide (activated, basic, Brockmann I, standard grade, ~150 mesh, 58 Å) from Sigma Aldrich. For TLC, Merck silica gel 60 F254 aluminium-backed sheets were used. Size exclusion chromatography (SEC) was carried out using Bio-Beads SX-1, 200–400 mesh (Bio Rad).

All synthetic procedures are found in Chapter 3, subsection 3.3.1.

NMR spectra were recorded on Bruker AVII400, Bruker AVIII400, Bruker AVII500 and Bruker AVIII500 spectrometers. The residual solvent peak was used as internal reference. Multiplicities (s = singlet, d = doublet, t = triplet, q = quartet, and m = multiplet)

and coupling constant(s) are reported wherever possible. MALDI-TOF-MS spectra were measured using a Waters MALDI Micro MX or at the EPSRC National Mass Spectrometry service (Swansea, Wales, UK) using the Applied Biosystems Voyager DE-STR. UV-vis absorption spectra were recorded at ambient temperature with a Perkin-Elmer Lambda 20 using quartz 1 cm cuvettes.

A.2 Extinction coefficients of oligomers

Table A.1: Collated extinction coefficients for selected non-porphyrin compounds.

Compound	Solvent	λ_{max} / nm ($\log \epsilon$)	Ref.
T6	$CHCl_3$	278 (5.04)	[24]
T8	CH_2Cl_2	644 (3.96), 590 (4.25), 563 (4.39), 525 (4.55), 440 (5.62), 317 (5.17)	[169]

Table A.2: Collated extinction coefficients for porphyrin oligomers with 3,5-di(*tert*-butyl)phenyl sidegroups in the *meso* positions.

Oligomer	Solvent	λ_{max} / nm ($\log \epsilon$)	Ref.
P1	CH_2Cl_2 1% pyr	646 (4.75), 594 (4.09), 454 (5.42), 441 (5.59)	[23]
***l*-P2**	CH_2Cl_2 1% pyr	741 (5.11), 675 (4.91), 494 (5.34), 458 (5.62)	[23]
***l*-P3**	CH_2Cl_2 1% pyr	763 (5.25), 498 (5.32), 460 (5.64)	[23]
***l*-P4**	CH_2Cl_2 1% pyr	799 (5.23), 460 (5.61)	[23]
***l*-P5**	CH_2Cl_2 1% pyr	706 (5.43), 460 (5.72)	[23]
***l*-P6**	CH_2Cl_2 1% pyr	814 (5.53), 462 (5.80)	[23]
***c*-P5**	Toluene	747 (5.23), 719 (5.20), 489 (5.60), 430 (5.38)	[235]
***c*-P5T5$_{cor}$**	Toluene	832 (5.28), 789 (5.34), 752 (5.36), 493 (5.63), 428 (5.45)	[235]
***c*-P5T5$_{Fc}$**	Toluene	837 (5.26), 794 (5.34), 756 (5.34), 494 (5.60), 431 (5.40)	[235]
***c*-P6**	$CHCl_3$	788 (5.36), 475 (5.63)	[24]
***c*-P6•T6**	$CHCl_3$	852 (5.52), 810 (5.61), 774 (5.51), 483 (5.68)	[24]
***c*-P8**	$CHCl_3$ 1% pyr	817 (5.72), 492 (5.94), 466 (5.92)	[237]
***c*-P10**	$CHCl_3$ 1% pyr	822 (5.71), 596 (4.76), 468 (5.89)	[237]

Table A.3: Collated extinction coefficients for porphyrin oligomers with 3,5-bis(octyloxy)phenyl sidegroups in the *meso* positions.

Oligomer	Solvent	λ_{max} / nm ($\log \epsilon$)	Ref.
P1	CH_2Cl_2 1% pyr	639 (4.77), 588 (4.13), 454 (5.45), 443 (5.64)	[370]
***l*-P2**	CH_2Cl_2 1% pyr	735 (5.06), 669 (4.77), 586 (4.35), 494 (5.32), 460 (5.61)	[370]
***l*-P3**	$CHCl_3$ 1% pyr	755 (5.28), 590 (5.52), 500 (5.40), 462 (5.72)	[24]
***l*-P4**	CH_2Cl_2 1% pyr	772 (5.54), 588 (4.86), 496 (5.79), 462 (5.91)	[371]
***l*-P6**	Toluene 1% pyr	804 (5.64), 466 (5.76)	[24]
***l*-P6**	$CHCl_3$	813 (5.56), 519 (5.56), 439 (5.34)	[24]
***l*-P8**	CH_2Cl_2 1% pyr	812 (5.72), 591 (4.83), 496 (5.88), 465 (5.92)	[370]
***c*-P5T5$_{cor}$**	Toluene	825 (5.30), 783 (5.34), 746 (5.34), 494 (5.62), 428 (5.36)	[235]
***c*-P5T5$_{Fc}$**	Toluene	828 (5.28), 785 (5.34), 749 (5.34), 494 (5.60), 431 (5.38)	[235]
***c*-P6**	$CHCl_3$	783 (5.36), 473 (5.63)	[24]
***c*-P6•T6**	$CHCl_3$	841 (5.45), 800 (5.51), 765 (5.40), 486 (5.60)	[24]
***c*-P8**	$CHCl_3$ 1% pyr	802 (5.26), 490 (5.59), 464 (5.64)	[169]
***c*-P8•T8**	$CHCl_3$	848 (5.53), 798 (5.18), 757 (5.04), 498 (5.53), 441 (5.49)	[169]
***c*-P10**	Toluene 1% pyr	806 (5.87), 491 (6.06), 471 (6.08)	[237]
***c*-P12**	Toluene 1% pyr	810 (5.85), 491 (6.02), 473 (6.02)	[25]

Table A.4: Collated extinction coefficients for porphyrin oligomers with 3,5-bis(trihexylsilyl)phenyl (THS) sidegroups in the *meso* positions.

Oligomer	Solvent	λ_{max} / nm (log ϵ)	Ref.
P1	CH_2Cl_2	625 (4.64), 578 (4.26), 446 (5.51), 4.37 (5.69)	[186]
***l*-P2**	CH_2Cl_2	708 (5.06), 652 (4.81), 576 (4.36), 488 (5.34), 454 (5.58)	[186]
***l*-P2**	CH_2Cl_2:THF:pyr (10:10:1)	741 (5.07), 674 (4.89), 588 (4.34), 495 (5.29), 459 (5.59)	[31]
***l*-P3**	CH_2Cl_2	738 (5.24), 501 (4.49), 492 (5.41), 453 (5.64)	[186]
***l*-P4**	CH_2Cl_2	761 (5.38), 747 (5.38), 581 (4.64), 491 (5.61), 452 (5.72)	[186]
***l*-P5**	CH_2Cl_2	769 (5.51), 581 (4.69), 491 (5.70), 452 (5.76)	[186]
***l*-P6**	CH_2Cl_2	776 (5.61), 582 (4.79), 491 (5.80), 453 (5.84)	[186]
***c*-P6•T6**	CH_2Cl_2	850 (5.61), 808 (5.70), 772 (5.57), 612 (4.59), 482 (5.76)	[186]
***c*-P6**	CH_2Cl_2	772 (5.45), 748 (5.49), 593 (4.62), 473 (5.71)	[186]
Free base ***c*-P6**	CH_2Cl_2	791 (5.47), 771 (5.49), 659 (5.30), 449 (5.72)	[186]
Polymer	CH_2Cl_2	780 (4.83), 468 (5.01)	[183]
***c*-P8**	Toluene + 1% pyr.	818 (5.54), 597 (4.62), 495 (5.74), 469 (5.68)	This work
***c*-P9**	Toluene + 1% pyr.	821 (5.60), 600 (4.66), 487 (5.78), 472 (5.77)	This work
***c*-P10**	Toluene + 1% pyr.	821 (5.73), 598 (4.81), 495 (5.89, sh.), 471 (5.92)	This work
***c*-P11**	Toluene + 1% pyr.	820 (5.70), 596 (4.79), 493 (5.88), 471 (5.89)	This work
***c*-P12**	Toluene + 1% pyr.	821 (5.88), 596 (4.88), 488 (6.06), 472 (6.07)	This work
***c*-P13**	Toluene + 1% pyr.	821 (5.75), 595 (4.83), 490 (5.91), 472 (5.93)	This work
***c*-P16**	Toluene + 1% pyr.	829 (5.89), 594 (4.97), 491 (6.03), 473 (6.05)	This work
***t*-P12•T6$_2$**	$CHCl_3$	873 (5.71), 831 (5.72), 791 (5.6), 528 (5.89)	[27]
***t*-P12•T6$_2$**	CH_2Cl_2	867 (5.61), 828 (5.63), 786 (5.55), 529 (5.89)	This work
***t*-P12•T6$_2$**	CH_2Cl_2 10% THF	867 (5.61), 828 (5.63), 786 (5.55), 529 (5.89)	This work

A.3 GPC retention times of THS porphyrin oligomers

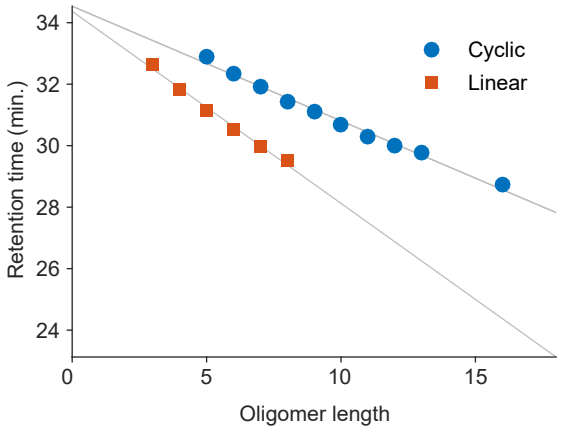

Figure A.1: Analytical GPC retention times for THS porphyrin oligomers. Using two JIAGEL-H columns in series (3H-A then 4H-A), with THF:1% pyridine eluent and a 1 mL min^{-1} flow rate. The lines show linear regression fits: $RT = m \cdot N + c$ where RT is retention time and N is oligomer length. For cyclic oligomers, $m = -0.373$ min and $c = 34.54$ min. For linear oligomers, $m = -0.625$ min and $c = 34.37$ min. For both fits, $R^2 = 0.989$.

B
Cover designs

This appendix presents cover picture designs proposed for the publication M. D. Peeks, T. D. W. Claridge and H. L. Anderson, 'Aromatic and antiaromatic ring currents in a molecular nanoring', *Nature*, 2017, **541**, 200–203.

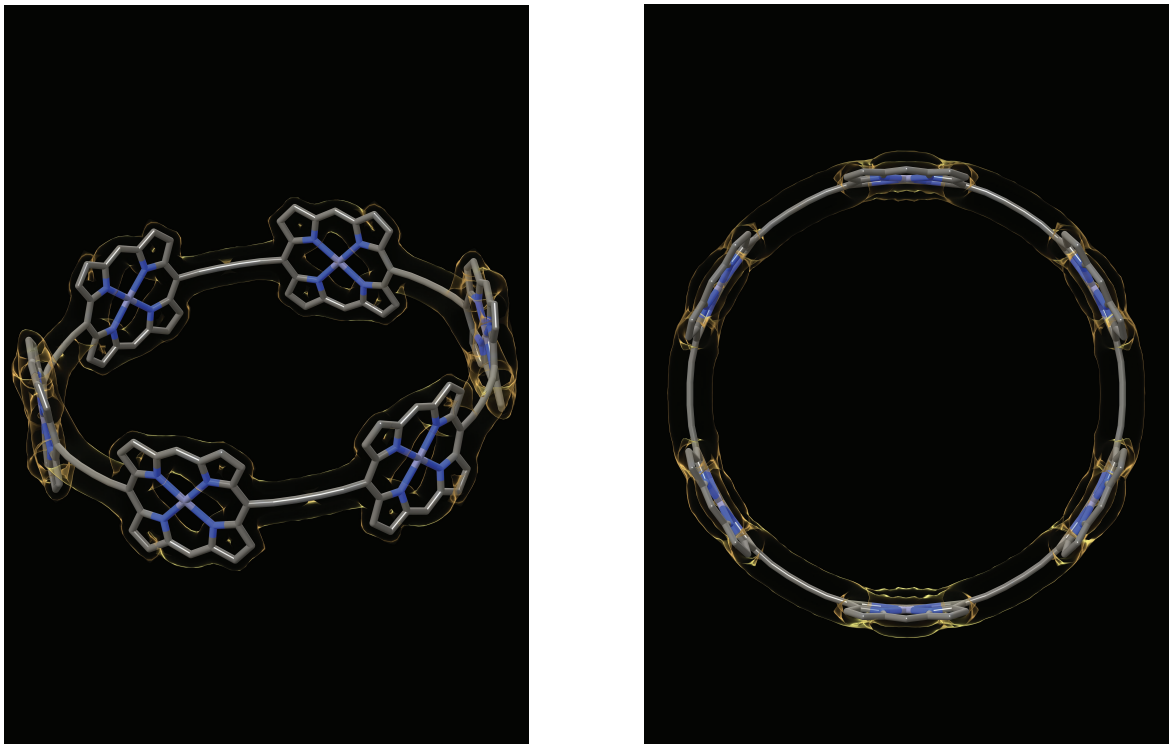

(a) **(b)**

Figure B.1: These designs show the ***c*-P6** nanoring surrounded by an ACID isosurface for the 6+ oxidation state. The figure was generated in Chimera.

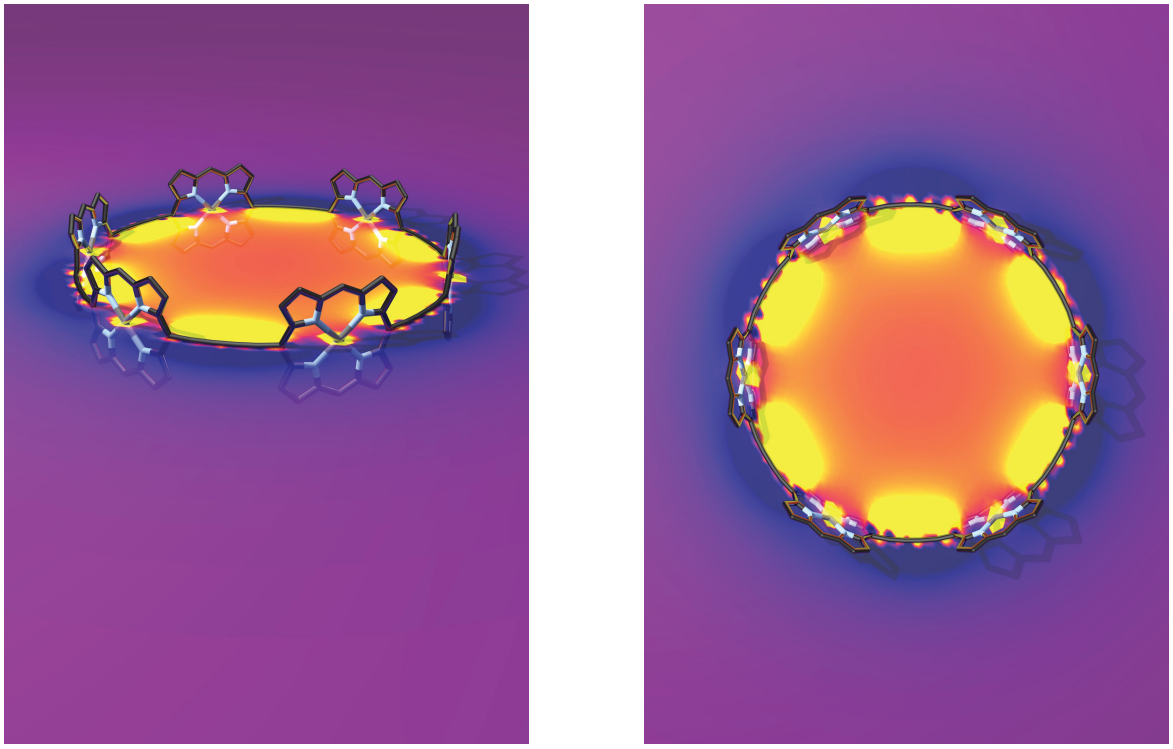

(a) Side view **(b)** Top view

Figure B.2: These designs show the ***c*-P6** nanoring on a NICS(0)$_{zz}$ plane, for the 6+ oxidation state. The figure was generated using Blender.

References

1. M. Vicente and K. Smith, 'Syntheses and Functionalizations of Porphyrin Macrocycles', *Curr. Org. Synth.*, 2014, **11**, 3–28.
2. T. Tanaka and A. Osuka, 'Conjugated porphyrin arrays: synthesis, properties and applications for functional materials', *Chem. Soc. Rev.*, 2015, **44**, 943–969.
3. S.-P. Wang, S. Li, J. Wu, Y.-F. Shen and B.-Y. Zhu, 'Recent advances in the template-directed synthesis of porphyrin nanorings', *Chem. Comm.*, 2016, 1–14.
4. S. Hiroto, Y. Miyake and H. Shinokubo, 'Synthesis and Functionalization of Porphyrins through Organometallic Methodologies', *Chem. Rev.*, 2016, **117**, 2910–3043.
5. D. Kondratiuk, 'Synthesis and properties of giant porphyrin nanorings', Ph.D. Thesis, University of Oxford, 2013.
6. P. Liu, 'New templates for porphyrin nanorings', Ph.D. Thesis, University of Oxford, 2016.
7. N. Kamonsutthipaijit, 'Self-assembly and template-directed synthesis in multi-strand porphyrin arrays', Ph.D. Thesis, University of Oxford, 2016.
8. R. Willstätter, 'Chlorophyll', *J. Am. Chem. Soc.*, 1915, **37**, 323–345.
9. R. Robinson, 'Richard Willstatter. 1872-1942', *Obit. Not. Fellows Roy. Soc.*, 1953, **8**, 609–634.
10. A. W. Johnson, 'Aromaticity in macrocyclic polypyrrolic ring systems', *Pure Appl. Chem.*, 1971, **28**, 195–218.
11. E. Vogel, 'The porphyrins from the 'annulene chemist's' perspective', *Pure Appl. Chem.*, 1993, **65**, 143–152.
12. B. J. Littler, Y. Ciringh and J. S. Lindsey, 'Investigation of Conditions Giving Minimal Scrambling in the Synthesis of *trans*-Porphyrins from Dipyrromethanes and Aldehydes', *J. Org. Chem.*, 1999, **64**, 2864–2872.
13. B. J. Littler, M. A. Miller, C.-H. Hung, R. W. Wagner, D. F. O'Shea, P. D. Boyle and J. S. Lindsey, 'Refined Synthesis of 5-Substituted Dipyrromethanes', *J. Org. Chem.*, 1999, **64**, 1391–1396.
14. D. M. Guldi, 'Fullerene–porphyrin architectures; photosynthetic antenna and reaction center models', *Chem. Soc. Rev.*, 2002, **31**, 22–36.
15. M. Gilbert and B. Albinsson, 'Photoinduced charge and energy transfer in molecular wires', *Chem. Soc. Rev.*, 2015, **44**, 845–862.
16. S. Venkataramani, U. Jana, M. Dommaschk, F. D. Sonnichsen, F. Tuczek and R. Herges, 'Magnetic Bistability of Molecules in Homogeneous Solution at Room Temperature', *Science*, 2011, **331**, 445–448.
17. A. M. Bowen, M. W. Jones, J. E. Lovett, T. G. Gaule, M. J. McPherson, J. R. Dilworth, C. R. Timmel and J. R. Harmer, 'Exploiting orientation-selective DEER: determining molecular structure in systems containing Cu(II) centres', *Phys. Chem. Chem. Phys.*, 2016, **18**, 5981–5994.
18. D. P. Arnold, A. W. Johnson and M. Mahendran, 'Some reactions of meso-formyloctaethylporhyrin', *J. Chem. Soc., Perkin Trans. 1*, 1978, 366–370.
19. D. P. Arnold and L. J. Nitschinsk, 'Porphyrin dimers linked by conjugated butadiynes', *Tetrahedron*, 1992, **48**, 8781–8792.
20. D. P. Arnold, 'Two Rings Are Better Than One: Adventures in Porphyrin Chemistry', *Synlett*, 2000, **2000**, 296–305.

21. H. L. Anderson, 'Conjugated Porphyrin Ladders', *Inorg. Chem.*, 1994, **33**, 972–981.
22. H. L. Anderson, 'Building molecular wires from the colours of life: conjugated porphyrin oligomers', *Chem. Comm.*, 1999, 2323–2330.
23. P. N. Taylor and H. L. Anderson, 'Cooperative Self-Assembly of Double-Strand Conjugated Porphyrin Ladders', *J. Am. Chem. Soc.*, 1999, **121**, 11538–11545.
24. M. Hoffmann, J. Kärnbratt, M.-H. Chang, L. M. Herz, B. Albinsson and H. L. Anderson, 'Enhanced π conjugation around a porphyrin[6] nanoring.', *Angew. Chem. Int. Ed.*, 2008, **47**, 4993–4996.
25. M. C. O'Sullivan, J. K. Sprafke, D. V. Kondratuk, C. Rinfray, T. D. W. Claridge, A. Saywell, M. O. Blunt, J. N. O'Shea, P. H. Beton, M. Malfois and H. L. Anderson, 'Vernier templating and synthesis of a 12-porphyrin nano-ring.', *Nature*, 2011, **469**, 72–75.
26. S. A. L. Rousseaux, J. Q. Gong, R. Haver, B. Odell, T. D. W. Claridge, L. M. Herz and H. L. Anderson, 'Self-Assembly of Russian Doll Concentric Porphyrin Nanorings', *J. Am. Chem. Soc.*, 2015, **137**, 12713–12718.
27. P. Neuhaus, A. Cnossen, J. Q. Gong, L. M. Herz and H. L. Anderson, 'A Molecular Nanotube with Three-Dimensional π-Conjugation', *Angew. Chem. Int. Ed.*, 2015, **54**, 7344–7348.
28. S. J. Cole, G. C. Curthoys, E. A. Magnusson and J. N. Phillips, 'Ligand binding by metalloporphyrins. III. Thermodynamic functions for the addition of substituted pyridines to nickel(II) and zinc(II) porphyrins', *Inorg. Chem.*, 1972, **11**, 1024–1028.
29. H. J. Hogben, J. K. Sprafke, M. Hoffmann, M. Pawlicki and H. L. Anderson, 'Stepwise effective molarities in porphyrin oligomer complexes: preorganization results in exceptionally strong chelate cooperativity.', *J. Am. Chem. Soc.*, 2011, **133**, 20962–20969.
30. M. U. Winters, J. Kärnbratt, M. Eng, C. J. Wilson, H. L. Anderson and B. Albinsson, 'Photophysics of a butadiyne-linked porphyrin dimer: Influence of conformational flexibility in the ground and first singlet excited state', *J. Phys. Chem. C*, 2007, **111**, 7192–7199.
31. M. D. Peeks, P. Neuhaus and H. L. Anderson, 'Experimental and Computational Evaluation of the Barrier to Torsional Rotation in a Butadiyne-Linked Porphyrin Dimer', *Phys. Chem. Chem. Phys.*, 2016, **18**, 5264–5274.
32. R. van Grondelle, J. P. Dekker, T. Gillbro and V. Sundstrom, 'Energy transfer and trapping in photosynthesis', *Biochim. Biophys. Acta, Bioenerg.*, 1994, **1187**, 1–65.
33. G. McDermott, S. M. Prince, A. A. Freer, A. M. Hawthornthwaite-Lawless, M. Z. Papiz, R. J. Cogdell and N. W. Isaacs, 'Crystal structure of an integral membrane light-harvesting complex from photosynthetic bacteria', *Nature*, 1995, **374**, 517–521.
34. T. Higashino and H. Imahori, 'Porphyrins as excellent dyes for dye-sensitized solar cells: recent developments and insights.', *Dalton Trans.*, 2015, **44**, 448–463.
35. NREL, *Best Research Cell Efficiency*, 2016, `http://www.nrel.gov/pv/` (visited on 12/12/2016).
36. W. Shockley and H. J. Queisser, 'Detailed Balance Limit of Efficiency of p-n Junction Solar Cells', *J. Appl. Phys.*, 1961, **32**, 510–519.
37. T. D. Mody, 'Pharmaceutical development and medical applications of porphyrin-type macrocycles', *J. Porph. Phthal.*, 2000, **4**, 362–367.
38. M. Ethirajan, Y. Chen, P. Joshi and R. K. Pandey, 'The role of porphyrin chemistry in tumor imaging and photodynamic therapy.', *Chem. Soc. Rev.*, 2011, **40**, 340–362.
39. M. Stepień, N. Sprutta and L. Latos-Grażyński, 'Figure Eights, Möbius Bands, and More: Conformation and Aromaticity of Porphyrinoids', *Angew. Chem. Int. Ed.*, 2011, **50**, 4288–4340.
40. J. Mack, 'Expanded, Contracted, and Isomeric Porphyrins: Theoretical Aspects', *Chem. Rev.*, 2016, **117**, 3444–3478.
41. E. Vogel, P. Röhrig, M. Sicken, B. Knipp, A. Herrmann, M. Pohl, H. Schmickler and J. Lex, 'The Thiophene Analogue of Porphyrin: Tetrathiaporphyrin Dication', *Angew. Chem. Int. Ed.*, 1989, **28**, 1651–1655.

42. E. Vogel, N. Jux, J. Dörr, T. Pelster, T. Berg, H.-S. Böhm, F. Behrens, J. Lex, D. Bremm and G. Hohlneicher, 'Furan-Based Porphyrins: Tetraoxa[4n + 2]porphyrin Dications with 18π-, 22π-, or 26π-Electron Systems', *Angew. Chem. Int. Ed.*, 2000, **39**, 1101–1105.
43. J. L. Sessler and D. Seidel, 'Synthetic Expanded Porphyrin Chemistry', *Angew. Chem. Int. Ed.*, 2003, **42**, 5134–5175.
44. S. Saito and A. Osuka, 'Expanded porphyrins: intriguing structures, electronic properties, and reactivities.', *Angew. Chem. Int. Ed.*, 2011, **50**, 4342–4373.
45. A. Osuka and S. Saito, 'Expanded porphyrins and aromaticity', *Chem. Comm.*, 2011, **47**, 4330–4339.
46. J. I. Wu, I. Fernández and P. v. R. Schleyer, 'Description of aromaticity in porphyrinoids.', *J. Am. Chem. Soc.*, 2013, **135**, 315–321.
47. M. Pawlicki and L. Latos-Grażyński, 'Aromaticity Switching in Porphyrinoids', *Chem. – Asian. J.*, 2015, **10**, 1438–1451.
48. T. Soya, W. Kim, D. Kim and A. Osuka, 'Stable [48]-, [50]-, and [52]Dodecaphyrins(1.1.0.1.1.0.1.1.0.1.1.0): The Largest Hückel Aromatic Molecules', *Chem. – Eur. J.*, 2015, **21**, 8341–8346.
49. P. v. R. Schleyer, 'Introduction: Aromaticity', *Chem. Rev.*, 2001, **101**, 1115–1118.
50. P. v. R. Schleyer, 'Introduction: Delocalization–Pi and Sigma', *Chem. Rev.*, 2005, **105**, 3433–3435.
51. N. Martín and L. T. Scott, 'Challenges in aromaticity: 150 years after Kekulé's benzene', *Chem. Soc. Rev.*, 2015, **44**, 6397–6400.
52. J.-B. Michel, Y. K. Shen, A. P. Aiden, A. Veres, M. K. Gray, J. P. Pickett, D. Hoiberg, D. Clancy, P. Norvig, J. Orwant, S. Pinker, M. A. Nowak and E. L. Aiden, 'Quantitative Analysis of Culture Using Millions of Digitized Books', *Science*, 2011, **331**, 176–182.
53. A. Kekulé, 'Ueber die Constitution und die Metamorphosen der chemischen Verbindungen und über die chemische Natur des Kohlenstoffs', *Annalen der Chemie und Pharmacie*, 1858, **106**, 129–159.
54. A. S. Couper, 'Sur une nouvelle théorie chimique', *Annales de Chimie et de Physique*, 1858, **53**, 469–489.
55. A. Kekulé, 'Sur la constitution des substances aromatiques', *Bulletin Mensuel de la Société Chimique de Paris*, 1865, **3**, 98–110.
56. A. Kekulé, 'Untersuchungen über aromatische Verbindungen Ueber die Constitution der aromatischen Verbindungen. I. Ueber die Constitution der aromatischen Verbindungen.', *Justus Liebigs Ann. Chem.*, 1866, **137**, 129–196.
57. J. Thiele, 'Zur Kenntniss der ungesättigten Verbindungen. Theorie der ungesättigten und aromatischen Verbindungen', *Justus Liebigs Ann. Chem.*, 1899, **306**, 87–142.
58. R. Willstätter and E. Waser, 'Über Cyclo-octatetraen', *Ber. Dtsch. Chem. Ges.*, 1911, **44**, 3423–3445.
59. E. C. Crocker, 'Application of the octet theory to single-ring aromatic compounds', *J. Am. Chem. Soc.*, 1922, **44**, 1618–1630.
60. J. W. Armit and R. Robinson, 'CCXI.—Polynuclear heterocyclic aromatic types. Part II. Some anhydronium bases', *J. Chem. Soc., Trans.*, 1925, **127**, 1604–1618.
61. A. T. Balaban, P. v. R. Schleyer and H. S. Rzepa, 'Crocker, Not Armit and Robinson, Begat the Six Aromatic Electrons', *Chem. Rev.*, 2005, **105**, 3436–3447.
62. L. Pauling and G. W. Wheland, 'The Nature of the Chemical Bond. V. The Quantum-Mechanical Calculation of the Resonance Energy of Benzene and Naphthalene and the Hydrocarbon Free Radicals', *J. Chem. Phys.*, 1933, **1**, 362–374.
63. E. Hückel, 'Grundzüge der Theorie ungesättigter und aromatischer Verbindungen', *Zeitschrift für Elektrochemie und angewandte physikalische Chemie*, 1937, **43**, 752–788.
64. J. Berson, *Chemical Creativity: Ideas from the Work of Woodward, Hückel, Meerwein, and Others*, Wiley, 1999.
65. W. V. E. Doering and F. L. Detert, 'Cycloheptatrienylium Oxide', *J. Am. Chem. Soc.*, 1951, **73**, 876–877.

66. A. A. Frost and B. Musulin, 'A Mnemonic Device for Molecular Orbital Energies', *J. Chem. Phys.*, 1953, **21**, 572–573.

67. T. Bally and S. Masamune, 'Cyclobutadiene', *Tetrahedron*, 1980, **36**, 343–370.

68. M. Kertesz, C. H. Choi and S. Yang, 'Conjugated polymers and aromaticity', *Chem. Rev.*, 2005, **105**, 3448–3481.

69. P. Pascal, 'Magnetochemical Researches', *Ann. Chim. Phys*, 1910, **19**, 5–70.

70. A. Pacault, J. Hoarau and A. Marchand, in *Advances in Chemical Physics*, ed. I. Prigogine, John Wiley & Sons, Inc., 1961, vol. 3, pp. 171–238.

71. R. Gleiter and G. Haberhauer, *Aromaticity and other conjugation effects*, Wiley-VCH, Weinheim, 2012.

72. H. J. Dauben, J. D. Wilson and J. L. Laity, 'Diamagnetic Susceptibility Exaltation in Hydrocarbons', *J. Am. Chem. Soc.*, 1969, **91**, 1991–1998.

73. R. Gershoni-Poranne and A. Stanger, 'Magnetic criteria of aromaticity', *Chem. Soc. Rev.*, 2015, **44**, 6597–6615.

74. P. v. R. Schleyer and H. Jiao, 'What is aromaticity?', *Pure Appl. Chem.*, 1996, **68**, 209–218.

75. F. Sondheimer and R. Wolovsky, 'Unsaturated Macrocyclic Compounds. XXI. 1 The Synthesis of a Series of Fully Conjugated Macrocyclic Polyene-polyynes (Dehydro-annulenes) from 1,5-Hexadiyne', *J. Am. Chem. Soc.*, 1962, **84**, 260–269.

76. F. Sondheimer, 'Recent advances in the chemistry of large-ring conjugated systems', *Pure Appl. Chem.*, 1963, **7**, 363–388.

77. F. Sondheimer, I. C. Calder, J. A. Elix, Y. Gaoni, P. J. Garratt, K. Grohmann, G. Di Maio, J. Mayer, M. V. Sargent and R. Wolovsky, Aromaticity, Chem. Soc. Spec. Publ. No. 21, ed. W. D. Ollis, The Chemical Society, London, 1967, pp. 75–108.

78. F. Sondheimer, 'Annulenes', *Acc. Chem. Res.*, 1972, **5**, 81–91.

79. R. Breslow, 'Aromatic Character', *Chem. Eng. News*, 1965, **43**, 90–100.

80. E. Steiner and P. W. Fowler, 'Four- and two-electron rules for diatropic and paratropic ring currents in monocyclic π-systems', *Chem. Comm.*, 2001, 2220–2221.

81. H. C. Longuet-Higgins, Aromaticity, Chem. Soc. Spec. Publ. No. 21, ed. W. D. Ollis, The Chemical Society, London, 1967, pp. 109–112.

82. J. A. Pople and K. G. Untch, 'Induced Paramagnetic Ring Currents', *J. Am. Chem. Soc.*, 1966, **88**, 4811–4815.

83. P. W. Fowler and E. Steiner, 'Patterns of Ring Currents in Conjugated Molecules: A Few-Electron Model Based on Orbital Contributions', *J. Phys. Chem. A*, 2001, **105**, 9553–9562.

84. P. Lazzeretti, 'Ring currents', *Prog. Nucl. Magn. Reson. Spectrosc.*, 2000, **36**, 1–88.

85. J. A. N. F. Gomes and R. B. Mallion, 'Aromaticity and ring currents', *Chem. Rev.*, 2001, **101**, 1349–1383.

86. E. Vogel, Aromaticity, Chem. Soc. Spec. Publ. No. 21, ed. W. D. Ollis, The Chemical Society, London, 1967, pp. 113–147.

87. J. A. Cissell, T. P. Vaid and A. L. Rheingold, 'An Antiaromatic Porphyrin Complex: Tetraphenylporphyrinato(silicon)$(L)_2$ (L = THF or Pyridine)', *J. Am. Chem. Soc.*, 2005, **127**, 12212–12213.

88. W. Shakespeare, *The Tragedy of Macbeth*, 1606.

89. P. v. R. Schleyer, C. Maerker, A. Dransfeld, H. Jiao and N. J. R. v. Eikema Hommes, 'Nucleus-Independent Chemical Shifts: A Simple and Efficient Aromaticity Probe', *J. Am. Chem. Soc.*, 1996, **118**, 6317–6318.

90. P. v. R. Schleyer, H. Jiao, N. J. R. v. Eikema Hommes, V. G. Malkin and O. L. Malkina, 'An Evaluation of the Aromaticity of Inorganic Rings: Refined Evidence from Magnetic Properties', *J. Am. Chem. Soc.*, 1997, **119**, 12669–12670.

91. S. Klod and E. Kleinpeter, 'Ab initio calculation of the anisotropy effect of multiple bonds and the ring current effect of arenes—application in conformational and configurational analysis', *J. Chem. Soc., Perkin Trans. 2*, 2001, 1893–1898.

92. R. Gershoni-Poranne and A. Stanger, 'The NICS-XY-scan: Identification of local and global ring currents in multi-ring systems', *Chem. – Eur. J.*, 2014, **20**, 5673–5688.

93. A. Stanger, 'Nucleus-independent chemical shifts (NICS): distance dependence and revised criteria for aromaticity and antiaromaticity.', *J. Org. Chem.*, 2006, **71**, 883–893.

94. Z. Chen, C. S. Wannere, C. Corminboeuf, R. Puchta and P. v. R. Schleyer, 'Nucleus-independent chemical shifts (NICS) as an aromaticity criterion', *Chem. Rev.*, 2005, **105**, 3842–3888.

95. R. Herges and D. Geuenich, 'Delocalization of Electrons in Molecules', *J. Phys. Chem. A*, 2001, **105**, 3214–3220.

96. E. U. Wallenborn, R. F. Haldimann, F. G. Klärner and F. Diederich, 'Theoretical investigation of the origin of regioselectivity in the formation of methanofullerenes by addition of diazo compounds: A model study', *Chem. – Eur. J.*, 1998, **4**, 2258–2265.

97. D. Geuenich, K. Hess, F. Köhler and R. Herges, 'Anisotropy of the induced current density (ACID), a general method to quantify and visualize electronic delocalization', *Chem. Rev.*, 2005, **105**, 3758–3772.

98. J. Jusélius, D. Sundholm and J. Gauss, 'Calculation of current densities using gauge-including atomic orbitals', *J. Chem. Phys.*, 2004, **121**, 3952–3963.

99. H. Fliegl, D. Sundholm, S. Taubert, J. Jusélius and W. Klopper, 'Magnetically induced current densities in aromatic, antiaromatic, homoaromatic, and nonaromatic hydrocarbons', *J. Phys. Chem. A*, 2009, **113**, 8668–8676.

100. H. Fliegl and D. Sundholm, 'Aromatic Pathways of Porphins, Chlorins, and Bacteriochlorins', *J. Org. Chem.*, 2012, **77**, 3408–3414.

101. J. Kruszewski and T. Krygowski, 'Definition of aromaticity basing on the harmonic oscillator model', *Tetrahedron Lett.*, 1972, **13**, 3839–3842.

102. T. M. Krygowski, M. K. Cyrański, Z. Czarnocki, G. Häfelinger and A. R. Katritzky, 'Aromaticity: A theoretical concept of immense practical importance', *Tetrahedron*, 2000, **56**, 1783–1796.

103. T. M. Krygowski and M. K. Cyrański, 'Structural Aspects of Aromaticity', *Chem. Rev.*, 2001, **101**, 1385–1420.

104. C. S. Wannere and P. v. R. Schleyer, 'How Aromatic Are Large $(4n+2)\pi$ Annulenes?', *Org. Lett.*, 2003, **5**, 865–868.

105. C. H. Choi and M. Kertesz, 'Bond length alternation and aromaticity in large annulenes', *J. Chem. Phys.*, 1998, **108**, 6681–6688.

106. M. K. Cyrański, 'Energetic Aspects of Cyclic Pi-Electron Delocalization: Evaluation of the Methods of Estimating Aromatic Stabilization Energies', *Chem. Rev.*, 2005, **105**, 3773–3811.

107. P. v. R. Schleyer and F. Pühlhofer, 'Recommendations for the Evaluation of Aromatic Stabilization Energies', *Org. Lett.*, 2002, **4**, 2873–2876.

108. M. Mammen, E. I. Shakhnovich and G. M. Whitesides, 'Using a Convenient, Quantitative Model for Torsional Entropy To Establish Qualitative Trends for Molecular Processes That Restrict Conformational Freedom', *J. Org. Chem.*, 1998, **63**, 3168–3175.

109. F. Feixas, E. Matito, J. Poater and M. Solà, 'Quantifying aromaticity with electron delocalisation measures', *Chem. Soc. Rev.*, 2015, **44**, 6434–6451.

110. M. Palusiak and T. M. Krygowski, 'Application of AIM Parameters at Ring Critical Points for Estimation of π-Electron Delocalization in Six-Membered Aromatic and Quasi-Aromatic Rings', *Chem. – Eur. J.*, 2007, **13**, 7996–8006.

111. E. Clar, *The Aromatic Sextet*, Wiley, London, 1972.

112. M. Solà, 'Forty years of Clar's aromatic π-sextet rule', *Front. Chem.*, 2013, **1**, 4–11.

113. L. Gross, F. Mohn, N. Moll, B. Schuler, A. Criado, E. Guitian, D. Pena, A. Gourdon and G. Meyer, 'Bond-Order Discrimination by Atomic Force Microscopy', *Science*, 2012, **337**, 1326–1329.

114. J. L. von. Rosenberg, J. E. Mahler and R. Pettit, 'The Bicyclo[5,1,0]Octadienyl Cation,1A New Stable Carbonium Ion', *J. Am. Chem. Soc.*, 1962, **84**, 2842–2843.

115. F. Stahl, P. v. R. Schleyer, H. Jiao, H. F. Schaefer, K.-H. Chen and N. L. Allinger, 'Resurrection of Neutral Tris-homoaromaticity', *J. Org. Chem.*, 2002, **67**, 6599–6611.

116. E. Heilbronner, 'Hückel molecular orbitals of Möbius-type conformations of annulenes', *Tetrahedron Lett.*, 1964, **5**, 1923–1928.

117. D. Ajami, O. Oeckler, A. Simon and R. Herges, 'Synthesis of a Möbius aromatic hydrocarbon', *Nature*, 2003, **426**, 819–821.

118. P. W. Fowler and H. S. Rzepa, 'Aromaticity rules for cycles with arbitrary numbers of half-twists', *Phys. Chem. Chem. Phys.*, 2006, **8**, 1775–1777.

119. H. S. Rzepa, 'Möbius Aromaticity and Delocalization', *Chem. Rev.*, 2005, **105**, 3697–3715.

120. Z. S. Yoon, A. Osuka and D. Kim, 'Möbius aromaticity and antiaromaticity in expanded porphyrins', *Nat. Chem.*, 2009, **1**, 113–122.

121. N. C. Baird, 'Quantum organic photochemistry. II. Resonance and aromaticity in the lowest $3\pi\pi^*$ state of cyclic hydrocarbons', *J. Am. Chem. Soc.*, 1972, **94**, 4941–4948.

122. M. Rosenberg, C. Dahlstrand, K. Kilså and H. Ottosson, 'Excited state aromaticity and antiaromaticity: opportunities for photophysical and photochemical rationalizations.', *Chem. Rev.*, 2014, **114**, 5379–5425.

123. Y. M. Sung, M.-C. Yoon, J. M. Lim, H. Rath, K. Naoda, A. Osuka and D. Kim, 'Reversal of Hückel (anti)aromaticity in the lowest triplet states of hexaphyrins and spectroscopic evidence for Baird's rule', *Nat. Chem.*, 2015, **7**, 418–422.

124. J. Oh, Y. M. Sung, W. Kim, S. Mori, A. Osuka and D. Kim, 'Aromaticity reversal in the lowest excited triplet state of archetypical Möbius heteroannulenic systems', *Angew. Chem. Int. Ed.*, 2016, **55**, 6487–6491.

125. S. Taubert, D. Sundholm and F. Pichierri, 'Magnetically Induced Currents in [n]Cycloparaphenylenes, $n = 6$–11', *J. Org. Chem.*, 2010, **75**, 5867–5874.

126. T. Kawase, 'The Synthesis and Physicochemical and Supramolecular Properties of Strained Phenylacetylene Macrocycles', *Synlett*, 2007, **2007**, 2609–2626.

127. T. J. Sisto, M. R. Golder, E. S. Hirst and R. Jasti, 'Selective Synthesis of Strained [7]Cycloparaphenylene: An Orange-Emitting Fluorophore', *J. Am. Chem. Soc.*, 2011, **133**, 15800–15802.

128. J. Xia and R. Jasti, 'Synthesis, characterization, and crystal structure of [6]cycloparaphenylene', *Angew. Chem. Int. Ed.*, 2012, **51**, 2474–2476.

129. N. Toriumi, A. Muranaka, E. Kayahara, S. Yamago and M. Uchiyama, 'In-Plane Aromaticity in Cycloparaphenylene Dications: A Magnetic Circular Dichroism and Theoretical Study', *J. Am. Chem. Soc.*, 2015, **137**, 82–85.

130. A. C. Bleszynski-Jayich, W. E. Shanks, B. Peaudecerf, E. Ginossar, F. von Oppen, L. Glazman and J. G. E. Harris, 'Persistent Currents in Normal Metal Rings', *Science*, 2009, **326**, 272–275.

131. M. Mayor and C. Didschies, 'A giant conjugated molecular ring.', *Angew. Chem. Int. Ed.*, 2003, **42**, 3176–3179.

132. O. Hod, E. Rabani and R. Baer, 'Magnetoresistance of Nanoscale Molecular Devices', *Acc. Chem. Res.*, 2006, **39**, 109–117.

133. D. Rai, O. Hod and A. Nitzan, 'Magnetic Field Control of the Current through Molecular Ring Junctions', *J. Phys. Chem. Lett.*, 2011, **2**, 2118–2124.

134. A. Soncini, P. W. Fowler and L. W. Jenneskens, 'Ring currents in large [$4n + 2$]-annulenes', *Phys. Chem. Chem. Phys.*, 2004, **6**, 277–284.

135. E. I. Tellgren, T. Helgaker and A. Soncini, 'Non-perturbative magnetic phenomena in closed-shell paramagnetic molecules.', *Phys. Chem. Chem. Phys.*, 2009, **11**, 5489–5498.

136. V. Chandrasekhar, R. A. Webb, M. J. Brady, M. B. Ketchen, W. J. Gallagher and A. Kleinsasser, 'Magnetic response of a single, isolated gold loop', *Phys. Rev. Lett.*, 1991, **67**, 3578–3581.

137. A. Heckmann and C. Lambert, 'Organic mixed-valence compounds: A playground for electrons and holes', *Angew. Chem. Int. Ed.*, 2012, **51**, 326–392.

138. K. Susumu, P. R. Frail, P. J. Angiolillo and M. J. Therien, 'Conjugated chromophore arrays with unusually large hole polaron delocalization lengths.', *J. Am. Chem. Soc.*, 2006, **128**, 8380–8381.

139. M. J. Therien, P. J. Angiolillo and J. Rawson, 'Extreme electron polaron spatial delocalization in π-conjugated materials', *Proc. Natl. Acad. Sci. USA*, 2015, **112**, 13779–13783.

140. N. Takeda, S. Asaoka and J. R. Miller, 'Nature and Energies of Electrons and Holes in a Conjugated Polymer, Polyfluorene', *J. Am. Chem. Soc.*, 2006, **128**, 16073–16082.

141. L. Zaikowski, P. Kaur, C. Gelfond, E. Selvaggio, S. Asaoka, Q. Wu, H.-C. Chen, N. Takeda, A. R. Cook, A. Yang, J. Rosanelli and J. R. Miller, 'Polarons, Bipolarons, and Side-By-Side Polarons in Reduction of Oligofluorenes', *J. Am. Chem. Soc.*, 2012, **134**, 10852–10863.

142. J. Bakalis, A. R. Cook, S. Asaoka, M. Forster, U. Scherf and J. R. Miller, 'Polarons, compressed polarons, and bipolarons in conjugated polymers', *J. Phys. Chem. C*, 2014, **118**, 114–125.

143. N. Takeda and J. R. Miller, 'Poly(3-decylthiophene) Radical Anions and Cations in Solution: Single and Multiple Polarons and Their Delocalization Lengths in Conjugated Polymers', *J. Phys. Chem. B*, 2012, **116**, 14715–14723.

144. T. D. Nguyen, G. Hukic-Markosian, F. Wang, L. Wojcik, X.-G. Li, E. Ehrenfreund and Z. V. Vardeny, 'Isotope effect in spin response of π-conjugated polymer films and devices.', *Nat. Mater.*, 2010, **9**, 345–352.

145. F. C. Grozema, P. T. van Duijnen, Y. A. Berlin, M. A. Ratner and L. D. A. Siebbeles, 'Intramolecular Charge Transport along Isolated Chains of Conjugated Polymers: Effect of Torsional Disorder and Polymerization Defects', *J. Phys. Chem. B*, 2002, **106**, 7791–7795.

146. J. Roncali, 'Synthetic Principles for Bandgap Control in Linear π-Conjugated Systems', *Chem. Rev.*, 1997, **97**, 173–206.

147. A. Pron, P. Gawrys, M. Zagorska, D. Djurado and R. Demadrille, 'Electroactive materials for organic electronics: preparation strategies, structural aspects and characterization techniques', *Chem. Soc. Rev.*, 2010, **39**, 2577–2632.

148. J. M. Tour, 'Molecular electronics. Synthesis and testing of components', *Acc. Chem. Res.*, 2000, **33**, 791–804.

149. R. L. Carroll and C. B. Gorman, 'The genesis of molecular electronics', *Angew. Chem. Int. Ed.*, 2002, **41**, 4378–4400.

150. N. Robertson and C. A. McGowan, 'A comparison of potential molecular wires as components for molecular electronics.', *Chem. Soc. Rev.*, 2003, **32**, 96–103.

151. R. M. Metzger, 'Unimolecular Electronics', *Chem. Rev.*, 2015, **115**, 5056–5115.

152. R. E. Martin and F. Diederich, 'Linear Monodisperse π-Conjugated Oligomers: Model Compounds for Polymers and More', *Angew. Chem. Int. Ed.*, 1999, **38**, 1350–1377.

153. W. B. Davis, M. A. Ratner and M. R. Wasielewski, 'Conformational gating of long distance electron transfer through wire-like bridges in donor-bridge-acceptor molecules', *J. Am. Chem. Soc.*, 2001, **123**, 7877–7886.

154. N. Yoshida, T. Ishizuka, A. Osuka, D. H. Jeong, H. S. Cho, D. Kim, Y. Matsuzaki, A. Nogami and K. Tanaka, 'Fine Tuning of Photophysical Properties of *meso–meso*-Linked Zn^{II}-Diporphyrins by Dihedral Angle Control', *Chem. – Eur. J.*, 2003, **9**, 58–75.

155. L. Venkataraman, J. E. Klare, C. Nuckolls, M. S. Hybertsen and M. L. Steigerwald, 'Dependence of single-molecule junction conductance on molecular conformation.', *Nature*, 2006, **442**, 904–907.

156. T. K. Ahn, K. S. Kim, D. Y. Kim, S. B. Noh, N. Aratani, C. Ikeda, A. Osuka and D. Kim, 'Relationship between Two-Photon Absorption and the π-Conjugation Pathway in Porphyrin Arrays through Dihedral Angle Control', *J. Am. Chem. Soc.*, 2006, **128**, 1700–1704.

157. M.-H. Chang, M. Hoffmann, H. L. Anderson and L. M. Herz, 'Dynamics of excited-state conformational relaxation and electronic delocalization in conjugated porphyrin oligomers.', *J. Am. Chem. Soc.*, 2008, **130**, 10171–10178.

158. A. A. Kocherzhenko, K. B. Whaley, G. Sforazzini, H. L. Anderson, M. Wykes, D. Beljonne, F. C. Grozema and L. D. A. Siebbeles, 'Effects of the Environment on Charge Transport in Molecular Wires', *J. Phys. Chem. C*, 2012, **116**, 25213–25225.

159. L. Sun, Y. A. Diaz-Fernandez, T. A. Gschneidtner, F. Westerlund, S. Lara-Avila and K. Moth-Poulsen, 'Single-molecule electronics: from chemical design to functional devices.', *Chem. Soc. Rev.*, 2014, **43**, 7378–7411.

160. V. S.-Y. Lin, S. G. DiMagno and M. J. Therien, 'Highly Conjugated, Acetylenyl Bridged Porphyrins: New Models for Light-Harvesting Antenna Systems', *Science*, 1994, **264**, 1105–1111.

161. V. S.-Y. Lin and M. J. Therien, 'The Role of Porphyrin-to-Porphyrin Linkage Topology in the Extensive Modulation of the Absorptive and Emissive Properties of a Series of Ethynyl- and Butadiynyl-Bridged Bis- and Tris(porphinato)zinc Chromophores', *Chem. – Eur. J.*, 1995, **1**, 645–651.

162. H. A. Collins, M. Khurana, E. H. Moriyama, A. Mariampillai, E. Dahlstedt, M. Balaz, M. K. Kuimova, M. Drobizhev, V. X. D. Yang, D. Phillips, A. Rebane, B. C. Wilson and H. L. Anderson, 'Blood-vessel closure using photosensitizers engineered for two-photon excitation', *Nat. Photon.*, 2008, **2**, 420–424.

163. J. D. Wilkinson, G. Wicks, A. Nowak-Król, Ł. G. Łukasiewicz, C. J. Wilson, M. Drobizhev, A. Rebane, D. T. Gryko and H. L. Anderson, 'Two-photon absorption in butadiyne-linked porphyrin dimers: torsional and substituent effects', *J. Mat. Chem. C*, 2014, **2**, 6802–6809.

164. Y. Nakamura, N. Aratani and A. Osuka, 'Cyclic porphyrin arrays as artificial photosynthetic antenna: synthesis and excitation energy transfer.', *Chem. Soc. Rev.*, 2007, **36**, 831–845.

165. G. Sedghi, K. Sawada, L. J. Esdaile, M. Hoffmann, H. L. Anderson, D. Bethell, W. Haiss, S. J. Higgins and R. J. Nichols, 'Single Molecule Conductance of Porphyrin Wires with Ultralow Attenuation', *J. Am. Chem. Soc.*, 2008, **130**, 8582–8583.

166. G. Sedghi, V. M. García-Suárez, L. J. Esdaile, H. L. Anderson, C. J. Lambert, S. Martín, D. Bethell, S. J. Higgins, M. Elliott, N. Bennett, J. E. Macdonald and R. J. Nichols, 'Long-range electron tunnelling in oligo-porphyrin molecular wires', *Nat. Nanotech.*, 2011, **6**, 517–523.

167. G. Sedghi, L. J. Esdaile, H. L. Anderson, S. Martin, D. Bethell, S. J. Higgins and R. J. Nichols, 'Comparison of the conductance of three types of porphyrin-based molecular wires: β-meso,β-fused tapes, meso-butadiyne-linked and twisted meso-meso linked oligomers', *Adv. Mat.*, 2012, **24**, 653–657.

168. P. N. Taylor, J. Huuskonen, G. Rumbles, R. T. Aplin, E. Williams and H. L. Anderson, 'Conjugated porphyrin oligomers from monomer to hexamer', *Chem. Comm.*, 1998, 909–910.

169. M. Hoffmann, C. J. Wilson, B. Odell and H. L. Anderson, 'Template-directed synthesis of a π-conjugated porphyrin nanoring.', *Angew. Chem. Int. Ed.*, 2007, **46**, 3122–3125.

170. J. K. Sprafke, B. Odell, T. D. W. Claridge and H. L. Anderson, 'All-or-nothing cooperative self-assembly of an annulene sandwich', *Angew. Chem. Int. Ed.*, 2011, **50**, 5572–5575.

171. M. J. Frampton, H. Akdas, A. R. Cowley, J. E. Rogers, J. E. Slagle, P. A. Fleitz, M. Drobizhev, A. Rebane and H. L. Anderson, 'Synthesis, Crystal Structure, and Nonlinear Optical Behavior of β-Unsubstituted *meso–meso E*-Vinylene-Linked Porphyrin Dimers', *Org. Lett.*, 2005, **7**, 5365–5368.

172. J. S. Lindsey, S. Prathapan, T. E. Johnson and R. W. Wagner, 'Porphyrin building blocks for modular construction of bioorganic model systems', *Tetrahedron*, 1994, **50**, 8941–8968.

173. R. W. Wagner, T. E. Johnson, F. Li and J. S. Lindsey, 'Synthesis of Ethyne-Linked or Butadiyne-Linked Porphyrin Arrays Using Mild, Copper-Free, Pd-Mediated Coupling Reactions', *J. Org. Chem.*, 1995, **60**, 5266–5273.

174. M. Pawlicki, M. Morisue, N. K. S. Davis, D. G. McLean, J. E. Haley, E. Beuerman, M. Drobizhev, A. Rebane, A. L. Thompson, S. I. Pascu, G. Accorsi, N. Armaroli and H. L. Anderson, 'Engineering conjugation in para-phenylene-bridged porphyrin tapes', *Chem. Sci.*, 2012, **3**, 1541–1547.

175. A. Tsuda, H. Furuta and A. Osuka, 'Syntheses, structural characterizations, and optical and electrochemical properties of directly fused diporphyrins.', *J. Am. Chem. Soc.*, 2001, **123**, 10304–10321.

176. R. Stranger, J. E. McGrady, D. P. Arnold, I. Lane and G. A. Heath, 'Communication between Porphyrin Rings in the Butadiyne-Bridged Dimer Ni(OEP)(μ-C_4)Ni(OEP): A Density Functional Study', *Inorg. Chem.*, 1996, **35**, 7791–7797.

177. T. Yanai, D. P. Tew and N. C. Handy, 'A new hybrid exchange-correlation functional using the Coulomb-attenuating method (CAM-B3LYP)', *Chem. Phys. Lett.*, 2004, **393**, 51–57.

178. L. Rintoul, S. R. Harper and D. P. Arnold, 'A systematic theoretical study of the electronic structures of porphyrin dimers: DFT and TD-DFT calculations on diporphyrins linked by ethane, ethene, ethyne, imine, and azo bridges.', *Phys. Chem. Chem. Phys.*, 2013, **15**, 18951–18964.

179. M. K. Kuimova, M. Balaz, H. L. Anderson and P. R. Ogilby, 'Intramolecular rotation in a porphyrin dimer controls singlet oxygen production.', *J. Am. Chem. Soc.*, 2009, **131**, 7948–7949.

180. M. K. Kuimova, S. W. Botchway, A. W. Parker, M. Balaz, H. A. Collins, H. L. Anderson, K. Suhling and P. R. Ogilby, 'Imaging intracellular viscosity of a single cell during photoinduced cell death.', *Nat. Chem.*, 2009, **1**, 69–73.

181. A. Vyniauskas, M. Qurashi, N. Gallop, M. Balaz, H. L. Anderson and M. K. Kuimova, 'Unravelling the effect of temperature on viscosity-sensitive fluorescent molecular rotors', *Chem. Sci.*, 2015, **6**, 5773–5778.

182. M. Drobizhev, Y. Stepanenko, A. Rebane, C. J. Wilson, T. E. Screen and H. L. Anderson, 'Strong cooperative enhancement of two-photon absorption in double-strand conjugated porphyrin ladder arrays', *J. Am. Chem. Soc.*, 2006, **128**, 12432–12433.

183. F. C. Grozema, C. Houarner-Rassin, P. Prins, L. D. A. Siebbeles and H. L. Anderson, 'Supramolecular control of charge transport in molecular wires.', *J. Am. Chem. Soc.*, 2007, **129**, 13370–13371.

184. M. U. Winters, J. Kärnbratt, H. E. Blades, C. J. Wilson, M. J. Frampton, H. L. Anderson and B. Albinsson, 'Control of electron transfer in a conjugated porphyrin dimer by selective excitation of planar and perpendicular conformers', *Chem. – Eur. J.*, 2007, **13**, 7385–7394.

185. A. Tsuda, H. Hu, R. Tanaka and T. Aida, 'Planar or perpendicular? Conformational preferences of π-conjugated metalloporphyrin dimers and trimers in supramolecular tubular arrays', *Angew. Chem. Int. Ed.*, 2005, **44**, 4884–4888.

186. C. E. Tait, P. Neuhaus, M. D. Peeks, H. L. Anderson and C. R. Timmel, 'Transient EPR Reveals Triplet State Delocalization in a Series of Cyclic and Linear π-Conjugated Porphyrin Oligomers', *J. Am. Chem. Soc.*, 2015, **137**, 8284–8293.

187. M. J. Frisch, G. W. Trucks, H. B. Schlegel, G. E. Scuseria, M. A. Robb, J. R. Cheeseman, G. Scalmani, V. Barone, B. Mennucci, G. A. Petersson, H. Nakatsuji, M. Caricato, X. Li, H. P. Hratchian, A. F. Izmaylov, J. Bloino, G. Zheng, J. L. Sonnenberg, M. Hada, M. Ehara, K. Toyota, R. Fukuda, J. Hasegawa, M. Ishida, T. Nakajima, Y. Honda, O. Kitao, H. Nakai, T. Vreven, J. A. Montgomery Jr., J. E. Peralta, F. Ogliaro, M. Bearpark, J. J. Heyd, E. Brothers, K. N. Kudin, V. N. Staroverov, R. Kobayashi, J. Normand, K. Raghavachari, A. Rendell, J. C. Burant, S. S. Iyengar, J. Tomasi, M. Cossi, N. Rega, J. M. Millam, M. Klene, J. E. Knox, J. B. Cross, V. Bakken, C. Adamo, J. Jaramillo, R. Gomperts, R. E. Stratmann, O. Yazyev, A. J. Austin, R. Cammi, C. Pomelli, J. W. Ochterski, R. L. Martin, K. Morokuma, V. G. Zakrzewski, G. A. Voth, P. Salvador, J. J. Dannenberg, S. Dapprich, A. D. Daniels, Ö. Farkas, J. B. Foresman, J. V. Ortiz, J. Cioslowski and D. J. Fox, *Gaussian 09 Revision D.01*, software, Wallingford CT, 2009.

188. A. D. Becke, 'Density-functional thermochemistry. III. The role of exact exchange', *J. Chem. Phys.*, 1993, **98**, 5648–5652.

189. R. Ditchfield, W. J. Hehre and J. A. Pople, 'Self-Consistent Molecular-Orbital Methods. IX. An Extended Gaussian-Type Basis for Molecular-Orbital Studies of Organic Molecules', *J. Chem. Phys.*, 1971, **54**, 724–728.

190. W. J. Hehre, R. Ditchfield and J. A. Pople, 'Self-Consistent Molecular Orbital Methods. XII. Further Extensions of Gaussian-Type Basis Sets for Use in Molecular Orbital Studies of Organic Molecules', *J. Chem. Phys.*, 1972, **56**, 2257–2261.

191. P. C. Hariharan and J. A. Pople, 'The influence of polarization functions on molecular orbital hydrogenation energies', *Theor. Chim. Acta*, 1973, **28**, 213–222.

192. V. A. Rassolov, J. A. Pople, M. A. Ratner and T. L. Windus, '6-31G$*$ basis set for atoms K through Zn', *J. Chem. Phys.*, 1998, **109**, 1223–1229.

193. P. J. Hay and W. R. Wadt, 'Ab initio effective core potentials for molecular calculations. Potentials for the transition metal atoms Sc to Hg', *J. Chem. Phys.*, 1985, **82**, 270–283.

194. P. J. Hay and W. R. Wadt, 'Ab initio effective core potentials for molecular calculations. Potentials for K to Au including the outermost core orbitals', *J. Chem. Phys.*, 1985, **82**, 299–310.

195. E. F. Pettersen, T. D. Goddard, C. C. Huang, G. S. Couch, D. M. Greenblatt, E. C. Meng and T. E. Ferrin, 'UCSF Chimera—a visualization system for exploratory research and analysis', *J. Comp. Chem.*, 2004, **25**, 1605–1612.

196. G. U. Bublitz and S. G. Boxer, 'Effective polarity of frozen solvent glasses in the vicinity of dipolar solutes', *J. Am. Chem. Soc.*, 1998, **120**, 3988–3992.

197. J. Kärnbratt, M. Gilbert, J. K. Sprafke, H. L. Anderson and B. Albinsson, 'Self-Assembly of Linear Porphyrin Oligomers into Well-Defined Aggregates', *J. Phys. Chem. C*, 2012, **116**, 19630–19635.

198. M. Hutin, J. K. Sprafke, B. Odell, H. L. Anderson and T. D. Claridge, 'A discrete three-layer stack aggregate of a linear porphyrin tetramer: solution-phase structure elucidation by NMR and X-ray scattering', *J. Am. Chem. Soc.*, 2013, **135**, 12798–12807.

199. H. L. Anderson, 'Supramolecular orientation of conjugated porphyrin oligomers in stretched polymers', *Adv. Mat.*, 1994, **6**, 834–836.

200. M. Drobizhev, Y. Stepanenko, Y. Dzenis, A. Karotki, A. Rebane, P. N. Taylor and H. L. Anderson, 'Extremely Strong Near-IR Two-Photon Absorption in Conjugated Porphyrin Dimers: Quantitative Description with Three-Essential-States Model', *J. Phys. Chem. B*, 2005, **109**, 7223–7236.

201. F. Santoro, A. Lami, R. Improta, J. Bloino and V. Barone, 'Effective method for the computation of optical spectra of large molecules at finite temperature including the Duschinsky and Herzberg-Teller effect: the Q_x band of porphyrin as a case study.', *J. Chem. Phys.*, 2008, **128**, 224311–224317.

202. V. Barone, J. Bloino, M. Biczysko and F. Santoro, 'Fully Integrated Approach to Compute Vibrationally Resolved Optical Spectra: From Small Molecules to Macrosystems', *J. Chem. Theory Comput.*, 2009, **5**, 540–554.

203. F. V. A. Camargo, H. L. Anderson, S. R. Meech and I. A. Heisler, 'Full Characterization of Vibrational Coherence in a Porphyrin Chromophore by Two-Dimensional Electronic Spectroscopy', *J. Phys. Chem. A*, 2015, **119**, 95–101.

204. K. O. Hartman, G. L. Carlson, R. E. Witkowski and W. G. Fateley, 'The measurement of conformational equilibria via the infrared studies of 1,1-dibromo-3-fluorobutadiene-1,3 and 1,1-dichloro-3-fluorobutadiene-1,3', *Spectrochim. Acta Mol. Biomol. Spectrosc.*, 1968, **24**, 157–167.

205. J. R. Durig, J. Liu, T. S. Little and V. F. Kalasinsky, 'Conformational analysis, barriers to internal rotation, vibrational assignment, and ab initio calculations of 1,2-difluoroethane', *J. Phys. Chem.*, 1992, **96**, 8224–8233.

206. K. Hagen and K. Hedberg, 'Conformational analysis. I. Molecular structure, composition, trans-gauche energy and entropy differences, and potential hindering internal rotation of gaseous oxalyl chloride as determined by electron diffraction', *J. Am. Chem. Soc.*, 1973, **95**, 1003–1009.

207. K. Okuyama, T. Hasegawa, M. Ito and N. Mikami, 'Electronic spectra of tolan in a supersonic free jet: large-amplitude torsional motion', *J. Phys. Chem.*, 1984, **88**, 1711–1716.

208. W. Olson and D. Papousek, 'High-resolution infrared spectra of ethanelike molecules and the barrier to internal rotation: The ν_9, ν_{13} band of dimethylacetylene', *J. Mol. Spectrosc.*, 1971, **37**, 527–534.

209. P. W. Thulstrup, S. V. Hoffmann, B. K. V. Hansen and J. Spanget-Larsen, 'Unique interplay between electronic states and dihedral angle for the molecular rotor diphenyldiacetylene.', *Phys. Chem. Chem. Phys.*, 2011, **13**, 16168–16174.

210. J. A. Sebree and T. S. Zwier, 'The excited states and vibronic spectroscopy of diphenyldiacetylene and diphenylvinylacetylene', *Phys. Chem. Chem. Phys.*, 2012, **14**, 173–183.

211. S. J. Greaves, E. L. Flynn, E. L. Futcher, E. Wrede, D. P. Lydon, P. J. Low, S. R. Rutter and A. Beeby, 'Cavity ring-down spectroscopy of the torsional motions of 1,4-bis(phenylethynyl)benzene', *J. Phys. Chem. A*, 2006, **110**, 2114–2121.

212. M. Wierzbicka, I. Byliska, C. Czaplewski and W. Wiczk, 'Experimental and theoretical studies of the spectroscopic properties of simple symmetrically substituted diphenylacetylene derivatives', *RSC Adv.*, 2015, **5**, 29294–29303.

213. M. J. G. Peach, E. I. Tellgren, P. Saek, T. Helgaker and D. J. Tozer, 'Structural and electronic properties of polyacetylene and polyyne from hybrid and Coulomb-attenuated density functionals', *J. Phys. Chem. A*, 2007, **111**, 11930–11935.

214. A. Berlicka, L. Latos-Grazyski and T. Lis, '1H NMR investigation of high-spin and low-spin iron(III) meso-ethynylporphyrins', *Inorg. Chem.*, 2005, **44**, 4522–4533.

215. Y.-J. Chen, S.-S. Chen, S.-S. Lo, T.-H. Huang, C.-C. Wu, G.-H. Lee, S.-M. Peng and C.-Y. Yeh, 'Porphyrin dimers bridged by a platinumdiacetylide unit', *Chem. Comm.*, 2006, **5**, 1015–1017.

216. G. W. Coates, A. R. Dunn, L. M. Henling, D. A. Dougherty and R. H. Grubbs, 'Phenyl–Perfluorophenyl Stacking Interactions: A New Strategy for Supermolecule Construction', *Angew. Chem. Int. Ed.*, 1997, **36**, 248–251.

217. C. Glock, F. M. Younis, S. Ziemann, H. Görls, W. Imhof, S. Krieck and M. Westerhausen, '2,6-Diisopropylphenylamides of Potassium and Calcium: A Primary Amido Ligand in s-Block Metal Chemistry with an Unprecedented Catalytic Reactivity', *Organometallics*, 2013, **32**, 2649–2660.

218. M. Gdaniec, W. Jankowski, M. J. Milewska and T. Pooñski, 'Supramolecular Assemblies of Hydrogen-Bonded Carboxylic Acid Dimers Mediated by PhenylPentafluorophenyl Stacking Interactions', *Angew. Chem. Int. Ed.*, 2003, **42**, 3903–3906.

219. J. K. D. Surette, M.-A. MacDonald, M. J. Zaworotko and R. D. Singer, 'X-ray crystal structure of 1,4-diphenylbutadiyne', *J. Chem. Crystallogr.*, 1994, **24**, 715–717.

220. F. R. Fronczek and M. S. Erickson, 'Refinements of the crystal structures of 1,4-diphenylbutadiyne and its complex with two moles of $Co_2(CO)_6$', *J. Chem. Crystallogr.*, 1995, **25**, 737–742.

221. M. Shi and H.-X. Qian, 'NHC Pd(II) complex Cu(I) co-catalyzed homocoupling reaction of terminal alkynes', *Appl. Organomet. Chem.*, 2006, **20**, 771–774.

222. I. J. Bruno, J. C. Cole, P. R. Edgington, M. Kessler, C. F. Macrae, P. McCabe, J. Pearson and R. Taylor, 'New software for searching the Cambridge Structural Database and visualizing crystal structures.', *Acta Crystallogr., Sect. B: Struct. Sci., Cryst. Eng. Mater.*, 2002, **58**, 389–397.

223. F. H. Allen, 'The Cambridge Structural Database: a quarter of a million crystal structures and rising.', *Acta Crystallogr., Sect. B: Struct. Sci., Cryst. Eng. Mater.*, 2002, **58**, 380–388.

224. R. Thomas, S. S. Mallajyosula, S. Lakshmi, S. K. Pati and G. Kulkarni, 'Conjugation in 1,4-diphenylbutadiyne and 1,2-diphenylacetylene: A combined experimental and theoretical study', *J. Mol. Struct.*, 2009, **922**, 46–50.

225. L. D. Movsisyan, M. D. Peeks, G. M. Greetham, M. Towrie, A. L. Thompson, A. W. Parker and H. L. Anderson, 'Photophysics of Threaded sp-Carbon Chains: The Polyyne is a Sink for Singlet and Triplet Excitation', *J. Am. Chem. Soc.*, 2014, **136**, 17996–18008.

226. M. M. Yildizhan, D. Fazzi, A. Milani, L. Brambilla, M. Del Zoppo, W. A. Chalifoux, R. R. Tykwinski and G. Zerbi, 'Photogenerated cumulenic structure of adamantyl endcapped linear carbon chains: an experimental and computational investigation based on infrared spectroscopy.', *J. Chem. Phys.*, 2011, **134**, 124512.

227. R. L. Martin, 'Natural transition orbitals', *J. Chem. Phys.*, 2003, **118**, 4775–4777.

228. C. H. Hendon, D. Tiana, A. T. Murray, D. R. Carbery and A. Walsh, 'Helical frontier orbitals of conjugated linear molecules', *Chem. Sci.*, 2013, **4**, 4278–4284.

229. M. Liu, V. I. Artyukhov, H. Lee, F. Xu and B. I. Yakobson, 'Carbyne from First Principles: Chain of C Atoms, a Nanorod or a Nanorope', *ACS Nano*, 2013, **7**, 10075–10082.

230. M. D. Peeks, T. D. W. Claridge and H. L. Anderson, 'Aromatic and antiaromatic ring currents in a molecular nanoring', *Nature*, 2017, **541**, 200–203.

231. A. Lorke, R. Johannes Luyken, A. O. Govorov, J. P. Kotthaus, J. M. Garcia and P. M. Petroff, 'Spectroscopy of Nanoscopic Semiconductor Rings', *Phys. Rev. Lett.*, 2000, **84**, 2223–2226.

232. E. L. Spitler, C. A. Johnson and M. M. Haley, 'Renaissance of Annulene Chemistry', *Chem. Rev.*, 2006, **106**, 5344–5386.

233. D. Loss and P. Goldbart, 'Period and amplitude halving in mesoscopic rings with spin', *Phys. Rev. B*, 1991, **43**, 13762–13765.

234. D. V. Kondratuk, L. M. A. Perdigão, A. M. S. Esmail, J. N. O'Shea, P. H. Beton and H. L. Anderson, 'Supramolecular nesting of cyclic polymers', *Nat. Chem.*, 2015, **7**, 317–322.

235. P. Liu, Y. Hisamune, M. D. Peeks, B. Odell, J. Q. Gong, L. M. Herz and H. L. Anderson, 'Synthesis of Five-Porphyrin Nanorings by Using Ferrocene and Corannulene Templates', *Angew. Chem. Int. Ed.*, 2016, **55**, 8358–8362.

236. J. K. Sprafke, D. V. Kondratuk, M. Wykes, A. L. Thompson, M. Hoffmann, R. Drevinskas, W.-H. Chen, C. K. Yong, J. Kärnbratt, J. E. Bullock, M. Malfois, M. R. Wasielewski, B. Albinsson, L. M. Herz, D. Zigmantas, D. Beljonne and H. L. Anderson, 'Belt-shaped π-systems: relating geometry to electronic structure in a six-porphyrin nanoring.', *J. Am. Chem. Soc.*, 2011, **133**, 17262–17273.

237. S. Liu, D. V. Kondratuk, S. A. L. Rousseaux, G. Gil-Ramírez, M. C. O'Sullivan, J. Cremers, T. D. W. Claridge and H. L. Anderson, 'Caterpillar Track Complexes in Template-Directed Synthesis and Correlated Molecular Motion', *Angew. Chem. Int. Ed.*, 2015, **54**, 5355–5359.

238. D. de Bellefeuille, M. S. Askari, B. Lassalle-Kaiser, Y. Journaux, A. Aukauloo, M. Orio, F. Thomas and X. Ottenwaelder, 'Reversible Double Oxidation and Protonation of the Non-Innocent Bridge in a Nickel(II) Salophen Complex', *Inorg. Chem.*, 2012, **51**, 12796–12804.

239. S. L. Matthews and D. M. Heinekey, 'An oxidized active site model for the FeFe hydrogenase: Reduction with hydrogen gas', *Inorg. Chem.*, 2011, **50**, 7925–7927.

240. Y. Murata, F. Cheng, T. Kitagawa and K. Komatsu, 'Generation of Fullerenyl Cation $(EtO)_2P^+(OH)CH_2$ $-C_{60}^+$ from RC_{60}–H and from RC_{60}–C_{60} R (R = $CH_2P(O)(OEt)_2$)', *J. Am. Chem. Soc.*, 2004, **126**, 8874–8875.

241. S. Grimme, J. Antony, S. Ehrlich and H. Krieg, 'A consistent and accurate ab initio parametrization of density functional dispersion correction (DFT-D) for the 94 elements H-Pu', *J. Chem. Phys.*, 2010, **132**, 154104–154120.

242. Y. Zhao and D. G. Truhlar, 'The M06 suite of density functionals for main group thermochemistry, thermochemical kinetics, noncovalent interactions, excited states, and transition elements: two new functionals and systematic testing of four M06-class functionals and 12 other functionals', *Theor. Chem. Acc.*, 2008, **120**, 215–241.

243. J.-D. Chai and M. Head-Gordon, 'Long-range corrected hybrid density functionals with damped atom–atom dispersion corrections', *Phys. Chem. Chem. Phys.*, 2008, **10**, 6615–6620.

244. N. G. Connelly and W. E. Geiger, 'Chemical Redox Agents for Organometallic Chemistry.', *Chem. Rev.*, 1996, **96**, 877–910.

245. G. Karunanithy, A. Cnossen, H. Müller, M. D. Peeks, N. H. Rees, T. D. W. Claridge, H. L. Anderson and A. J. Baldwin, 'Harnessing NMR relaxation interference effects to characterise supramolecular assemblies', *Chem. Comm.*, 2016, **52**, 7450–7453.

246. D. F. Evans, '400. The determination of the paramagnetic susceptibility of substances in solution by nuclear magnetic resonance', *J. Chem. Soc. (Resumed)*, 1959, 2003.

247. R. Tamura, M. Ikuta, T. Hirahara and M. Tsukada, 'Positive magnetic susceptibility in polygonal nanotube tori', *Phys. Rev. B*, 2005, **71**, 1–7.

248. Y. Yamamoto, Y. Hirata, M. Kodama, T. Yamaguchi, S. Matsukawa, K.-Y. Akiba, D. Hashizume, F. Iwasaki, A. Muranaka, M. Uchiyama, P. Chen, K. M. Kadish and N. Kobayashi, 'Synthesis, reactions, and electronic properties of 16 pi-electron octaisobutyltetraphenylporphyrin.', *J. Am. Chem. Soc.*, 2010, **132**, 12627–12638.

249. M. Gouterman, 'Spectra of porphyrins', *J. Mol. Spectrosc.*, 1961, **6**, 138–163.

250. C. L. Perrin and T. J. Dwyer, 'Application of two-dimensional NMR to kinetics of chemical exchange', *Chem. Rev.*, 1990, **6**, 935–967.

251. E. M. Schubert, 'Utilizing the Evans Method with a Superconducting NMR Spectrometer in the Undergraduate Laboratory', *J. Chem. Ed.*, 1992, **69**, 62.

252. D. H. Grant, 'Paramagnetic Susceptibility by NMR: The "Solvent Correction" Reexamined', *J. Chem. Ed.*, 1995, **72**, 39–40.

253. C. Piguet, 'Paramagnetic Susceptibility by NMR: The "Solvent Correction" Removed for Large Paramagnetic Molecules', *J. Chem. Ed.*, 1997, **74**, 815–816.

254. J. Jeener, B. H. Meier, P. Bachmann and R. R. Ernst, 'Investigation of exchange processes by two-dimensional NMR spectroscopy', *J. Chem. Phys.*, 1979, **71**, 4546–4553.

255. M. L. H. Green, L. L. Wong and A. Sella, 'Relationship between intramolecular chemical exchange and NMR-observed rate constants', *Organometallics*, 1992, **11**, 2660–2668.

256. P. Bujak, I. Kulszewicz-Bajer, M. Zagorska, V. Maurel, I. Wielgus and A. Pron, 'Polymers for electronics and spintronics', *Chem. Soc. Rev.*, 2013, **42**, 8895–8999.

257. D. Xiang, X. Wang, C. Jia, T. Lee and X. Guo, 'Molecular-Scale Electronics: From Concept to Function', *Chem. Rev.*, 2016, **116**, 4318–4440.

258. C. J. Lambert, 'Basic concepts of quantum interference and electron transport in single-molecule electronics', *Chem. Soc. Rev.*, 2015, **44**, 875–888.

259. M. Magoga and C. Joachim, 'Conductance of molecular wires connected or bonded in parallel', *Phys. Rev. B*, 1999, **59**, 16011–16021.

260. M. L. Perrin, E. Burzurí and H. S. J. van der Zant, 'Single-molecule transistors', *Chem. Soc. Rev.*, 2015, **44**, 902–919.

261. S. V. Aradhya and L. Venkataraman, 'Single-molecule junctions beyond electronic transport', *Nat. Nanotech.*, 2013, **8**, 399–410.

262. E. Lörtscher, 'Wiring molecules into circuits', *Nat. Nanotech.*, 2013, **8**, 381–384.

263. R. J. Nichols, W. Haiss, S. J. Higgins, E. Leary, S. Martin and D. Bethell, 'The experimental determination of the conductance of single molecules.', *Phys. Chem. Chem. Phys.*, 2010, **12**, 2801–2815.

264. A. K. Feldman, M. L. Steigerwald, X. Guo and C. Nuckolls, 'Molecular electronic devices based on single-walled carbon nanotube electrodes', *Acc. Chem. Res.*, 2008, **41**, 1731–1741.

265. N. J. Tao, 'Electron transport in molecular junctions.', *Nat. Nanotech.*, 2006, **1**, 173–181.

266. T. Hines, I. Diez-Perez, J. Hihath, H. Liu, Z. S. Wang, J. Zhao, G. Zhou, K. Müllen and N. Tao, 'Transition from tunneling to hopping in single molecular junctions by measuring length and temperature dependence', *J. Am. Chem. Soc.*, 2010, **132**, 11658–11664.

267. Q. Lu, K. Liu, H. Zhang, Z. Du, X. Wang and F. Wang, 'From tunneling to hopping: A comprehensive investigation of charge transport mechanism in molecular junctions based on oligo(p-phenylene ethynylene)s', *ACS Nano*, 2009, **3**, 3861–3868.

268. B. Giese, 'Long-distance charge transport in DNA: The hopping mechanism', *Acc. Chem. Res.*, 2000, **33**, 631–636.

269. W. B. Davis, W. A. Svec, M. A. Ratner and M. R. Wasielewski, 'Molecular-wire behaviour in p-phenylenevinylene oligomers', *Nature*, 1998, **396**, 60–63.

270. T. Sakanoue and H. Sirringhaus, 'Band-like temperature dependence of mobility in a solution-processed organic semiconductor.', *Nat. Mater.*, 2010, **9**, 736–740.

271. J. F. Chang, T. Sakanoue, Y. Olivier, T. Uemura, M. B. Dufourg-Madec, S. G. Yeates, J. Cornil, J. Takeya, A. Troisi and H. Sirringhaus, 'Hall-effect measurements probing the degree of charge-carrier delocalization in solution-processed crystalline molecular semiconductors', *Phys. Rev. Lett.*, 2011, **107**, 066601.

272. J. Hankache and O. S. Wenger, 'Organic Mixed Valence', *Chem. Rev.*, 2011, **111**, 5138–5178.

273. C. Creutz and H. Taube, 'Direct approach to measuring the Franck-Condon barrier to electron transfer between metal ions', *J. Am. Chem. Soc.*, 1969, **91**, 3988–3989.

274. C. Wurster and E. Schobig, 'Ueber die Einwirkung oxydirender Agentien auf Tetramethylparaphenylendiamin', *Ber. Dtsch. Chem. Ges.*, 1879, **12**, 1807–1813.

275. F. Wudl, G. Smith and E. J. Hufnagel, 'Unusually Stable Organic Radical', *Chem. Commun.*, 1970, 1453–1454.

276. C. Lambert and G. Nöll, 'The Class II/III Transition in Triarylamine Redox Systems', *J. Am. Chem. Soc.*, 1999, **121**, 8434–8442.

277. M. B. Robin and P. Day, 'Mixed Valence Chemistry-A Survey and Classification', *Adv. Inorg. Chem. Radiochem.*, 1968, **10**, 247–422.

278. B. Badger and B. Brocklehurst, 'Absorption spectra of dimer cations. Part 1.—Olefins', *Trans. Faraday Soc.*, 1969, **65**, 2576–2581.

279. S. F. Nelsen, ''Almost delocalized' intervalence compounds', *Chem. – Eur. J.*, 2000, **6**, 581–588.

280. K. D. Demadis, C. M. Hartshorn and T. J. Meyer, 'The Localized-to-Delocalized Transition in Mixed-Valence Chemistry', *Chem. Rev.*, 2001, **101**, 2655–2686.

281. S. F. Nelsen, R. F. Ismagilov and D. R. Powell, 'Charge Localization in a Dihydrazine Analogue of Tetramethyl-*p*-phenylenediamine Radical Cation', *J. Am. Chem. Soc.*, 1996, **118**, 6313–6314.

282. M. Jurow, A. E. Schuckman, J. D. Batteas and C. M. Drain, 'Porphyrins as molecular electronic components of functional devices', *Coord. Chem. Rev.*, 2010, **254**, 2297–2310.

283. Z. F. Liu, S. Wei, H. Yoon, O. Adak, I. Ponce, Y. Jiang, W. D. Jang, L. M. Campos, L. Venkataraman and J. B. Neaton, 'Control of single-molecule junction conductance of porphyrins via a transition-metal center', *Nano Lett.*, 2014, **14**, 5365–5370.

284. B. K. Kang, N. Aratani, J. K. Lim, D. Kim, A. Osuka and K. H. Yoo, 'Length and temperature dependence of electrical conduction through dithiolated porphyrin arrays', *Chem. Phys. Lett.*, 2005, **412**, 303–306.

285. B. K. Kang, N. Aratani, J. K. Lim, D. Kim, A. Osuka and K. H. Yoo, 'Electrical transport properties and their reproducibility for linear porphyrin arrays', *Mater. Sci. Eng., C*, 2006, **26**, 1023–1027.

286. Z. Li, T. H. Park, J. Rawson, M. J. Therien and E. Borguet, 'Quasi-ohmic single molecule charge transport through highly conjugated meso-to-meso ethyne-bridged porphyrin wires', *Nano Lett.*, 2012, **12**, 2722–2727.

287. J. Rawson, P. J. Angiolillo, P. R. Frail, I. Goodenough and M. J. Therien, 'Electron Spin Relaxation of Hole and Electron Polarons in π-Conjugated Porphyrin Arrays: Spintronic Implications', *J. Phys. Chem. B*, 2015, **119**, 7681–7689.

288. T. M. Wilson, T. Hori, M.-C. Yoon, N. Aratani, A. Osuka, D. Kim and M. R. Wasielewski, 'Rapid Intramolecular Hole Hopping in meso-meso and meta-Phenylene Linked Linear and Cyclic Multiporphyrin Arrays', *J. Am. Chem. Soc.*, 2010, **132**, 1383–1388.

289. H. J. Shine, A. G. Padilla and S.-M. Wu, 'Ion radicals. 45. Reactions of zinc tetraphenylporphyrin cation radical perchlorate with nucleophiles', *J. Org. Chem.*, 1979, **44**, 4069–4075.

290. J. Jaumot, A. de Juan and R. Tauler, 'MCR-ALS GUI 2.0: New features and applications', *Chemom. Intell. Lab. Syst.*, 2015, **140**, 1–12.

291. C. Ruckebusch and L. Blanchet, 'Multivariate curve resolution: A review of advanced and tailored applications and challenges', *Anal. Chim. Acta*, 2013, **765**, 28–36.

292. G. H. Golub and C. Reinsch, 'Singular value decomposition and least squares solutions', *Numerische Mathematik*, 1970, **14**, 403–420.

293. M. Maeder, 'Evolving factor analysis for the resolution of overlapping chromatographic peaks', *Anal. Chem.*, 1987, **59**, 527–530.

294. O. A. Vydrov and G. E. Scuseria, 'Assessment of a long-range corrected hybrid functional', *J. Chem. Phys.*, 2006, **125**, 234109.

295. J. Tomasi, B. Mennucci and R. Cammi, 'Quantum Mechanical Continuum Solvation Models', *Chem. Rev.*, 2005, **105**, 2999–3094.

296. National Institute of Standards and Technology, *NIST Computational Chemistry Comparison and Benchmark Database*, ed. R. D. Johnson, 2016, `http://cccbdb.nist.gov` (visited on 08/12/2016).

297. D. P. Arnold, R. D. Hartnell, G. A. Heath, L. Newby and R. D. Webster, 'Remarkable homology in the electronic spectra of the mixed-valence cation and anion radicals of a conjugated bis(porphyrinyl)butadiyne.', *Chem. Commun.*, 2002, 754–755.

298. G. J. Wilson and D. P. Arnold, 'Time-Dependent Density Functional Molecular Orbital and Excited State Calculations on Bis(porphyrinyl)butadiynes in the Monocationic, Neutral, Monoanionic, and Dianionic Oxidation States', *J. Phys. Chem. A*, 2005, **109**, 6104–6113.

299. P. A. Lane, X. Wei and Z. V. Vardeny, 'Studies of charged excitations in pi-conjugated oligomers and polymers by optical modulation', *Phys. Rev. Lett.*, 1996, **77**, 1544–1547.

300. D. P. Arnold, G. A. Heath and D. A. James, 'Porphyrin Dimers Linked by Conjugated Butadiyne Bridges: Preparations, Spectra, Voltammetry and Reductive Spectroelectrochemistry of {[M(OEP)](μ-C_4)[M(OEP)]}($M_2 \equiv H_4$, Co_2, Ni_2, Cu_2, Zn_2, Pd_2, Pt_2, Co/Ni, Ni/Cu, Ni/Zn)', *J. Porph. Phthal.*, 1999, **3**, 5–31.

301. G. Heimel, 'The Optical Signature of Charges in Conjugated Polymers.', *ACS Cent. Sci.*, 2016, **2**, 309–315.

302. R. Österbacka, C. P. An, X. M. Jiang and Z. V. Vardeny, 'Two-Dimensional Electronic Excitations in Self-Assembled Conjugated Polymer Nanocrystals', *Science*, 2000, **287**, 839–842.

303. A. J. Heeger, S. Kivelson, J. R. Schrieffer and W. P. Su, 'Solitons in conducting polymers', *Rev. Mod. Phys.*, 1988, **60**, 781–850.

304. C. R. Fincher, M. Ozaki, A. J. Heeger and A. G. MacDiarmid, 'Donor and acceptor states in lightly doped polyacetylene, $(CH)_x$', *Phys. Rev. B*, 1979, **19**, 4140–4148.

305. M. G. Kaplunov, T. P. Panova and Y. G. Borodko, 'Infrared spectra of high–conductivity tetracyanoquinodimethane complexes: Vibronic effects', *Phys. Status Solidi A*, 1972, **13**, K67–K69.

306. J. R. Reimers and N. S. Hush, 'Modeling the bacterial photosynthetic reaction center. VII. Full simulation of the intervalence hole-transfer absorption spectrum of the special-pair radical cation', *J. Chem. Phys.*, 2003, **119**, 3262–3277.

307. M. J. Rice, 'Organic linear conductors as systems for the study of electron-phonon interactions in the organic solid state', *Phys. Rev. Lett.*, 1976, **37**, 36–39.

308. M. J. Rice, N. O. Lipari and S. Strässler, 'Dimerized organic linear-chain conductors and the unambiguous experimental determination of electron-molecular-vibration coupling constants', *Phys. Rev. Lett.*, 1977, **39**, 1359–1362.

309. M. J. Rice, V. M. Yartsev and C. S. Jacobsen, 'Investigation of the nature of the unpaired electron states in the organic semiconductor N-methyl-N-ethylmorpholinium-tetracyanoquinodimethane', *Phys. Rev. B*, 1980, **21**, 3437–3446.

310. R. C. Rocha and A. P. Shreve, 'Exploring the Localized-to-Delocalized Boundary in Mixed-Valence Systems Using Infrared Spectroelectrochemistry', *Inorg. Chem.*, 2004, **43**, 2231–2233.

311. R. Warratz and F. Tuczek, 'Low-energy bands of ferrocene-ferrocenium dimers: Bandshape analysis with a four-level two-mode vibronic coupling configuration interaction (VCCI) model including asymmetry', *Inorg. Chem.*, 2009, **48**, 3591–3607.

312. C. Kvarnström, H. Neugebauer, A. Ivaska and N. S. Sariciftci, 'Vibrational signatures of electrochemical p- and n-doping of poly(3,4- ethylenedioxythiophene) films: An in situ attenuated total reflection Fourier transform infrared (ATR-FTIR) study', *J. Mol. Struct.*, 2000, **521**, 271–277.

313. J. M. Zhuo, L. H. Zhao, P. J. Chia, W. S. Sim, R. H. Friend and P. K. H. Ho, 'Direct evidence for delocalization of charge carriers at the fermi level in a doped conducting polymer', *Phys. Rev. Lett.*, 2008, **100**, 186601.

314. M. Zamadar, S. Asaoka, D. C. Grills and J. R. Miller, 'Giant infrared absorption bands of electrons and holes in conjugated molecules', *Nat. Commun.*, 2013, **4**, 2818.

315. J. Yin, Z. Wang, D. Fazzi, Z. Shen and C. Soci, 'First-Principles Study of the Nuclear Dynamics of Doped Conjugated Polymers', *J. Phys. Chem. C*, 2016, **120**, 1994–2001.

316. D. Comoretto, C. Cuniberti, G. F. Musso, G. Dellepiane, F. Speroni, C. Botta and S. Luzzati, 'Optical properties and long-lived charged photoexcitations in polydiacetylenes', *Phys. Rev. B*, 1994, **49**, 8059–8066.

317. Z. Gasyna and P. N. Schatz, 'Analysis of the intervalence band in the oxidized photosynthetic bacterial reaction center', *J. Phys. Chem.*, 1996, **100**, 1445–1448.

318. R. Österbacka, X. M. Jiang, C. P. An, B. Horovitz and Z. V. Vardeny, 'Photoinduced Quantum Interference Antiresonances in π-Conjugated Polymers', *Phys. Rev. Lett.*, 2002, **88**, 226401.

319. M. Wohlgenannt and Z. Valy Vardeny, 'Photophysics properties of blue-emitting polymers', *Synth. Met.*, 2002, **125**, 55–63.

320. C. Castiglioni, J. Lopez Navarrete, G. Zerbi and M. Gussoni, 'A simple interpretation of the vibrational spectra of undoped, doped and photoexcited polyacetylene: Amplitude mode theory in the GF formalism', *Solid State Commun.*, 1988, **65**, 625–630.

321. A. Cravino, H. Neugebauer, S. Luzzati, M. Catellani, A. Petr, L. Dunsch and N. S. Sariciftci, 'Positive and Negative Charge Carriers in Doped or Photoexcited Polydithienothiophenes: A Comparative Study Using Raman, Infrared, and Electron Spin Resonance Spectroscopy', *J. Phys. Chem. B*, 2002, **106**, 3583–3591.

322. J. M. Speck, M. Korb, T. Rüffer, A. Hildebrandt and H. Lang, 'Substituent influence on charge transfer interactions in α, α'-Diferrocenylthiophenes', *Organometallics*, 2014, **33**, 4813–4823.

323. C. H. Londergan, J. C. Salsman, S. Ronco and C. P. Kubiak, 'Infrared activity of symmetric bridging ligand modes in pyrazine-bridged hexaruthenium mixed-valence clusters', *Inorg. Chem.*, 2003, **42**, 926–928.

324. Y. Hoshino, S. Higuchi, J. Fiedler, C. Y. Su, A. Knödler, B. Schwederski, B. Sarkar, H. Hartmann and W. Kaim, 'Long-range electronic coupling in various oxidation states of a C_4-linked tris(β-diketonato)ruthenium dimer', *Angew. Chem. Int. Ed.*, 2003, **42**, 674–677.

325. D. Lin-Vien, N. B. Colthup, W. G. Fateley and J. G. Grasselli, *The handbook of infrared and Raman characteristic frequencies of organic molecules*, Elsevier, 1991.

326. X. M. Jiang, R. Österbacka, O. Korovyanko, C. P. An, B. Horovitz, R. A. J. Janssen and Z. V. Vardeny, 'Spectroscopic studies of photoexcitations in regioregular and regiorandom polythiophene films', *Adv. Func. Mater.*, 2002, **12**, 587–597.

327. U. Fano, 'Effects of configuration interaction on intensities and phase shifts', *Phys. Rev.*, 1961, **124**, 1866–1878.

328. M. D. Sturge, H. J. Guggenheim and M. H. L. Pryce, 'Antiresonance in the Optical Spectra of Transition-Metal Ions in Crystals', *Phys. Rev. B*, 1970, **2**, 2459–2471.

329. F. Lapointe, I. Gaufrès, I. Tremblay, N. Y. W. Tang, R. Martel and P. Desjardins, 'Fano resonances in the midinfrared spectra of single-walled carbon nanotubes', *Phys. Rev. Lett.*, 2012, **109**, 097402.

330. B. Horovitz, R. Österbacka and Z. V. Vardeny, 'Multiple Fano effect in charge density wave systems', *Synth. Met.*, 2004, **141**, 179–183.

331. H. Johansson, C. Brabec, H. Neugebauer, C. Kvarnström, J. Hummelen, R. Janssen and N. Sariciftci, 'Photoinduced FT-IR spectroscopy of conjugated polymer/fullerene composites embedded into conventional host polymer matrices', *Synth. Met.*, 1999, **101**, 192–193.

332. J. Torras, J. Casanovas and C. Alemán, 'Reviewing extrapolation procedures of the electronic properties on the π-conjugated polymer limit', *J. Phys. Chem. A*, 2012, **116**, 7571–7583.

333. W. Kuhn, 'Über das Absorptionsspektrum der Polyene', *Helv. Chim. Acta*, 1948, **31**, 1780–1799.

334. H. Meier, U. Stalmach and H. Kolshorn, 'Effective conjugation length and UV/vis spectra of oligomers', *Acta Polym.*, 1997, **48**, 379–384.

335. P. Parkinson, D. V. Kondratuk, C. Menelaou, J. Q. Gong, H. L. Anderson and L. M. Herz, 'Chromophores in molecular nanorings: When is a ring a ring?', *J. Phys. Chem. Lett.*, 2014, **5**, 4356–4361.

336. J. Gierschner, J. Cornil and H. J. Egelhaaf, 'Optical bandgaps of π-conjugated organic materials at the polymer limit: Experiment and theory', *Adv. Mat.*, 2007, **19**, 173–191.

337. A. Gilbert and J. Baggott, *Essentials of Molecular Photochemistry*, Blackwell Scientific Publications, 1991.

338. A. Girlando, A. Painelli and Z. G. Soos, 'Electron–phonon coupling in conjugated polymers: Reference force field and transferable coupling constants for polyacetylene', *J. Chem. Phys.*, 1993, **98**, 7459–7465.

339. J. R. Norris, R. A. Uphaus, H. L. Crespi and J. J. Katz, 'Electron spin resonance of chlorophyll and the origin of signal I in photosynthesis.', *Proc. Natl. Acad. Sci. USA*, 1971, **68**, 625–628.

340. A. Schweiger and G. Jeschke, *Principles of Pulse Electron Paramagnetic Resonance*, Oxford University Press, Oxford, 2001.

341. T. Nakanishi, K. Terakura and T. Ando, 'Theory of Fano effects in an Aharonov-Bohm ring with a quantum dot', *Phys. Rev. B*, 2004, **69**, 115307.

342. B. Babić and C. Schönenberger, 'Observation of Fano resonances in single-wall carbon nanotubes', *Phys. Rev. B*, 2004, **70**, 195408.

343. K. Kobayashi, H. Aikawa, S. Katsumoto and Y. Iye, 'Mesoscopic Fano effect through a quantum dot in an Aharonov–Bohm ring', *Phys. E (Amsterdam, Neth.)*, 2004, **22**, 468–473.

344. R. Herges, 'Topology in Chemistry: Designing Möbius Molecules', *Chem. Rev.*, 2006, **106**, 4820–4842.

345. M. Kataoka, 'Magnetic susceptibility and aromaticity in the excited states of benzene', *J. Chem. Res.*, 2004, **2004**, 573–574.

346. P. B. Karadakov, 'Ground- and Excited-State Aromaticity and Antiaromaticity in Benzene and Cyclobutadiene', *J. Phys. Chem. A*, 2008, **112**, 7303–7309.

347. R. Breslow, H. W. Chang, R. Hill and E. Wasserman, 'Stable Triplet States of Some Cyclopentadienyl Cations', *J. Am. Chem. Soc.*, 1967, **89**, 1112–1119.

348. J. Wirz, 'Electronic Structure and Photophysical Properties of Planar Conjugated Hydrocarbons with a 4n-Membered Ring, Part II', *Jerusalem Symp. Quantum Chem. Biochem.*, 1977, **X**, 283–294.

349. J.-Y. Shin, K. S. Kim, M.-C. Yoon, J. M. Lim, Z. S. Yoon, A. Osuka and D. Kim, 'Aromaticity and photophysical properties of various topology-controlled expanded porphyrins', *Chem. Soc. Rev.*, 2010, **39**, 2751–2767.

350. J.-i. Aihara, 'Aromaticity-Based Theory of Pericyclic Reactions', *Bull. Chem. Soc. Jpn.*, 1978, **51**, 1788–1792.

351. R. Papadakis and H. Ottosson, 'The excited state antiaromatic benzene ring: a molecular Mr Hyde?', *Chem. Soc. Rev.*, 2015, **44**, 6472–6493.

352. C. E. Tait, P. Neuhaus, H. L. Anderson and C. R. Timmel, 'Triplet State Delocalization in a Conjugated Porphyrin Dimer Probed by Transient Electron Paramagnetic Resonance Techniques', *J. Am. Chem. Soc.*, 2015, **137**, 6670–6679.

353. C. E. Tait, P. Neuhaus, M. D. Peeks, H. L. Anderson and C. R. Timmel, 'Excitation wavelength-dependent EPR study on the influence of the conformation of multiporphyrin arrays on triplet state delocalization', *Phys. Chem. Chem. Phys.*, 2016, **18**, 5275–5280.

354. S. Richert, M. D. Peeks, C. E. Tait, H. L. Anderson and C. R. Timmel, 'Photogenerated triplet states in supramolecular porphyrin ladder assemblies: An EPR study', *Phys. Chem. Chem. Phys.*, 2016, **18**, 24171–24175.

355. C.-K. Yong, P. Parkinson, D. V. Kondratuk, W.-H. Chen, A. Stannard, A. Summerfield, J. K. Sprafke, M. C. O'Sullivan, P. H. Beton, H. L. Anderson and L. M. Herz, 'Ultrafast delocalization of excitation in synthetic light-harvesting nanorings', *Chem. Sci.*, 2015, **6**, 181–189.

356. J. Q. Gong, L. Favereau, H. L. Anderson and L. M. Herz, 'Breaking the Symmetry in Molecular Nanorings', *J. Phys. Chem. Lett.*, 2016, **7**, 332–338.

357. S. Masamune, F. A. Souto-Bachiller, T. Machiguchi and J. E. Bertie, 'Cyclobutadiene is not square', *J. Am. Chem. Soc.*, 1978, **100**, 4889–4891.

358. S. I. Allec, N. V. Ilawe and B. M. Wong, 'Unusual Bandgap Oscillations in Template-Directed π-Conjugated Porphyrin Nanotubes', *J. Phys. Chem. Lett.*, 2016, **7**, 2362–2367.

359. S. Zilberg and Y. Haas, 'Two-State Model of Antiaromaticity: The Triplet State. Is Hund's Rule Violated?', *J. Phys. Chem. A*, 1998, **102**, 10851–10859.

360. L. Adamska, I. Nayyar, H. Chen, A. K. Swan, N. Oldani, S. Fernandez-Alberti, M. R. Golder, R. Jasti, S. K. Doorn and S. Tretiak, 'Self-Trapping of Excitons, Violation of Condon Approximation, and Efficient Fluorescence in Conjugated Cycloparaphenylenes', *Nano Lett.*, 2014, **14**, 6539–6546.

361. F. De Proft and P. Geerlings, 'Relative hardness as a measure of aromaticity', *Phys. Chem. Chem. Phys.*, 2004, **6**, 242–248.

362. I. H. Nayyar, E. R. Batista, S. Tretiak, A. Saxena, D. L. Smith and R. L. Martin, 'Localization of electronic excitations in conjugated polymers studied by DFT', *J. Phys. Chem. Lett.*, 2011, **2**, 566–571.

363. H. Vazquez, R. Skouta, S. Schneebeli, M. Kamenetska, R. Breslow, L. Venkataraman and M. Hybertsen, 'Probing the conductance superposition law in single-molecule circuits with parallel paths', *Nat. Nanotech.*, 2012, **7**, 663–667.

364. S. Richert, J. Cremers, I. Kuprov, M. D. Peeks, H. L. Anderson and C. R. Timmel, 'Constructive quantum interference in a bis-copper six-porphyrin nanoring', *Nat. Commun.*, 2017, **8**, 14842.

365. W. Chen, H. Li, J. R. Widawsky, C. Appayee, L. Venkataraman and R. Breslow, 'Aromaticity decreases single-molecule junction conductance', *J. Am. Chem. Soc.*, 2014, **136**, 918–920.

366. S. K. S. Mazinani, R. V. Meidanshahi, J. L. Palma, P. Tarakeshwar, T. Hansen, M. A. Ratner and V. Mujica, 'Polarizability as a Molecular Descriptor for Conductance in Organic Molecular Circuits', *J. Phys. Chem. C*, 2016, **120**, 26054–26060.

367. T. A. Su, M. Neupane, M. L. Steigerwald, L. Venkataraman and C. Nuckolls, 'Chemical principles of single-molecule electronics', *Nat. Rev. Mater.*, 2016, **1**, 16002.

368. A. A. Kocherzhenko, F. C. Grozema and L. D. A. Siebbeles, 'Single molecule charge transport: from a quantum mechanical to a classical description.', *Phys. Chem. Chem. Phys.*, 2011, **13**, 2096–2110.

369. C. S. Wannere, K. W. Sattelmeyer, H. F. Schaefer and P. v. R. Schleyer, 'Aromaticity: The Alternating C–C Bond Length Structures of [14]-, [18]-, and [22]-Annulene', *Angew. Chem. Int. Ed.*, 2004, **43**, 4200–4206.

370. C. J. Wilson, 'Large porphyrin-based π-systems', Ph.D. Thesis, University of Oxford, 2006.

371. M. U. Winters, E. Dahlstedt, H. E. Blades, C. J. Wilson, M. J. Frampton, H. L. Anderson and B. Albinsson, 'Probing the efficiency of electron transfer through porphyrin-based molecular wires.', *J. Am. Chem. Soc.*, 2007, **129**, 4291–4297.